Modeling and Experimental Investigation of Renewable Energy and Ammonia-Based Systems for Carbon Capturing and Useful Outputs

by

Khaled H. M. Al-Hamed

A Thesis Submitted in Partial Fulfillment

of the Requirements for the Degree of

Doctor of Philosophy in Mechanical Engineering

in

The Faculty of Engineering and Applied Science

University of Ontario Institute of Technology

Oshawa, Ontario, Canada

April 2022

© Khaled H. M. Al-Hamed, 2022

Thesis Examination Information

Submitted by: **Khaled H. M. Al-Hamed**

Doctor of Philosophy in **Mechanical Engineering**

Thesis title: **Modeling and Experimental Investigation of Renewable Energy and Ammonia-Based Systems for Carbon Capturing and Useful Outputs**

An oral defense of this thesis took place on April 13, 2022 in front of the following examining committee:

Examining Committee:

Chair of Examining Committee	Dr. Martin Agelin-Chaab
Research Supervisor	Dr. Ibrahim Dincer
Examining Committee Member	Dr. Bekir Yilbas
Examining Committee Member	Dr. Dipal Patel
University Examiner	Dr. Matthew Harker
External Examiner	Dr. Nuri Azbar, Ege University

The above committee determined that the thesis is acceptable in form and content and that a satisfactory knowledge of the field covered by the thesis was demonstrated by the candidate during an oral examination. A signed copy of the Certificate of Approval is available from the School of Graduate and Postdoctoral Studies.

Abstract

This thesis work focuses on developing ammonia-based carbon capturing systems that produce useful chemical outputs to offset the energy penalty typically imposed by implementing a carbon capture retrofitting to a power plant. These systems have been investigated through models that are based on exergy and economics tools. The motivation, and the objectives of this work are mentioned. Next, a thorough literature review of the topic of ammonia-based carbon capture systems is provided here to identify the gaps in knowledge. This review concluded that there is a significant lack in experimental investigations of ammonia-based carbon capture systems that are powered by renewable energy sources. Also, the direction of future carbon capture systems is moving towards co-producing of useful and valuable chemicals to offset the costs of operating such systems. By knowing this, renewable energy and ammonia-based carbon capturing systems that produce ammonium bicarbonate are developed and described. Thermodynamic models of the present carbon capturing systems are established using the energy and exergy tools. After that, exergoeconomic models are explained for these systems. Results of the simulation work show that the use of an electrochemical ammonia synthesizer has 13.3% lower energy requirements compared to the use of a proton-exchange membrane electrolyzer and the Haber-Bosch process for ammonia synthesis. The cost of producing ammonium bicarbonate is almost 16% of the market price of this chemical commodity. This indicates that the developed carbon capturing system are financially feasible to produce monetary value.

Keywords: Carbon capture; ammonia; efficiency; power plant; renewable energy.

Author's Declaration

I hereby declare that this thesis consists of original work of which I have authored. This is a true copy of the thesis, including any required final revisions, as accepted by my examiners.

I authorize the University of Ontario Institute of Technology (Ontario Tech University) to lend this thesis to other institutions or individuals for the purpose of scholarly research. I further authorize University of Ontario Institute of Technology (Ontario Tech University) to reproduce this thesis by photocopying or by other means, in total or in part, at the request of other institutions or individuals for the purpose of scholarly research. I understand that my thesis will be made electronically available to the public.

_____ Khaled H. M. Al-Hamed

Acknowledgements

Professor Dr. Ibrahim Dincer is a very excellent supervisor who has guided me throughout my graduate studies and has kindly provided me with valuable feedback.

I would like to thank all my colleagues and friends in the Clean Energy Research Laboratory (CERL) who have helped me and encouraged me to complete this work. Special thanks to Dr. Dogan Erdemir, Andre Bolt, and Khalid Altayib for their support during my research.

Also, I would like to thank the committee members who have given me their effective feedback on my research. I would like to thank Dr. Bekir Sami Yilbas for his encouragement and support throughout my university studies. Lastly, I would like to acknowledge the support of my family and friends over the course of my graduate studies and I deeply appreciate them.

Statement of Contributions

Parts of the work described in this thesis have been published as:

K. H. M. Al-Hamed and I. Dincer, “A comparative review of potential ammonia-based carbon capture systems,” *J. Environ. Manage.*, vol. 287, p. 112357, Jun. 2021, doi: 10.1016/j.jenvman.2021.112357.

K. H. M. Al-Hamed and I. Dincer, “A novel multigeneration ammonia-based carbon capturing system powered by a geothermal power plant for cleaner applications,” *J. Clean. Prod.*, vol. 321, p. 129017, Oct. 2021, doi: 10.1016/j.jclepro.2021.129017.

K. H. M. Al-Hamed and I. Dincer, “Analysis and economic evaluation of a unique carbon capturing system with ammonia for producing ammonium bicarbonate,” *Energy Convers. Manag.*, p. 115062, Dec. 2021, doi: 10.1016/j.enconman.2021.115062.

K. H. M. Al-Hamed and I. Dincer, “A new solar energy-based integrated carbon capturing system with a gas turbine-supercritical CO_2 combined power cycle,” *Energy Convers. Manag.*, vol. 251, p. 114999, Jan. 2022, doi: 10.1016/j.enconman.2021.114999.

K. H. M. Al-Hamed and I. Dincer, “Development and optimization of a multigeneration geothermal and solid-oxide fuel cell-based integrated system with carbon capturing,” *Appl. Therm. Eng.*, p. 118037, Jan. 2022, doi: 10.1016/j.applthermaleng.2022.118037.

K. H. M. Al-Hamed and I. Dincer, “Exergoeconomic analysis and optimization of a solar energy-based integrated system with oxy-combustion for combined power cycle and carbon capturing,” *Energy*, p. 123814, Jul. 2022, doi: 10.1016/j.energy.2022.123814.

Table of Contents

Thesis Examination Information ii
Abstract iii
Author's Declaration iv
Acknowledgements v
Statement of Contributions vi
Table of Contents vii
List of Figures ix
List of Tables xv
Nomenclature xvii
Chapter 1: Introduction 1
1.1 Current challenges 7
1.2 Motivation 8
1.3 Objectives 9
1.4 Novelties 10
1.5 Thesis Outline 10
Chapter 2: Literature Review 11
2.1 Carbon capturing methods 11
2.1.1 Carbon capturing strategies 11
2.1.2 Carbon capturing technologies 13
2.2 Novel ammonia-based systems of carbon capture 20
2.2.1 Renewable energy-based systems of carbon capture 20
2.2.2 Energy savings-focused systems of carbon capture 24
2.2.3 Integrated Gasification Combined Cycle (IGCC)-based systems of carbon capture 29
2.3 Comparative assessments 31
2.4 Future directions 35
2.5 Closing remarks on the literature review 36
2.6 Research gaps in the literature 38
Chapter 3: Systems Development and Experimental Setup 39
3.1 Carbon capturing system 1 39
3.2 Carbon capturing system 2 40
3.3 Carbon capturing system 3 42

3.4 Experimental setup and procedure 46
3.5 Calibration Data 52
Chapter 4: Modeling 55
4.1 Thermodynamic and exergoeconomic modeling of system 1 55
4.2 Thermodynamic and exergoeconomic modeling of system 2 65
4.3 Thermodynamic and exergoeconomic modeling of system 3 83
4.4 Multi-objective optimization procedure 94
4.5 Scale-up analysis 95
Chapter 5: Results and Discussion 98
5.1 Modeling results of system 1 98
5.1.1 Parametric studies of system 1 101
5.2 Modeling results of system 2 106
5.2.1 Parametric studies of system 2 115
5.2.2 Optimization study results of system 2 141
5.3 Modeling results of system 3 144
5.3.1 Parametric studies of system 3 152
5.3.2 Optimization study results of system 3 172
5.4 Experimental investigation results 175
5.5 Scale-up study results 181
Chapter 6: Conclusions and Recommendations 188
6.1 Conclusions 188
6.2 Recommendations 189
References 190
Appendix 207

List of Figures

Figure 1.1: Growth in carbon capturing capacity over the next decades (adapted from [4]). 2
Figure 2.1: Main categories of carbon capture technologies (adapted from [59]). 15
Figure 2.2: Illustration of the adsorption technology of CO_2 capture. 15
Figure 2.3: Illustration of the cryogenic technology of CO_2 capturing (adapted from [63]). 16
Figure 2.4: Illustration of the absorption technology of CO_2 capturing (adapted from [68]). 17
Figure 2.5: Illustration of the membrane technology of CO_2 capturing (adapted from [14]). 18
Figure 2.6: Categories of the novel ammonia-based system of carbon capture. 21
Figure 2.7: A thermal solar cell-assisted carbon capture system (adapted from [24]). 22
Figure 2.8: A renewable energy carbon capture system to produce urea and ammonia from the flue gases of an oxy-fuel combustion power plant (adapted from [79]). 24
Figure 2.9: A wind turbine-based carbon capture system with the production of ammonium bicarbonate (adapted from [81]). 25
Figure 2.10: A double-stage CO_2 absorber ammonia-based carbon capture system (adapted from [86]). 27
Figure 2.11: A diagram of a typical IGCC with a pre-combustion carbon separation system (adapted from [93]). 30
Figure 2.12: Comparative assessment of the energy requirements for the considered ammonia-based carbon capture systems. Data for these systems are taken from references mentioned in Table 2.3. 33
Figure 2.13: Comparative assessment of the CO_2 removal efficiency for the considered ammonia-based carbon capture systems. Data for these systems are taken from references mentioned in Table 2.3. 34
Figure 2.14: Comparative assessment of the price of products and carbon tax savings for the considered ammonia-based carbon capture systems. The logarithmic scale is used for clarity. Data for these systems are taken from references mentioned in Table 2.3. 35
Figure 2.15: Evolution of carbon capture systems. 37
Figure 3.1: A wind turbine-based carbon capture system with the production of ammonium bicarbonate. 40
Figure 3.2: A multigeneration integrated system based on geothermal energy and solid-oxide fuel cell with carbon capture. 43
Figure 3.3: A gas turbine-supercritical carbon dioxide integrated system with a solar energy-based carbon capture unit. 44
Figure 3.4: Experimental setup of ammonia-based carbon capture and ammonium bicarbonate production unit for the baseline case. 47
Figure 3.5: Experimental setup of the proposed ammonia-based carbon capture and ammonium bicarbonate production unit for the catalyst and induction heating cases. 48

Figure 3.6: a) Pieces of the steel catalyst used in the experimental setup. b) A closer look at the batch reactor with the induction heater and the catalyst pieces. 49
Figure 3.7: Experimental procedure for the proposed ammonia-based carbon capture and ammonium bicarbonate production unit. 50
Figure 3.8: Samples of the produced ammonium bicarbonate after the natural drying process for a) baseline case with 80%mol of CO_2, b) catalyst case with 80%mol of CO_2, and c) Induction heating case with 80%mol of CO_2. 50
Figure 3.9: Voltage versus temperature thermocouple calibration graph for a stainless-steel type K thermocouple. 53
Figure 3.10: Reference temperature versus thermocouple temperature calibration graph for a stainless-steel type K thermocouple. 54
Figure 4.1: A flowsheet of the modeled system produced by ASPEN Plus. N2-COMP is the nitrogen compressor, ASR is the Ammonia Synthesis Reactor, CO2CAPT is the carbon capture reactor, and SEP is the Separator. 56
Figure 4.2: A flowsheet of the PEM electrolyzer produced by ASPEN Custom Modeler. 64
Figure 5.1: Polarization curve for the PEM electrolyzer. 102
Figure 5.2: Power density curve against current density for the PEM electrolyzer. 102
Figure 5.3: Hydrogen production rate curve against power input for the PEM electrolyzer. 103
Figure 5.4: PEM electrolyzer energy efficiency against current density. 103
Figure 5.5: PEM electrolyzer exergy efficiency against current density. 104
Figure 5.6: Ammonium bicarbonate production rate against wind turbine power input. The percentages represent the ammonia conversion ratio in the carbon capture reactor. 105
Figure 5.7: CO_2 capture rate against wind turbine power input. The percentages represent the ammonia conversion ratio in the carbon capture reactor. 105
Figure 5.8: Energy requirement for CO_2 capture against wind turbine power input. The percentages represent the ammonia conversion ratio in the carbon capture reactor. 106
Figure 5.9: A logarithmic plot of the exergy destruction rate of the thermal components in system 2. A logarithmic scale is used for clarity to show the smaller values better. 111
Figure 5.10: A plot of the geothermal energy/exergy for CO_2 capture and the geothermal fluid mass flow rate versus geothermal fluid temperature. 117
Figure 5.11: A plot of electric power values for turbines 1,2, and EAS versus geothermal fluid temperature. 118
Figure 5.12: A plot of exergy destruction rates for turbines 1,2, and flash chambers 1,2 versus geothermal fluid temperature. 119
Figure 5.13: A plot of the geothermal energy/exergy for CO_2 capture and geothermal fluid mass flow rate versus faradaic efficiency. 120
Figure 5.14: A plot of electric power values and exergy destruction rate for electrochemical ammonia synthesizer versus faradaic efficiency. 121
Figure 5.15: A plot of energy requirement for CO_2 capture versus faradaic efficiency. 122
Figure 5.16: A plot of ammonia and ammonium bicarbonate production rates versus mass flow rate of natural gas. 122

Figure 5.17: A plot of SOFC subsystem energy and exergy efficiencies versus mass flow rate of natural gas. 123
Figure 5.18: Effects of geothermal fluid temperature on the overall exergy destruction rate and the total investment cost rates of the integrated system, turbine 1, and turbine 2. .. 124
Figure 5.19: Effects of geothermal fluid temperature on the unit cost of products of the integrated system, turbine 1, and turbine 2. 124
Figure 5.20: Effects of geothermal fluid temperature on the exergy destruction cost rates of the integrated system, turbine 1, and turbine 2. 125
Figure 5.21: Effects of geothermal fluid temperature on exergoeconomic factors of the integrated system, turbine 1, and turbine 2. 126
Figure 5.22: Effects of faradaic efficiency on the overall exergy destruction rate and the total investment cost rates of the integrated system, and EAS. 127
Figure 5.23: Effects of faradaic efficiency on the unit cost of products of the integrated system, and EAS. 127
Figure 5.24: Effects of faradaic efficiency on the exergy destruction cost rates of the integrated system, and EAS. 128
Figure 5.25: Effects of faradaic efficiency on exergoeconomic factors of the integrated system, and EAS. 129
Figure 5.26: Effects of air compressor pressure ratio on the overall exergy destruction rate and the total investment cost rates of the integrated system, air compressor, and turbine 3. 130
Figure 5.27: Effects of air compressor pressure ratio on the unit cost of products of the integrated system, air compressor, and turbine 3. 130
Figure 5.28: Effects of air compressor pressure ratio on the exergy destruction cost rates of the integrated system, air compressor, and turbine 3. 131
Figure 5.29: Effects of air compressor pressure ratio on exergoeconomic factors of the integrated system, air compressor, and turbine 3. 132
Figure 5.30: Effects of air compressor isentropic efficiency on the overall exergy destruction rate and the total investment cost rates of the integrated system, and air compressor. 133
Figure 5.31: Effects of air compressor isentropic efficiency on the unit cost of products of the integrated system, and air compressor. 134
Figure 5.32: Effects of air compressor isentropic efficiency on the exergy destruction cost rates of the integrated system, and air compressor. 135
Figure 5.33: Effects of air compressor isentropic efficiency on exergoeconomic factors of the integrated system, and air compressor. 135
Figure 5.34: Effects of turbine 3 isentropic efficiency on the overall exergy destruction rate and the total investment cost rates of the integrated system, and turbine 3. 136
Figure 5.35: Effects of turbine 3 isentropic efficiency on the unit cost of products of the integrated system, and turbine 3. 137
Figure 5.36: Effects of turbine 3 isentropic efficiency on the exergy destruction cost rates of the integrated system, and turbine 3. 138

Figure 5.37: Effects of turbine 3 isentropic efficiency on exergoeconomic factors of the integrated system, and turbine 3. 138
Figure 5.38: Effects of boiler pressure on the overall exergy destruction rate and the total investment cost rates of the integrated system, and turbine 4. 139
Figure 5.39: Effects of boiler pressure on the unit cost of products of the integrated system, and turbine 4. 140
Figure 5.40: Effects of boiler pressure on the exergy destruction cost rates of the integrated system, and turbine 4. 140
Figure 5.41: Effects of boiler pressure on exergoeconomic factors of the integrated system, and turbine 4. 141
Figure 5.42: Pareto front of the optimization study between overall exergy destruction rate and overall unit cost of product. 143
Figure 5.43: Exergy destruction rates of the components in the integrated system. A logarithmic scale is used for clarity. 148
Figure 5.44: A plot of overall energy and exergy efficiencies and thermal energy storage ratio (ε) versus solar irradiance. 153
Figure 5.45: A plot of overall energy and exergy efficiencies and thermal energy storage ratio (ε) versus temperature of fluid leaving the parabolic solar collectors (state 2). 153
Figure 5.46: A plot of solar energy and exergy required for CO_2 capture versus temperature of fluid leaving the parabolic solar collectors (state 2). 154
Figure 5.47: A plot of thermal energy storage ratio (ε) and EAS power input versus faradaic efficiency of EAS. 155
Figure 5.48: A plot of overall energy and exergy efficiencies versus faradaic efficiency of EAS. 156
Figure 5.49: A plot of mass flow rate entering T2 (state 24) and net power production versus C1 compression ratio. 156
Figure 5.50: A plot of overall energy and exergy efficiencies versus C1 compression ratio. 157
Figure 5.51: A plot of mass flow rate entering T2 (state 24) and net power production versus C1 and C2 isentropic efficiency. 158
Figure 5.52: A plot of overall energy and exergy efficiencies versus C1 and C2 isentropic efficiency 158
Figure 5.53: A plot of mass flow rate entering T2 (state 24) and net power production versus T2 and T3 isentropic efficiency. 159
Figure 5.54: A plot of overall energy and exergy efficiencies versus T2 and T3 isentropic efficiency 160
Figure 5.55: A plot of mass flow rate entering T2 (state 24) and net power production versus T2 inlet temperature (state 24). 161
Figure 5.56: A plot of overall energy and exergy efficiencies versus T2 inlet temperature (state 24) 161
Figure 5.57: A plot of carbon dioxide capture rate versus mass flow rate of natural gas (state 21) 162

Figure 5.58: A plot of ammonium bicarbonate production rate (state 18) versus conversion rate..... 163
Figure 5.59: A plot of overall exergy destruction rate and overall unit cost of products versus solar irradiance..... 163
Figure 5.60: A plot of overall total investment cost rate and overall exergoeconomic factor versus solar irradiance..... 164
Figure 5.61: A plot of overall exergy destruction rate and overall unit cost of products versus temperature of fluid leaving the parabolic solar collectors (state 2). 165
Figure 5.62: A plot of overall total investment cost rate and overall exergoeconomic factor versus temperature of fluid leaving the parabolic solar collectors (state 2). 166
Figure 5.63: A plot of overall exergy destruction rate and overall unit cost of products versus C1 compression ratio. 167
Figure 5.64: A plot of overall total investment cost rate and overall exergoeconomic factor versus C1 compression ratio. 167
Figure 5.65: A plot of overall exergy destruction rate and overall unit cost of products versus C1 and C2 isentropic efficiency. 168
Figure 5.66: A plot of overall total investment cost rate and overall exergoeconomic factor versus C1 and C2 isentropic efficiency. 168
Figure 5.67: A plot of overall exergy destruction rate and overall unit cost of products versus T2 and T3 isentropic efficiency. 169
Figure 5.68: A plot of overall total investment cost rate and overall exergoeconomic factor versus T2 and T3 isentropic efficiency. 170
Figure 5.69: A plot of overall exergy destruction rate and overall unit cost of products versus T2 inlet temperature (state 24). 170
Figure 5.70: A plot of overall total investment cost rate and overall exergoeconomic factor versus T2 inlet temperature (state 24). 171
Figure 5.71: A plot of overall energy and exergy efficiencies versus time of day. 172
Figure 5.72: A plot of turbine 1 power production versus time of day. 172
Figure 5.73: A plot of the Pareto front of the optimization study of the integrated system. 174
Figure 5.74: A plot of the batch reactor temperature over time for the different runs. .. 175
Figure 5.75: Mean operating temperature of the batch reactor for all the experimental runs. 176
Figure 5.76: A plot of the solution pH level over time after the run is done for the Catalyst case with 80%mol of CO_2. 177
Figure 5.77: A plot of the supplied current to the induction heater over time for the Induction heating cases. 178
Figure 5.78: A plot of the energy consumption of the induction heater for the Induction heating cases. 178
Figure 5.79: A plot of the main effects of the selected factors and interaction on the mass production of ammonium bicarbonate. 180
Figure 5.80: A plot of the mass production of ammonium bicarbonate over the different experimental runs. 181

Figure 5.81: A plot of the full-scale reactor capital cost over a range of ammonium bicarbonate production rates. The percentages represent the initial concentration of CO_2 in the reactor for the induction heating case. 182
Figure 5.82: A plot of the full-scale reactor capital cost over a range of ammonium bicarbonate production rates for the three cases. The percentage chosen is 80%mol of CO_2. 183
Figure 5.83: A plot of surface area over volume of the batch reactor over a range of scaling factor. 184
Figure 5.84: A plot of batch reactor temperature over time for different scaling factors for 30%mol of CO_2. 185
Figure 5.85: A plot of batch reactor temperature over time for different scaling factors for 80%mol of CO_2. 186
Figure 5.86: A plot of batch reactor temperature over time for different cooling fluid temperatures for 80%mol of CO_2. 186
Figure 5.87: A plot of batch reactor temperature over time for different initial temperatures for 80%mol of CO_2. 187

List of Tables

Table 2.1: A summary of the benefits and challenges of the carbon capturing strategies [12,47,58]. 14
Table 2.2: A summary of the potential benefits and key challenges of the carbon capturing technologies. 19
Table 2.3: List of systems used in the comparative study. 32
Table 2.4: Comparative assessment of the operational costs for the considered ammonia-based carbon capture systems. NA stands for Not Available. 34
Table 3.1: Assignment levels to the main factors. 51
Table 3.2: Full factorial design of experiment with three factors and two levels (2^3)..... 51
Table 3.3: Measurement devices and their characteristics..... 52
Table 3.4: Absolute and relative errors of the experimental setup. 52
Table 3.5: Summary of novelties in the integrated systems and experimental setup. 53
Table 4.1: Mass and energy balance equations for the carbon capture system. 58
Table 4.2: The entropy and exergy balance equations for the carbon capture system. 59
Table 4.3: Purchase cost functions for each component in system 1 with additional relations. 66
Table 4.4: Mass and energy balance equations. 72
Table 4.5: Entropy and exergy balance equations. 72
Table 4.6: Cost balance equations for each component in system 2 with their corresponding auxiliary equations and assumptions. 78
Table 4.7: Captial investment cost functions for each component in system 2 with additoinal relations. 79
Table 4.8: Exergoeconomic performance parameters for each component in system 2 and the overall system. 81
Table 4.9: Mass and energy balance equations. 88
Table 4.10: Entropy and exergy balance equations. 88
Table 4.11: Cost balance equations. 92
Table 4.12: Captial investment cost functions. 93
Table 4.13: Decision variables and constraints for system 2. 95
Table 4.14: Decision variables and constraints for system 3. 95
Table 5.1: Input parameter values used for system 1 model. 98
Table 5.2: Output parameter values resulted from system 1 model. 99
Table 5.3: Thermodynamic state points of system 1. 100
Table 5.4: Exergy destruction rates of the components of system 1. 101
Table 5.5: Input values used for system 2 model. 109
Table 5.6: Output values produced from system 2 model. 109
Table 5.7: Thermodynamic state points of system 2. 110
Table 5.8: Molar basis composition of the exhaust gases of system 2. 110
Table 5.9: Exergy rate, unit cost, and cost rates of all the state points in system 2. 113
Table 5.10: Exergy rate, unit cost, and cost rates of all heat transfer and work streams in system 2, and exergy destruction rates of all components. NA for not applicable. 114

Table 5.11: Total investment cost rates and exergoeconomic performance parameters for each component in system 2 and the overall system. 116
Table 5.12: The selected objective functions models with their corresponding statistical indicators computed from Eureqa software after 5 minutes of search time. 142
Table 5.13: Decision variables values for the optimum operation points and their corresponding values of the two objective functions presented for system 2..... 143
Table 5.14: Input values used for system 3 model..... 145
Table 5.15: Output quantities resulting from system 3 model..... 146
Table 5.16: Thermodynamic state points of system 3. 147
Table 5.17: Molar basis composition of the exhaust gases in the integrated system..... 147
Table 5.18: Exergy rate, unit cost, and cost rates of all state points..... 149
Table 5.19: Exergy rate, unit cost, cost rates of all heat transfer and work streams, and exergy destruction rates for all components. NA for not applicable. 150
Table 5.20: Total investment cost rates and exergoeconomic performance parameters for all components and the integrated system. 151
Table 5.21: Objective functions models generated by Eureqa after five minutes of search time. 173
Table 5.22: Decision variables values for the optimum solutions and their corresponding objective functions values presented for system 3..... 174
Table 5.23: pH level measurements of the end solutions of the different experimental runs. 177
Table 5.24: Comprehensive ANOVA results for all factors and their interactions. 179
Table 5.25: ANOVA results for the selected factors and interaction. 179
Table 5.26: Regression equation for the selected factors and interaction..... 180
Table 5.27: Geometric parameters of the scaled-up batch reactor..... 184

Nomenclature

A	Area (m^2); hysteresis of the SMA (kJ kg^{-1})
AF	Air to fuel ratio
$\dot{C}$	Cost rate (\$ s^{-1})
C	Heat capacity (J mol^{-1} K^{-1}); molar concentration (mol m^{-3})
c	Unit cost (\$ kJ^{-1}); power coefficient
CC	Capital cost (\$)
COP	Coefficient of performance
CRF	Capital recovery factor
D	Diameter (m)
E	Energy requirement to capture carbon dioxide (kJ kg^{-1})
e	Energy consumption by the electromagnetic induction heater (kJ)
$\dot{E}x$	Exergy rate (kW)
ex	Specific exergy (kJ kg^{-1})
F	Faraday's constant (C $kmol^{-1}$)
f	Exergoeconomic factor
FE	Faradaic efficiency
H	Heat of the reaction (J mol^{-1})
h	Specific enthalpy (kJ kg^{-1})
HHV	Higher heating value (kJ kg^{-1})
I	Current (A)
i	Current density (A m^{-2}); interest rate (%)
k	Reaction constants (m s^{-1})
L	Length of a single module (m)
LHV	Lower heating value (kJ kg^{-1})
$LMTD$	Logarithmic mean temperature difference (K)
M	Molecular weight (kg $kmol^{-1}$)
$\dot{m}$	Mass flow rate (kg s^{-1})
m	Produced mass of ammonium bicarbonate (kg); shape memory alloy mass in an elastocaloric cooling device (kg)
$\dot{N}$	Molar flow rate (kmol s^{-1}); rate of phase transformation cycles (Hz)
N	Number of operating hours in a year (h); cost exponent; number of cells; moles of reactants (mol)
n	System life (y); number of electrons in an anode reaction (C $kmol^{-1}$); total number of constituents in exhaust gases; total number of solar modules
P	Pressure (kPa)
$\dot{Q}$	Heat transfer rate (kW)
q	Heat or cooling transfer per cycle per unit of mass (kJ kg^{-1})

R	Electric resistance (Ω); oxygen to air mass ratio; specific energy for CO_2 capture (kJ kg^{-1}); specific exergy for CO_2 capture (kJ kg^{-1}); universal gas constant (kJ $kmol^{-1}$ K^{-1}); correlation coefficient
r	Pressure ratio; rate of reaction (mol s^{-1} m^{-3})
$\dot{S}$	Entropy rate (kW K^{-1}); solar irradiance (kW m^{-2})
s	Specific entropy (kJ kg^{-1} K^{-1})
T	Temperature (K)
t	Thickness (m); operation time of the induction heater (s)
U	Overall heat transfer coefficient (kW m^{-2} K^{-1})
$\dot{V}$	Volume flow rate (m^3 s^{-1})
V	Voltage (V); volume (m^3); wind upstream air speed (m s^{-1})
v	Specific volume (m^3 kg^{-1})
$\dot{W}$	Work rate (kW)
w	Width of a single module (m); specific compressor work (kJ kg^{-1})
x	Mass ratio of component i
Y	Scaling factor
$\dot{Z}$	Total investment cost rate ($ s^{-1})
Z	Purchase investment cost ($)
z	Number of electrons per one mole of ammonia produced

Greek Letters

β	Molar ratio of super oxygen molecules over one mole of methane
γ	Specific heat ratio
Δ	Change of properties across states
ε	Thermal energy storage ratio
η	Efficiency
λ	Excess air factor
ρ	Electric resistivity (Ω m); air density (kg m^{-3}); power density (kW m^{-2})
σ	Membrane proton conductivity (Ω^{-1} m^{-1}); standard error (uncertainty)
φ	Maintenance factor

Subscripts

AB	Ammonium bicarbonate reactor
act	Activation
anode	Anode electrode
AR	Air regenerator
ASR	Ammonia Synthesis Reactor
ASU	Air separation unit
avg	Average
C1,2	Air compressor 1, and 2
c	Cold side of elastocaloric cooling device

cathode	Cathode electrode
CH_4	Methane
cell	Cell
cond1,2	Condenser 1,2
CO_2	Carbon dioxide
CO2CAPT	Carbon dioxide capture reactor
CO_2-captured	Carbon dioxide captured
D	Destruction
dest	Destruction
EAS	Electrochemical ammonia synthesizer
ECD	Elastocaloric cooling device
el	Electrode
en	Energy
ex	Exergy
F	Fuel stream
flash1,2	Flash chamber 1,2
FR	Fuel regenerator
FS	Full-scale
gen	Generation
HX1,2,3,4	Heat exchanger 1,2,3,4
H_2	Hydrogen
H_2O	Water
i	Summation variable
id	Ideal
in	Inlet
is	Isentropic
j	State number
k	Component under consideration
loss	Heat transfer rate losses
LS	Lab-scale
MED	Multi-Effect Desalination unit
Mem	Membrane
NH_4	Ammonia
N2-COMP	Nitrogen Compressor
o	Reference state
O_2	Oxygen
ohm	Ohmic
out	Outlet
P	Product stream
PEM	Proton-Exchange Membrane

q	Heat transfer stream
Rwater	Recycled water stream
s	Isentropic
sep	Separator
SOFC	Solid-Oxide Fuel Cell
solar	Parabolic solar collectors
Space	Space heating for the community
TES	Thermal energy storage
T1,2,3,4	Turbine 1,2,3,4
w	Work stream
WGSMR	Water gas shift membrane reactor
wind	Wind energy
X	General variable under consideration
ZVS	Zero-voltage switching unit

Acronyms

AB	Ammonium bicarbonate
AP	Acidification Potential
ASR	Ammonia Synthesis Reactor
ASU	Air Separation Unit
CaL	Calcium salt
CERL	Clean Energy Research Laboratory
CO	Carbon monoxide
COP	Coefficient of Performance
CO_2	Carbon dioxide
CO2CAPT	Carbon dioxide capture reactor
CPU	Compression and Purification Unit
CRS	Cold-Rich Split
CSB	Cold Split Bypass
CSS	Cold Solvent Split
CuAlNi	Copper-Aluminum-Nickel metal alloy
DC	Direct current
DMC	Dimethyl carbonate
e^-	Electron
EAS	Electrochemical ammonia synthesizer
ECD	Elastocaloric Cooling Device
EES	Engineering Equation Solver software
EPA	Environmental Protection Agency
F-Principle	Fuel Principle
$GtCO_2$	Giga ton of carbon dioxide
HX	Heat exchanger

H^+	Proton
H_2	Hydrogen
H_2O	Water
HTP	Human Toxicity Potential
IEA	International Energy Agency
IGCC	Integrated Gasification Combined Cycle
LCA	Life Cycle Assessment
LVC	Lean Vapor Compression
MEA	Monoethanolamine
MED	Multi-Effect Desalination
N_2	Nitrogen
N2-COMP	Nitrogen Compressor
NA	Not Available
NH_3	Ammonia
NH_4HCO_3	Ammonium bicarbonate
NO_x	Nitrogen oxides
O_2	Oxygen
O^{-2}	Oxide ion
PEM	Proton-Exchange Membrane
pH	Potential hydrogen
Ph.D.	Doctor of Philosophy
PV	Photovoltaic
PZ	Piperazine
P-Principle	Product Principle
RSS	Rich Solvent Split
RVC	Rich Vapor Compression
SEP	Separator
SMA	Shape Memory Alloy
SOFC	Solid-Oxide Fuel Cell
SPECO	Specific Exergy Costing
SRC	Steam Rankine Cycle
ST	Steam turbine
S-CO_2	Supercritical Carbon Dioxide
TES	Thermal Energy Storage
WGSMR	Water-Gas Shift Membrane Reactor
ZVS	Zero-voltage switching

Chapter 1: Introduction

Global warming is defined as the rise in the average temperature of the earth. This rise has devastating effects on the environment and natural habitats of animals and people, such as heat waves, sea level risings, and heavy droughts [1]. A simple linear correlation between this global phenomenon and the release of carbon dioxide (CO_2) has been established and the researchers found that for each one-thousand tons of carbon dioxide released to the atmosphere, a 0.0000000015°C rise in the average earth's temperature occurs [2]. As a result, it is of utmost importance to reduce our global emissions of carbon dioxide in order to limit the severe effects of global warming. The most dominant source of CO_2 emissions is fossil fuel power plants [3]. If the world is to make a significant drop in these harmful emissions, it is essential to focus global efforts on capturing the carbon dioxide leaving these power plants. A recent global report by the International Energy Agency (IEA) shows that carbon capture technologies are essential to meet the 2050 emissions reduction targets set by the Paris Agreement [4]. This shows the need to use carbon capturing technologies to break this trend of the power sector and reach the emissions reduction targets by 2050. Since renewable energy sources, like wind and solar energy, are not yet mature enough to meet the rising global demands of energy, fossil fuels will continue to be an essential source of energy in the coming decades. One of the key methods to potentially reduce carbon emissions is the waste to energy option, such as gasification and pyrolysis. Fossil fuel-based gasification has been shown to reduce carbon emissions by 40% as presented in a review by Yang et al. [5]. In addition, using carbon capture and storage technology, it is possible to reduce the environmentally damaging effects of using these kinds of fuels. This technology is predicted, by the IEA as shown in Figure 1.1, to achieve exponentially higher carbon capture capacities. There are three main steps of this technology, namely CO_2 separation, transportation to the storage site, and compressing the CO_2 gas and storing it underground. The most expensive step is the first one by a factor of more than three to ten times the combined costs of the transport and storage steps [6]. For this reason, a tremendous amount of research has been conducted to effectively reduce the capital and operational costs of the CO_2 separation step to make this technology more economically feasible, and as a result, increase its adaptation [7–9].

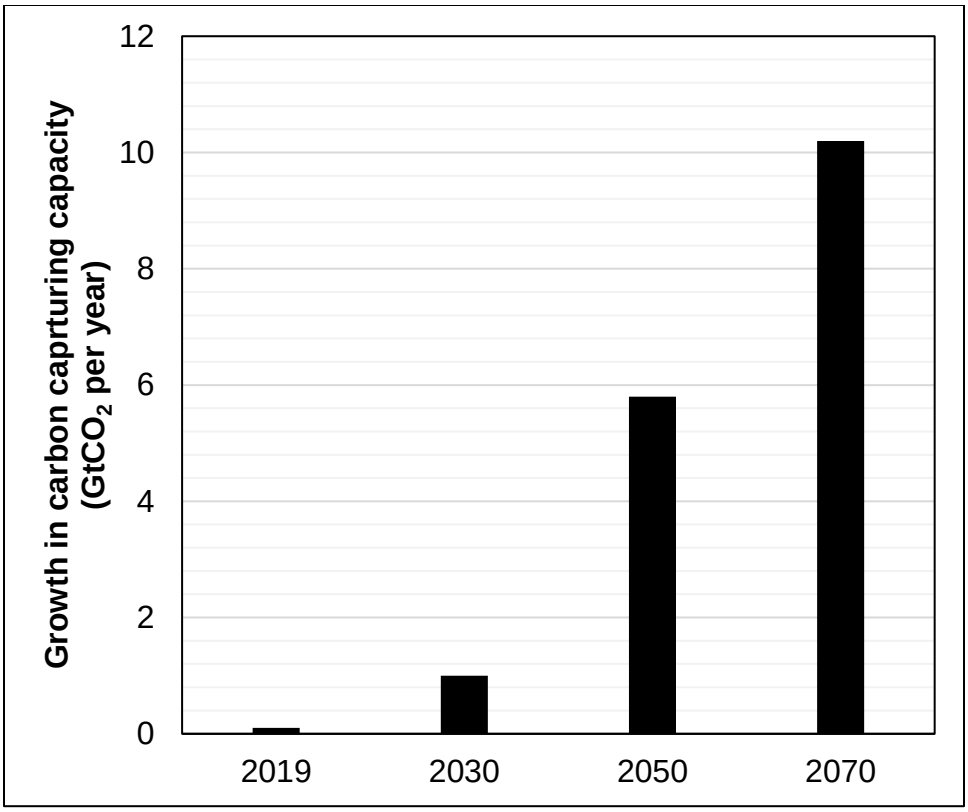

Figure 1.1: Growth in carbon capturing capacity over the next decades (adapted from [4]).

There are current policies in the United States of America regarding carbon capture technologies. The two most notable tax credits, namely the Coal Gasification Investment Credit, and the Advanced Coal Project Investment Credit, have already accumulated more than 2.5 billion US dollars to support research and development efforts in the field of coal-based carbon capture [10]. The Low Carbon Security Act of 2008 targets to lower greenhouse emissions by 2030 to the levels that existed in the country back in 1990. This act includes giving bonus allowances to companies that implement carbon capture technologies for the first 10 years of operation. Such legislation could provide incentives to adopt carbon capture technologies by the fossil-fuel industry. Even though there are current policies in the US that support carbon capture technologies, more strict measures are needed in order to reach zero-net emissions by 2050 in the country as concluded by Hamilton et al. [10].

Carbon capturing systems have recently gained increasing attention in the literature and several researchers have investigated new ways to improve the efficiency of this process [1,11,12]. The most developed and commercialized method of carbon capture is using

chemical solvents to separate the carbon dioxide from the flue gases; however, the literature has discussed other promising methods, such as cryogenics [13], membrane separations methods [14], adsorption [15–17], and microbial [18]. For example, Jayaweera et al. [19] investigated the use of mixed-salt carbon capturing technology which was successful at removing more than 90% of CO_2 from thermal power plants. The modeling results showed that using mixed salts reduces the energy requirements by almost 44% compared to using monoethanolamine (MEA) as a solvent. MEA is the traditional solvent used in such carbon capturing systems. Hanak et al. [20] proposed and modeled the use of ammonia as an alternative solvent to MEA for the carbon dioxide separation from exhaust gases of a supercritical coal-fired power plant. Their results indicate that using ammonia at a pressure range between 12.5 and 17.5 bar can decrease the energy requirements of the carbon capturing process by as much as 15.7%. Another method to reducing the energy requirements was undertaken by Liu [21]. They investigated the use of different configurations of a stripper by the use of regeneration techniques, such as advanced flash stripper, and rich-split process. The results presented a case for the use of such configurations to reduce energy requirements for carbon dioxide capture. The reductions are as low as 2.78 MJ per one kilogram of CO_2 captured compared to 4.91 MJ per one kilogram of CO_2 captured [21]. Novek et al. [22] proposed the use of organic solvents as catalysts to induce the chemical separation of carbon dioxide from the flue gases in an ammonia medium. Some of the organic solvents used are acetone, acetaldehyde, or dimethoxymethane. The results of their investigation showed that using acetaldehyde, which is the best performing organic solvent out of the three, cut down the energy requirements by almost 75%. This is compared to using the traditional chilled ammonia process. Furthermore, the operating temperature was reduced by 53°C.

One of the trends in the carbon capturing literature is the use of small-scale renewable energy sources to supply the energy needed for carbon capturing rather than using the thermal energy generated by the fossil fuel-based power plant. This approach helps to reduce the consumption of further fossil fuels to capture the carbon dioxide leaving the power plant. For instance, Wang et al. [23] proposed the use of thermal solar cells to supply heat to the CO_2 absorber. In a later study, Liu et al. [24] parametrically studied the case of using this solar-assisted carbon capturing system in Xi'an city to make sure that this system

is economically feasible. Two configurations were studied, namely vacuum tubes, and parabolic trough collectors. Their results show that the price of vacuum tubes for the thermal solar cells has to decrease to 57.10 \$ m^{-2}, and the price of parabolic trough collectors must reduce to 50.84 \$ m^{-2}. Ishaq et al. [25] introduced using a combination of photovoltaic solar cells and wind turbines to drive a carbon capturing system. Under some operating conditions, their system can capture 1,387 tons of CO_2 in a year. In addition, their proposed system produces urea from ammonia and the captured carbon dioxide at a rate of 86.4 kmol a day. In another work by Sánchez et al. [26], the authors took the process of producing chemicals from carbon dioxide using renewable energy sources a step further to produce Dimethyl carbonate (DMC), which is a chemical used in multiple applications in the industry, most notably is the manufacturing of lithium-ion batteries [27]. Siddiqui et al. [28] implemented the use of wind turbines to drive the production of aqueous ammonia from renewable hydrogen and nitrogen using the Haber-Bosch process for CO_2 capturing and ammonium bicarbonate production. They modeled the system using ASPEN Plus and the results of this modeling showed that it costs between \$0.1 and \$0.23 to capture one kilogram of CO_2 using this system. Also, the energy requirement for capturing one kilogram of carbon dioxide is evaluated to be relatively high at a value of 5.62 MJ. This is higher than the typical chilled ammonia process which has an energy requirement of 3.22 MJ kg^{-1} of CO_2 captured [29].

The main disadvantage of retrofitting carbon capture systems is the loss of net thermal efficiency of the thermal power plant by almost 11% [30]. For this reason, a new approach of using renewable energy sources to support the carbon capturing process has been proposed in the literature. For instance, Mokheimer et al. [31] investigated the use of carbon capturing with and without the assistance of solar energy. Their simulation results of this comparison showed that increasing the use of solar energy, improves the avoided carbon dioxide up to a value of 262 ktons each year of operation. Siddiqui et al. [28] proposed an integrated system where wind energy is used to produce hydrogen and then ammonia to use this ammonia in a reaction with carbon dioxide leaving a thermal power plant to produce a useful chemical commodity. The hydrogen is produced using a proton-exchange membrane electrolyzer and the ammonia is produced using the Haber-Bosch process. Their simulation results show that their integrated system can capture carbon at a

rate of 3.5 kg s^{-1} at a cost rate between 0.1 and 0.23 \$ kg^{-1} of CO_2. Ravikumar et al. [32] investigated the environmental cost of implementing carbon capturing with the assistance of renewable energy sources through the life cycle assessment method. Their study compared the use of renewable energy to supply electricity to the grid or to use this energy source to help in carbon capturing to produce methanol. From the results, it has shown that it is viable to use the renewable energy to produce methanol using carbon capturing only if the CO_2 intensity drops below 67 g CO_2 kWh^{-1} [32]. An extensive review of renewable energy-based carbon capturing systems has recently been conducted by Al-Hamed and Dincer [33]. A different technology that improves the thermal efficiency of power generation, that has been attracting the attention in the literature, is supercritical carbon dioxide power cycles. For example, Surywanshi et al. [34] compared (through simulation) the use of supercritical carbon dioxide power cycles with and without the feature of carbon capture. Their findings have concluded that using carbon capturing with a supercritical carbon dioxide power cycles imposes an energy penalty in the efficiency by almost 1.44%, but the carbon capturing feature avoids almost 3.25×10^9 kg of carbon dioxide released yearly.

The exergoeconomic analysis of integrated energy systems have been a useful method for evaluating and optimizing the performance and economics of such systems simultaneously. This method combines the fundamentals of thermodynamics and economics to assess an integrated energy system for their viability and compare it to other equivalent systems. The main advantage of using this method lies in evaluating the costs of the different exergy streams in the system which inherently includes the exergetic inefficiencies of each component in the integrated system [35]. One disadvantage of this method compared to the techno-economic analysis is that it is more complicated, and it requires the thermodynamic results of a complete exergy analysis of the system, unlike techno-economic which only requires energy analysis. There are multiple methods that have been proposed in the literature, the most common on is called the Specific Exergy Costing (SPECO) method introduced by Lazzaretto and Tsatsaronis [36] back in 2002. This method has a few advantages, namely its simplicity in implementation, its ability to show the costing details of exergy streams in the system, and its systematic approach unlike the other approaches that are based on experience or changing postulates. Several researchers in the literature

have used this method in analyzing different types of integrated energy systems. For example, Wang et al. [37] applied the exergoeconomic method on a coal purification integrated system that features CO_2 capturing, an organic Rankine cycle, and an absorption refrigeration cycle. Their results of this modeling showed that the total efficiency in terms of exergetic performance is 17.6% and the majority of exergy losses occurred in the CO_2 capturing unit of the integrated system. The authors concluded that an optimization study to reduce these losses in the integrated system. Zhang et al. [38] studied a polygeneration system that produces electric power, chilled and hot water stream separately, and hydrogen production using a proton-exchange membrane electrolyzer. This system is fueled by natural gas and biomass. They applied the SPECO method to analyze this system exergoeconomically, and their results showed that it was possible to compute the unit costs of each of the useful outputs of the polygeneration system with reasonable accuracy [38]. The unit costs of electricity, hydrogen, hot water stream, and chilled water stream are 5.24 \$ GJ^{-1}, 20.4 \$ GJ^{-1}, 42.0 \$ GJ^{-1}, 44.4 \$ GJ^{-1}, respectively. Another example is the work done by Ghorbani et al. [39] where they used the SPECO method of the exergoeconomic analysis to study a hybrid system of Solid-Oxide Fuel Cell (SOFC) with gas turbine and an organic Rankine cycle. In addition, they optimized the system using a multi-objective optimization method to maximize the exergy efficiency of the system and minimize the exergetic cost rate of the hybrid system. The hybrid system has an overall exergy efficiency of 46.8% at the optimum point. Alirahmi et al. [40] investigated and optimized a multigeneration system that uses electric power from a geothermal power plant to produce hydrogen and cooling. Their optimization study that focused on the exergy efficiency and the cost rate and their chosen point have an efficiency of 37.9%, and the cost rate is 15.09 USD h^{-1}. Abdollahi Haghghi et al. [41] introduced a new multigeneration system based on a SOFC. Their thermodynamic analysis showed that the energy and exergy efficiency are 77.6% and 47.1%, respectively. This showed that having the multigeneration feature increased the overall efficiencies compared to using a simple SOFC system. He et al. [42] implemented an exergoeconomic analysis to estimate the production costs of liquid fuels as valuable chemicals from a carbon capture system proposed by the authors. Their simulation work has shown that such a system has an overall exergy efficiency of 65.13% which is much higher than typical chemical processing plants. Also, the unit cost of

producing liquid fuels has been estimated to be 109 $ MWh^{-1} of exergy. Knowing this unit cost helps in determining the economic feasibility of the valuable products made by such systems. Such a demonstration of the use of the exergoeconomic analysis on a carbon-capture-and-utilization system helps us in comparing different systems economically and thermodynamically. One of the important devices that could have a significant impact on carbon capture and utilization technologies is the electrochemical ammonia synthesizer. This device has multiple advantages over the traditional way of producing, the Haber-Bosch process. Some of these advantages are ambient pressure and temperature operating conditions, lower energy requirements, and inherent separation of ammonia from the other outlet gases due to the design of this kind of electrolyzer [43,44]. A recent investigation by Zhang et al. [45] showed a reasonable faradaic efficiency of an electrochemical ammonia synthesizer working under ambient conditions where a nanowire array made from carbon cloth was used as a catalyst.

1.1 Current challenges

There are a number of challenges that block the advancement and widespread adaptation of carbon capture and storage technology globally. To begin with, the energy penalty of the CO_2 separation process is huge. The drop in the net efficiency of a power plant with carbon capture technology is around 10 percentage points [6]. This is equivalent to the difference between a gas turbine power cycle and a combined power cycle that consists of a gas turbine and a steam Rankine cycle. This energy penalty is directly causing higher capital and operational costs of the power plant.

Another challenge that needs to be resolved is the scarcity of pilot-scale plants of the different and somewhat new CO_2 separation/capture technologies, except for the chemical absorbent-based plants. This means that there is a lack of technical knowledge and expertise in building and running such plants.

The third challenge is the incorrect public perception regarding the maturity of renewable energy sources and the overestimation of its current potential to reduce carbon emissions. This leads to underestimating the need to reduce carbon emissions through carbon capture and storage technologies which is a more immediate solution and necessary to reach the

2050 emissions targets [4,46]. More specific challenges to this technology will be discussed throughout this review.

There are current policies in the United States of America regarding carbon capture technologies. The two most notable tax credits, namely the Coal Gasification Investment Credit, and the Advanced Coal Project Investment Credit, have already accumulated more than 2.5 billion US dollars to support research and development efforts in the field of coal-based carbon capture [10]. The Low Carbon Security Act of 2008 targets to lower greenhouse emissions by 2030 to the levels that existed in the country back in 1990. This act includes giving bonus allowances to companies that implement carbon capture technologies for the first 10 years of operation. Such legislation could provide incentives to adopt carbon capture technologies by the fossil-fuel industry. Even though there are current policies in the US that support carbon capture technologies, more strict measures are needed in order to reach zero-net emissions by 2050 in the country as concluded by Hamilton et al. [10].

1.2 Motivation

As the need to reduce CO_2 emissions increases in the power sector, which represents 25% of total emissions, the higher the capacity of the carbon capture technologies is needed. Increasing this capacity is limited by one major factor, that is the energy penalty, which is typically in the range of 10-12%, associated with retrofitting a carbon capture unit at the end of a fossil-fuel power plant which directly causes economic losses to the industry. The economic losses can be as high as 3.4 US kWh^{-1}. In order to overcome this problem, this Ph.D. work proposes systems where the captured CO_2 is turned into a useful and valuable chemical commodity to offset the energy penalty caused by the carbon capturing in the power plant. Producing a useful chemical substance will utilize more energy which will be supplied by the electricity from various renewable energy sources. This is not to overload the thermal power plant and to limit the use of carbon-based fuels. In doing so, the power industry will see economic value in investing in such co-producing carbon capture systems to either offset the costs of the system or generate some added value from the plant. This will motivate the industry to adopt more of such systems and reduce the CO_2 emissions

over the next 3 decades while the renewable energy technology matures further to replace carbon-emitting power plants.

1.3 Objectives

The general objective of this thesis work is to investigate ammonia-based carbon capturing systems that are powered by renewable energy sources through modeling and experimentation. The thesis study is classified as an experimental investigation and a modeling study. The specific objectives of the thesis experimental investigation are listed as follows:

- To build a chemical batch reactor for producing ammonium bicarbonate from aqueous ammonia and incoming CO_2 from flue gases.
- To study the effects of using catalysts and electromagnetic induction heating on the batch reactor for producing ammonium bicarbonate.
- To evaluate the costs of introducing catalysts and induction heating on the production costs of ammonium bicarbonate using this new batch reactor.

The modeling study consists of the following specific objectives as follows:

- To develop ammonia-based carbon capture systems with useful chemical outputs.
- To perform a thermodynamic analysis on the systems using energy and exergy tools.
- To conduct parametric studies on the systems using the models to observe their thermal and chemical behavior under varying operating conditions.
- To study the effects of chemical conversion efficiency on the ammonium bicarbonate production.
- To evaluate the potential cost benefits of producing the useful chemical commodities and compare them to existing carbon capture systems.
- To optimize the developed carbon capture systems using multi-objective optimization methods. The objective functions of this optimization study are minimizing unit cost of useful products and maximizing overall exergy efficiency of the integrated systems.
- Scale-up study and cost assessment of the developed carbon capture systems.

1.4 Novelties

The ammonia-based carbon capture systems with ammonium bicarbonate have only been briefly investigated in the literature and have not been assessed thoroughly using exergy and economic tools. For this reason, the first point of novelty is to investigate new carbon capture systems using exergy analysis. Another point of novelty is assessing the potential of this system in terms of cost benefits to attract the power industry to adopting such systems that generates value from capturing CO_2. These systems will also be compared to other existing systems to evaluate their advantages and limitations which are missing in the literature. In addition, there is no experimental setup for producing ammonium bicarbonate from aqueous ammonia and carbon dioxide from flue gases that are enhanced using electrochemical induction heating that selectively heats metallic catalysts in the reactor. Building a batch reactor with enhanced ammonium bicarbonate production using a combination of catalysts and induction heating is a novelty of this work and it fills a necessary gas in the literature to support the simulation studies and to demonstrate the concept.

1.5 Thesis Outline

This thesis work started with an introduction, in chapter 1, to the carbon capturing technologies and their importance in reducing greenhouse gas emissions and to reach the emissions targets agreed upon by many governments. In chapter 2, a comprehensive literature review of the most recent carbon capturing systems proposed and studied by previous works are discussed and compared in terms of energy requirements, carbon dioxide efficiency, and other factors. Knowledge gaps in the literature are identified which are to be filled throughout this thesis work. Next, the carbon capturing systems developed in this work are mentioned and described in chapter 3. In addition, the experimental setup of the batch reactor to capture carbon dioxide and produce ammonium bicarbonate is explained. In chapter 4, the thermodynamic modeling of the carbon capturing systems is outlined in detail. Later, the exergoeconomic analysis of each system is described. This chapter ends with the optimization procedure used. In chapter 5, the results of the modeling of these carbon capturing systems are presented and discussed through base cases and parametric studies. Also, the results of the experimental investigation of the batch reactor are given. Finally, the thesis outlines the main conclusions and future work recommendations in chapter 6.

Chapter 2: Literature Review

This chapter starts with the existing methods of carbon capture, which are classified as strategies and technologies. Then, the discussion shifts to the most recent ammonia-based carbon capturing systems published in the literature. After that, a comparative assessment of the novel ammonia-based systems of carbon capture is presented. The opportunities and future directions of research in this field are proposed. Next, some conclusions drawn from the review and comparative assessment of the ammonia-based carbon capturing systems are given. Finally, the knowledge gaps in the literature are outlined.

2.1 Carbon capturing methods

Carbon capturing methods can be classified based on the strategy or the technology of carbon separation. Both of these classification ways will be discussed in this section starting with the strategies.

2.1.1 Carbon capturing strategies

There are three basic carbon capturing strategies, namely pre-combustion, oxy-fuel combustion, and post-combustion. Each of these strategies will be defined and then their advantages and limitations will be discussed briefly.

2.1.1.1 Pre-combustion carbon capture strategy

This strategy is defined as the process of separating the carbon from a fossil fuel prior to the combustion step and producing hydrogen for combustion. This way the carbon is removed at an earlier stage and no need to separate it from the mixture of exhaust gases. Only hydrogen is burned in the combustor to produce clean exhaust gases that consist of water vapor, nitrogen, and excess oxygen. To give an example of a pre-combustion carbon capture process, coal reacts with air in a fuel-rich and high-temperature environment, and then it is oxidized to form syngas in a process called gasification [47]. Then, this syngas reacts with steam to produce CO_2 and H_2 in a process called the water-gas shift reaction. The hydrogen is used to produce high-temperature heat for power generation or other purposes, while the CO_2 is captured and prevented from being released to the environment. The complexity of this process is two folds. One is the chemical reactions have to take place under high pressure and temperature [48], and the air-fuel ratio has to be controlled

to prevent early combustion of the input fuel [49]. Also, this technology is only feasible when integrated with combined power cycles which limits the flexibility of the use of such a process to capture CO_2. The main advantage of this strategy is that the CO_2 captured is at high concentrations (around 45% vol) which makes the process easier in terms of energy requirements, required solvent concentrations, and the size of the capturing unit [50].

2.1.1.2 Oxy-fuel combustion carbon capture strategy

This second strategy is aimed at producing a high concentration of CO_2 in the exhaust gases, usually higher than 80%, to ease the separation process of CO_2 from the rest of the exhaust gases. This is done mainly by combusting the fossil fuel with high purity oxygen which ideally results in CO_2, water vapor, excess oxygen, and small traces of nitrogen products. Since nitrogen is absent in the products, the concentration of CO_2 rises in the mixture of exhaust gases. The main advantage of having a high concentration of CO_2 in the exhaust gases is easiness, compared to the post-combustion strategy, in separating the CO_2 from the exhaust gases using chemical solvents or low-temperature separation processes [51].

One point to be mentioned is that the energy demands of the air separation unit (ASU) and compression and purification unit (CPU) are crippling this strategy of carbon capture. For instance, a typical oxy-fuel combustion process reduces the overall net efficiency by around 10% for a thermal power plant fueled by coal [52]. Fortunately, this efficiency penalty can be reduced using design optimization of the components and waste energy management, like what Escudero et al. [53] did who used these steps to reduce the efficiency penalty by 3.2 percentage points. This is a 30.4% reduction. If such advances are continued, this strategy could be more energetically and economically desirable.

2.1.1.3 Post-combustion carbon capture strategy

The post-combustion carbon capture strategies are defined simply as the set of methods that separate CO_2 emissions from the flue gases at their point of release. This method is commonly used due to its simplicity and flexibility in several industrial applications. In contrast to the previous strategies, the post-combustion carbon capture strategy can be done

wherever flue gases are released from the point of source and the CO_2 can be separated in a simple chemical process at ambient pressure and low to intermediate temperature levels (313–393 K) [11]. To illustrate, a typical post-combustion carbon capture process using amine solvents would only require two main thermal components, namely the absorber, and the stripper [54]. The flue gases, leaving the carbon-emitting plant, enter the absorber and the CO_2 gets absorbed by the lean amine solution and the remaining harmless gases leave the absorber to the environment. The lean solution becomes a rich solution and leaves the absorber to go to the stripper where the CO_2 is separated at an intermediate temperature and ambient pressure from the solvent solution. This process only requires a heat source that can be easily supplied by a reboiler or an electric heater. The simplicity and application flexibility and low energy requirements are some of the advantages of this process.

The limitations of this strategy are the energy penalty due to the regeneration energy needed to separate the solvent used in the process, and the low concentration of CO_2 in the exhaust gases which means higher mass flow rates of the solvent are required to absorb the CO_2 and this leads to larger equipment sizes and higher capital and operations costs compared to the other two strategies. These limitations can be overcome using process design optimization and recirculation techniques [55,56]. Table 2.1 summarizes some of the main benefits and challenges of each of these carbon capturing strategies.

2.1.2 Carbon capturing technologies

Next, the second way of classifying the carbon capturing methods is discussed here. This method categorizes the methods according to the process used in capturing the CO_2 from the exhaust gases. There are five main categories of carbon capture technologies. These are shown in Figure 2.1.

2.1.2.1 Adsorption

Adsorption for carbon capture is defined as the physical process in which CO_2 is attached (adsorbed) to a solid surface while other flue gases pass by without attachment. This process is illustrated in Figure 2.2. Some of the adsorbents that are used for this purpose

are zeolites, activated carbon, and metallic oxides [57]. So far, there are no large-scale carbon capture plants that are based on this technology. This is because it has some significant limitations that need to be overcome before becoming commercial. Some of these limitations are low CO_2 selectivity, stronger affinity to water vapor, and recyclability of the current adsorbents [15–17].

Table 2.1: A summary of the benefits and challenges of the carbon capturing strategies [12,47,58].

Carbon capturing strategies	**Benefits**	**Challenges**
Pre-combustion carbon capture strategy	• Fully developed approach • Higher CO_2 concentration produced by the pre-combustion processing to improve carbon capturing efficiency • Fossil fuel flexible • Can produce pure CO_2 at high pressures for later sequestration and/or transport	• Higher capital and operational costs • More complex designs are required • Temperature swing related heat transfer problem
Oxy-fuel combustion carbon capture strategy	• Highest CO_2 concentration produced by the oxy-fuel combustion processing to improve carbon capturing efficiency • Lower NO_x emissions compared to other strategies • It has the possibility of using cold thermal energy storage for separating the oxygen • The overall space requirement of the system is less	• The use of an air separation unit reduces the overall system efficiency • Highest capital and operational costs • Production of high purity oxygen can cause corrosion issues
Post-combustion carbon capture strategy	• Very compatible with current power plants for seamless retrofitting • The maturity level of this strategy is high because there are commercial plants that use this strategy • The simplest approach of the three strategies and complexity of the operation is minimal • Lower capital and operational costs compared to the others	• Lower CO_2 concentration reduces carbon capturing efficiency • High heat load requirements and regeneration abilities are limited • High water utilization • Produces CO_2 at ambient pressures and requires compression for transport

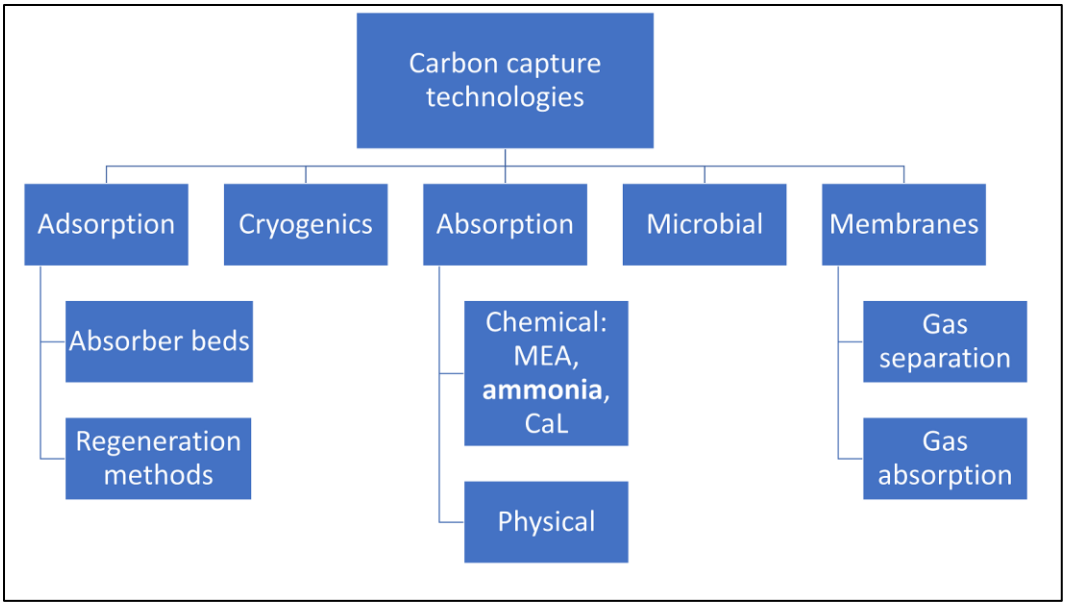

Figure 2.1: Main categories of carbon capture technologies (adapted from [59]).

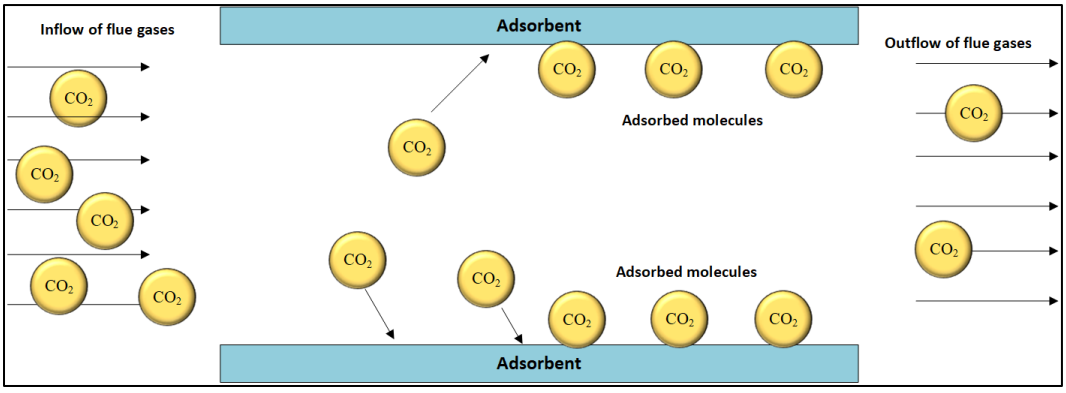

Figure 2.2: Illustration of the adsorption technology of CO_2 capture.

2.1.2.2 Cryogenics

The second carbon capturing technology discussed here is named cryogenics (very low-temperature processes). This technology uses the thermal processes of deposition (also called desublimation) and condensation to separate CO_2 from the flue gases [60]. This process is illustrated in Figure 2.3. The maturity of this technology has reached pilot-scale setups. For example, Zanganeh et al. [13] have reported the pilot setup which integrates oxy-fuel combustion of coal with a cryogenic CO_2 separation and compression unit, this setup is located in The CANMET Energy Technology Centre in Ottawa, Canada. Lab-scale experimental setups have also been built in the USA and Malaysia [60,61]. Such technology has two distinct advantages, which are the production of high-purity CO_2, and

integration with other low-temperature systems for cold energy storage. One main disadvantage of this technology is the energy penalty associated with it [62].

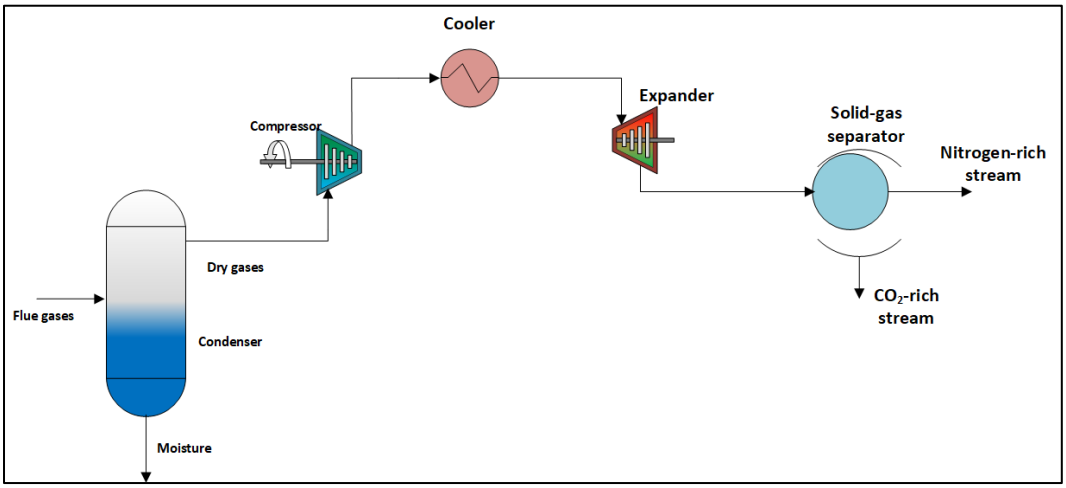

Figure 2.3: Illustration of the cryogenic technology of CO_2 capturing (adapted from [63]).

2.1.2.3 Absorption

The absorption carbon capturing technology has two main types. The first type, as illustrated in Figure 2.1, is the chemical absorption-type which is defined as absorbing CO_2 from flue gases by chemically reacting with a solvent to form a relatively unstable compound that can be easily separated in a later stage. This process is illustrated in Figure 2.4. Some of the common solvents used for this technology are MEA, ammonia, and hydroxide [64]. The most commonly used and commercialized process for post-combustion carbon capture is the chemical absorption process [58]. This is mainly due to the unique advantages of this process over the other processes in terms of lower energy requirements compared to cryogenics processes, more stable and scalable than membrane-separation processes, and can capture CO_2 from high concentration gas sources, such as flue gases, unlike adsorption processes [57,65].

The physical absorption carbon capturing technology works by absorbing CO_2 from flue gases according to Henry's law [66]. One example of a physical absorbent that is suitable for this task is imidazolium-based ionic liquids [67]. The main advantages of such absorbents are their nonflammable and nontoxic properties, high thermal stability, and lower volatility than chemical absorbents.

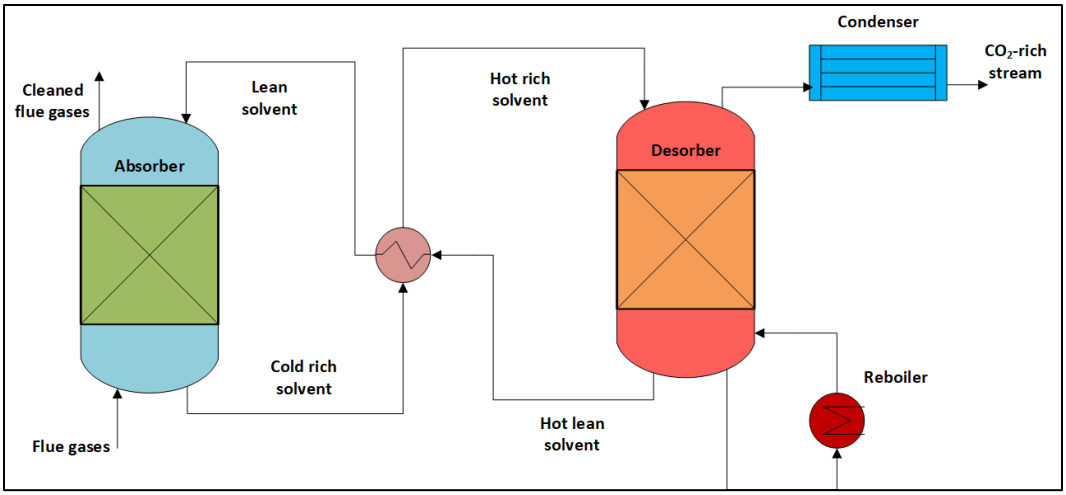

Figure 2.4: Illustration of the absorption technology of CO_2 capturing (adapted from [68]).

2.1.2.4 Microbial

Microbial technologies of carbon capturing are based on the bio-fixation of microalgae which fixes the CO_2 for cell growth. Two examples of such microalgae are Chlorella sp. and Tetraselmis suecica [69]. The benefits of using this technology are its selectivity in low CO_2 concentration flue gases, it is environmentally friendly as it uses biological substances and can be activated using solar energy, and it can be used for the co-production of food, fuel, and other useful chemical and biological materials [70]. Furthermore, this process can be integrated with a wastewater treatment system to co-produce carbon capturing and treated water for industrial use as it has been demonstrated experimentally by Lu et al. [18]. However, these microalgae materials are sensitive to other flue gases and can be damaged easily. Another limitation of this technology is the necessary use of electricity to capture CO_2 which means lowering the power production of the overall system. Using waste heat and/or regeneration is not possible [71]. The integration of this technology with existing thermal power plants has not been studied extensively and only the use of microbial fuel cells has been considered [72,73].

2.1.2.5 Membranes

The last category of carbon capturing technologies is membrane-based technologies. These are subdivided into gas separation, and gas absorption. Gas separation is a process where the flue gases pass along membranes and the CO_2 is separated according to its permeation rate and selectivity of the membrane. This process is illustrated in Figure 2.5. There are three main factors that affect this permeation of CO_2. 1) The partial pressure difference

across the membrane. 2) Membrane diffusion coefficient. 3) The relative sizes of the molecules [57]. The main disadvantage of this technology of CO_2 separation is the low selectivity of the membranes which makes it economically unfeasible for commercial use for now. Future advances in membrane selectivity are needed [74].

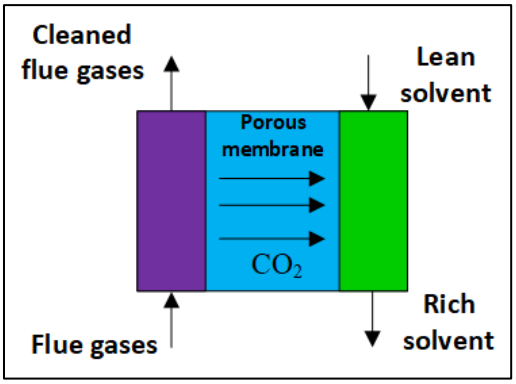

Figure 2.5: Illustration of the membrane technology of CO_2 capturing (adapted from [14]).

Secondly, gas absorption using membrane technology is when the membranes separate the flue gases on one side and the CO_2 solvent on the other side. This arrangement offers an advantage which is that it can be compact [57]. However, there are several challenges that need to be overcome for this technology to reach full maturity, like the high energy requirements, low CO_2 selectivity, and the need for a drying process to remove water since the membranes are usually polymers and they have high water permeability [75].

2.1.2.6 Summary of carbon capturing technologies

Table 2.2 summarizes the carbon capturing technologies discussed above in terms of their potential benefits and key challenges. Some of the common challenges in these technologies are noticed to be the degradation of the materials used, as well as the high energy requirements needed to operate the systems. Future work in this field should focus primarily on these two limitations to increase the adaptation of carbon capture technologies.

It is also important to note that hybrids of these technologies have been proposed by several researchers in the literature. For example, the hybrid system of membrane and cryogenics has been proposed by Song et al. [76]. Also, the adsorption technology was combined with membrane technology as studied in a paper by Janusz-Cygan et al. [77]. It seems that using hybrids of these technologies could open up a new area of interesting research. A more

extensive review on the topic of hybrids was given by Song et al. [78]. There are advantages of utilizing hybrid CO_2 capture systems. For example, combining the absorption technology with membrane technology could reduce investment costs as the carbon capturing process happens in parallel. Another example is when adsorption and absorption technologies are hybridized, multiple advantages are possible, like decreasing operating temperature of the adsorption process, higher regeneration, and thermal stability [78].

Table 2.2: A summary of the potential benefits and key challenges of the carbon capturing technologies.

Carbon capturing technology	**Potential benefits**	**Key challenges**
Adsorption	• Continuous operation • Simplicity • Low energy requirements	• Low CO_2 selectivity • Stronger affinity to water vapor • Recyclability of the current adsorbents
Cryogenics	• Pilot-scale setups exist • High-purity CO_2 production • Possible integration with other low-temperature systems for cold energy storage	• High energy penalty • High capital costs
Absorption	• Variety of solvents available, such as MEA and ammonia • Easily scalable • Low energy requirements • High-thermal stability • Simple operation • Lower capital and operational costs • High CO_2 selectivity • Some commercial plants exist	• The volatility of chemical solvents • Solvent degradation • Solvents are corrosive
Microbial	• Environmentally benign • Uses solar energy • Good CO_2 selectivity • Possible co-production of food and other useful chemicals	• Easily damaged by flue gases • The bio-fixation process is not well understood
Membranes	• Compactness • Simplicity • Environmentally benign • Potential for high energy efficiencies	• Low CO_2 selectivity • No pilot-scale setups yet • High costs • High energy requirements

2.2 Novel ammonia-based systems of carbon capture

This section will describe the different categories of recently (2015-2020) published ammonia-based carbon capture systems. There are three categories as shown in Figure 2.6.

2.2.1 Renewable energy-based systems of carbon capture

The first kind of these systems is the ones that are powered by renewable energy sources, such as wind turbines and solar cells. One example of this type is presented by Liu et al. [24] where they have designed a system of capturing carbon using thermal solar collectors as shown in Figure 2.7. There are three main parts of this system, namely the coal-fired steam turbine cycle, the chilled-ammonia carbon capture cycle, and the solar collector with thermal energy storage unit. The novelty of this system is the use of a renewable energy source, solar energy, in this case, to provide thermal energy to the Reboiler of the chilled-ammonia process for capturing the carbon released by the Boiler of the coal power plant. Their paper discussed the economic and technical aspects of such a system. They focus on finding the feasible price of solar collectors such that the levelized cost of electricity and the cost of carbon removed are lower than the chosen reference point. It has been found out that vacuum tube solar collectors are cheaper to operate compared to parabolic trough type [24]. To reach the economic feasibility of this system, the price of vacuum tube solar collectors must be reduced down to \$57.10 m^{-2} for the case of Xi'an city, while it must be reduced to \$50.84 m^{-2}.

This indicates that it takes less reduction in costs for the vacuum tube type than the parabolic trough type. A comprehensive comparative study was conducted by Wang et al. [23] to show the effects of changing solar collectors area and type on the two different carbon capture processes, namely the chilled ammonia process, and the conventional MEA-based process. The main conclusion of the economic comparative study is that the chilled ammonia process is more favorable than the MEA-based process. This shows that an ammonia-based carbon capture process assisted with solar cells is a promising option for future implementations in terms of economic feasibility than the conventional processes.

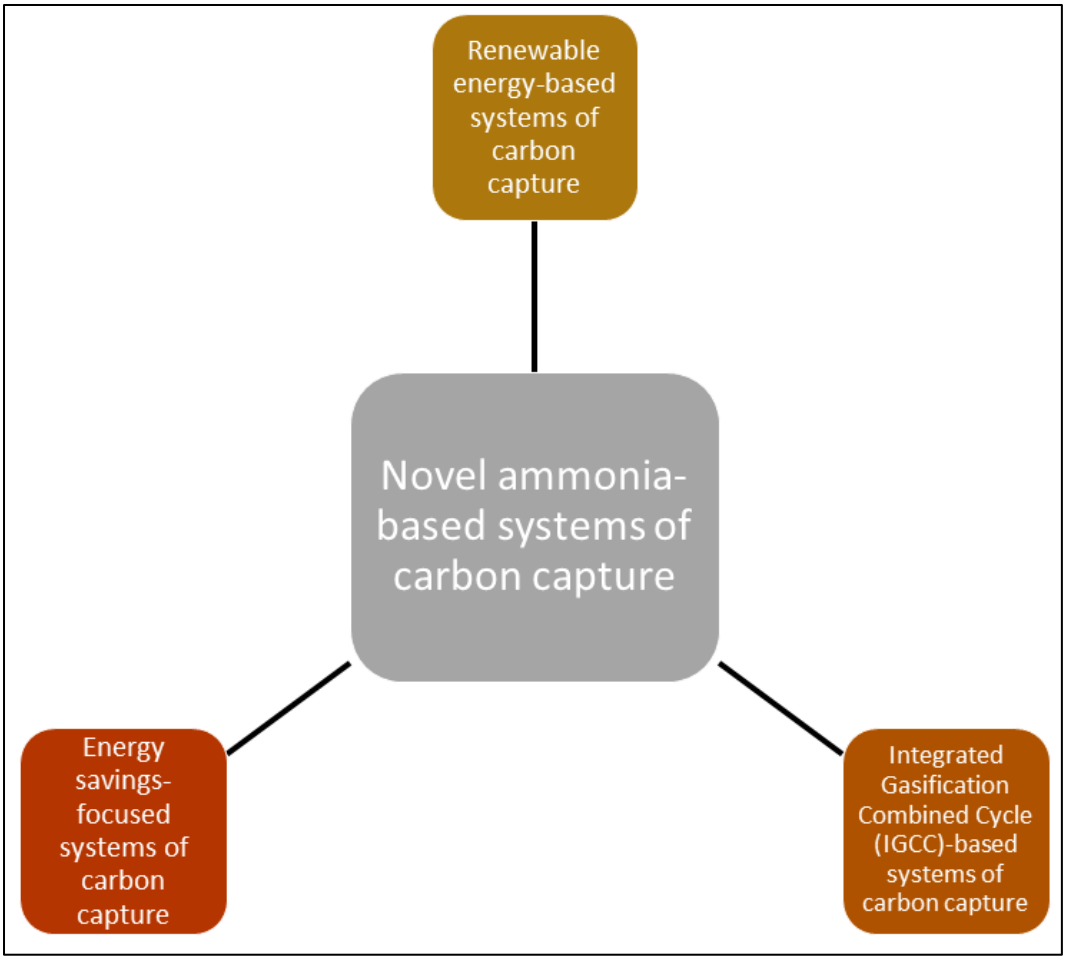

Figure 2.6: Categories of the novel ammonia-based system of carbon capture.

Koohestanian et al. [79] investigated the use of renewable energy to separate CO_2 from the flue gases of an oxy-fuel combustion power plant. A layout of their system is presented in Figure 2.8. The process starts by electrolyzing purified water to hydrogen and oxygen. The oxygen is taken to the power plant for the oxy-combustion process along with a separated oxygen stream from the air separation unit. Both the electrolyzer and the air separation unit are powered using renewable energy sources as well as some part of the electricity generated by the power plant. The hydrogen stream coming out of the electrolyzer mixes with the nitrogen leaving the air separation unit to make ammonia. Next, the flue gases that result from the oxy-combustion power plant are directed to the carbon capturing unit to separate the CO_2 from the rest of the gases. Once separated this stream goes to the urea unit to mix with ammonia to produce urea and water. The water is recirculated in the system while the urea is sold as a commodity. The estimated price of this urea is $3.5 million in a year. The rate of CO_2 removal is also estimated at 14892 tons yearly. The next step

suggested by the authors is to build a prototype of this system after the simulation work has been carried out using thermodynamic and chemical principles to verify the results and encourage the industry to adopt such a scheme.

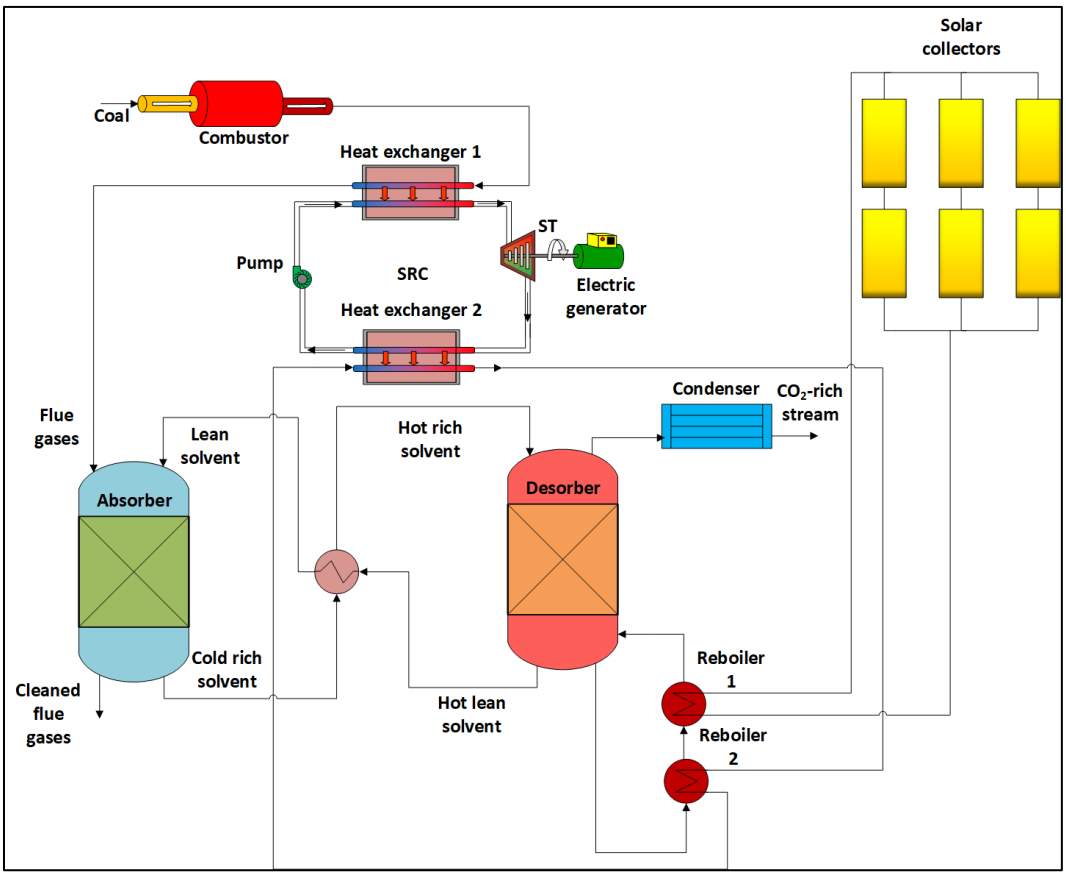

Figure 2.7: A thermal solar cell-assisted carbon capture system (adapted from [24]).

A hybrid approach of using renewable energy sources has been adopted by Ishaq et al. [25]. In their system, a stream of water is injected into a proton-exchange membrane (PEM) electrolyzer to produce hydrogen and oxygen. This electrolyzer is powered by wind turbines. In parallel, solar photovoltaic (PV) cells are used to power a cryogenic air separation unit to separate nitrogen from the incoming air stream. The resulting hydrogen and nitrogen are mixed in an ammonia synthesis reactor to produce ammonia. The last chemical process is the production of urea using this ammonia stream with the flue gases leaving a thermal plant that carries CO_2. Urea and water are produced from this chemical reaction, and the urea is sold as a commodity. The authors have investigated this system using ASPEN Plus and Engineering Equation Solver (EES) software pieces to conduct the thermodynamic analysis. The results of this analysis show that this system has the potential

to capture 1387 tons of CO_2 in a period of a year which is only 10% of the previous system. This process is limited by the concentration of CO_2 that exists in the flue gases, the higher the concentration the better the rate of CO_2 removal. This is why an oxy-combustion process is suggested for the thermal plant, but this requires major changes in current plants which could cause higher capital costs and reduces the economic feasibility of such an approach. Other results show that the system by Ishaq et al. [25] has overall energy and exergy efficiencies of 44.4% and 32.2%, respectively. The rate of urea production is 86.4 kmol in a day. This amounts to 1894 tons of urea in a year. Another study by Sánchez et al. [26] took this urea production step further and used the urea to produce DMC as a final product of the carbon capture process. The process proposed by them is also powered by multiple renewable energy sources, such as wind and solar. The DMC process inputs are renewable energy-based urea and renewable energy-based methanol. These are mixed in a DMC reactor to produce ammonia and DMC. In terms of economics, adding the DMC step after urea production is valuable since it reduces the production costs of DMC to $636 per ton compared to the conventional methods of producing DMC which typically costs between $1003 and $1346 for a ton [80]. On the other hand, the urea production costs using this process do not provide any significant production cost reductions compared to the conventional urea production processes that already exist in the market. Environmentally, the DMC production process adds more CO_2 emissions while the urea production process is nearly carbon neutral. So, adding the extra DMC process shows an economic advantage but has an environmental disadvantage over only urea production from the carbon capture process.

More recently, Siddiqui et al. [81] investigated a novel renewable-energy-based system for carbon capturing and ammonium bicarbonate production. The renewable energy source is wind turbines. The system schematic diagram is shown in Figure 2.9. The electricity coming from the wind turbines is supplied to the PEM electrolyzer to separate hydrogen and oxygen from the input water. The hydrogen is then taken to an ammonia synthesis reactor to chemically react with nitrogen to produce ammonia. Having dry ammonia is dangerous so water steam is mixed with this ammonia to make aqueous ammonia. The last step is to use this aqueous ammonia and react it with the CO_2 from the flue gases leaving the industrial thermal plant to make ammonium bicarbonate. Siddiqui et al. [81] conducted a thermodynamic analysis using the ASPEN Plus program. Their results show that this

system can absorb 640.1 kg of CO_2 per 1 MWh of supplied electricity from the wind turbines. Also, the costs of carbon capturing range drastically from $0.1 per one kilogram of CO_2 captured up to $0.23 per one kilogram of CO_2 captured using this system. The ammonium bicarbonate produced using this process can be sold as a commodity for food companies and other industries.

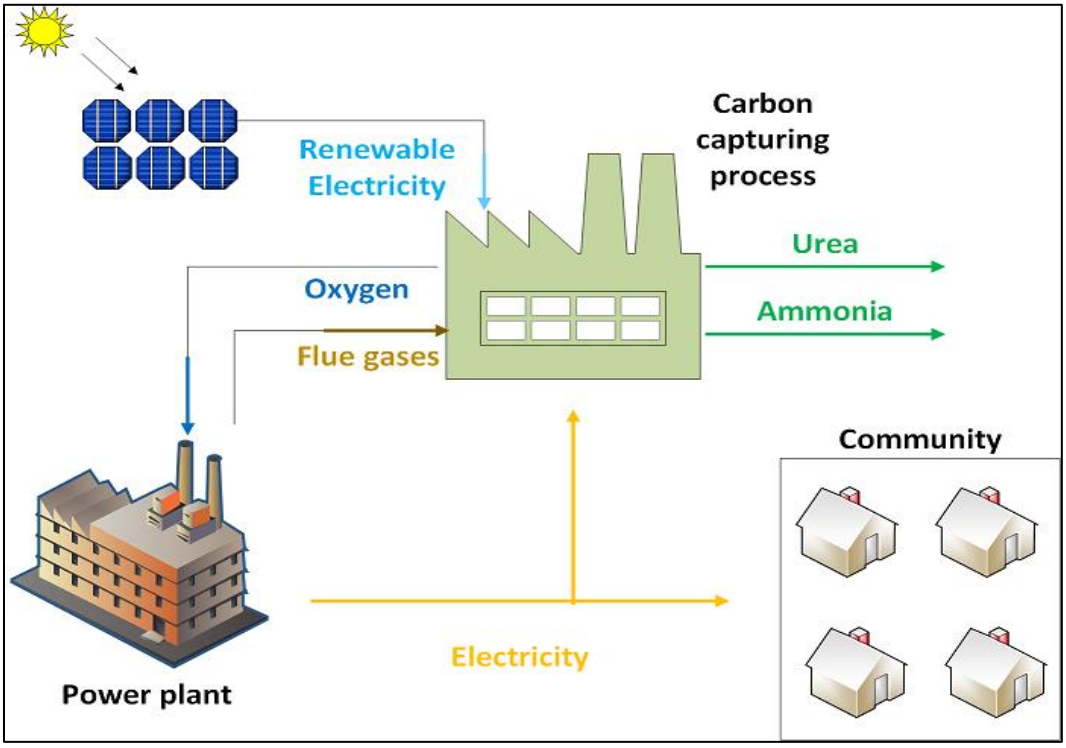

Figure 2.8: A renewable energy carbon capture system to produce urea and ammonia from the flue gases of an oxy-fuel combustion power plant (adapted from [79]).

2.2.2 Energy savings-focused systems of carbon capture

The second type of ammonia-based carbon capture systems to be reviewed here are the systems that have been designed for the sole purpose of reducing the energy requirements of the carbon capture system through the reconfiguration of the simple ammonia-based carbon capture which has been experimentally demonstrated back in 2014 by Lombardo et al. [82]. To start with, Bak et al. [83] conducted an experimental study on a lab-scale chilled ammonia process for carbon capture and measured the ammonia slip (ammonia release to the environment) as well as the rate of CO_2 removal under various operating conditions. Their experimental results show that the rate of CO_2 removal is 80% which is lower than what standard commercialized carbon capture technologies can provide at 85%, but the

ammonia slip was successfully maintained below 1% and this is better than what exists in conventional processes.

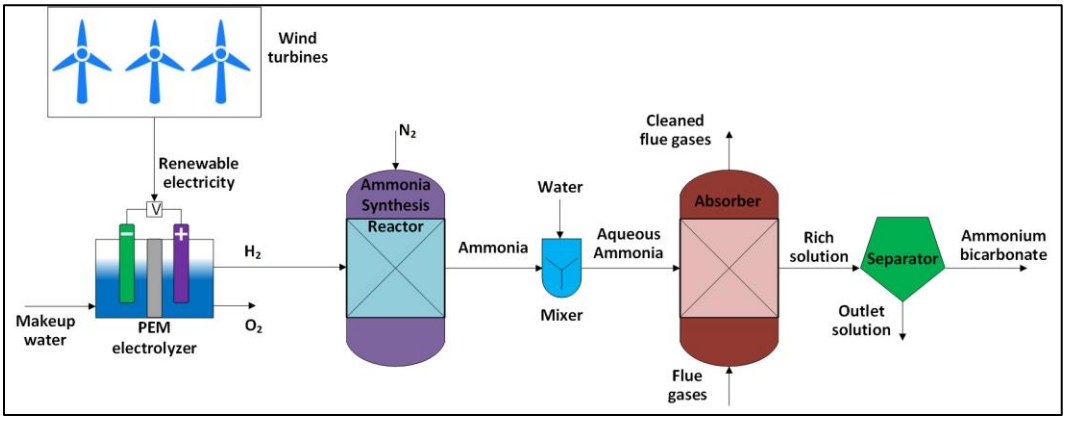

Figure 2.9: A wind turbine-based carbon capture system with the production of ammonium bicarbonate (adapted from [81]).

One study that shows how the energy requirements for carbon capture can be reduced by changing the operation of the simple ammonia-based carbon capture unit was presented by Bonalumi et al. [84]. They have used Aspen Plus software to simulate a cooled ammonia process which is a better alternative to the typical chilled ammonia process discussed previously. It is better in two aspects. There is no salt precipitation in the cooled ammonia process, unlike the chilled ammonia process. Another advantage is that the specific primary energy consumption for carbon avoided is lower for the cooled process, at 2.58 MJ kg^{-1} of CO_2 removed, than the chilled process, which is at 2.86 MJ kg^{-1} of CO_2. The main differences between these two operational ways of the ammonia-based carbon capture process are the regeneration pressure and temperature. The cooled process has regeneration pressure and temperature of 500 kPa and 378.8 K, respectively, while the chilled process has them at 2000 kPa and 368.6 K, respectively. The same authors conducted a techno-economic analysis of these ammonia-based processes when integrated with coal power plants [85]. Another study by Liu and Chen [86] that implemented a double-stage CO_2 absorber system showed a significant reduction in energy requirement of the ammonia-based carbon capture process by almost 25% and the rate of CO_2 removal has been maintained above 90%. Their system diagram is presented in Figure 2.10.

A different approach in reducing the costs associated with the installation of an ammonia-based carbon capture system is to reduce the size of the absorber column for the aqueous ammonia and carbon dioxide reaction. Reducing this size could help increase the economic

feasibility of such a system. One way to do this is to use chemical promotors to accelerate the rate of CO_2 absorption by the aqueous ammonia in the column. In 2018, Jiang et al. [87] proposed to use piperazine (PZ) which helps accelerate the rate of CO_2 absorption. They have simulated the addition of such a promotor using Aspen Plus and have found that the column height can be cut by as much as 35 % while maintaining the same or lower levels of energy consumption compared to the non-promoted case. The trend found is as the more PZ added to the aqueous ammonia the shorter the column can be for the same rate of CO_2 removal which was set at 85% in their study. Also, in their study, they have investigated the use of advanced flash strippers which resulted in reducing the energy requirements by nearly 7% compared to a simple flash stripper process with PZ. Detailed economic analysis of this system with the PZ promotion has not yet been studied and it has been recommended for future research. Also, other organic promotors to be added to the aqueous ammonia for an enhanced rate of CO_2 absorption need to be investigated and analyzed thermodynamically and economically in future works.

Obek et al. [88] compared different configurations of the ammonia-based carbon capture system to study their carbon capture efficiency and their potential energy savings. The three different configurations are called Lean Vapor Compression (LVC), Rich Solvent Split (RSS), and Rich Vapor Compression (RVC). Details of these configurations can be found in their paper [88]. The first thing compared was the carbon capture efficiency which was also compared to two reference cases which are an MEA-based carbon capture system and a simple ammonia-based carbon capture system. These two have carbon capture efficiencies of 92.66%, and 97.80%, respectively.

The three configurations considered in their study resulted in efficiency values of 97.24%, 97.61%, and 98.06% for LVC, RSS, and RVC, respectively. There are two main conclusions that can be drawn from these results. Firstly, ammonia-based systems are better at chemically absorbing carbon from flue gases than MEA which supports the claim to put more attention on investigating ammonia as a suitable absorbent for carbon capture technologies. Secondly, the three proposed configurations offer little improvement on the reference case of a simple ammonia-based system. Moving to the comparison of the energy savings of these three configurations compared to the reference case of a simple ammonia-based system, it has been found that the highest energy savings are found when using the

LVC configuration which provides 34.5% energy consumption reduction [88]. This is followed by the RSS configuration which has only a 6.4% reduction, while the RVC configuration increased the energy consumption by 0.3%. This comparative study shows us what kind of configuration has better chances at reducing the energy requirements for an ammonia-based carbon capture system and motivates future research in the direction of using the LVC configuration. Economic analysis on this configuration is required. Once this analysis shows economic feasibility, then moving on to the experimental stage and prototyping becomes justifiable. A study that presents complete energy and economic evaluations of an ammonia-based carbon capture system with the advanced flash stripper and a cold-rich split (CRS) has been conducted by Jiang et al. [89]. Their results will be discussed in the next section in more detail as part of the comparative study.

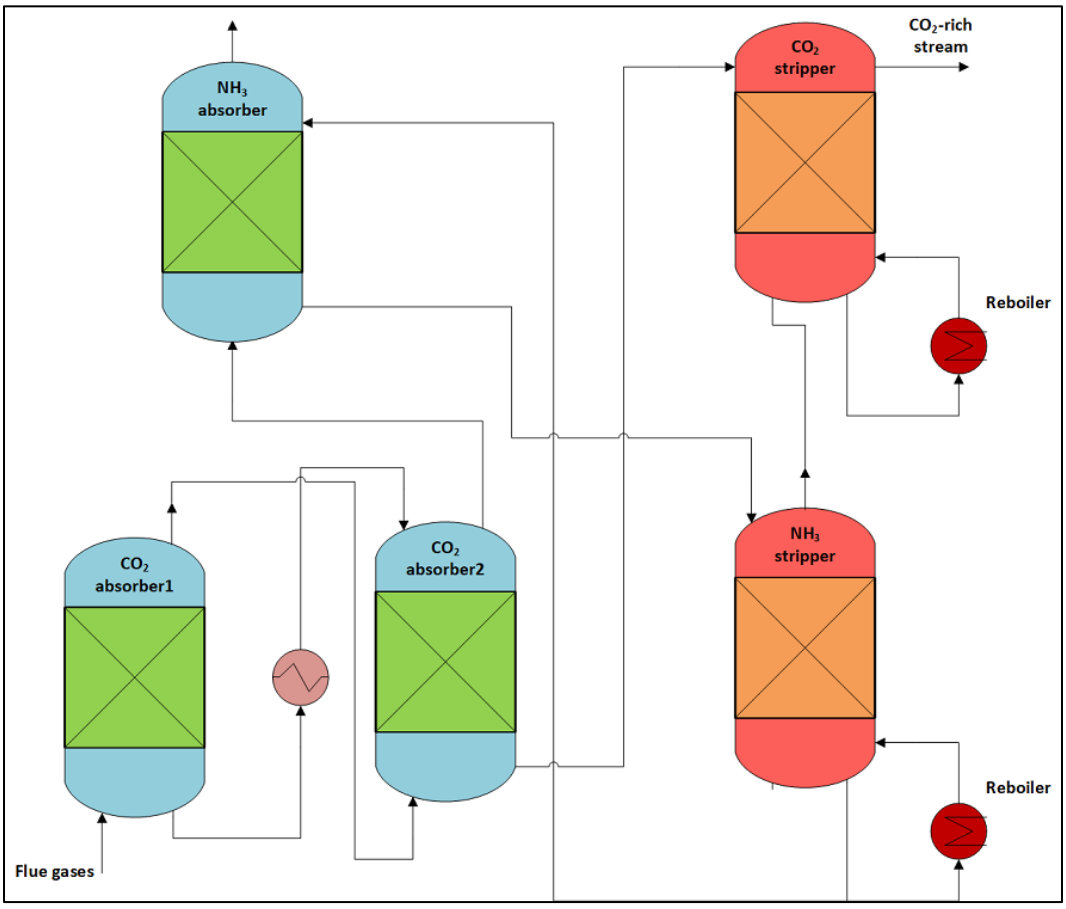

Figure 2.10: A double-stage CO_2 absorber ammonia-based carbon capture system (adapted from [86]).

More recently, Liu et al. [90] expanded on the comparison of different configurations over the research article explained above by Obek et al. [88] where they have included two more

possible configurations for ammonia-based carbon capture systems, which are cold split bypass (CSB), and the combination of CSB and LVC. Their simulation results show that using the CSB configuration decreases energy requirements by a significant amount at a reduction value of 34.2% compared to a typical ammonia-based system. Furthermore, the combination of CSB and LVC does not give noticeable energy reductions as it only reduces the energy requirements by an additional 0.2% to get a value of 34.4%. This combination does not seem like a viable option since using two configurations in a single system increases the capital costs and does not offer any energy savings potential.

A distinct method has been adopted where the ammonia-based carbon capture system reduces the energy requirements by using ammonia to provide some of the cooling needed by the typical chilled ammonia process. Wang et al. [91] developed a system that integrates an ammonia-based carbon capturing unit with an absorption chiller for supplying a cooling load. This cooling load provides a useful commodity that can be sold to cover some of the costs of operating the carbon capture system. The authors have conducted a thermodynamic analysis on this integrated system and found that the system can reach a rate of CO_2 removal of 90%, while the specific regeneration energy and the cooling load are 3.4 MJ kg^{-1} of CO_2, and 113.3 MW, respectively.

Lastly, Ullah et al. [92] introduced a combined modification of the typical ammonia-based carbon capture system to reduce the energy requirements and compared to the typical system as well as other modifications. They combined RVC (which was introduced earlier) with cold solvent split (CSS) processes. Their simulation results show that this new combination reduced the energy requirements by 20.2% compared to the typical chilled ammonia process and this is a much better reduction than other modifications, such as RSS which gives an 11.6% reduction, and inter-heating processes which provide only an 8.26% reduction. Also, the authors conducted a capital cost estimate to see if the additional components for this combined modification would save money. Their findings show that the combined modification of RVC and CSSP saves about $707 thousand every year. Therefore, the proposed modification is economically justifiable.

2.2.3 Integrated Gasification Combined Cycle (IGCC)-based systems of carbon capture

IGCC-with pre-combustion carbon separation systems are fossil fuel-consuming power generating systems that first gasify the fuel by transforming it into syngas. Then, carbon is separated from this gas before combustion to produce high-temperature clean exhaust gases to be given to a gas turbine. After that, the waste heat of these exhaust gases is recovered by supplying heat to a steam Rankine cycle for further power generation. This last step is what gives these systems the name combined cycles. A diagram of a typical IGCC with a pre-combustion carbon separation system is shown in Figure 2.11. At a rate of CO_2 removal of 85%, the efficiency of such a system can reach a reasonable value of 34.6% when the used fuel is pulverized coal [93].

The third category of carbon capture systems discussed here is regarding systems that combine ammonia-based carbon capture technologies with IGCC systems. There are two possibilities for this combination, either the carbon capturing happens prior to the combustion so it is named pre-combustion, or the carbon capturing takes place after the combustion, so it is called post-combustion. The main reason behind making this combination is that it has been shown that using chemical absorption methods to separate the carbon from the syngas increases the overall efficiency of the power generating system with high levels of carbon capture. For example, Bonalumi and Giuffrida [94] reached high net efficiency values of 41.7% with a rate of CO_2 removal reaching 90%. They have used a cooled ammonia process to capture the CO_2 post-combustion from an IGCC system. The fossil fuel used in their study is pulverized coal. This shows the potential of using ammonia-based carbon capturing technologies in IGCC systems. Furthermore, the specific primary energy consumption for CO_2 avoided was calculated to be comparatively low at a value of 2.3 MJ kg^{-1} of CO_2.

Petrescu et al. [95] have conducted simulations and Life Cycle Assessments (LCAs) for four cases comparing several supercritical pulverized coal power plants with and without post-combustion carbon capture. In the case of carbon capture, three solvents were used, namely MEA, aqueous ammonia, and calcium oxide. For the aqueous ammonia case, the overall efficiency of the system reached 35.09% when the rate of CO_2 removal is 85%.

This is slightly higher than the typical IGCC with the pre-combustion carbon separation system mentioned earlier, and it is lower than the cooled ammonia case mentioned above since the process used was the chilled ammonia process instead of a cooled ammonia process. Another conclusion that can be made from their study is that ammonia is a better solvent than MEA in terms of several environmental indicators, such as Acidification Potential (AP), and Human Toxicity Potential (HTP).

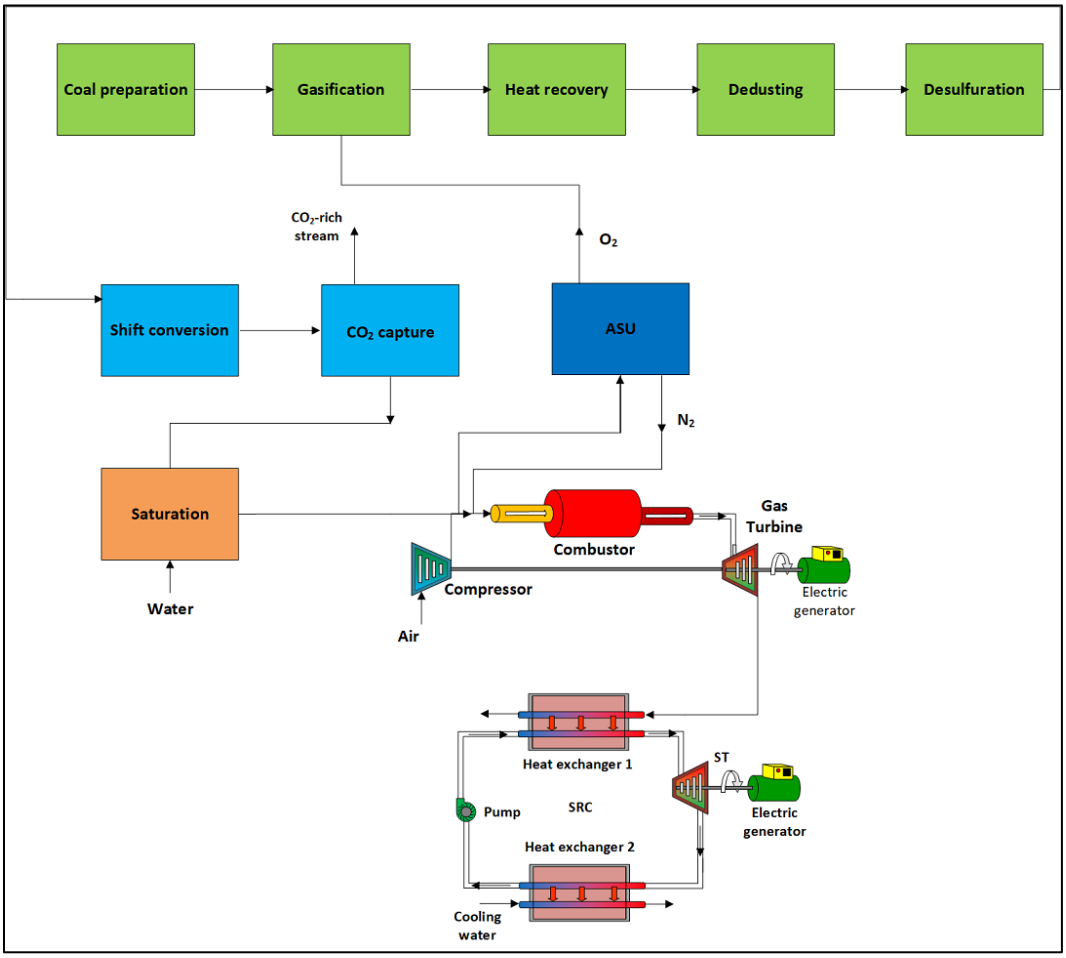

Figure 2.11: A diagram of a typical IGCC with a pre-combustion carbon separation system (adapted from [93]).

Asif et al. [96] have investigated the use of an ammonia blend as a solvent for carbon capturing in an IGCC system. Three cases of their proposed system have been studied, namely IGCC without carbon capture, IGCC with pre-combustion carbon capture, and IGCC with post-combustion carbon capture. After validating their model against experimental values, the results of the simulations show that there are only minor efficiency losses when the carbon capturing is implemented compared to the IGCC without carbon

capture case. The efficiency loss for the post-combustion case is 1.1%, while the pre-combustion case has a loss of 4.3%. This is mainly due to the higher steam content mixed with CO_2 which needs to be compressed and stored along with the carbon in the pre-combustion case compared to the post-combustion case. The steam content is higher because of the use of the water gas shift reactor in the pre-combustion case. These results show that post-combustion carbon capture is more efficient than pre-combustion. In both cases, the carbon capture rate was set to 92% [96]. It has been suggested that further economic analyses of these different cases be conducted for future research to understand the economic feasibility of the carbon capture cases.

2.3 Comparative assessments

In this section, a comparative assessment in terms of several parameters of the novel ammonia-based systems of carbon capture will be presented. Before going into the comparative assessments, a list of the ammonia-based systems of carbon capture is provided along with descriptions in Table 2.3. The first parameter to be compared is the energy requirements for the CO_2 capturing in a system. Figure 2.12 presents a comparison of the energy requirements to capture one kilogram of CO_2 for each of the selected ammonia-based carbon capture systems. There are some interesting findings that deserve to be mentioned. Firstly, the chilled ammonia process system is considered to be the reference system in this comparison, and it has an energy requirement of 3.22 MJ kg^{-1} of CO_2 captured and all other systems have significantly lower energy requirements except for the wind turbine-based system. This indicates that recent research efforts in developing new carbon capture systems are moving in a promising direction. The use of ammonia as a solvent is proving beneficial and can take an important part in future carbon capturing technologies due to its potential in producing lower energy requirement systems compared to other solvents and other carbon capture technologies, such as cryogenics. Secondly, the lowest energy requirement out of these selected carbon capture systems is the advanced flash stripper with CRS system, which is based on the combination of the advanced flash stripper and cold rich split processes. The use of combined reconfigurations of the chilled ammonia process system is another good direction in lowering the energy requirements to reach economically feasible carbon capture solutions. Thirdly, the wind turbine-based

system, which is based on the use of wind turbines and a hydrogen-producing electrolyzer, has the highest energy requirement for capturing carbon at a value of 5.62 MJ kg^{-1} of CO_2 removed. This higher level of energy requirements for this system is attributed to two deficiencies. The deficiency in hydrogen production by the electrolyzer and the other deficiency is that the ammonia is not recycled and is produced by the system using the Haber-Bosch synthesis process [81]. Ammonia is consumed to produce the ammonium bicarbonate product. Both of these processes are energy-consuming and result in higher energy requirements to capture the CO_2 from the flue gases. Future investigations should consider recycling the ammonia produced and using better configurations to lower the energy requirements of the wind turbine-based system.

Table 2.3: List of systems used in the comparative study.

System	**System description**	**References**
Chilled ammonia process	The typical Chilled Ammonia Process (CAP)	Valenti et al. [29]
Solar-assisted system	A thermal solar collector-assisted carbon capture system	Liu et al. [24], Versteeg and Rubin [97]
Wind turbine-based system	A wind turbine-based carbon capture system with the production of ammonium bicarbonate	Siddiqui et al. [81]
Advanced flash stripper with CRS system	Advanced flash stripper with a cold rich split for an ammonia-based carbon capture system	Jiang et al. [89]
Combined RVC and CSS system	Combined RVC and CSS modifications on the chilled ammonia process	Ullah et al. [92]
Cooled IGCC-based system	IGCC with post-combustion carbon capture at the cooled mode	Bonalumi and Giuffrida [94]

In Figure 2.13, the removal efficiencies of CO_2 from the flue gases for the ammonia-based systems are compared. The first thing to notice is that the lowest removal efficiency is 84.3% which is by the advanced flash stripper with-CRS system. This system has the lowest energy requirement as discussed earlier. So, a careful reconsideration of this system combined processes should be looked at in future works to improve the CO_2 removal efficiency without compromising the energy requirements of the system. Another thing to be noticed in the figure is all the other systems are performing close to the reference system at around 88.4%. This shows that advancing the designs of ammonia-based systems to lower their energy requirements does not necessarily affect the CO_2 removal efficiency of these new systems. As long as the CO_2 removal efficiency does not fall far from the

standard 85% value then the newly designed ammonia-based system should be proficient [98].

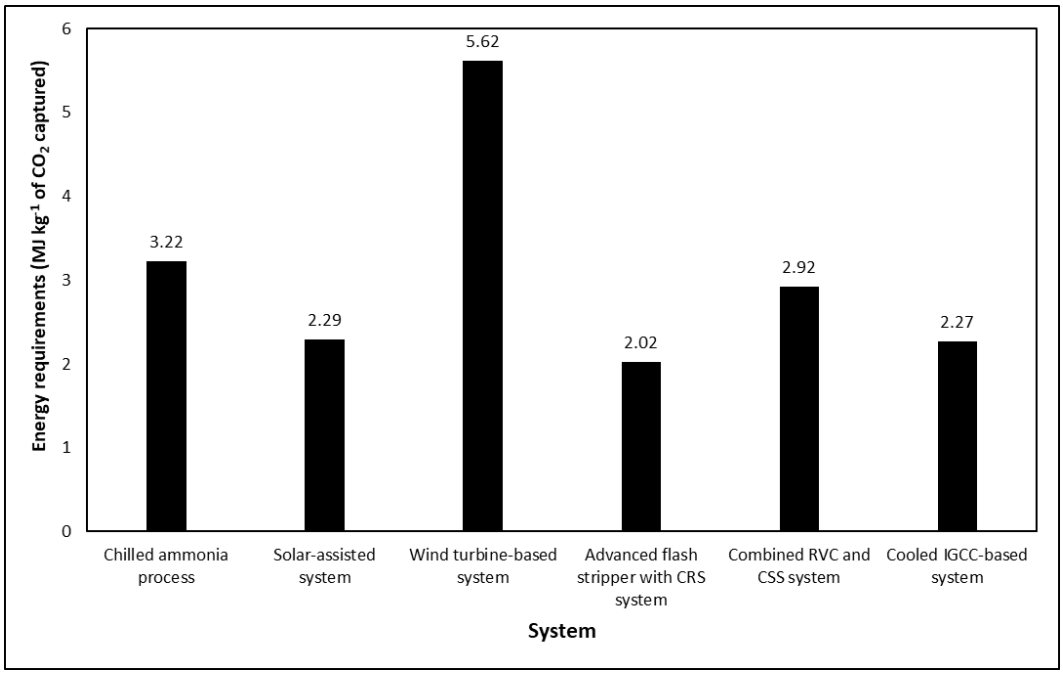

Figure 2.12: Comparative assessment of the energy requirements for the considered ammonia-based carbon capture systems. Data for these systems are taken from references mentioned in Table 2.3.

In Table 2.4, the third parameter of this comparative assessment is presented, that is the operational costs of running each of the selected ammonia-based carbon capture systems. For a typical chilled ammonia process system, the cost for capturing a ton of CO_2 is C$59.95. The only new system with lower costs is the advanced flash stripper with-CRS system at a value of C$51.68 ton^{-1} of CO_2. Unfortunately, this is not a significant improvement for the sole reason that it costs more to use additional processes than to use a simple chilled ammonia process. The costs are lower because the energy requirements of the advanced flash stripper with-CRS system are significantly lower than the chilled ammonia process system. Regarding the renewable energy-based systems of carbon capture, they cost more to operate than the reference chilled ammonia process system due to the additional costs of adding solar cells for the solar-assisted system and adding a hydrogen electrolyzer, and consuming ammonia for the wind turbine-based system. The solar-assisted system and the wind turbine-based system have operational costs of C$76.2 and C$136 of ton^{-1} of CO_2 captured, respectively. The combined RVC and CSS system and the cooled IGCC-based system have no data regarding their operational costs

according to the literature, so there is a need to conduct economic studies for them and other recently developed systems of carbon capturing using ammonia as a solvent.

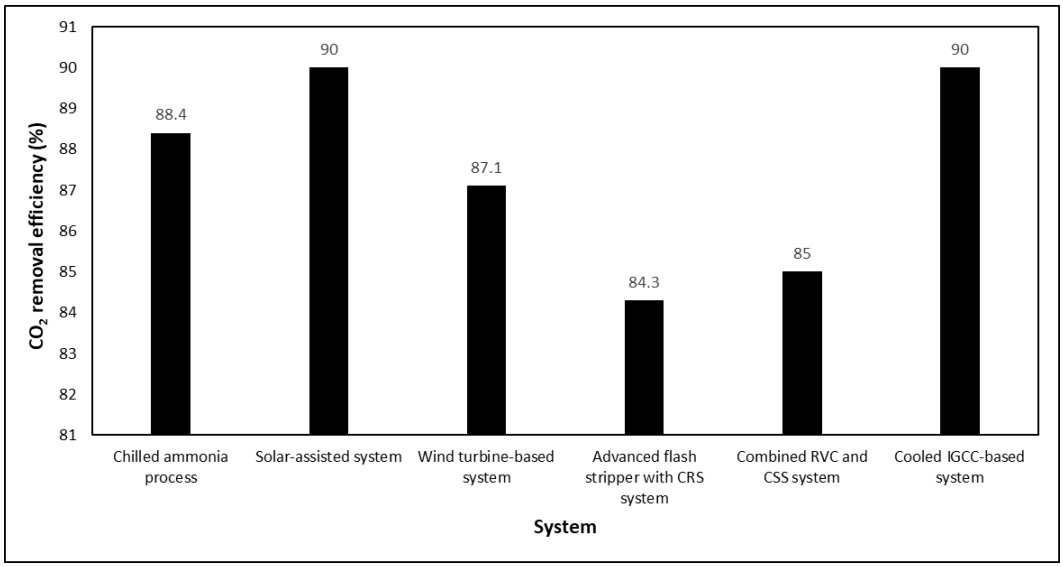

Figure 2.13: Comparative assessment of the CO_2 removal efficiency for the considered ammonia-based carbon capture systems. Data for these systems are taken from references mentioned in Table 2.3.

Table 2.4: Comparative assessment of the operational costs for the considered ammonia-based carbon capture systems. NA stands for Not Available.

System	**Operational costs (C$ ton^{-1} of CO_2 captured)**	**Sources**
Chilled ammonia process	59.95	Valenti et al. [29]
Solar-assisted system	76.2	Versteeg and Rubin [97]
Wind turbine-based system	136	Siddiqui et al. [81]
Advanced flash stripper with CRS system	51.68	Jiang et al. [89]
Combined RVC and CSS system	NA	NA
Cooled IGCC-based system	NA	NA

An interesting and important parameter that has not been considered before to show the potential of a carbon capture system is the economic value of the products of such a system. There are mainly three economically valuable outputs that can be produced by carbon capturing systems, namely carbon tax savings, electricity or heat, and chemical products. Increasing the value of these outputs can help mitigate the operational costs of the system and increase the chances of making profits from a carbon capture system to reach a point of economic feasibility and attract the fossil fuel industry to adapting such technologies and systems.

Figure 2.14 shows the combined price of output products and carbon tax savings for the selected ammonia-based systems of carbon capture. There are a few points that can be mentioned about the result of this figure. To begin with, the price of the output of the wind turbine-based system is C$7.699 MJ^{-1} of input energy which is much higher than the other systems by orders of magnitudes, and this is mainly because of the value of the chemical material produced by the system, that is ammonium bicarbonate. This shows the potential of designing carbon capture systems that produce useful chemicals to generate some economic value to compensate for the operational costs of the carbon capturing process. This way the system becomes environmental and economic. Other systems only provide electricity and carbon tax savings which are much less valuable and do not have much potential to cover the costs of the carbon capturing process. The second highest value shown in the figure is C$0.0198 MJ^{-1} of input energy. This value is because of the low energy requirements of the advanced flash stripper with-CRS system which is inversely proportional to the carbon tax savings of any carbon capture system.

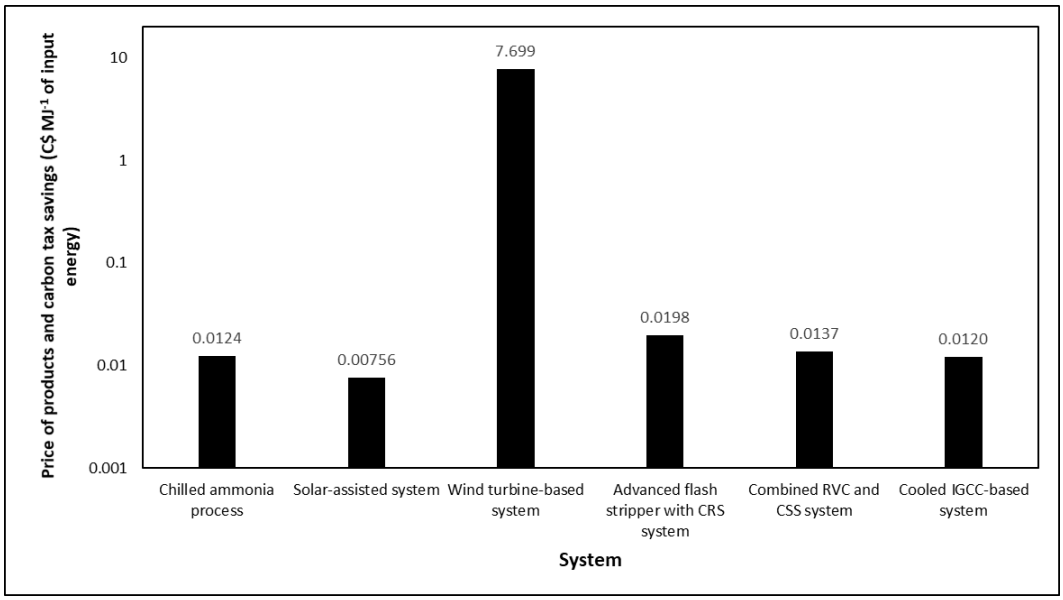

Figure 2.14: Comparative assessment of the price of products and carbon tax savings for the considered ammonia-based carbon capture systems. The logarithmic scale is used for clarity. Data for these systems are taken from references mentioned in Table 2.3.

2.4 Future directions

This section will mention a list of possible future research directions and opportunities in the field of ammonia-based systems of carbon capture:

- Conducting comprehensive economic feasibility studies on the newly proposed ammonia-based systems of carbon capture.

- Building pilot-scale setups for these systems to demonstrate the concepts experimentally and to explore the technical difficulties of operating such systems.
- Encouraging the fossil fuel industry to adapt the carbon capture systems through simulations, economic studies, experimentation, and awareness of its importance to climate change.
- Introducing more system designs to produce useful chemical commodities alongside the carbon capturing system to reduce the overall operational costs of the system. Some possible chemical commodities include ammonium bicarbonate, urea, and DMC.
- Using different configurations to reduce the problem of ammonia slip down to less than 1%. This can be done by ammonia recycling or/and utilization in some chemical processes.
- Performing detailed economic analysis of ammonia-based carbon capture systems with the PZ promotion has not yet been studied and it is recommended for future research. Also, other organic promotors to be added to the aqueous ammonia for the enhanced rate of CO_2 absorption need to be investigated and analyzed thermodynamically and economically in future works.
- Focusing future efforts on the LVC configuration since it showed the highest energy savings potential of 34% [88]. Economic analysis on this configuration is required. Once this analysis shows economic feasibility, then moving on to the experimental stage and prototyping becomes justifiable.
- Investigating combinations of the three categories of the ammonia-based systems mentioned in this review paper. For example, it is interesting to see how a post-combustion carbon capturing IGCC system is integrated with renewable energy sources.

Figure 2.15 shows how designs of carbon capturing systems are evolving towards self-sustaining systems using the co-production of useful chemicals to compensate for the operational costs of the system.

2.5 Closing remarks on the literature review

In this chapter, a review of the most recent ammonia-based carbon capture systems, that were published between 2015 and 2020, has been conducted. These systems have been

presented and discussed in terms of their system designs, novel configurations and integrations, their advantages, and their limitations. These recent ammonia-based carbon capture systems are categorized into three categories, namely renewable energy-based systems, energy savings-focused systems, and IGCC-based systems.

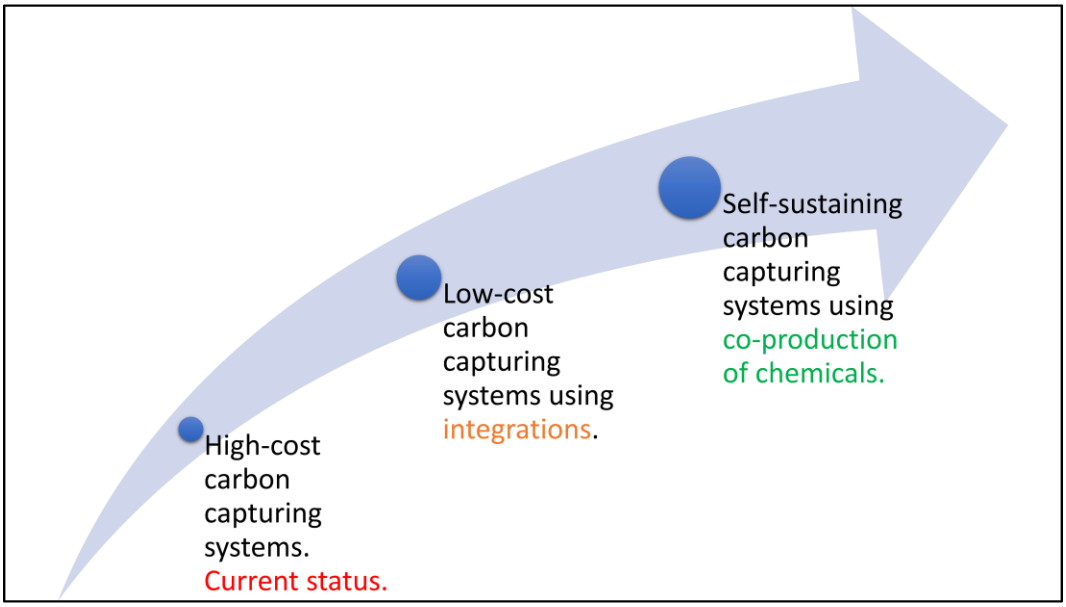

Figure 2.15: Evolution of carbon capture systems.

Compared to conventional carbon capture systems, renewable energy-based systems have the potential to lower energy requirements and lower exergy sources by using carbon-free heat sources, as well as such systems have been proposed to use the excess electricity produced by the renewable energy sources to co-produce useful chemical commodities to offset the operational costs of the carbon capture systems. Another promising approach to reducing energy requirements is through reconfigurations of the typical ammonia-based absorption process. The LVC configuration provides a 34.5% energy requirements reduction, which is the highest reduction of all the configurations proposed recently.

Furthermore, a comparative study of selected ammonia-based systems of carbon capture has been carried out. The chilled ammonia process was chosen as a reference system. In general, the novel ammonia-based systems have significantly lower energy requirements, which means that the effort in designing new configurations is successful and is going in the right direction to make carbon capturing systems more viable. However, the wind turbine-based system has higher energy requirements by 74.5%. The operational costs of the novel renewable energy-based systems are considerably higher than the reference

system and future work needs to focus on reducing these costs to achieve economic feasibility. Finally, the economic advantage of co-producing chemicals has been demonstrated. The price of the output of the chemical-producing carbon capture system is orders of magnitudes higher than the other systems which do not produce any chemical commodities.

2.6 Research gaps in the literature

From the above literature review, a list of research gaps in the literature are outlined here:

- There is a knowledge gap in the open literature of carbon capture technologies in studying the use of geothermal power plants as an energy supply for carbon capture. Another knowledge gap in the literature is the use of electrochemical ammonia synthesizers for ammonia production as a solvent for capturing carbon dioxide to produce a useful chemical commodity.
- A lack in investigating the exergoeconomics of the use of an ammonia-based carbon capturing unit on a solid-oxide fuel cell hybrid system and producing ammonium bicarbonate as a method of utilizing carbon dioxide. This is important because it provides the economic feasibility of the integrated system.
- There is a lack in the optimization of this integrated system in terms of exergetic performance and costs of products.
- There exists a knowledge gap in the literature on how concentrated solar collectors can be used to assess in carbon capturing from the exhaust gases of an oxy-combustion Brayton cycle.
- There seems no work on the exergoeconomics of an oxy-combustion Brayton cycle integrated with a supercritical carbon dioxide cycle, and the system features a solar energy-based carbon capture and utilization unit for the production of ammonium bicarbonate as a valuable chemical using carbon dioxide from the oxy-combustion process.
- Also, the optimization of this integrated system has yet to be investigated through multi-objective optimization methods.

Chapter 3: Systems Development and Experimental Setup

In this chapter, the ammonia-based carbon capturing systems investigated in this work are described through mentioning the operations of the systems and their components. Also, the experimental setup for the ammonium bicarbonate batch reactor along with its procedure are explained.

3.1 Carbon capturing system 1

The first system considers a carbon capturing system that splits water (H_2O) for hydrogen generation, then produces ammonia to react with the incoming CO_2 stream from a thermal power plant to make ammonium bicarbonate. Ammonium bicarbonate is an inorganic salt that is produced when carbon dioxide, water, and ammonia react chemically. The chemical formula for this salt is NH_4HCO_3. Ammonium bicarbonate has several applications, such as baking in the food industry, adhesives, farming, and cleaning products [99,100]. The plastics and leather industries are consuming more ammonium bicarbonate year to year as the demands on plastics and leather in the fashion industry continue to increase. The health hazard for this chemical is minor and it can cause minimum respiratory irritation upon inhalation and contact with eyes or skin can cause irritation. This chemical commodity is valuable and can be sold to potentially compensate for the operational costs of the carbon capturing system. The system is schematically shown in Figure 3.1. The system starts by receiving power from a renewable energy source which is a wind-turbine farm in this case to electrolyze distilled water for hydrogen generation. The hydrogen is required to be at a high-pressure level to react with nitrogen for the production of ammonia. This can be achieved in two possible ways. Compressing the hydrogen after it leaves the electrolyzer and the problem with this is the high costs of purchasing a specialized hydrogen-type compressor and the increased power input for it. Another cheaper way is to pump the water to the desired pressure level, which is 10 bars in this process before it enters the PEM electrolyzer so that the hydrogen output has a high-pressure level as required for the ammonia synthesis reactor. If the hydrogen pressure required for the process was more than 70 bars, then using a hydrogen compressor could be more feasible, but the desired pressure for hydrogen in his process is much lower at 10 bras only. Next, the hydrogen enters an ammonia synthesis reactor along with nitrogen in order to produce ammonia.

Before the nitrogen enters the reactor, it gets compressed by a compressor to the operating pressure of the reactor. This pressure is necessary to increase the amount of ammonia produced and reduce the reaction time. Dry ammonia leaves the reactor at high pressure of around 10 bar which is operatable according to a study by Vojvodic et al. [101]. A valve is used to depressurize the ammonia before it enters the mixer to mix with water for making aqueous ammonia. After that, the aqueous ammonia is supplied to the absorber to react with the incoming CO_2 to produce ammonium bicarbonate similar to the work of Siddiqui et al. [81]. This absorber can be replaced with an ambient pressure reactor that works as a batch reactor to produce as much ammonium bicarbonate as possible. For a large-scale plant, a parallel set of these batch reactors can be used to keep the process steady state. Typically, ammonium bicarbonate precipitation is minimized in such absorbers to avoid clogging, but in this case, more ammonium bicarbonate is desired and the extraction of this ammonium bicarbonate from the reactor is needed. While one batch reactor is producing solid ammonium bicarbonate, another parallel batch reactor can continue to absorb CO_2 from the incoming flue gases. Lastly, a separator is used to separate the ammonium bicarbonate from the rich solution. The separated rich solution can be recycled to capture more CO_2 from the incoming flue gases stream.

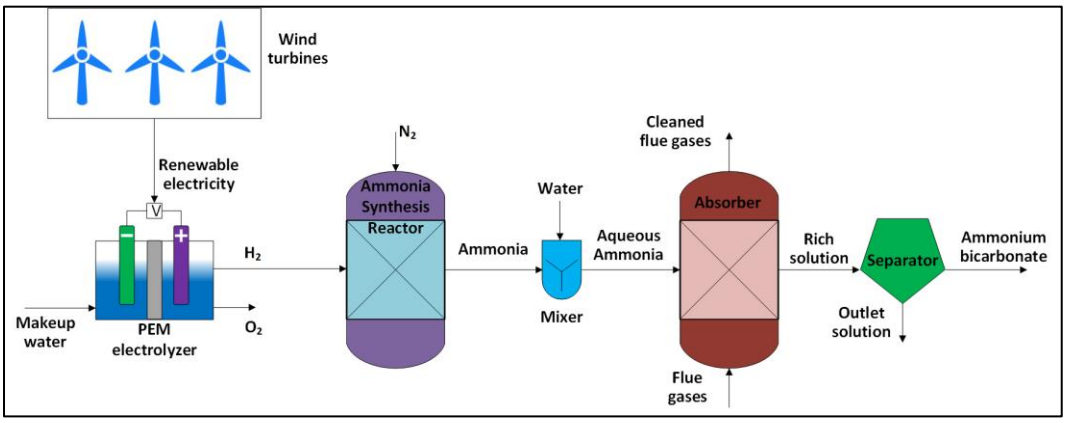

Figure 3.1: A wind turbine-based carbon capture system with the production of ammonium bicarbonate.

3.2 Carbon capturing system 2

In Figure 3.2, a schematic diagram of the second proposed integrated system in this work is presented. Natural gas, stream 17, is injected into the integrated system, and it goes through the fuel regenerator to preheat the fuel before it mixes with steam (stream 43), with

a molar ratio of 2:1 steam to methane. Then the mixture goes to the anode side of the SOFC. In parallel, air (stream 19) at ambient temperature and pressure with values of 293 K and 101 kPa, respectively, enters the system through an air compressor where it gets compressed with a ratio of around 8. Then it goes through the air regenerator in which air receives heat from the exhaust gases stream (stream 29), and then it goes to the cathode side of the SOFC which is stream 21. Inside the SOFC, an electrochemical reaction takes place that generates electric power by oxidizing the fuel and the steam. Stream 22 leaving the anode side of the SOFC contains carbon dioxide, carbon monoxide, steam, and hydrogen, with molar percentages of 16%, 4%, 65%, and 15%, respectively. Oxygen and nitrogen, with molar percentages of 7.5%, and 92.5%, respectively, leave the cathode side of the SOFC, which is stream 23. The next thermal component is the water-gas shift membrane reactor (WGSMR) and afterburner which completes the chemical reaction by oxidizing the carbon monoxide with steam to produce carbon dioxide and hydrogen in stream 22. The hydrogen permeates to the other side to react with oxygen to produce high-temperature exhaust gases in stream 25. The resulting stream 24 from the anode side of the WGSMR-afterburner contains carbon dioxide (24.7%) and steam (75.3%), while the other stream, named stream 25, contains nitrogen, steam, and excess oxygen (2.21%). Stream 24 goes to condenser 1 to separate the water from the carbon dioxide and this carbon dioxide in stream 28 goes to the ammonium bicarbonate reactor. The other exhaust gases in stream 25 that are at high temperature and pressure are expanded in turbine 3 to produce power. Then, these exhaust gases in stream 26 pass through four heat exchangers to recover some waste heat, in order, they are fuel regenerator, air regenerator, boiler, and heater.

The Steam Rankine Cycle (SRC) operates by absorbing waste heat from the exhaust gases in stream 30 in the boiler. The heat is absorbed to produce high-pressure (1,500 kPa) superheated steam. This steam in stream 34 is expanded in turbine 4 to produce more power. A mixture of saturated water leaves the turbine in stream 35, and it gets completely condensed as it passes through condenser 2 and it supplies waste heat to the multi-effect desalination (MED) unit for freshwater production. The last step in the SRC is for the condensed water to be pumped to a high pressure using a pump that completes the cycle. The heater uses low-temperature exhaust gases in stream 31 to provide space heating to the community.

Next, the carbon capturing subsystem which is powered by the geothermal power plant is described. The geothermal power plant is supplied by a production well which supplies high pressure (3,338 kPa) and high temperature (513 K) water stream (stream 1) [102,103]. Flash chamber 1 is used to lower the pressure of this stream down to 500 kPa and produce a gas phase of water in stream 2. Next, the steam (stream 3) is separated from the liquid water (stream 5) in separator 1. The steam is expanded in turbine 1 to produce electric power, and then stream 4 goes directly to the reinjection well. Some of the geothermal fluid is supplied to the carbon capturing unit for additional ammonium bicarbonate production as shown on stream 45. The water stream (stream 5) leaving separator 1 goes through the steps of flashing, separation, and expansion again to produce more electric power. This makes it a double-flash geothermal power plant. Most of this electricity is supplied to the electrochemical ammonia synthesizer. This synthesizer accepts nitrogen (stream 12) and water (stream 11) streams with a molar ratio of 1:3 of nitrogen to water. This device produces ammonia in stream 14 and oxygen in stream 13 using this renewable electricity. Ammonia proceeds to the mixer in which it mixes with water (stream 44) to produce aqueous ammonia (stream 15), while the oxygen stream is released to the environment. The ammonia and water enter the mixer with a molar ratio of 1:1. Finally, to capture the carbon dioxide and produce ammonium bicarbonate, the aqueous ammonia reacts with the high purity carbon dioxide to produce ammonium bicarbonate.

3.3 Carbon capturing system 3

Figure 3.3 displays the schematic diagram of the integrated system introduced here. The integrated system can be divided into three parts, namely the solar energy part, the gas turbine-supercritical carbon dioxide combined cycle part, and the carbon capturing unit. Beginning with the solar energy part, stream 1 which is liquid water is at high pressure and low temperature is heated by absorbing heat from the concentrated solar collectors which makes the water turn to a high pressure and high temperature steam. Then, this steam is split into two streams, where a portion of the steam goes to the thermal energy storage for later use when the sun is absent, while the other portion is sent to turbine 1 (T1) where the steam in stream 4 is expanded to produce electric power to supply energy to the elastocaloric cooling device (ECD) for meeting the cooling demands and to supply energy to the electrochemical ammonia synthesizer (EAS).

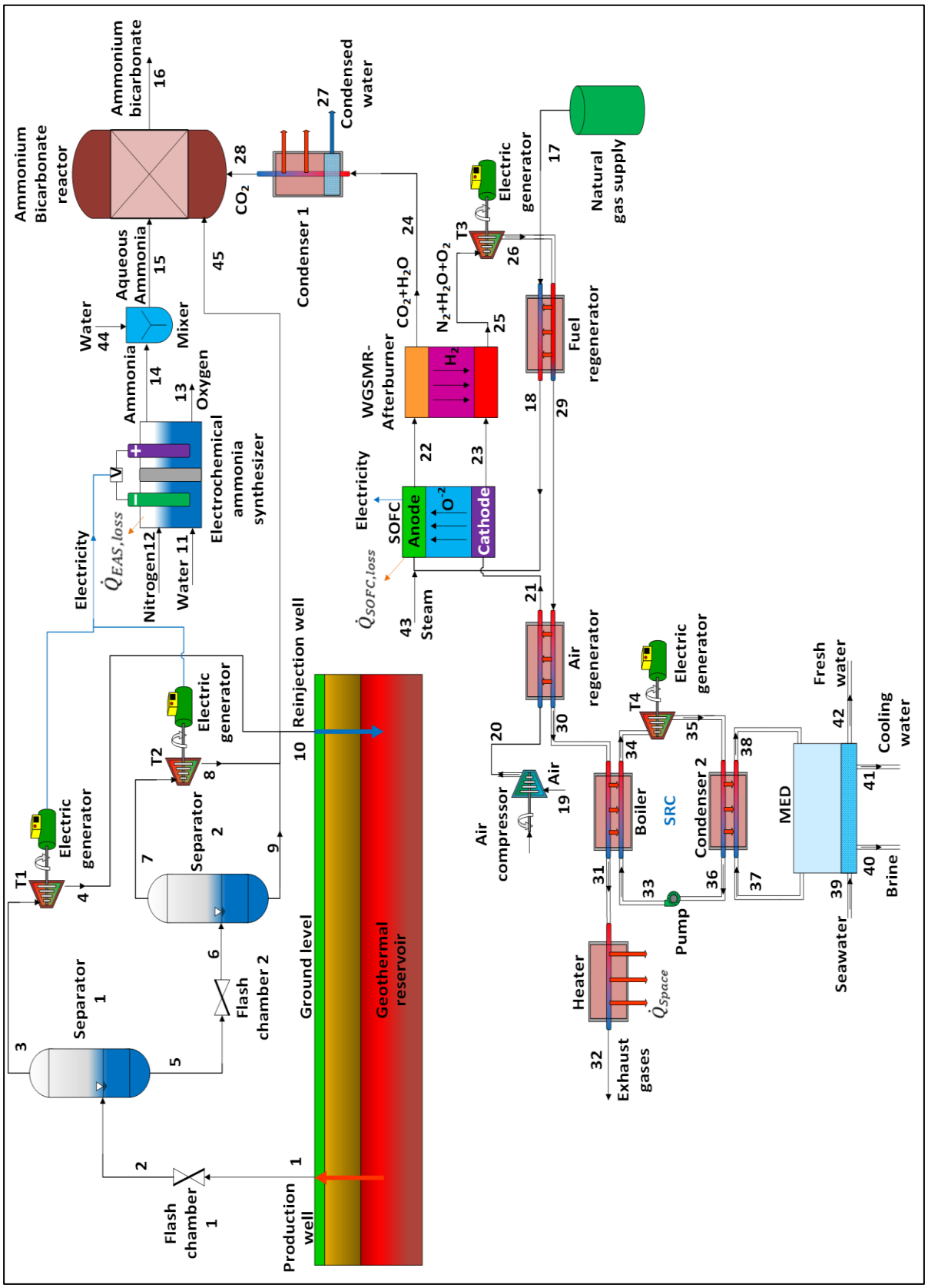

Figure 3.2: A multigeneration integrated system based on geothermal energy and solid-oxide fuel cell with carbon capture.

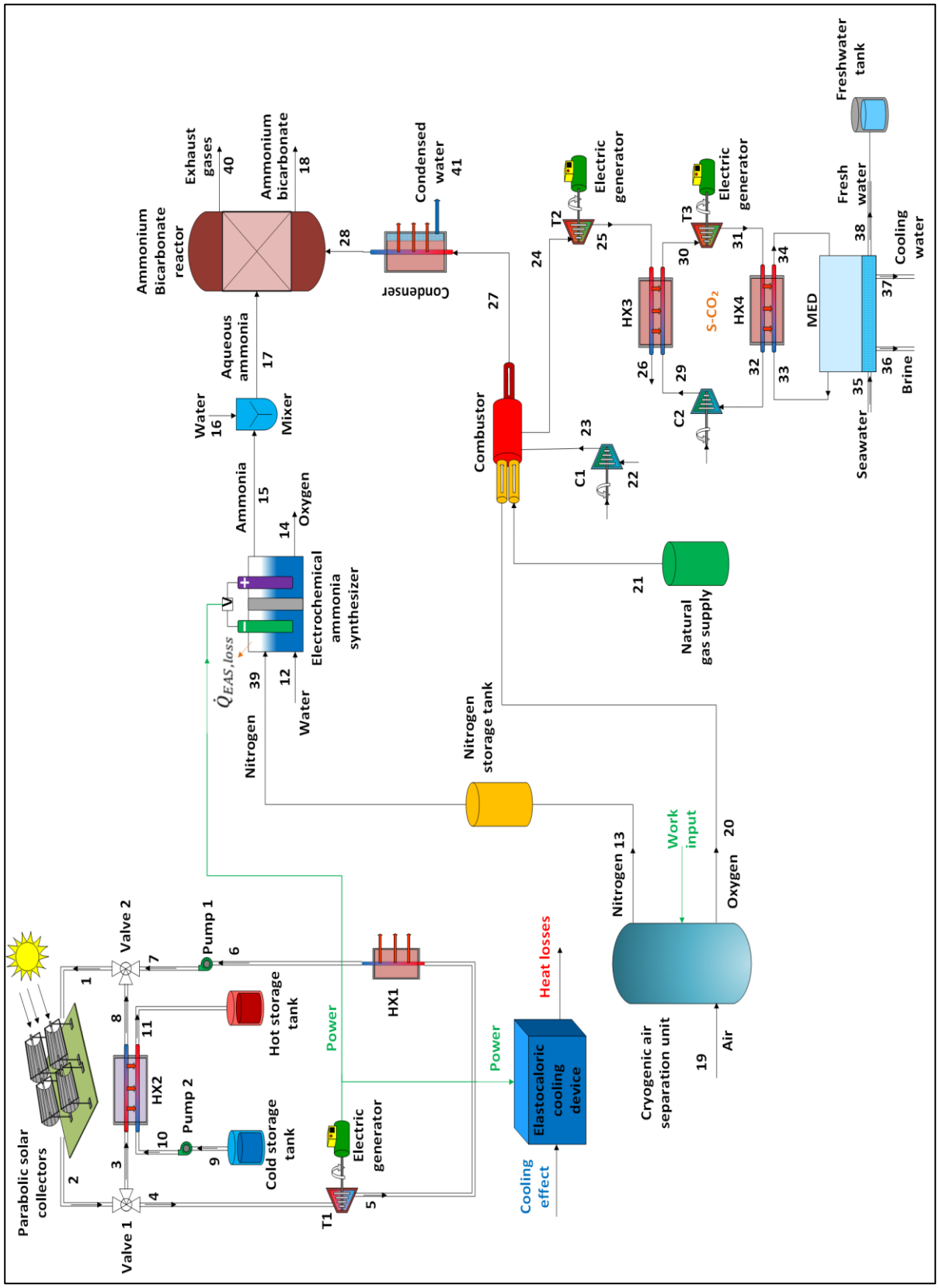

Figure 3.3: A gas turbine-supercritical carbon dioxide integrated system with a solar energy-based carbon capture unit.

The elastocaloric cooling device utilizes the electric power to produce a cooling effect using a shape memory alloy (SMA). This alloy transforms from the austinite phase to the martensite phase which is a process that releases heat and decreases its entropy. This transformation is induced using mechanical stress which is applied on the device. After that, the applied mechanical stress is removed, and the phase transformation is reversed from martensite to austinite where the SMA absorbs heat from the surroundings and provide the cooling effect at this stage of the transformation.

Secondly, the gas turbine-supercritical carbon dioxide combined cycle part is described. It starts with taking air and separating the oxygen from the nitrogen using a cryogenic air separation unit which requires work input from turbine 2 (T2). Two streams leave the air separation unit (ASU), one oxygen-rich stream called stream 20, and a nitrogen-rich stream called stream 13 in the schematic diagram. The nitrogen-rich stream is stored in a storage tank to control its supply to the electrochemical ammonia synthesizer. The oxygen-rich stream goes to the combustor and gets burned with the natural gas coming from the supply (stream 21) to produce carbon dioxide-rich exhaust gases (stream 27) that contain carbon dioxide, steam, excess oxygen, and some residual nitrogen. The thermal energy produced from this combustion are absorbed by the incoming air that was pressurized using compressor 1 to have air at high pressure and temperature (stream 24). This stream gets expanded by turbine 2 (T2) to produce electric power that supplies energy to compressor 1, and the ASU. The expanded air stream then proceeds to heat exchanger 3 (HX3) to supply thermal energy to the bottoming cycle in which supercritical carbon dioxide is used as a working fluid.

Stream 27 contains steam which can be extracted using the condenser which means the stream leaving this component (stream 28) predominantly has carbon dioxide with some residual oxygen and nitrogen. This is desirable for the carbon capturing unit. The supercritical carbon dioxide (S-CO_2) cycle works by absorbing heat from the expanded air stream from the gas turbine cycle at a very high-pressure level. Then, the working fluid is depressurized in turbine 3 (T3) to create more electric power. Next, the working fluid in this cycle losses its thermal energy to the multi-effect desalination (MED) unit in order to utilize this waste heat to further produce freshwater from seawater. Compressor 2 (C2) completes the S-CO_2 cycle by increasing the pressure of the working fluid again.

The last part of this integrated system is the carbon capturing unit. This unit receives three streams from the other two parts mentioned earlier, which are an electric power stream from the solar energy, nitrogen stream from the nitrogen storage tank, and a CO_2-rich stream leaving the condenser. This unit begins by producing ammonia at the electrochemical ammonia synthesizer using nitrogen, water, and electricity. The produced ammonia goes to the mixer where it mixes with a stream of water to make aqueous ammonia. Finally, the aqueous ammonia comes in contact with the CO_2-rich stream to produce ammonium bicarbonate in solid form and some residual oxygen and nitrogen gases that are released to the environment.

3.4 Experimental setup and procedure

The experimental setup of the proposed ammonia-based carbon capturing unit for the production of ammonium bicarbonate is presented for the baseline case in Figure 3.4. This baseline represents a typical ammonium bicarbonate production batch reactor without any additions. There are two additions that will be studied in this experimental investigation, which are adding a metallic ferromagnetic catalyst which will be called the catalyst case. The second addition is the electromagnetic induction heater for selective heating of the metallic catalyst, and this will be called the induction heating case. This means that there are three cases studied in total for this experimental investigation of the ammonium bicarbonate production unit. The components of the setup include the batch reactor which a three-neck glass flask with a total volume of 500 mL. One neck is attached using a glass connector to the gas inlets of ammonia and carbon dioxide. These gas inlets are controlled using a valve as shown in the figure. At the bottom of the glass flask, there is another valve for controlling the volume of water displaced by the inlet gases and the volume is measured by a graduated cylinder below the batch reactor. The reaction temperature is measured using a stainless-steel thermocouple type K. This thermocouple is connected to a data logger and then this logger is attached to a computer for taking measurements. The entire experimental setup is done inside a fume hood for safety reasons and to exhaust any leakage gases if they do occur during performing the experiments. The fume hood inside

temperature is measured to be 23.6°C, the outside temperature is 23.8°C, and the face velocity is 190 ft min^{-1}.

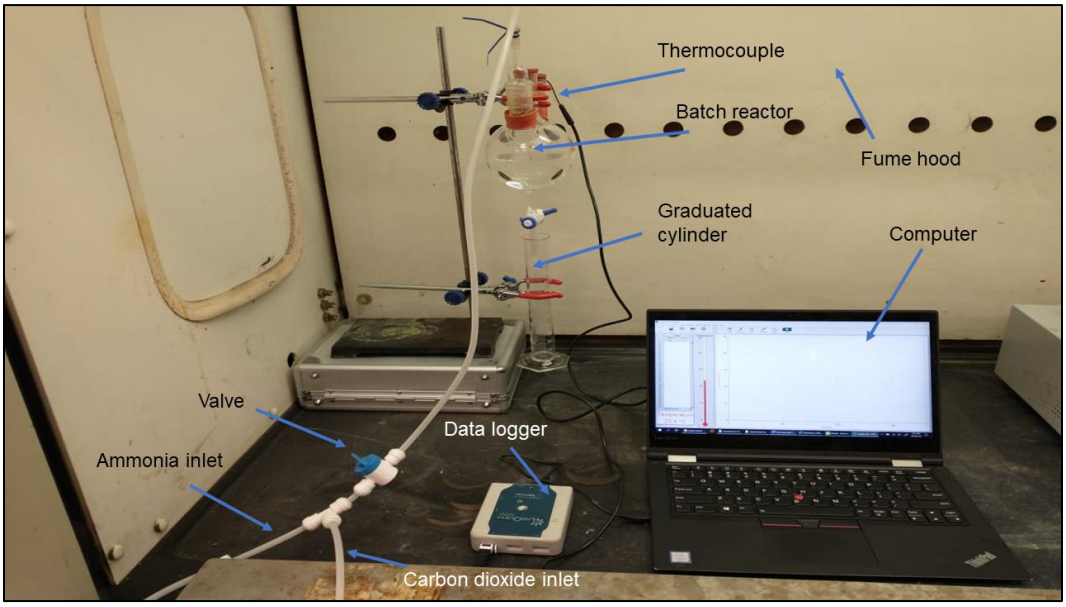

Figure 3.4: Experimental setup of ammonia-based carbon capture and ammonium bicarbonate production unit for the baseline case.

In Figure 3.5, the experimental setup of the proposed ammonia-based carbon capturing unit to produce ammonium bicarbonate is shown for the catalyst and induction heating cases. This experimental setup has the following additional components. Firstly, the 22-Gauge carbon steel catalyst pieces with a total area of 39 cm^2 and a total mass of 19.4 g. Secondly, the electromagnetic induction heater which consist of a zero-voltage switching (ZVS) unit and a copper coil wrapped around the batch reactor. In addition, a DC power source that provides a stable 24V supply of electricity to the induction heater is used in this setup. A clamp multimeter for measuring the current through the wire attached to the ZVS is utilized. Finally, an extension cord with a power switch is put here to control the switching of the induction heater depending on the temperature of the batch reactor. A closer look at the batch reactor with the induction heater is shown in Figure 3.6.

The experimental procedure for the baseline and the catalyst cases are identical. A flow chart of the experimental procedure explained above is shown in Figure 3.7. The procedure starts with adding distilled water to the batch reactor with a specific volume and leaving the remaining volume of the 500-mL glass flask filled with ambient air. By controlling the gas valve, ammonia is injected with a 100 mL into the batch reactor. This is measured by

how much this injected ammonia displaces water through the bottom of the batch reactor and this displaced water is captured using the graduated cylinder. The reason behind injecting 100 mL is to keep the ammonia-water solution at a pH level between 7 and 10.5. This range is where ammonium bicarbonate is formed according to studies and modeling done by Chen et al. [104]. Similarly, carbon dioxide is injected to the batch reactor with different volumes such that the concentration of carbon dioxide relative to the air-carbon dioxide mixture is either of three chosen compositions, which are 30%mol, 50%mol, or 80%mol of CO_2. The experiment timer starts when the carbon dioxide is injected to the reactor and the experiment runs for 30 minutes for each trial. Each trial is repeated twice to reduce errors. During this time, multiple temperature measurements are taken. After the run is done, the solution is drained from the batch reactor and its pH level is measured using a Vernier pH sensor. Lastly, the solution samples are left to dry out to separate the ammonium bicarbonate salt from the ammonia-water solution. The salt mass is measured using a very accurate mass balance made by Mettler Toledo with a measurement increment of 0.1 mg.

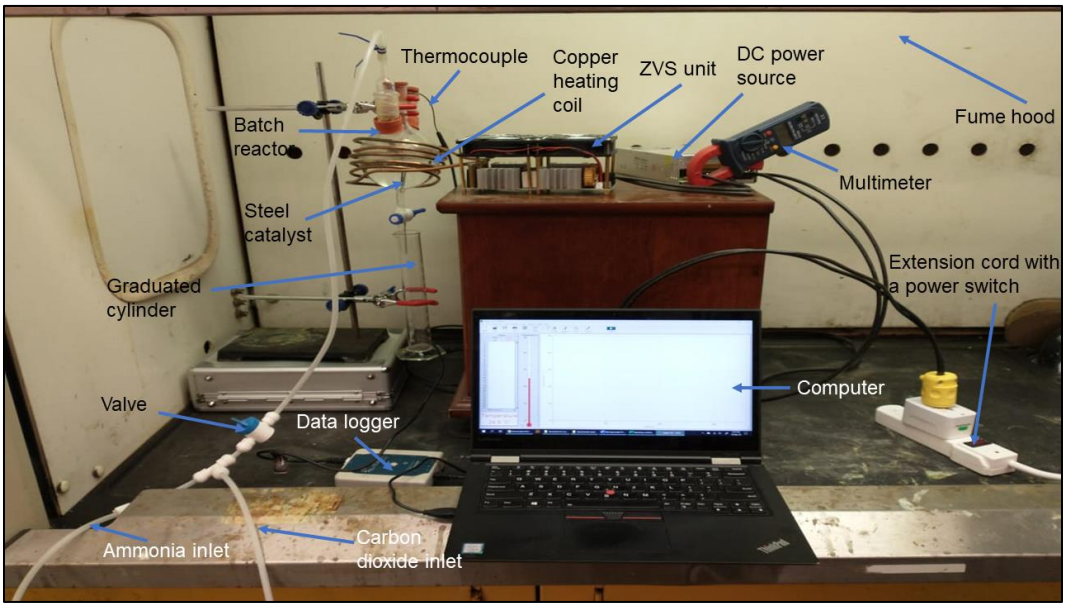

Figure 3.5: Experimental setup of the proposed ammonia-based carbon capture and ammonium bicarbonate production unit for the catalyst and induction heating cases.

For the induction heating case, the experimental procedure differs from the above one by turning ON the induction heater so that the metallic catalyst is selectively heated. The induction heater is turned on when the temperature of the batch reactor is at or below 35°C and it is turned OFF when the temperature is at 40°C. this is because having a temperature

higher than 40°C could inhibit the production of ammonium bicarbonate. The time intervals of turning the induction heater ON and OFF are recorded during the experiment. Another thing that is measured is the current through the wire that supplies electricity to the induction heater which could help us determine the power input to the heater. This is measured every 5 minutes. Also, some typical samples of the produced ammonium bicarbonate are presented in Figure 3.8.

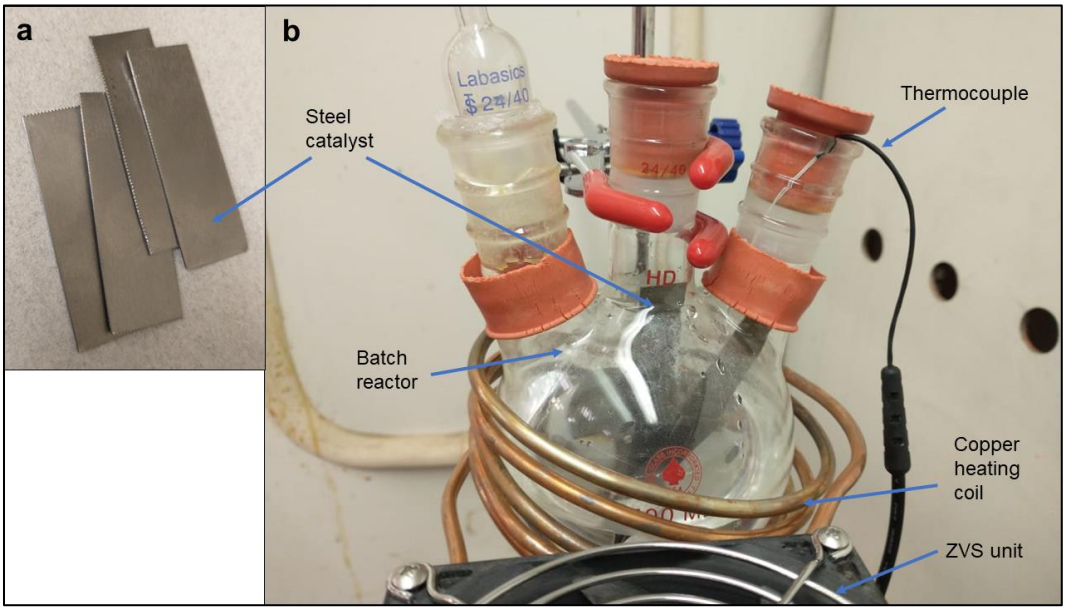

Figure 3.6: a) Pieces of the steel catalyst used in the experimental setup. b) A closer look at the batch reactor with the induction heater and the catalyst pieces.

One quantity is defined here to evaluate some parameters of the experimental setup. Firstly, the energy consumption of the induction heater over the period of experimental runs and this is found using this expression:

$$e_{ZVS} = V_{ZVS} \times I_{avg} \times \Delta t_{operation} \tag{3.1}$$

where e_{ZVS} is the energy consumption by the induction heater using the zero-voltage switching unit in kJ, V_{ZVS} is the applied voltage to the ZVS unit in V, I_{avg} is the average supplied current measured during the experiment in A, and $\Delta t_{operation}$ is the operation time of the induction heater in seconds. The experimental investigation is concerned with an ammonium bicarbonate batch reactor that has two novel features, which are using a steel catalyst, and an induction heater to enhance the production of ammonium bicarbonate mass. There are three main factors that are being considered in this experimental design, namely CO_2 concentration in flue gases, existence of steel catalyst, and usage of induction

heating. In addition, the interactions between these main factors are considered for this study. Each of the three main factors has two levels, labeled as -1 and +1 as shown in Table 3.1. The labels A, B, and C are used for the three factors as CO_2 concentration, steel catalyst, and induction heater, respectively. This results in a full factorial design of experiment with 8 experiments that need to be run as presented in Table 3.2.

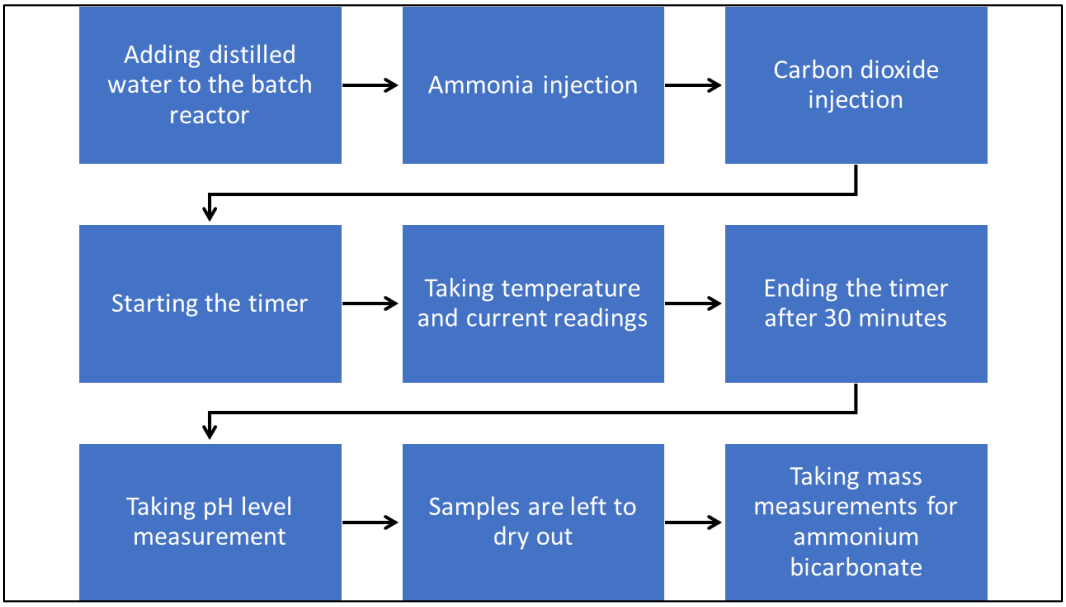

Figure 3.7: Experimental procedure for the proposed ammonia-based carbon capture and ammonium bicarbonate production unit.

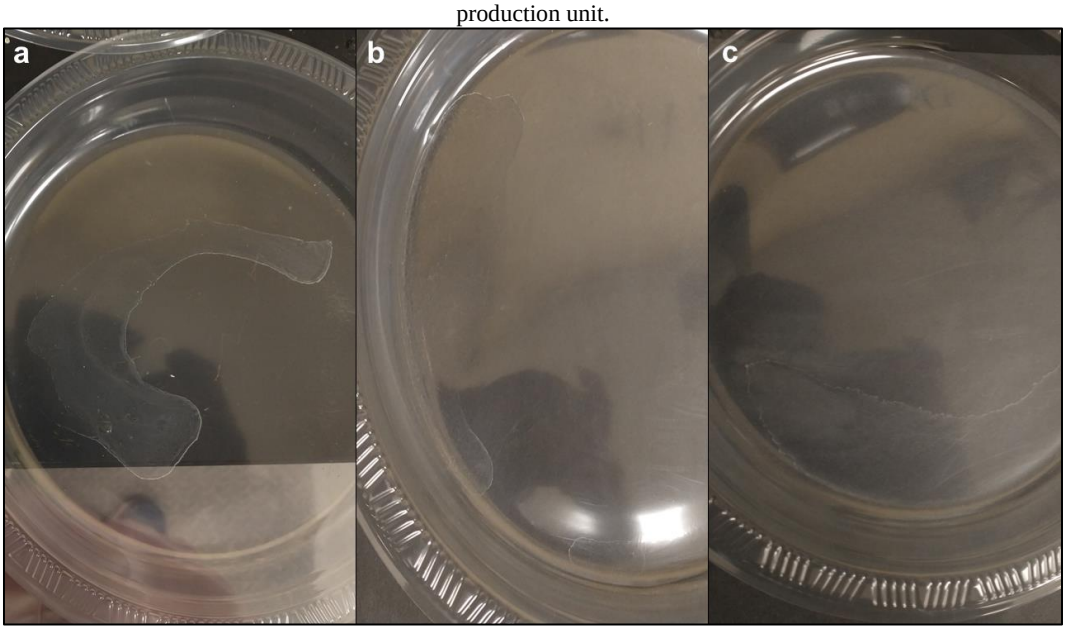

Figure 3.8: Samples of the produced ammonium bicarbonate after the natural drying process for a) baseline case with 80%mol of CO_2, b) catalyst case with 80%mol of CO_2, and c) Induction heating case with 80%mol of CO_2.

Table 3.1: Assignment levels to the main factors.

Levels	CO_2 concentration (A)	Steel catalyst (B)	Induction heater (C)
-1	30%mol	Without catalyst	Heater is OFF
+1	80%mol	With catalyst	Heater is ON

Table 3.2: Full factorial design of experiment with three factors and two levels (2^3).

Runs	A	B	C
1	-1	-1	-1
2	+1	-1	-1
3	-1	+1	-1
4	+1	+1	-1
5	-1	+1	+1
6	+1	+1	+1
7	-1	-1	+1
8	+1	-1	+1

The treatment of the experimental results from this factorial design of experiment is conducted using the analysis of variance (ANOVA) to see the significance of the factors and their interactions on the ammonium bicarbonate mass produced from the batch reactor. Factors and interactions are chosen as significant according to their probability to violate the null hypotheses of the respective factor or interaction with a p-value of 0.05.

Table 3.3 presents the measurement devices used in this experimental setup along with their respective ranges and accuracies. These are used to find the errors caused by the devices. Table 3.4 shows the absolute and relative errors for each measurement device used to acquire data from the experimental setup.

The energy consumption uncertainty calculation is determined by the following relation due to the propagation of error of measurements from the ampere meter and voltmeter.

$$\sigma_{ZVS} = \sqrt{\left(\frac{\partial e_{ZVS}}{\partial V}\right)^2 \sigma_V^2 + \left(\frac{\partial e_{ZVS}}{\partial I}\right)^2 \sigma_I^2} \tag{3.2}$$

where σ_{ZVS} is the standard error (uncertainty) in energy consumption by the ZVS, σ_V is the standard error (uncertainty) by the voltmeter, and σ_I is the standard error (uncertainty) by the ampere meter.

Table 3.3: Measurement devices and their characteristics.

Devices	**Parameter**	**Range**	**Accuracy**
Graduated cylinder	Volume	36-100 mL	±0.5 mL
Thermocouple type K	Temperature	0-80°C	±2.2°C
Vernier pH sensor	pH level	0-14 pH	±0.02 pH
Multimeter – ASTROAI AUTO RANGING 202D DIGITAL	Electric current	0-20 A	±2.5%
MN35 Voltmeter	Voltage	0-100 V	±0.5%
Mass scale - Mettler Toledo AB204-S	Mass	0-1 g	±0.1 mg

Table 3.4: Absolute and relative errors of the experimental setup.

Devices	**Parameter**	**Reference value**	**Absolute error**	**Relative error (%)**
Graduated cylinder	Volume	50 mL	2 mL	2.1
Thermocouple type K	Temperature	60°C	2.2°C	3.67
Vernier pH sensor	pH level	7 pH	0.02 pH	0.2
Multimeter – ASTROAI AUTO RANGING 202D DIGITAL	Electric current	10 A	0.02 A	2.5
MN35 Voltmeter	Voltage	24	0.012 V	0.5
Mass scale - Mettler Toledo AB204-S	Mass	0.5 g	0.1 mg	0.02

To summarize and reemphasize the novelties of the integrated systems and the experimental setup, a list of the main novelties is presented in Table 3.5. The main novelties of the integrated systems revolve around the integration of thermal components and recently developed electrochemical components to produce multiple useful outputs and have the feature of carbon capture and utilization. For the experimental setup, the main novel feature is the use of a cheap industrial catalyst in conjunction with an induction heater for the enhancement of ammonium bicarbonate production. Also, the selective heating feature done by the induction heater is another novelty in this experimental setup.

3.5 Calibration Data

Calibration of the thermocouple used in the experimental setup is mentioned here. A thermal bath is used to heat water to set temperature levels and the temperature readout of a reference thermocouple and the used thermocouple, that needs calibration, are both recorded along with the voltage of the thermocouple. The set temperature is increased by an increment of 5°C, then the readouts are taken after they stabilize. Figure 3.9 shows the voltage measured against the thermocouple temperature readout. It shows a logarithmic fit curve between these two variables which is expected for this type of thermocouple. Figure 3.10 presents a graph that shows the difference between the set temperature and the

temperature readout by the thermocouple. The relation presented by the fit curve is used when controlling and reporting the temperature for the experiments.

Table 3.5: Summary of novelties in the integrated systems and experimental setup.

System	Novelties
System 1	- The production of ammonium bicarbonate from captured CO_2 and green ammonia is proposed under exergetic terms for the first time. - The economics and cost analysis for the production of ammonium bicarbonate from green ammonia and captured CO_2 is investigated for the first time in the literature. - Novel exergy and exergoeconomic analyses are conducted on this integrated system.
System 2	- An electrochemical ammonia synthesizer is implemented for the first time for carbon capturing and production of ammonium bicarbonate. - The implementation of a geothermal power plant as a clean source of electricity is proposed for the first time in the open literature. - Original exergoeconomic analysis and optimization methods are applied on this integrated system.
System 3	- The first integration of a solar energy-based carbon capture system with an oxy-combustion Brayton cycle for multigeneration is proposed. - The first integration of an oxy-combustion Brayton cycle with a supercritical CO_2 power cycle for combined electric power generation is introduced. - Novel exergoeconomic analysis and optimization methods are applied on this integrated system.
Experimental setup	- It is the first time in the literature to build an experimental setup to produce ammonium bicarbonate with the use of a steel catalyst. - A novel selective heating approach to reduce heat losses is introduced in this experimental setup. - It is the first time to use an electromagnetic induction heater for the enhancement of ammonium bicarbonate production.

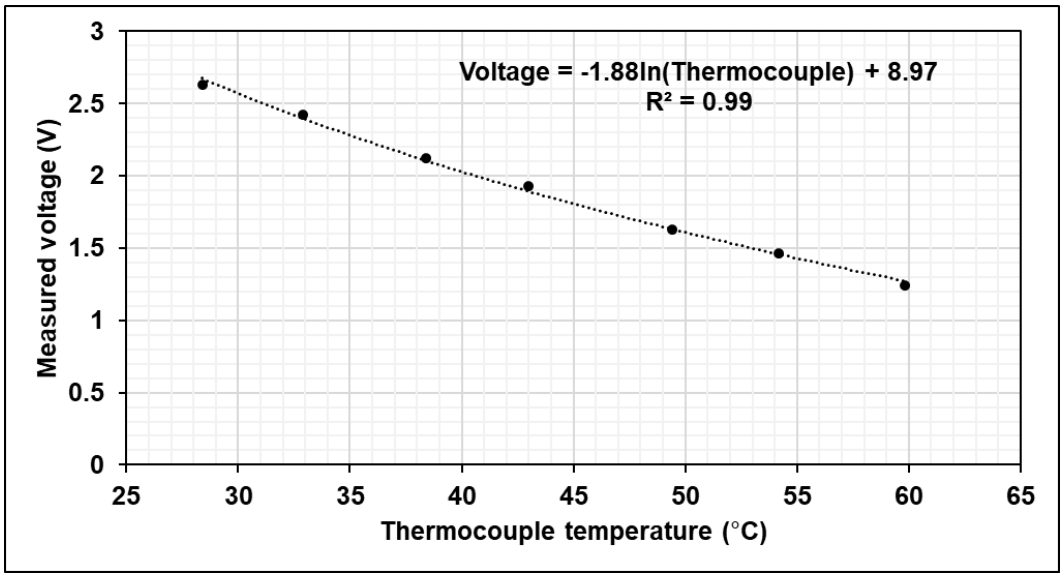

Figure 3.9: Voltage versus temperature thermocouple calibration graph for a stainless-steel type K thermocouple.

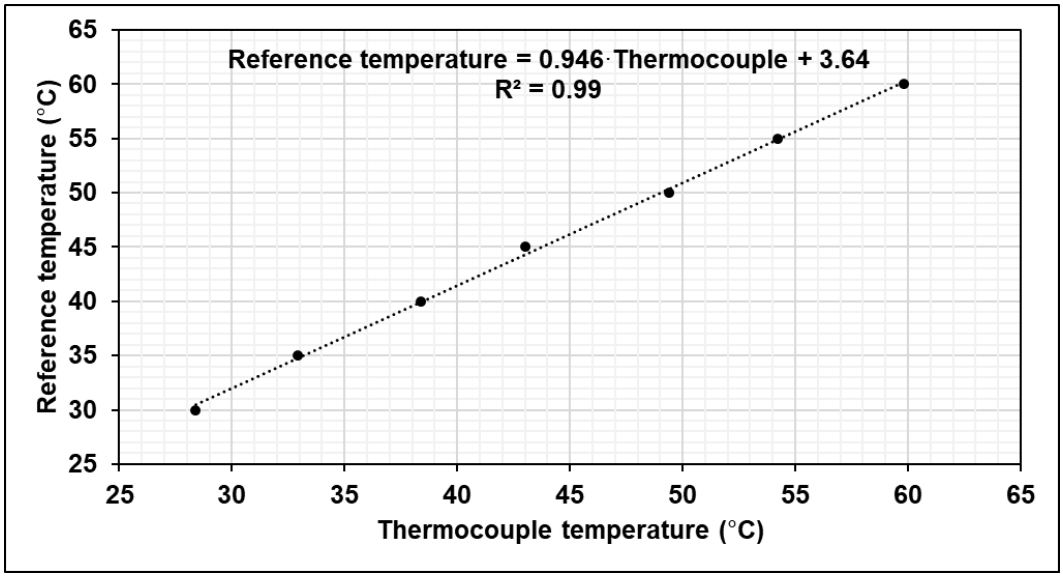

Figure 3.10: Reference temperature versus thermocouple temperature calibration graph for a stainless-steel type K thermocouple.

Chapter 4: Modeling

This chapter mentions the thermodynamic and exergoeconomic modeling for each carbon capturing system presented in this work. In addition, the multi-objective optimization procedure implemented for the integrated systems is described.

4.1 Thermodynamic and exergoeconomic modeling of system 1

This section will describe the analyses and models used to simulate the ammonia-based carbon capture system. The main assumptions of the thermodynamic model used to analyze the system are listed as follows:

- All components operate under the conditions of steady-state and uniform flow.
- The changes of potential energy and kinetic energy across each component of the system are considered small compared to the enthalpy values and the work and heat magnitudes [105].
- The pressure losses across the reactors, the PEM electrolyzer, and the pipes are neglected.
- The compressors used in the system are assumed to behave under adiabatic conditions and have an isentropic efficiency of 85%.
- The reference point used in this thermodynamic analysis consists of ambient pressure and temperature of 1 bar, and 298 K, respectively.

Now, the balance equations are written in their most general form under the steady-state and uniform flow conditions. To begin with, the mass balance equation is expressed as

$$\sum_{in} \dot{m}_{in} = \sum_{out} \dot{m}_{out} \tag{4.3}$$

This form of the mass conservation law states that the summation of the mass flow rates going into a component equals the summation of the outlet mass flow rates. Similarly, the energy balance equation is stated, after the above general assumptions are made, as follows.

$$\dot{Q} + \sum_{in} \dot{m}_{in}(h_{in}) = \sum_{out} \dot{m}_{out}(h_{out}) + \dot{W} \tag{4.4}$$

In this form of the energy conservation law, it is assumed that the heat is positive when it is entering the closed system (component) and power is positive when it is produced by the closed system. In a similar manner, the entropy balance equation is formulated as

$$\sum_k \frac{\dot{Q}_k}{T_k} + \sum_{in} \dot{m}_{in}(s_{in}) = \sum_{out} \dot{m}_{out}(s_{out}) + \dot{S}_{gen} \tag{4.5}$$

The statement of the 2nd law of thermodynamics is the entropy generation rate of an open system is a positive magnitude. T_k is the temperature at which the heat is added to the system in units of Kelvin. The last balance equation to be stated in this thermodynamic analysis is the exergy balance equation in the steady-state form.

$$\sum_k (1 - \frac{T_o}{T_k})\dot{Q}_k + \sum_{in} \dot{m}_{in}(ex_{in}) = \sum_{out} \dot{m}_{out}(ex_{out}) + \dot{W} + \dot{E}x_{dest} \tag{4.6}$$

This equation can be used to find the exergy destruction rate of a single component, but another simpler way to calculate the exergy destruction rate is possible using the following relation.

$$\dot{E}x_{dest} = T_o \dot{S}_{gen} \tag{4.7}$$

where T_o is the reference temperature used in the analysis. Before going to the specific assumption of each component of the system, the flowsheet produced by ASPEN Plus is first presented in Figure 4.1 with showing the components that are to model the large-scale system under steady-state conditions, and the numbers of state points used. The PEM electrolyzer will be discussed and modeled separately in a later subsection.

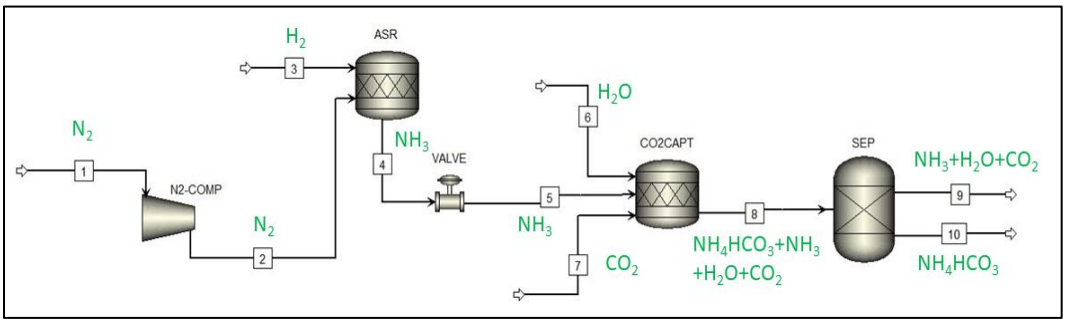

Figure 4.1: A flowsheet of the modeled system produced by ASPEN Plus. N2-COMP is the nitrogen compressor, ASR is the Ammonia Synthesis Reactor, CO2CAPT is the carbon capture reactor, and SEP is the Separator.

Starting with the first component in the flowsheet, the nitrogen compressor is modeled according to the isentropic efficiency definition presented here

$$\eta_{is,N2-COMP} = \frac{h_{2,is} - h_1}{h_2 - h_1} \tag{4.8}$$

and the compressor has negligible heat losses compared to the power input. Next is the ammonia synthesis reactor. This reactor has the following chemical reaction (4.R1) happening inside it.

$$N_2 + 3H_2 \rightleftharpoons 2NH_3 \tag{4.R1}$$

This reaction is exothermic and reversible. It is also assumed that the supplies of nitrogen and hydrogen are enough based on their molar ratio for the possibility of a complete reaction. After that, the valve is simply modeled as an isenthalpic process, meaning the inlet-specific enthalpy of stream 4 is equal to the outlet-specific enthalpy of stream 5. For the carbon capture reactor, the overall chemical reaction of this process is shown in 4.R2.

$$CO_2 + NH_3 + H_2O \longrightarrow NH_4HCO_3 \tag{4.R2}$$

This reactor receives flue gases with high concertation of CO_2. The resultant product of ammonium bicarbonate is in the solid phase. The reaction kinetics of producing ammonium bicarbonate are derived from the thermodynamic model of the CO_2-NH_3-H_2O system to determine the concentrations of each solid and liquid phase component. This chemical system is modeled and implemented in ASPEN Plus using the extended UNIQUAC model developed by Darde et al. [106]. Furthermore, in this study, there is no catalyst, and this reaction does not need a catalyst as it has been shown experimentally that ammonium bicarbonate is produced at ambient temperature levels [107]. The reaction here is assumed to produce ammonium bicarbonate at a 100% rate because the reaction type is batch, and any excess products are recycled in the reactor to produce more ammonium bicarbonate over time. The last component in this flowsheet is the separator which separates the solid ammonium bicarbonate from the outlet solution leaving the carbon capture reactor. This separator is adiabatic and the pressure losses across it are negligible. Also, it operates under a constant temperature level. The purity of the ammonium bicarbonate is initially set to 100%. The fluid packages used in this ASPEN Plus model are mentioned next. Firstly, the

fluid package setting for water, hydrogen, and oxygen (O_2) is UNIFAC. Secondly, the fluid package for nitrogen, ammonia, and carbon dioxide is NRTL. Lastly, the fluid package for ammonium bicarbonate is extended UNIQUAC. Also, the module used for the nitrogen compressor is a compressor module from ASPEN Plus with an isentropic efficiency of 85%, the ASR and carbon capture reactor are modeled using the STOICH reactor module with the chemical reactions of 4.R1 and 4.R2 inputted in these reactors, respectively. The valve module is used as a valve in the model with a discharge pressure of 1 bar. The Separator module from ASPEN Plus is used for the separator with ammonium bicarbonate separation efficiency of 99% and other gases are released as a mixture.

Now, the mass and energy balance equations for each of these components are presented in Table 4.1. The entropy and exergy balance equations of each of these components are shown in Table 4.2, respectively.

Table 4.1: Mass and energy balance equations for the carbon capture system.

Component	**Mass Balance**	**Energy Balance**
Nitrogen Compressor	$\dot{m}_1 = \dot{m}_2$	$\dot{m}_1\, h_1 + \dot{W}_{N2-COMP} = \dot{m}_2\, h_2$
Ammonia synthesis reactor	$\dot{m}_2 + \dot{m}_3 = \dot{m}_4$	$\dot{m}_2\, h_2 + \dot{m}_3\, h_3 = \dot{m}_4\, h_4 + \dot{Q}_{ASR}$
Valve	$\dot{m}_4 = \dot{m}_5$	$\dot{m}_4\, h_4 = \dot{m}_5\, h_5$
Carbon capture reactor	$\dot{m}_5 + \dot{m}_6 + \dot{m}_7 = \dot{m}_8$	$\dot{m}_5\, h_5 + \dot{m}_6\, h_6 + \dot{m}_7\, h_7 = \dot{m}_8\, h_8 + \dot{Q}_{CO2CAPT}$
Separator	$\dot{m}_8 = \dot{m}_9 + \dot{m}_{10}$	$\dot{m}_8\, h_8 + \dot{Q}_{sep} = \dot{m}_9\, h_9 + \dot{m}_{10}\, h_{10}$

In order to evaluate the performance of this system, two commonly used performance parameters are defined now. The first one is the CO_2 capture efficiency which is defined as

$$\eta_{CO_2-captured} = 1 - \frac{\dot{m}_9 x_{CO_2}}{\dot{m}_7 x_{CO_2}} \tag{4.9}$$

where x_{CO_2} is the mass flow rate ratio of CO_2 in the gas mixtures. The second parameter is the energy requirement per 1 kg of CO_2 captured. This is found using the following expression:

$$E_{CO_2-captured} = \frac{\dot{W}_{PEM}}{\dot{m}_7 x_{CO_2} - \dot{m}_9 x_{CO_2}} \tag{4.10}$$

Table 4.2: The entropy and exergy balance equations for the carbon capture system.

Component	**Entropy Balance**	**Exergy Balance**
Nitrogen Compressor	$\dot{m}_1 s_1 + \dot{S}_{gen,N2-COMP} = \dot{m}_2 s_2$	$\dot{m}_1 ex_1 + \dot{W}_{N2-COMP} = \dot{m}_2 ex_2 + \dot{E}x_{dest,N2-COMP}$
Ammonia synthesis reactor	$\dot{m}_2 s_2 + \dot{m}_3 s_3 + \dot{S}_{gen,ASR} = \dot{m}_4 s_4 + \frac{\dot{Q}_{ASR}}{T_{ASR}}$	$\dot{m}_2 ex_2 + \dot{m}_3 ex_3 = \dot{m}_4 ex_4 + (1 - \frac{T_o}{T_{ASR}})\dot{Q}_{ASR} + \dot{E}x_{dest,ASR}$
Valve	$\dot{m}_4 s_4 + \dot{S}_{gen,valve} = \dot{m}_5 s_5$	$\dot{m}_4 ex_4 = \dot{m}_5 ex_5 + \dot{E}x_{dest,valve}$
Carbon capture reactor	$\dot{m}_5 s_5 + \dot{m}_6 s_6 + \dot{m}_7 s_7 + \dot{S}_{gen,CO2CAPT} = \dot{m}_8 s_8 + \frac{\dot{Q}_{CO2CAPT}}{T_o}$	$\dot{m}_5 ex_5 + \dot{m}_6 ex_6 + \dot{m}_7 ex_7 = \dot{m}_8 ex_8 + \dot{E}x_{dest,CO2CAPT}$
Separator	$\dot{m}_8 s_8 + \frac{\dot{Q}_{sep}}{T_{sep}} + \dot{S}_{gen,sep} = \dot{m}_9 s_9 + \dot{m}_{10} s_{10}$	$\dot{m}_8 ex_8 + (1 - \frac{T_o}{T_{sep}})\dot{Q}_{sep} = \dot{m}_9 ex_9 + \dot{m}_{10} ex_{10} + \dot{E}x_{dest,sep}$

The value of the power input to the nitrogen compressor is not included in the above expression because it is very small compared to the power input to the PEM electrolyzer. From the simulation work, the nitrogen compressor power input is less than 0.8% of the PEM electrolyzer power input.

The wind turbine output power is described using the following

$$\dot{W}_{wind} = \frac{1}{2}\rho_{air} C_p A_s V_{wind,up}^3 \tag{4.11}$$

where ρ_{air} is the density of air, C_p is the power coefficient which reaches up to a maximum value of 0.59, A_s is the area swept by the blades of the wind turbine, $V_{wind,up}$ is the upstream air speed. A reasonable value for the power coefficient is 0.35 and this value is chosen in this study [108]. The PEM electrolyzer model is explained next. The electrochemical reactions that take place in the electrolyzer are at two places, namely the anode side and the cathode side. 4.R3 and 4.R4 show these reactions as follows:

Anode: $H_2O \longrightarrow 2H^+ + 1/2O_2 + 2e^-$ (4.R3)

Cathode: $2H^+ + 2e^- \longrightarrow H_2$ (4.R4)

The modeling of this device has three sections, namely voltage modeling, material modeling, and thermodynamic modeling. Starting with the voltage modeling, the PEM electrolyzer has many cells. Assuming that all cells share the same voltage, the cell voltage can be found using this expression:

$$V_{cell} = V_{id} + V_{act} + V_{ohm} \tag{4.12}$$

Here, it is assumed that diffusion and parasitic overpotentials are negligible according to experimental results of PEM electrolyzers [109,110]. The first term on the right side of the previous equation is the ideal voltage of the cell and it can be found using this formula which is adapted from Siddiqui et al. [81]:

$$V_{id} = 1.229 - \frac{8.5}{1000}(T_{PEM} - 298) \tag{4.13}$$

where T_{PEM} is the PEM electrolyzer operating temperature in Kelvin. The second term is the activation overpotential which represents the additional voltage required to start the electrochemical reactions at both electrodes. Therefore, this expression is actually divided into two overpotentials, one for the anode side and one for the cathode side. Mathematically, they are expressed as

$$V_{act} = V_{act,anode} + V_{act,cathode} \tag{4.14}$$

and

$$V_{act,anode} = \frac{R_u T_{PEM}}{F} \ln(\frac{i_{anode}}{i_{o,anode}}) \tag{4.15}$$

where R_u is the universal gas constant with a value of 8.314 J mol^{-1} K^{-1}, F is the Faraday's constant which has a value of 96485 C mol^{-1}, i_{anode} is the current density at the anode in units of A cm^{-2}, and $i_{o,anode}$ is the reference current density at the anode which is set to be at a value of 1×10^{-10} A cm^{-2} [111]. Similarly, for the cathode side, the activation overpotential is

$$V_{act,cathode} = \frac{R_u T_{PEM}}{F} \ln(\frac{i_{cathode}}{i_{o,cathode}}) \tag{4.16}$$

where $i_{cathode}$ is the current density at the cathode in units of A cm^{-2}, and $i_{o,cathode}$ is the reference current density at the cathode which is set to be at a value of 1×10^{-3} A cm^{-2} [111].

Since the parasitic overpotentials are ignored in this analysis, the following relation holds true.

$$i_{useful} = i_{anode} = i_{cathode} \tag{4.17}$$

The last overpotential considered is the ohmic losses overpotential. This overpotential is due to the resistances of the electrodes and the membrane. These resistances are added linearly as

$$V_{ohm} = (R_{anode} + R_{cathode} + R_{membrane}) i_{useful} A_{cell} \tag{4.18}$$

where A_{cell} is the effective area of the cell in cm^2, and the resistances due to the anode and cathode electrodes have the same expression and value. The expression for calculating an electrode resistance is

$$R_{el} = \frac{t_{el}\rho_{el}}{A_{cell}} \tag{4.19}$$

where t_{el} is the thickness of the electrode which is set to be 1.3 mm, and ρ_{el} is the electrode resistivity and it has a value of 7.5 mΩ cm [110]. The membrane resistance is calculated in the same manner using the following expression:

$$R_{mem} = \frac{t_{mem}}{\sigma_{mem} A_{cell}} \tag{4.20}$$

where is the thickness of the electrode which is set to be 0.127 mm, while σ_{mem} is the membrane proton conductivity. This conductivity is found using the following model developed by Kopitzke et al. [112].

$$\sigma_{mem} = 2.29 \exp\left(-\frac{7829}{R_u T_{PEM}}\right) \tag{4.21}$$

This is the end of the voltage modeling part of the PEM electrolyzer. The potential in the PEM cell model is a function of the characteristics of the cell, such as resistances and cell area, and the potential also depends on the operating temperature of the PEM cell. According to the above model, mass and energy flows do not affect the potential of the PEM cell. The mass and energy flows are only affected by two parameters, the area of the cell and the number of cells in the PEM electrolyzer stack. Next is the material modeling

part. The first thing that can be directly calculated is the number of moles of hydrogen produced according to the cell voltage, the useful current, and the number of cells (N_{cell}) which are all related in this mathematical expression

$$n_e F \dot{N}_{H_2} = i_{useful} A_{cell} N_{cell} \tag{4.22}$$

where n_e is the number of electrons in the anode reaction (it is 2 electrons per mole), and $\dot{N}_{H_2O}$ is the molar flow rate of hydrogen produced in mol s^{-1}. Another important relationship is between the input power to the PEM electrolyzer ($\dot{W}_{PEM}$) and the voltage and useful current. This is expressed simply as

$$\dot{W}_{PEM} = \frac{V_{cell} i_{useful} A_{cell} N_{cell}}{1000} \tag{4.23}$$

The unit of this input power is kW. From the overall chemical reaction of the electrolyzer which is shown below, it is possible to find a molar-based relation for the water consumed.

$$H_2O \longrightarrow H_2 + 1/2O_2 \tag{4.R5}$$

The number of moles of hydrogen produced is assumed to be the same as the number of moles of water consumed. It is possible to relate the consumed water with the inlet water stream mass flow rate and the recycled water stream (Rwater) as follows:

$$\frac{\dot{N}_{H_2O} M_{H_2O}}{1000} = \dot{m}_{Water} - \dot{m}_{Rwater} \tag{4.24}$$

where M_{H_2O} is the molecular weight of water which is 18 g mol^{-1}. Finding the oxygen mass flow rate requires these two relations,

$$\dot{N}_{O_2} = \frac{\dot{N}_{H_2}}{2} \tag{4.25}$$

and

$$\dot{m}_{Oxygen} = \frac{\dot{N}_{O_2} M_{O_2}}{1000} \tag{4.26}$$

where $M_{O_2}$is the oxygen molecular weight which has a value of 32 g mol^{-1}, and the mass flow rate is in kg s^{-1}. The last equation to be mentioned in this part of the modeling is the mass flow rate of the PEM electrolyzer

$$\dot{m}_{Water} = \dot{m}_{Oxygen} + \dot{m}_{Hydrogen} + \dot{m}_{Rwater} \tag{4.27}$$

The thermodynamic analysis of this PEM electrolyzer can be conducted. The energy balance equation is written as

$$\begin{aligned} \dot{m}_{Water}\, h_{Water} + \dot{W}_{PEM} & \\ = \dot{m}_{Oxygen} h_{Oxygen} + \dot{m}_{Hydrogen}\, h_{Hydrogen} & \\ + \dot{m}_{Rwater}\, h_{Rwater} + \dot{Q}_{PEM,loss} & \end{aligned} \tag{4.28}$$

The entropy balance equation is

$$\begin{aligned} \dot{m}_{Water}\, s_{Water} + \dot{S}_{gen,PEM} & \\ = \dot{m}_{Oxygen} s_{Oxygen} + \dot{m}_{Hydrogen}\, s_{Hydrogen} & \\ + \dot{m}_{Rwater}\, s_{Rwater} + \frac{\dot{Q}_{PEM,loss}}{T_{PEM}} & \end{aligned} \tag{4.29}$$

And lastly, the exergy balance equation is expressed as

$$\begin{aligned} \dot{m}_{Water}\, ex_{Water} + \dot{W}_{PEM} & \\ = \dot{m}_{Oxygen} ex_{Oxygen} + \dot{m}_{Hydrogen}\, ex_{Hydrogen} & \\ + \dot{m}_{Rwater}\, ex_{Rwater} + \left(1 - \frac{T_o}{T_{PEM}}\right) \dot{Q}_{PEM,loss} & \\ + \dot{E}x_{dest,PEM} & \end{aligned} \tag{4.30}$$

In addition, some performance parameters for this PEM electrolyzer are defined here. The PEM energy efficiency is defined as

$$\eta_{en,PEM} = \frac{\dot{m}_{Hydrogen} LHV_{H_2}}{\dot{W}_{PEM}} \tag{4.31}$$

where LHV_{H_2} is the lower heating value of hydrogen. Similarly, the PEM exergy efficiency is

$$\eta_{ex,PEM} = \frac{\dot{m}_{Hydrogen} ex_{Hydrogen}}{\dot{W}_{PEM}} \tag{4.32}$$

The above model of the PEM electrolyzer is programmed using ASPEN Custom Modeler as it was done by Colbertaldo et al. [113], and the flowsheet is presented in Figure 4.2.

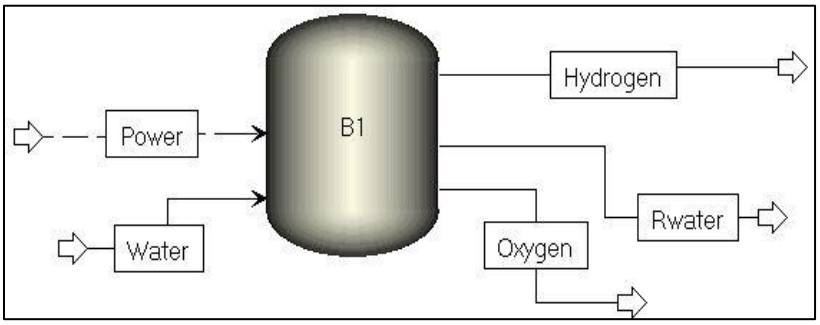

Figure 4.2: A flowsheet of the PEM electrolyzer produced by ASPEN Custom Modeler.

Next, a comprehensive exergoeconomic analysis is provided here. Starting with defining the cost rate of the total investment of each component

$$\dot{\boldsymbol{Z}}_{\boldsymbol{k}} = \frac{\boldsymbol{Z_k \times CRF \times \varphi}}{\boldsymbol{N}} \tag{4.33}$$

where Z_k is the purchase cost of component k in \$, φ is the maintenance factor and it is taken as 1.06 in this work [114], N is the number of hours of in a year in which the system is operating (7446 h), and *CRF* is the Capital Recovery Factor, and it is defined as follows

$$CRF = \frac{i_n(1+i_n)^n}{(1+i_n)^n - 1} \tag{4.34}$$

where i_n is the interest rate taken as 10%, and n is the system life and it is taken as 20 years [114]. The net investment cost rate of the system is the summation of these cost rates for each component, and this is expressed as

$$\dot{Z}_{net} = \sum_k \dot{Z}_k \tag{4.35}$$

The overall cost balance equation of this system is

$$\dot{C}_1 + \dot{C}_6 + \dot{C}_w + \dot{Z}_{net} = \dot{C}_9 + \dot{C}_{10} \tag{4.36}$$

where $\dot{C}_w$ is the work cost rate of the wind energy power input and it is defined as

$$\dot{C}_w = c_w \dot{W}_{PEM} \tag{4.37}$$

where c_w is the specific work cost of electricity. The electricity cost is chosen as \$0.0827 kWh^{-1} [115]. $\dot{C}_1$ and $\dot{C}_6$ are the material cost rates of nitrogen and water at states 1 and 6, respectively. These are calculated using the following expressions, respectively, as

$$\dot{C}_1 = c_1 \dot{m}_1 (ex_1) \tag{4.38}$$

$$\dot{C}_6 = c_6 \dot{m}_6 (ex_6) \tag{4.39}$$

Similarly, for cost rates of streams 9 and 10, their expressions are presented, respectively, as

$$\dot{C}_9 = c_9 \dot{m}_9 (ex_9) \tag{4.40}$$

$$\dot{C}_{10} = c_{10} \dot{m}_{10} (ex_{10}) \tag{4.41}$$

The auxiliary equation that complements the cost balance equation, which is based on the P-Principle from the SPECO method [14], is shown here

$$c_9 = c_{10} \tag{4.42}$$

Now, the purchase cost functions for each component in the system are listed in Table 4.3.

4.2 Thermodynamic and exergoeconomic modeling of system 2

The thermodynamic model of the second carbon capturing system is discussed in this section. This entire model has been implemented in the EES program created by F-Chart Software [116].

The general assumptions made in this model for each thermal component in the integrated system are adopted from previously published thermodynamic analysis-based papers [117–120], and they are listed as follows: (i) All thermal processes are considered to be steady-state. (ii) Both kinetic and potential energy differences across each thermal component are negligible. (iii) The pressure changes across heat exchangers and pipes that connect the components are assumed to be small.

Now, the model of every component in the integrated system will be presented. Starting with the air compressor, this device is assumed to operate under adiabatic conditions and has an isentropic efficiency of 70% and it is defined as [123]

$$\eta_C = \frac{h_{20,s} - h_{19}}{h_{20} - h_{19}} \tag{4.43}$$

Table 4.3: Purchase cost functions for each component in system 1 with additional relations.

Components	**Purchase Cost Functions ($)**	**Additional Relations**	**Sources**
PEM electrolyzer	$Z_{PEM} = 11000 \times \dot{W}_{PEM}$	None	[121]
Nitrogen compressor	$Z_{N2-COMP} = 71.1\left(\frac{\dot{m}_1}{0.92 - \eta_{is,N2-COMP}}\right)(r_p)\,ln(r_p)$	$r_p = \frac{P_2}{P_1}$	[122,123]
Ammonia synthesis reactor	$Z_{ASR} = \frac{610}{1.33} \times \dot{W}_{PEM}$	None	[124]
Carbon capture reactor	$\dot{Z}_{CO2CAPT} = \frac{0.56 \times 3600}{580}\dot{m}_7\ (C\$\ h^{-1})$	None	[125]
Separator	$Z_{sep} = \frac{1.218\left(42 + \frac{1.63\dot{m}_8}{3.6}\right)}{1000}$	None	[126]

To calculate the value of the specific enthalpy for an isentropic compressor ($h_{20,s}$), the air is assumed to be an ideal gas and it follows the ideal gas law. This means that the specific enthalpy of air depends on temperature only. The isentropic temperature of this thermal process can be found using this relation [123]

$$\frac{T_{8,s}}{T_7} = (r_p)^{\frac{\gamma-1}{\gamma}} \tag{4.44}$$

where r_p is the compression ratio, and γ is the specific heat ratio which is taken to be 1.4. Next, the models used for the air and fuel regenerators, the boiler, and the heater are mentioned next. These four heat exchangers are assumed to have negligible heat losses to the environment [119]. Another assumption made to calculate the specific enthalpy and entropy of the exhaust gases is the weighted averaging method [127]. All the constituents of the exhaust gases are assumed to follow the ideal gas law [128]. To find the specific enthalpy of the exhaust gases stream, this is used

$$h_j = \sum_{i=1}^{n_{max}} x_{i,j} h_{i,j} \tag{4.45}$$

where *j* represents the state point of the exhaust gases stream, and *i* is the constituent of the exhaust gases. $x_{i,j}$ is the mass ratio of the constituent *i* over the exhaust gases of state point *j*. The exhaust gases that go through these four heat exchangers are nitrogen, water, and excess oxygen. Similarly, the specific entropy of the exhaust gases is computed as follows

$$s_j = \sum_{i=1}^{n_{max}} x_{i,j} s_{i,j} \tag{4.46}$$

The modeling of the SOFC is simple and drawn from the results of the paper by Aguiar et al. [129]. The exhaust gases leaving the cathode side are simply nitrogen and oxygen, while the composition of the exhaust gases leaving the anode side (state 22) is assumed to be 65% H_2O, 4% CO, 15% H_2, 16% CO_2 molar basis. The temperature of the gases leaving the cathode side is set at 1,110 K, and for the anode side, it is 1,130 K. The steam, mixed with the natural gas before they enter the SOFC, is added at a molar ratio of 2:1 H_2O to CH_4. Methane is assumed to be the dominant component of the natural gas supply in this model [129]. The pressure drop across this device is assumed small and ignored in the analysis [130,131]. For the purposes of this study, knowing the composition of the inlet gases and the exhaust, as well as their temperatures are sufficient thermodynamically to calculate the specific enthalpies and entropies of the streams going in and out of the SOFC [132]. In calculating these quantities, the weighted average method is used again along with assuming all the gases are ideal gases [127]. The chemical reaction shown in 4.R6 that takes place on the cathode side is

$$2\lambda(O_2 + 3.76N_2) + 2e^- \longrightarrow (2\lambda - \beta)O_2 + 2\lambda \times 3.76N_2 + \beta O^{2-} \tag{4.R6}$$

where β is the molar ratio of super oxygen molecules over one mole of methane fuel. This represents the amount of super oxygen that permeates through the membrane in the SOFC. Also, the chemical reaction that takes place on the anode side is described in 4.R7 [129].

$$CH_4 + 2H_2O + \beta O^{2-} \longrightarrow 5[0.16CO_2 + 0.04CO + 0.65H_2O + 0.15H_2] \tag{4.R7}$$

Now, to find the amount of power produced, the following energy efficiency relation is used [130].

$$\eta_{en,SOFC} = \frac{\dot{W}_{SOFC}}{\dot{m}_{18} LHV_{CH_4}} \tag{4.47}$$

where LHV_{CH_4} is the lower heating value for methane taken at 50,000 kJ kg^{-1} [133]. The heat losses can be computed using the energy balance equation of the SOFC which will be presented later.

The WGSMR-afterburner model can be established in a similar way as SOFC by knowing the composition of the exhaust gases and their temperature [134]. All the hydrogen on the anode side permeates to the cathode side to react with the remaining oxygen. All the carbon monoxide is converted to carbon dioxide. 4.R8 describes this chemical reaction which produces hydrogen on the anode side [134].

$$5\times0.04CO + 5\times0.04H_2O \longrightarrow 5\times0.04CO_2 + 5\times0.04H_2 \tag{4.R8}$$

On the cathode side, the chemical reaction which releases thermal energy to the exhaust gases and determines the temperature of the exhaust gases leaving the cathode side is shown in 4.R9 [134].

$$5\times0.04H_2 + 5\times0.15H_2 + (2\lambda - \beta)O_2 + 2\lambda\times3.76N_2 \longrightarrow 2(\lambda - 1)O_2 + 0.95H_2O + 2\lambda\times3.76N_2 \tag{4.R9}$$

The exhaust gases leaving the anode of the WGSMR-afterburner are simply 1 mole of CO_2 and 3.05 moles of H_2O by chemically balancing the reactions, while the exhaust gases leaving the cathode side are steam, nitrogen, and excess oxygen. The temperature of the exhaust gases leaving the anode side is determined by using the energy balance equation on this thermal component which will be shown later. This reactor is assumed adiabatic and operates under constant pressure [134].

The stream of state 24 which contains carbon dioxide and water goes to condenser 1 where all of the water is assumed to be completely condensed and this heat exchanger operates by losing heat to the surroundings. Before this condenser, a significant pressure drop occurs to lower the temperature and pressure of the exhaust gases in stream 24 and make it easier to separate the carbon dioxide from the water. On the other hand, the exhaust gases leaving the cathode side of the WGSMR-afterburner move to be expanded by turbine 3 (T3). This

turbine is modeled to be an adiabatic turbine and it operates under a constant isentropic efficiency of 75%. This turbine isentropic efficiency is defined as [123]

$$\eta_{T3} = \frac{h_{25} - h_{26}}{h_{25} - h_{26,s}} \tag{4.48}$$

To calculate the value of the specific enthalpy for an isentropic turbine ($h_{26,s}$), the air is assumed to be an ideal gas and it follows the ideal gas law [127]. This means that the specific enthalpy of air depends on temperature only. The isentropic temperature of this thermal process can be found using this relation [123]

$$\frac{T_{26,s}}{T_{25}} = \left(\frac{P_{26}}{P_{25}}\right)^{\frac{\gamma_{25}-1}{\gamma_{25}}} \tag{4.49}$$

where γ_{25} is the specific heat ratio of nitrogen since it is the dominant component of the exhaust gases which is taken to be 1.3.

Turbines 1, 2, and 4 are modeled in the same way where they operate under adiabatic conditions, and they all share the same isentropic efficiency of 75% [123]. The isentropic efficiency is similarly defined for each turbine as shown in equation (4.46), but the fluid is water instead of air, and water is not assumed to be an ideal gas law. The properties of water are taken from the EES databases.

The pump power in the SRC is computed using this expression where the specific volume of the water is assumed to be constant and the internal energy does not change across the pump [119].

$$\dot{W}_{pump} = \dot{m}_{36} v_{36} (P_{33} - P_{36}) \tag{4.50}$$

For condenser 2, the assumptions are no heat losses to the environment and all the saturated water mixture leaving turbine 4 is completely condensed. The MED is modeled according to the thermodynamic model and results presented in a paper by El-Dessouky et al. [135]. The two flash chambers in the double-flash geothermal power plant are discussed next. The fluid is assumed to enter the two flash chambers as a compressed liquid, and it drops in pressure according to an isenthalpic process. The separators are assumed to separate the gas phase from the liquid phase without any residuals and these separators are assumed to be adiabatic and have no pressure losses across them.

Going to the electrochemical ammonia synthesizer, this device is assumed to operate under ambient pressure and temperature conditions as these are one of the advantages of using this device as it has been shown experimentally by Zhou et al. [136]. The chemical reaction on the cathode side of this device is presented in 4.R10.

$$0.5N_2 + 1.5H_2O + 3e^- \longrightarrow NH_3 + 1.5O^{2-} \quad (4.R10)$$

This chemical equation is presented by 1 mole of CO_2 leaving from condenser 1. The chemical reaction on the anode side is shown in 4.R11.

$$1.5O^{2-} \longrightarrow 0.75O_2 + 3e^- \quad (4.R11)$$

The faradaic efficiency (*FE*) of this electrochemical device is defined as follows [136]

$$FE = \frac{zF\dot{m}_{14}}{M_{NH_4}I} \quad (4.51)$$

where *z* is the number of electrons per one mole of ammonia produced, *F* is the Faraday constant at a value of 96485 C mol^{-1}, M_{NH_4} is the molecular weight of NH_4 which is 18 kg $kmol^{-1}$, and *I* is the current that passes through the wires in Amperes (A). The electric power consumed by this electrochemical device to produce ammonia is calculated by

$$\dot{W}_{EAS} = VI \quad (4.52)$$

where *V* is the overpotential of the device in volts (V). The *FE* and *V* values are taken from experimental results by Zhou et al. [136] since there is a lack of a complete model in the literature. The heat losses of this device are determined using the energy balance equation. Since the electric power source is the double-flash geothermal power plant, then this relation is true.

$$\dot{W}_{EAS} = \dot{W}_{T1} + \dot{W}_{T2} \quad (4.53)$$

This relation helps in determining the mass flow rate of the geothermal liquid to be withdrawn from the geothermal reservoir. The mixer operates under constant pressure, and water at an elevated temperature mixes with the ammonia stream at a molar ratio of 1:1. No heat losses occur during the mixing. For the ammonium bicarbonate (AB) reactor, the chemical reaction shown in 4.R12 takes place [81].

$$CO_2 + NH_3 + H_2O \longrightarrow NH_4HCO_3 \quad (4.R12)$$

This reaction releases heat to the environment and it happens under an ambient pressure level. All the mass and energy balance equations of every component in the integrated system are presented in Table 4.4. Also, all the entropy and exergy balance equations of every component in the integrated system are presented in Table 4.5.

Now, to evaluate the performance of the integrated system, several performance parameters are defined here. The first one is the net electric power produced by the integrated system and this is calculated using this expression

$$\dot{W}_{net} = \dot{W}_{SOFC} + \dot{W}_{T3} + \dot{W}_{T4} - \dot{W}_{C} + \dot{W}_{pump} \tag{4.54}$$

To evaluate the multigeneration performance of the SOFC subsystem, two kinds of efficiencies are defined here, namely energy and exergy. These are expressed, respectively, as

$$\eta_{en,SOFC} = \frac{\dot{W}_{net} + \dot{Q}_{space} + (\dot{m}_{42}h_{42} - \dot{m}_{39}h_{39})}{\dot{m}_{17}HHV_{CH4}} \tag{4.55}$$

$$\eta_{ex,SOFC} = \frac{\dot{W}_{net} + \dot{Q}_{space}\left(1 - \frac{T_o}{T_{space}}\right) + (\dot{m}_{42}ex_{42} - \dot{m}_{39}ex_{39})}{\dot{m}_{17}ex_{17}} \tag{4.56}$$

Next, three parameters are defined to understand the performance of the geothermal-based ammonia carbon capturing unit in the integrated system. The first one is the traditional measure which is the energy required to capture one kilogram of CO_2.

$$E_{CO_2-captured} = \frac{\dot{W}_{EAS}}{\dot{m}_{28}} \tag{4.57}$$

However, this parameter does not capture the performance of the double-flash geothermal power plant. So, two similar definitions that include this plant are presented here. They are the geothermal energy and exergy for CO_2 capture, and they are respectively expressed as

$$R_{en.CO_2-captured} = \frac{\dot{m}_1(h_1 - h_{10})}{\dot{m}_{28}} \tag{4.58}$$

$$R_{ex,CO_2-captured} = \frac{\dot{m}_1(ex_1 - ex_{10})}{\dot{m}_{28}} \tag{4.59}$$

Table 4.4: Mass and energy balance equations.

Component	Mass Balance	Energy Balance
Flash chamber 1	$\dot{m}_1 = \dot{m}_2$	$\dot{m}_1\, h_1 = \dot{m}_2\, h_2$
Separator 1	$\dot{m}_2 = \dot{m}_3 + \dot{m}_5$	$\dot{m}_2\, h_2 = \dot{m}_3\, h_3 + \dot{m}_5\, h_5$
Turbine 1 (T1)	$\dot{m}_3 = \dot{m}_4$	$\dot{m}_3\, h_3 = \dot{m}_4\, h_4 + \dot{W}_{T1}$
Flash chamber 2	$\dot{m}_5 = \dot{m}_6$	$\dot{m}_5\, h_5 = \dot{m}_6\, h_6$
Separator 2	$\dot{m}_6 = \dot{m}_7 + \dot{m}_9$	$\dot{m}_6\, h_6 = \dot{m}_7\, h_7 + \dot{m}_9\, h_9$
Turbine 2 (T2)	$\dot{m}_7 = \dot{m}_8$	$\dot{m}_7\, h_7 = \dot{m}_8\, h_8 + \dot{W}_{T2}$
Electrochemical ammonia synthesizer (EAS)	$\dot{m}_{11} + \dot{m}_{12} = \dot{m}_{13} + \dot{m}_{14}$	$\dot{m}_{11}\, h_{11} + \dot{m}_{12}\, h_{12} + \dot{W}_{EAS} = \dot{m}_{13}\, h_{13} + \dot{m}_{14}\, h_{14} + \dot{Q}_{EAS,loss}$
Mixer	$\dot{m}_{14} + \dot{m}_{44} = \dot{m}_{15}$	$\dot{m}_{14}\, h_{14} + \dot{m}_{44}\, h_{44} = \dot{m}_{15}\, h_{15}$
Ammonium bicarbonate (AB) reactor	$\dot{m}_{15} + \dot{m}_{28} = \dot{m}_{16}$	$\dot{m}_{15}\, h_{15} + \dot{m}_{28}\, h_{28} = \dot{m}_{16}\, h_{16} + \dot{Q}_{AB,loss}$
Air compressor	$\dot{m}_{19} = \dot{m}_{20}$	$\dot{m}_{19}\, h_{19} + \dot{W}_C = \dot{m}_{20}\, h_{20}$
Air regenerator	$\dot{m}_{20} = \dot{m}_{21}$, $\dot{m}_{29} = \dot{m}_{30}$	$\dot{m}_{20}\, h_{20} + \dot{m}_{29}\, h_{29} = \dot{m}_{21}\, h_{21} + \dot{m}_{30}\, h_{30}$
Fuel regenerator	$\dot{m}_{17} = \dot{m}_{18}$, $\dot{m}_{26} = \dot{m}_{29}$	$\dot{m}_{17}\, h_{17} + \dot{m}_{26}\, h_{26} = \dot{m}_{18}\, h_{18} + \dot{m}_{29}\, h_{29}$
Solid-Oxide Fuel Cell (SOFC)	$\dot{m}_{18} + \dot{m}_{21} + \dot{m}_{43} = \dot{m}_{22} + \dot{m}_{23}$	$\dot{m}_{18}\, h_{18} + \dot{m}_{21}\, h_{21} + \dot{m}_{43}\, h_{43} = \dot{m}_{22}\, h_{22} + \dot{m}_{23}\, h_{23} + \dot{W}_{SOFC} + \dot{Q}_{SOFC,loss}$
WGSMR-afterburner	$\dot{m}_{22} + \dot{m}_{23} = \dot{m}_{24} + \dot{m}_{25}$	$\dot{m}_{22}\, h_{22} + \dot{m}_{23}\, h_{23} = \dot{m}_{24}\, h_{24} + \dot{m}_{25}\, h_{25}$
Turbine 3 (T3)	$\dot{m}_{25} = \dot{m}_{26}$	$\dot{m}_{25}\, h_{25} = \dot{m}_{26}\, h_{26} + \dot{W}_{T3}$
Condenser 1	$\dot{m}_{24} = \dot{m}_{27} + \dot{m}_{28}$	$\dot{m}_{24}\, h_{24} = \dot{m}_{27}\, h_{27} + \dot{m}_{28}\, h_{28} + \dot{Q}_{cond1}$
Boiler	$\dot{m}_{30} = \dot{m}_{31}$, $\dot{m}_{33} = \dot{m}_{34}$	$\dot{m}_{30}\, h_{30} + \dot{m}_{33}\, h_{33} = \dot{m}_{31}\, h_{31} + \dot{m}_{34}\, h_{34}$
Heater	$\dot{m}_{31} = \dot{m}_{32}$	$\dot{m}_{31}\, h_{31} = \dot{m}_{32}\, h_{32} + \dot{Q}_{Space}$
Turbine 4 (T4)	$\dot{m}_{34} = \dot{m}_{35}$	$\dot{m}_{34}\, h_{34} = \dot{m}_{35}\, h_{35} + \dot{W}_{T4}$
Condenser 2	$\dot{m}_{35} = \dot{m}_{36}$, $\dot{m}_{37} = \dot{m}_{38}$	$\dot{m}_{35}\, h_{35} + \dot{m}_{37}\, h_{37} = \dot{m}_{36}\, h_{36} + \dot{m}_{38}\, h_{38}$
Pump	$\dot{m}_{36} = \dot{m}_{33}$	$\dot{m}_{36}\, h_{36} + \dot{W}_{pump} = \dot{m}_{33}\, h_{33}$
Multi-Effect Desalination (MED)	$\dot{m}_{38} = \dot{m}_{37}$, $\dot{m}_{39} = \dot{m}_{40} + \dot{m}_{41} + \dot{m}_{42}$	$\dot{m}_{38}\, h_{38} + \dot{m}_{39}\, h_{39} = \dot{m}_{37}\, h_{37} + \dot{m}_{40}\, h_{40} + \dot{m}_{41}\, h_{41} + \dot{m}_{42}\, h_{42}$

Table 4.5: Entropy and exergy balance equations.

Component	Entropy Balance	Exergy Balance
Flash chamber 1	$\dot{m}_1\, s_1 + \dot{S}_{gen,flash1} = \dot{m}_2\, s_2$	$\dot{m}_1\, ex_1 = \dot{m}_2\, ex_2 + \dot{E}x_{dest,flash1}$
Separator 1	$\dot{m}_2\, s_2 + \dot{S}_{gen,separator1} = \dot{m}_3\, s_3 + \dot{m}_5\, s_5$	$\dot{m}_2\, ex_2 = \dot{m}_3\, ex_3 + \dot{m}_5\, ex_5 + \dot{E}x_{dest,separator1}$
Turbine 1 (T1)	$\dot{m}_3\, s_3 + \dot{S}_{gen,T1} = \dot{m}_4\, s_4$	$\dot{m}_3\, ex_3 = \dot{m}_4\, ex_4 + \dot{W}_{T1} + \dot{E}x_{dest,T1}$
Flash chamber 2	$\dot{m}_5\, s_5 + \dot{S}_{gen,flash2} = \dot{m}_6\, s_6$	$\dot{m}_5\, ex_5 = \dot{m}_6\, ex_6 + \dot{E}x_{dest,flash2}$
Separator 2	$\dot{m}_6\, s_6 + \dot{S}_{gen,separator2} = \dot{m}_7\, s_7 + \dot{m}_9\, s_9$	$\dot{m}_6\, ex_6 = \dot{m}_7\, ex_7 + \dot{m}_9\, ex_9 + \dot{E}x_{dest,separator2}$

Turbine 2 (T2)	$\dot{m}_7\, s_7 + \dot{S}_{gen,T2} = \dot{m}_8\, s_8$	$\dot{m}_7\, ex_7 = \dot{m}_8\, ex_8 + \dot{W}_{T2} + \dot{E}x_{dest,T2}$
Electrochemical ammonia synthesizer (EAS)	$\dot{m}_{11}\, s_{11} + \dot{m}_{12}\, s_{12} + \dot{S}_{gen,EAS} = \dot{m}_{13}\, s_{13} + \dot{m}_{14}\, s_{14} + \frac{\dot{Q}_{EAS,loss}}{T_o}$	$\dot{m}_{11}\, ex_{11} + \dot{m}_{12}\, ex_{12} + \dot{W}_{EAS} = \dot{m}_{13}\, ex_{13} + \dot{m}_{14}\, ex_{14} + \dot{E}x_{dest,EAS}$
Mixer	$\dot{m}_{14}\, s_{14} + \dot{m}_{44}\, s_{44} + \dot{S}_{gen,mixer} = \dot{m}_{15}\, s_{15}$	$\dot{m}_{14}\, ex_{14} + \dot{m}_{44}\, ex_{44} = \dot{m}_{15}\, ex_{15} + \dot{E}x_{dest,mixer}$
Ammonium bicarbonate (AB) reactor	$\dot{m}_{15}\, s_{15} + \dot{m}_{28}\, s_{28} + \dot{S}_{gen,AB} = \dot{m}_{16}\, s_{16} + \frac{\dot{Q}_{AB,loss}}{T_o}$	$\dot{m}_{15}\, ex_{15} + \dot{m}_{28}\, ex_{28} = \dot{m}_{16}\, ex_{16} + \dot{E}x_{dest,AB}$
Air compressor	$\dot{m}_{19}\, s_{19} + \dot{S}_{gen,C} = \dot{m}_{20}\, s_{20}$	$\dot{m}_{19}\, ex_{19} + \dot{W}_C = \dot{m}_{20}\, ex_{20} + \dot{E}x_{dest,C}$
Air regenerator (AR)	$\dot{m}_{20}\, s_{20} + \dot{m}_{29}\, s_{29} + \dot{S}_{gen,AR} = \dot{m}_{21}\, s_{21} + \dot{m}_{30}\, s_{30}$	$\dot{m}_{20}\, ex_{20} + \dot{m}_{29}\, ex_{29} = \dot{m}_{21}\, ex_{21} + \dot{m}_{30}\, ex_{30} + \dot{E}x_{dest,AR}$
Fuel regenerator (FR)	$\dot{m}_{17}\, s_{17} + \dot{m}_{26}\, s_{26} + \dot{S}_{gen,FR} = \dot{m}_{18}\, s_{18} + \dot{m}_{29}\, s_{29}$	$\dot{m}_{17}\, ex_{17} + \dot{m}_{26}\, ex_{26} = \dot{m}_{18}\, ex_{18} + \dot{m}_{29}\, ex_{29} + \dot{E}x_{dest,FR}$
Solid-Oxide Fuel Cell (SOFC)	$\dot{m}_{18}\, s_{18} + \dot{m}_{21}\, s_{21} + \dot{m}_{43}\, s_{43} + \dot{S}_{gen,SOFC} = \dot{m}_{22}\, s_{22} + \dot{m}_{23}\, s_{23} + \frac{\dot{Q}_{SOFC,loss}}{T_o}$	$\dot{m}_{18}\, ex_{18} + \dot{m}_{21}\, ex_{21} + \dot{m}_{43}\, ex_{43} = \dot{m}_{22}\, ex_{22} + \dot{m}_{23}\, ex_{23} + \dot{W}_{SOFC} + \dot{E}x_{dest,SOFC}$
WGSMR-afterburner	$\dot{m}_{22}\, s_{22} + \dot{m}_{23}\, s_{23} + \dot{S}_{gen,WGSMR} = \dot{m}_{24}\, s_{24} + \dot{m}_{25}\, s_{25}$	$\dot{m}_{22}\, ex_{22} + \dot{m}_{23}\, ex_{23} = \dot{m}_{24}\, ex_{24} + \dot{m}_{25}\, ex_{25} + \dot{E}x_{dest,WGSMR}$
Turbine 3 (T3)	$\dot{m}_{25}\, s_{25} + \dot{S}_{gen,T3} = \dot{m}_{26}\, s_{26}$	$\dot{m}_{25}\, ex_{25} = \dot{m}_{26}\, ex_{26} + \dot{W}_{T3} + \dot{E}x_{dest,T3}$
Condenser 1	$\dot{m}_{24}\, s_{24} + \dot{S}_{gen,cond1} = \dot{m}_{27}\, s_{27} + \dot{m}_{28}\, s_{28} + \frac{\dot{Q}_{cond1}}{T_o}$	$\dot{m}_{24}\, ex_{24} = \dot{m}_{27}\, ex_{27} + \dot{m}_{28}\, ex_{28} + \dot{E}x_{dest,cond1}$
Boiler	$\dot{m}_{30}\, s_{30} + \dot{m}_{33}\, s_{33} + \dot{S}_{gen,boiler} = \dot{m}_{31}\, s_{31} + \dot{m}_{34}\, s_{34}$	$\dot{m}_{30}\, ex_{30} + \dot{m}_{33}\, ex_{33} = \dot{m}_{31}\, ex_{31} + \dot{m}_{34}\, ex_{34} + \dot{E}x_{dest,boiler}$
Heater	$\dot{m}_{31}\, s_{31} + \dot{S}_{gen,heater} = \dot{m}_{32}\, s_{32} + \frac{\dot{Q}_{Space}}{T_{Space}}$	$\dot{m}_{31}\, ex_{31} = \dot{m}_{32}\, ex_{32} + \dot{Q}_{Space}\left(1 - \frac{T_o}{T_{Space}}\right) + \dot{E}x_{dest,heater}$
Turbine 4 (T4)	$\dot{m}_{34}\, s_{34} + \dot{S}_{gen,T4} = \dot{m}_{35}\, s_{35}$	$\dot{m}_{34}\, ex_{34} = \dot{m}_{35}\, ex_{35} + \dot{W}_{T4} + \dot{E}x_{dest,T4}$

Condenser 2	$\dot{m}_{35}\, s_{35} + \dot{m}_{37}\, s_{37} + \dot{S}_{gen,cond2} = \dot{m}_{36}\, s_{36} + \dot{m}_{38}\, s_{38}$	$\dot{m}_{35}\, ex_{35} + \dot{m}_{37}\, ex_{37} = \dot{m}_{36}\, ex_{36} + \dot{m}_{38}\, ex_{38} + \dot{E}x_{dest,cond2}$
Pump	$\dot{m}_{36}\, s_{36} + +\dot{S}_{gen,pump} = \dot{m}_{33}\, s_{33}$	$\dot{m}_{36}\, ex_{36} + \dot{W}_{pump} = \dot{m}_{33}\, ex_{33} + +\dot{E}x_{dest,pump}$
Multi-Effect Desalination (MED)	$\dot{m}_{38}\, s_{38} + \dot{m}_{39}\, s_{39} + \dot{S}_{gen,MED} = \dot{m}_{37}\, s_{37} + \dot{m}_{40}\, s_{40} + \dot{m}_{41}\, s_{41} + \dot{m}_{42}\, s_{42}$	$\dot{m}_{38}\, ex_{38} + \dot{m}_{39}\, ex_{39} = \dot{m}_{37}\, ex_{37} + \dot{m}_{40}\, ex_{40} + \dot{m}_{41}\, ex_{41} + \dot{m}_{42}\, ex_{42} + \dot{E}x_{dest,MED}$

Moreover, an exergoeconomic analysis is conducted for the second carbon capturing system and the main objectives of this analysis are to find the costs associated with every stream in the system, and to calculate the unit cost of exergy for the product streams in the integrated system. Streams here can be material, work, and/or heat transfer. The exergoeconomic analysis of this integrated system comes after analyzing it using energy and exergy tools using the balance equations of mass, energy, entropy, and exergy. The exergoeconomic model is established which continues the previous analysis and extend it to study the economic aspects of this integrated system. There are multiple methods to conduct an exergoeconomic analysis and they have been reviewed in the literature [137–139]. The method used here is the SPECO approach which is one of the most commonly used methods to investigate integrated energy systems as in [36,122,140–142]. To begin with, the cost balance equation in its general form is expressed as

$$\sum_{in} \dot{C}_{in,k} + \dot{C}_{q,k} + \dot{Z}_k = \sum_{out} \dot{C}_{out,k} + \dot{C}_{w,k} \tag{4.60}$$

This equation has five terms that will be explained from left to right and each of these terms has units of \$ s^{-1}. The first term is the inlet material stream cost rate which is defined as

$$\dot{C}_{in} = c_{in}\dot{m}_{in}(ex_{in}) \tag{4.61}$$

where c_{in} is the unit cost (also called specific cost) of the inlet exergy stream in units of \$ kJ^{-1}. The second term of equation (4.58) is the heat transfer cost rate, and this is defined as

$$\dot{C}_{q,k} = c_{q,k}\left(1 - \frac{T_o}{T_k}\right)\dot{Q}_k \tag{4.62}$$

where $c_{q,k}$ is the unit cost of the heat transfer exergy of component *k* in units of \$ kJ^{-1}. The third term of equation (4.58) is the total investment cost rate of component *k*. This is calculated in two steps, calculating the capital investment using the cost function of the specific component in consideration which comes out as a value with units \$, then converting this value to a cost rate using the following formula [114].

$$\dot{Z}_k = \frac{Z_k \times CRF \times \varphi}{N \times 3600} \tag{4.63}$$

where $\dot{Z}_k$ is the total investment cost rate of component *k*, Z_k is the capital investment cost of component *k* in \$, and this is calculated using the cost function of component *k*, φ is the maintenance factor which accounts for the maintenance costs of component *k*, and it is assumed to be 1.06 in this study [114], N is the number of operating hours of the system in a year (7446 h), and *CRF* is the Capital Recovery Factor, and it can be calculated using this expression

$$CRF = \frac{i_n(1 + i_n)^n}{(1 + i_n)^n - 1} \tag{4.64}$$

where i_n is the interest rate assumed as 10%, and n is the system life and it is taken as 20 years in this work [114]. Cost functions for each component of the present integrated system will be taken from different sources of the literature to better represent the capital investment costs of each component. These cost functions will be listed later in this section. Moving on the right-hand side of equation (4.58), the next term is the outlet material stream cost rate which is defined as

$$\dot{C}_{out} = c_{out}\dot{m}_{out}(ex_{out}) \tag{4.65}$$

where c_{out} is the unit cost of the outlet exergy stream in units of \$ kJ^{-1}. The last term of equation (4.58) is the work cost rate which is

$$\dot{C}_{w,k} = c_{w,k}\dot{W}_k \tag{4.66}$$

where $c_{w,k}$ is the unit cost of the work exergy of component *k* in units of \$ kJ^{-1}, and $\dot{W}_k$ is the power output of component *k*. After applying the cost balance equation for every component in the integrated system, it can be noticed that the number of cost rate unknowns is more than the number of cost balance equations and this makes the system of equations unsolvable. To resolve this issue, the SPECO method introduces two principles called the Fuel Principle and the Product Principle, shortened to F-Principle and P-Principle, to obtain auxiliary equations so that the system of equations is complete (i.e. number of unknowns is equal to number of equations).

Before moving on to explain the F-Principle and P-Principle, it is better to clarify the terminology of fuel and product in the context of exergoeconomic analysis. A fuel stream is any exergy stream that acts as a supplier of exergy to the component under consideration, while a product stream is any exergy stream that acts as a receiver of exergy in the component and the stream is considered to be the desired output of the component. Two illustrative examples are given here to clarify it further. The first example is a heat exchanger. The hot fluid supplies exergy to the component through heat transfer, so the hot fluid stream is the fuel stream. The cold fluid in the heat exchanger is the product stream because it receives exergy as it passes through the component, and it is desirable to increase the temperature of this cold fluid using the heat exchanger. A second example is a turbine. The high-temperature and high-pressure material stream that passes through the turbine is considered the fuel stream since it supplies exergy to the turbine, while the power output of the turbine is the product stream because it receives exergy from the turbine, and the power output is the desired output of the turbine.

Now, the F-Principle can be explained, and it states that "the specific cost (cost per exergy unit) associated with this removal of exergy from a fuel stream must be equal to the average specific cost at which the removed exergy was supplied to the same stream in upstream components" [36]. Using this principle, it is possible to obtain auxiliary equations for each stream that exists the component under consideration, and it is associated with the definition of fuel stream. The P-Principle states that all exergy streams associated with the product streams share the same average unit cost [36]. Using these two principles, the necessary number of auxiliary equations to calculate every cost rate in the integrated

system is obtained. Further explanations and illustrations of these two principles can be found in papers by Lazzaretto and Tsatsaronis [36], and by Shokati et al. [114].

Several performance parameters based on the exergoeconomic analysis are described here and they are used to assess the exergoeconomic performance of each component in the integrated system as well as the entire integrated system. The first two are the average cost per unit exergy of fuel and the average cost per unit exergy of product which are respectively expressed as follows [143]:

$$c_{F,k} = \frac{\dot{C}_{F,k}}{\dot{E}x_{F,k}} \tag{4.67}$$

$$c_{P,k} = \frac{\dot{C}_{P,k}}{\dot{E}x_{P,k}} \tag{4.68}$$

where the subscripts *F* and *P* stand for fuel and product, respectively. Another exergoeconomic parameter is defined here and it is called the exergy destruction cost rate.

$$\dot{C}_{D,k} = c_{F,k}\dot{E}x_{dest,k} \tag{4.69}$$

Lastly, the exergoeconomic factor is defined as [143]:

$$f_k = \frac{\dot{Z}_k}{\dot{Z}_k + \dot{C}_{D,k}} \tag{4.70}$$

Now, it is time to show the specific equations used for each component for this exergoeconomic analysis. Table 4.6 presents the cost balance equations and auxiliary equations produced using the F-Principle and P-Principle for every component in the present integrated system, as well as related assumptions for the exergoeconomic study. Table 4.7 lists all the capital investment cost functions for each component in the present integrated system. Some of these cost functions require additional relations to calculate their values for the components which are also listed in the table. The overall cost rate of the present integrated system is simply the summation of all the cost rates of the components in the system.

$$\dot{Z}_{overall} = \sum_k \dot{Z}_k \tag{4.71}$$

Similarly, the overall exergy destruction rate of the present integrated system is the summation of all the exergy destruction rates of all the components in the system which is expressed mathematically as

$$\dot{E}x_{dest,overall} = \sum_k \dot{E}x_{dest,k} \tag{4.72}$$

Table 4.8 presents the explicit expressions for the exergoeconomic performance parameters, namely the average cost per unit exergy of fuel, the average cost per unit exergy of product, exergy destruction cost rate, and the exergoeconomic factor, for each component in the integrated system and for the overall integrated system.

Table 4.6: Cost balance equations for each component in system 2 with their corresponding auxiliary equations and assumptions.

Components	**Cost Balance Equations**	**Auxiliary Equations & Assumptions**
Flash chamber 1	$\dot{C}_1 + \dot{Z}_{flash1} = \dot{C}_2$	Assumption: $c_1 = 1.3\ \$\ GJ^{-1}$ [114]
Separator 1	$\dot{C}_2 + \dot{Z}_{separator1} = \dot{C}_3 + \dot{C}_5$	$\frac{\dot{C}_3 - \dot{C}_2}{\dot{m}_3\ ex_3 - \dot{m}_2\ ex_2} = \frac{\dot{C}_5 - \dot{C}_2}{\dot{m}_5\ ex_5 - \dot{m}_2\ ex_2}$, P-Principle
Turbine 1 (T1)	$\dot{C}_3 + \dot{Z}_{T1} = \dot{C}_4 + \dot{C}_{w,T1}$	$c_3 = c_4$, F-Principle
Flash chamber 2	$\dot{C}_5 + \dot{Z}_{flash2} = \dot{C}_6$	No auxiliary equation,
Separator 2	$\dot{C}_6 + \dot{Z}_{separator2} = \dot{C}_7 + \dot{C}_9$	$\frac{\dot{C}_7 - \dot{C}_6}{\dot{m}_7\ ex_7 - \dot{m}_6\ ex_6} = \frac{\dot{C}_9 - \dot{C}_6}{\dot{m}_9\ ex_9 - \dot{m}_6\ ex_6}$, P-Principle
Turbine 2 (T2)	$\dot{C}_7 + \dot{Z}_{T2} = \dot{C}_8 + \dot{C}_{w,T2}$	$c_7 = c_8$, F-Principle
Electrochemical ammonia synthesizer (EAS)	$\dot{C}_{11} + \dot{C}_{12} + \dot{C}_{w,EAS} + \dot{Z}_{EAS} = \dot{C}_{13} + \dot{C}_{14} + \dot{C}_{q,EAS}$	$c_{13} = c_{14} = c_{q,EAS}$, P-Principle $\dot{C}_{w,T1} + \dot{C}_{w,T2} = \dot{C}_{w,EAS}$, cost balance equation for the electricity transmission between turbines 1,2 and EAS. Assumption: $c_{12} = 34.1\ \$\ GJ^{-1}$ [144]
Mixer	$\dot{C}_{14} + \dot{C}_{44} + \dot{Z}_{Mixer} = \dot{C}_{15}$	Assumptions: $\dot{Z}_{Mixer} = 0$, $c_{44} = c_{34}$
Ammonium bicarbonate (AB) reactor	$\dot{C}_{15} + \dot{C}_{28} + \dot{Z}_{AB} = \dot{C}_{16} + \dot{C}_{q,AB}$	$c_{16} = c_{q,AB}$, P-Principle
Air compressor	$\dot{C}_{19} + \dot{C}_{w,c} + \dot{Z}_c = \dot{C}_{20}$	Assumptions: $c_{w,c} = c_{w,T3}$ because mechanical power for the air compressor is drawn from turbine 3. Another assumption is air is free: $\dot{C}_{19} = 0$

Air regenerator	$\dot{C}_{20} + \dot{C}_{29} + \dot{Z}_{AR} = \dot{C}_{21} + \dot{C}_{30}$	$c_{29} = c_{30}$, F-Principle
Fuel regenerator	$\dot{C}_{17} + \dot{C}_{26} + \dot{Z}_{FR} = \dot{C}_{18} + \dot{C}_{29}$	$c_{26} = c_{29}$, F-Principle Assumptions: $c_{17} = 0.004\ \$\ MJ^{-1}$, $\dot{C}_{17} = c_{17}\dot{m}_{17}LHV_{CH4}$ [145] where LHV_{CH4} is the lower heating value of methane and it is taken as 50000 kJ kg^{-1} [133].
Solid-Oxide Fuel Cell (SOFC)	$\dot{C}_{18} + \dot{C}_{21} + \dot{C}_{43} + \dot{Z}_{SOFC} = \dot{C}_{22} + \dot{C}_{23} + \dot{C}_{w,SOFC} + \dot{C}_{q,SOFC}$	$c_{w,SOFC} = c_{q,SOFC} = \frac{\dot{C}_{22} - (\dot{C}_{18} + \dot{C}_{43})}{\dot{m}_{22}\, ex_{22} - (\dot{m}_{18}\, ex_{18} + \dot{m}_{43}\, ex_{43})} = \frac{\dot{C}_{23} - \dot{C}_{21}}{\dot{m}_{23}\, ex_{23} - \dot{m}_{21}\, ex_{21}}$, P-Principle Assumption: $c_{43} = c_{34}$
WGSMR-afterburner	$\dot{C}_{22} + \dot{C}_{23} + \dot{Z}_{WGSMR} = \dot{C}_{24} + \dot{C}_{25}$	$\frac{\dot{C}_{23} - \dot{C}_{25}}{\dot{m}_{23}\, ex_{23} - \dot{m}_{25}\, ex_{25}} = \frac{\dot{C}_{22} - \dot{C}_{24}}{\dot{m}_{22}\, ex_{22} - \dot{m}_{24}\, ex_{24}}$, P-Principle
Turbine 3 (T3)	$\dot{C}_{25} + \dot{Z}_{T3} = \dot{C}_{26} + \dot{C}_{w,T3}$	$c_{25} = c_{26}$, F-Principle
Condenser 1	$\dot{C}_{24} + \dot{Z}_{cond1} = \dot{C}_{27} + \dot{C}_{28} + \dot{C}_{q,cond1}$	$c_{27} = c_{28} = c_{q,cond1}$, P-Principle
Boiler	$\dot{C}_{30} + \dot{C}_{33} + \dot{Z}_{boiler} = \dot{C}_{31} + \dot{C}_{34}$	$c_{30} = c_{31}$, F-Principle
Heater	$\dot{C}_{31} + \dot{Z}_{heater} = \dot{C}_{32} + \dot{C}_{q,space}$	$c_{31} = c_{32}$, F-Principle
Turbine 4 (T4)	$\dot{C}_{34} + \dot{Z}_{T4} = \dot{C}_{35} + \dot{C}_{w,T4}$	$c_{34} = c_{35}$, F-Principle
Condenser 2	$\dot{C}_{35} + \dot{C}_{37} + \dot{Z}_{cond2} = \dot{C}_{36} + \dot{C}_{38}$	$c_{35} = c_{36}$, F-Principle Assumption: $c_{37} = 0$
Pump	$\dot{C}_{36} + \dot{C}_{w,pump} + \dot{Z}_{pump} = \dot{C}_{33}$	Assumption: $c_{w,pump} = c_{w,T4}$ because mechanical power for the pump is drawn from turbine 4.
Multi-Effect Desalination (MED)	$\dot{C}_{38} + \dot{C}_{39} + \dot{Z}_{MED} = \dot{C}_{37} + \dot{C}_{40} + \dot{C}_{41} + \dot{C}_{42}$	$c_{40} = c_{41} = c_{42}$, P-Principle Assumption: $c_{39} = 0$, assuming seawater is free.

Table 4.7: Captial investment cost functions for each component in system 2 with additoinal relations.

Components	**Capital Investment Cost Functions**	**Additional Relations**	**Sources**
Flash chamber 1	$Z_{flash1} = 0$	None	[146]
Separator 1	$Z_{separator1} = \frac{1.218\left(42 + \frac{1.63\dot{m}_2}{3.6}\right)}{1000}$	None	[126]

Turbine 1 (T1)	$Z_{T1} = 6000(\dot{W}_{T1})^{0.7}$	None	[126]
Flash chamber 2	$Z_{flash2} = 0$	None	[146]
Separator 2	$Z_{separator2} = \frac{1.218\left(42 + \frac{1.63\dot{m}_6}{3.6}\right)}{1000}$	None	[126]
Turbine 2 (T2)	$Z_{T2} = 6000(\dot{W}_{T2})^{0.7}$	None	[126]
Electrochemical ammonia synthesizer (EAS)	$Z_{EAS} = \frac{2.6 \times 10^6}{150 \times 10^3}\dot{W}_{EAS}$	None	[121,147]
Mixer	$Z_{Mixer} = 0$	None	-
Ammonium bicarbonate (AB) reactor	$\dot{Z}_{AB} = \frac{0.56}{580}\dot{m}_{28}$ (\$ s^{-1})	None	[125]
Air compressor	$Z_c = 71.1\left(\frac{\dot{m}_{19}}{0.92 - \eta_C}\right)(r_p)\,ln(r_p)$	Pressure ratio is $r_p = \frac{P_{20}}{P_{19}}$ Isentropic efficiency for air compressor is $\eta_C = \frac{h_{20,s} - h_{19}}{h_{20} - h_{19}}$	[122,123]
Air regenerator	$Z_{AR} = 2681(A_{AR})^{0.59}$	Heat exchanger area is $A_{AR} = \frac{\dot{m}_{29}(h_{29} - h_{30})}{U_{AR}LMTD_{AR}}$, where $U_{AR} = 1.6$ kW m^{-2} K^{-1}, and $LMTD_{AR} = \frac{(T_{29} - T_{21}) - (T_{30} - T_{20})}{\ln\left(\frac{(T_{29} - T_{21})}{(T_{30} - T_{20})}\right)}$	[122]
Fuel regenerator	$Z_{FR} = 2681(A_{FR})^{0.59}$	Heat exchanger area is $A_{FR} = \frac{\dot{m}_{26}(h_{26} - h_{29})}{U_{FR}LMTD_{FR}}$, where $U_{FR} = 3.0$ kW m^{-2} K^{-1}, and $LMTD_{FR} = \frac{(T_{26} - T_{18}) - (T_{29} - T_{17})}{\ln\left(\frac{(T_{26} - T_{18})}{(T_{29} - T_{17})}\right)}$	[122]
Solid-Oxide Fuel Cell (SOFC)	$Z_{SOFC} = 1.1A_{SOFC}(2.96T_{SOFC} - 1907)$	Assuming $T_{SOFC} = T_{22}$, Area of SOFC is $A_{SOFC} = \frac{\dot{W}_{SOFC}}{\rho_{SOFC}}$, where $\rho_{SOFC} = 1.6$ kW m^{-2} is the power density of SOFC.	[148]
WGSMR-afterburner	$Z_{WGSMR} = \$92600$	None	[149]
Turbine 3 (T3)	$Z_{T3} = \dot{W}_{T3}(1318.5 - 98.328 \times ln\,(\dot{W}_{T3}))$	None	[148]
Condenser 1	$Z_{cond1} = 1773\dot{m}_{24}$	None	[114]

Boiler	$Z_{boiler} = 2143(A_{boiler})^{0.514}$	Heat exchanger area is $A_{boiler} = \frac{\dot{m}_{30}(h_{30}-h_{31})}{U_{boiler}LMTD_{boiler}}$, where $U_{boiler} =$ 2.0 kW m^{-2} K^{-1}, and $LMTD_{boiler} = \frac{(T_{30}-T_{34})-(T_{31}-T_{33})}{\ln\left(\frac{(T_{30}-T_{34})}{(T_{31}-T_{33})}\right)}$	[122]
Heater	$Z_{heater} = 2681(A_{heater})^{0.59}$	Heat exchanger area is $A_{heater} = \frac{\dot{m}_{31}(h_{31}-h_{32})}{U_{heater}LMTD_{heater}}$, where $U_{heater} = 1.6$ kW m^{-2} K^{-1}, and $LMTD_{heater} = \frac{(T_{31}-T_{space})-(T_{32}-T_o)}{\ln\left(\frac{(T_{31}-T_{space})}{(T_{32}-T_o)}\right)}$	[122]
Turbine 4 (T4)	$Z_{T4} = 6000\left(\dot{W}_{T4}\right)^{0.7}$	None	[126]
Condenser 2	$Z_{cond2} = 1773\dot{m}_{35}$	None	[114]
Pump	$Z_{pump} = 3540\left(\dot{W}_{pump}\right)^{0.71}$	None	[114]
Multi-Effect Desalination (MED)	$Z_{MED} = 0.5(800 \times 3.6 \times 24\dot{m}_{38})$	None	[142]

Table 4.8: Exergoeconomic performance parameters for each component in system 2 and the overall system.

Components	$\boldsymbol{c_F}$	$\boldsymbol{c_P}$	$\boldsymbol{\dot{C}_D}$	$\boldsymbol{f}$
Flash chamber 1	$c_{F,flash1} = c_1$	$c_{P,flash1} = c_2$	$\dot{C}_{D,flash1} = c_{F,flash1}\dot{E}x_{dest,flash1}$	$f_{flash1} = \frac{\dot{Z}_{flash1}}{\dot{Z}_{flash1} + \dot{C}_{D,flash1}}$
Separator 1	$c_{F,separator} = c_2$	$c_{P,separator} = c_3$	$\dot{C}_{D,separator1} = c_{F,separator1}\dot{E}x_{dest,separ}$	$f_{separator1} = \frac{\dot{Z}_{separator1}}{\dot{Z}_{separator1} + \dot{C}_{D,separ}}$
Turbine 1 (T1)	$c_{F,T1} = c_3$	$c_{P,T1} = c_{w,T1}$	$\dot{C}_{D,T1} = c_{F,T1}\dot{E}x_{dest,T1}$	$f_{T1} = \frac{\dot{Z}_{T1}}{\dot{Z}_{T1} + \dot{C}_{D,T1}}$
Flash chamber 2	$c_{F,flash2} = c_5$	$c_{P,flash2} = c_6$	$\dot{C}_{D,flash2} = c_{F,flash2}\dot{E}x_{dest,flash2}$	$f_{flash2} = \frac{\dot{Z}_{flash2}}{\dot{Z}_{flash2} + \dot{C}_{D,flash2}}$
Separator 2	$c_{F,separator} = c_6$	$c_{P,separator} = c_7$	$\dot{C}_{D,separator2} = c_{F,separator2}\dot{E}x_{dest,separ}$	$f_{separator2} = \frac{\dot{Z}_{separator2}}{\dot{Z}_{separator2} + \dot{C}_{D,separ}}$
Turbine 2 (T2)	$c_{F,T2} = c_7$	$c_{P,T2} = c_{w,T2}$	$\dot{C}_{D,T2} = c_{F,T2}\dot{E}x_{dest,T2}$	$f_{T2} = \frac{\dot{Z}_{T2}}{\dot{Z}_{T2} + \dot{C}_{D,T2}}$

Electrochemical ammonia synthesizer (EAS)	$c_{F,EAS} = c_{w,EAS}$	$c_{P,EAS} = c_{14}$	$\dot{C}_{D,EAS} = c_{F,EAS}\dot{E}x_{dest,EAS}$	$f_{EAS} = \frac{\dot{Z}_{EAS}}{\dot{Z}_{EAS} + \dot{C}_{D,EAS}}$
Mixer	$c_{F,Mixer} = c_{14} + c_{44}$	$c_{P,Mixer} = c_{15}$	$\dot{C}_{D,Mixer} = c_{F,Mixer}\dot{E}x_{dest,Mixer}$	$f_{Mixer} = \frac{\dot{Z}_{Mixer}}{\dot{Z}_{Mixer} + \dot{C}_{D,Mixer}}$
Ammonium bicarbonate (AB) reactor	$c_{F,AB} = c_{15} + c_{28}$	$c_{P,AB} = c_{16}$	$\dot{C}_{D,AB} = c_{F,AB}\dot{E}x_{dest,AB}$	$f_{AB} = \frac{\dot{Z}_{AB}}{\dot{Z}_{AB} + \dot{C}_{D,AB}}$
Air compressor	$c_{F,c} = c_{w,c}$	$c_{P,c} = c_{20}$	$\dot{C}_{D,c} = c_{F,c}\dot{E}x_{dest,c}$	$f_c = \frac{\dot{Z}_c}{\dot{Z}_c + \dot{C}_{D,c}}$
Air regenerator	$c_{F,AR} = c_{29}$	$c_{P,AR} = c_{21}$	$\dot{C}_{D,AR} = c_{F,AR}\dot{E}x_{dest,AR}$	$f_{AR} = \frac{\dot{Z}_{AR}}{\dot{Z}_{AR} + \dot{C}_{D,AR}}$
Fuel regenerator	$c_{F,FR} = c_{26}$	$c_{P,FR} = c_{18}$	$\dot{C}_{D,FR} = c_{F,FR}\dot{E}x_{dest,FR}$	$f_{FR} = \frac{\dot{Z}_{FR}}{\dot{Z}_{FR} + \dot{C}_{D,FR}}$
Solid-Oxide Fuel Cell (SOFC)	$c_{F,SOFC} = c_{18}$	$c_{P,SOFC} = c_{w,SOFC}$	$\dot{C}_{D,SOFC} = c_{F,SOFC}\dot{E}x_{dest,SOFC}$	$f_{SOFC} = \frac{\dot{Z}_{SOFC}}{\dot{Z}_{SOFC} + \dot{C}_{D,SOFC}}$
WGSMR-afterburner	$c_{F,WGSMR} = c_{22}$	$c_{P,WGSMR} = c_{25}$	$\dot{C}_{D,WGSMR} = c_{F,WGSMR}\dot{E}x_{dest,WGSMR}$	$f_{WGSMR} = \frac{\dot{Z}_{WGSMR}}{\dot{Z}_{WGSMR} + \dot{C}_{D,WGSMR}}$
Turbine 3 (T3)	$c_{F,T3} = c_{25}$	$c_{P,T3} = c_{w,T3}$	$\dot{C}_{D,T3} = c_{F,T3}\dot{E}x_{dest,T3}$	$f_{T3} = \frac{\dot{Z}_{T3}}{\dot{Z}_{T3} + \dot{C}_{D,T3}}$
Condenser 1	$c_{F,cond1} = c_{24}$	$c_{P,cond1} = c_{28}$	$\dot{C}_{D,cond1} = c_{F,cond1}\dot{E}x_{dest,cond1}$	$f_{cond1} = \frac{\dot{Z}_{cond1}}{\dot{Z}_{cond1} + \dot{C}_{D,cond1}}$
Boiler	$c_{F,boiler} = c_{30}$	$c_{P,boiler} = c_{34}$	$\dot{C}_{D,boiler} = c_{F,boiler}\dot{E}x_{dest,boiler}$	$f_{boiler} = \frac{\dot{Z}_{boiler}}{\dot{Z}_{boiler} + \dot{C}_{D,boiler}}$
Heater	$c_{F,heater} = c_{31}$	$c_{P,heater} = c_{q,space}$	$\dot{C}_{D,heater} = c_{F,heater}\dot{E}x_{dest,heater}$	$f_{heater} = \frac{\dot{Z}_{heater}}{\dot{Z}_{heater} + \dot{C}_{D,heater}}$
Turbine 4 (T4)	$c_{F,T4} = c_{34}$	$c_{P,T4} = c_{w,T4}$	$\dot{C}_{D,T4} = c_{F,T4}\dot{E}x_{dest,T4}$	$f_{T4} = \frac{\dot{Z}_{T4}}{\dot{Z}_{T4} + \dot{C}_{D,T4}}$

Condenser 2	$c_{F,cond2} = c_{35}$	$c_{P,cond2} = c_{38}$	$\dot{C}_{D,cond2} = c_{F,cond2}\dot{E}x_{dest,cond2}$	$f_{cond2} = \frac{\dot{Z}_{cond2}}{\dot{Z}_{cond2} + \dot{C}_{D,cond2}}$
Pump	$c_{F,pump} = c_{w,pump}$	$c_{P,pump} = c_{33}$	$\dot{C}_{D,pump} = c_{F,pump}\dot{E}x_{dest,pump}$	$f_{pump} = \frac{\dot{Z}_{pump}}{\dot{Z}_{pump} + \dot{C}_{D,pump}}$
Multi-Effect Desalination (MED)	$c_{F,MED} = c_{38}$	$c_{P,MED} = c_{42}$	$\dot{C}_{D,MED} = c_{F,MED}\dot{E}x_{dest,MED}$	$f_{MED} = \frac{\dot{Z}_{MED}}{\dot{Z}_{MED} + \dot{C}_{D,MED}}$
Integrated system	$c_{F,overall} = c_1 + c_{12} + c_{17} + c_{39} + c_{43} + c_{44}$	$c_{P,overall} = c_{w,SOFC} + c_{w,T3} + c_{w,T4} + c_{16} + c_{42} + c_{q,space}$	$\dot{C}_{D,overall} = c_{F,overall}\dot{E}x_{dest,overall}$	$f_{overall} = \frac{\dot{Z}_{overall}}{\dot{Z}_{overall} + \dot{C}_{D,overall}}$

4.3 Thermodynamic and exergoeconomic modeling of system 3

This section describes the model that is used on the third carbon capturing system to assess its thermodynamic performance. To begin with, the common assumptions among all the components in the integrated system are listed here:

- The steady state and uniform flows are assumed at every state/stream in the integrated system.
- The pressure losses are assumed to be very small and negligible across connecting pipes, valves, mixer, MED unit, parabolic solar collectors, EAS device, ammonium bicarbonate reactor, and heat exchangers.
- All gases, except steam, behaves in accordance with the ideal gas law.
- The reference temperature is 293 K, and the reference pressure is 101 kPa.
- The kinetic and potential energy differences across a component in the system are assumed to be too small compared to the enthalpy flows that are entering or exiting the component.
- The heat exchangers that have two fluids shown in the integrated system are assumed to have negligible heat losses.

- All compressors operate under adiabatic conditions and have an isentropic efficiency of 70%, while all turbines operate under adiabatic conditions and have an isentropic efficiency of 75%.

After that, the thermodynamic modeling for some specific components in the integrated system are mentioned. To begin with, the parabolic solar collector model is described. The heat transfer rate of solar energy absorbed by the collectors is calculated by knowing the solar irradiation and the effective surface area of the collectors

$$\dot{Q}_{solar} = \dot{S}_{solar} A_{solar} \tag{4.73}$$

The effective surface area of the collectors is found using the following expression

$$A_{solar} = n_{solar} L(w - D_o) \tag{4.74}$$

where n_{solar} is the number of modules, L is the length of a single module, D_o is the module outer diameter, and w is the width of a single module. The details of the design of each module are adopted from the experimental work by Zarza et al. [150]. The length of the module pipe is 12.27 m, the module outer diameter is 0.07 m, and the width of a single module is 5.76 m. The number of modules that can handle the electricity loads required by the electrochemical ammonia synthesizer and the elastocaloric cooling device can be 2,000 modules of the specific design chosen here. One ratio that defines the amount of thermal energy being stored in the thermal energy storage (TES) unit is expressed as

$$\varepsilon = \frac{\dot{m}_3}{\dot{m}_2} \tag{4.75}$$

The elastocaloric cooling device model is described now and it is adopted from the work of Qian et al. [151]. The energy balance equation applied on this device is

$$\dot{Q}_{cooling} + \dot{W}_{cooling} = \dot{Q}_{released} \tag{4.76}$$

In order to calculate the needed cooling power, it is necessary to estimate the energy Coefficient of Performance of the ECD ($COP_{en,ECD}$) and this is done by using the reverse Stirling thermodynamic model developed by Qian et al. [151]. It is assumed in this model that the material properties of hysteresis entropy change are constant, as well as the heat recovery to be complete. Firstly, the energy COP of the ECD is defined as

$$COP_{en,ECD} = \frac{\dot{Q}_{cooling}}{\dot{W}_{cooling}} \tag{4.77}$$

The cooling load can be expressed as

$$\dot{Q}_{cooling} = \dot{N}_{SMA} m_{ECD} q_{cooling} \tag{4.78}$$

where $\dot{N}$ is the rate of phase transformation cycles done by the SMA in Hz, and m_{ECD} is the SMA mass. The SMA mass is presumed to be constant, and it has magnitude of 10 kg, while $\dot{N}$ varies as the cooling load changes. $q_{cooling}$ is the cooling load per unit of mass per cycle which can be calculated using

$$q_{cooling} = T_c \Delta s - A_{SMA} \tag{4.79}$$

where T_c is the ECD cold side temperature in Kelvin, Δs is the phase transformation specific entropy change of the SMA (kJ kg^{-1} K^{-1}), and A represents the irreversibility of the phase transformation cycle and this is called the hysteresis of the SMA in units of kJ kg^{-1}. Then, the heat released per unit of mass per cycle is defined as

$$q_{released} = T_h \Delta s + A_{SMA} \tag{4.80}$$

where T_h is the ECD hot side temperature. After combining the above equations, the energy COP of the ECD becomes

$$COP_{en,ECD} = \frac{T_c \Delta s - A_{SMA}}{(T_h - T_c)\Delta s + 2A_{SMA}} \tag{4.81}$$

Next, the exergy analysis is considered for this cooling device, and this starts by applying the entropy and exergy balance equations as follows:

$$\frac{\dot{Q}_{cooling}}{T_{cooling}} + \dot{S}_{gen,ECD} = \frac{\dot{Q}_{released}}{T_o} \tag{4.82}$$

$$\dot{Q}_{cooling}\left(1 - \frac{T_o}{T_{cooling}}\right) + \dot{W}_{cooling} = \dot{E}x_{dest,ECD} \tag{4.83}$$

Also, the exergy COP of the ECD is defined as

$$COP_{ex,ECD} = \frac{\dot{Q}_{cooling}\left(\frac{T_o}{T_{cooling}} - 1\right)}{\dot{W}_{cooling}} \tag{4.84}$$

The cryogenic air separation unit is modeled here. The model used here is a simplified one based on the work and results of a paper by Skorek-Osikowska et al. [152]. The mass flow rate of the incoming air is based on the theoretical combustion of methane. The theoretical air to fuel mass ($AF_{theoretical}$) is 17.16. The actual air to fuel mass ratio (AF_{actual}) is found by multiplying the excess air factor (λ) by the theoretical ratio as

$$AF_{actual} = \lambda \times AF_{theoretical} = \frac{\dot{m}_{19}}{\dot{m}_{22}} \tag{4.85}$$

From the paper mentioned above, there are two important ratios that need to be defined which are the specific work of the ASU, and the oxygen to air mass ratio and these are expressed respectively as

$$w_{ASU} = \frac{\dot{W}_{ASU}}{\dot{m}_{20}} \tag{4.86}$$

and

$$R_{ASU} = \frac{\dot{m}_{20}}{\dot{m}_{19}} \tag{4.87}$$

Another piece of information is that the molar percentage of oxygen in the oxygen-rich stream (stream 20) is taken to be 95%, and the inlet and exit mass streams of this unit are assumed to share the same pressure and temperature levels. These are set at the same value of the ambient conditions as done by Skorek-Osikowska et al. [152]. Lastly, the chemical equation is represented as

$$2\lambda(O_2 + 3.76N_2) \longrightarrow 2\lambda(0.95O_2 + 0.05N_2) + 2\lambda(0.05O_2 + 3.71N_2) \tag{4.R13}$$

Moreover, the combustor model is described. The chemical combustion that takes place inside this device is assumed to be adiabatic and complete (i.e. all the methane is consumed and no monoxide exists in the exhaust gases). The pressure drop across the combustor has a ratio of 0.951 [153]. The chemical equation that represents the combustion is

$$CH_4 + 2\lambda(0.95O_2 + 0.05N_2) \longrightarrow CO_2 + 2H_2O + 2(0.95\lambda - 1)O_2 + 0.1\lambda N_2 \tag{4.R14}$$

The details of the models used for the compressors, turbines, heat exchangers, pumps, the MED unit, and the carbon capturing unit which includes the electrochemical ammonia synthesizer, mixer and the ammonium bicarbonate reactor have been discussed earlier.

Table 4.9 and Table 4.10 present the lists of balance equations for each component in the integrated system which are implemented in the Engineering Equation Solver software. To end this section, the performance parameters that are used to assess this integrated system are outlined. Firstly, the net electric power produced by the integrated system is calculated by

$$\dot{W}_{net} = \dot{W}_{T2} + \dot{W}_{T3} - \dot{W}_{ASU} - \dot{W}_{C1} - \dot{W}_{C2} \tag{4.88}$$

The mass flow rate of carbon dioxide going to the ammonium bicarbonate reactor is

$$\dot{m}_{CO_2} = \dot{m}_{28} x_{CO_2,28} \tag{4.89}$$

where $x_{CO_2,28}$ is the mass ratio of carbon dioxide in stream 28. Then, the overall energy and exergy efficiencies of the integrated system can be defined respectively as

$$\eta_{en,overall} = \frac{\dot{W}_{net} + \dot{Q}_{cooling} + \dot{m}_{11}(h_{11} - h_{10}) + (\dot{m}_{38}h_{38} - \dot{m}_{35}h_{35}) + (\dot{m}_{18}h_{18} - \dot{m}_{12}h_{12} - \dot{m}_{39}h_{39} - \dot{m}_{CO_2}h_{28})}{\dot{Q}_{solar} + \dot{m}_{21}HHV_{CH4}} \tag{4.90}$$

and the overall exergy efficiency is

$$\eta_{ex,overall} = \frac{\dot{W}_{net} + \dot{Q}_{cooling}\left(\frac{T_o}{T_{cooling}} - 1\right) + \dot{m}_{11}(ex_{11} - ex_{10}) + (\dot{m}_{38}ex_{38} - \dot{m}_{35}ex_{35}) + (\dot{m}_{18}ex_{18} - \dot{m}_{12}ex_{12} - \dot{m}_{39}ex_{39} - \dot{m}_{CO_2}ex_{28})}{\dot{Q}_{solar}\left(1 - \frac{T_o}{T_{solar}}\right) + \dot{m}_{21}ex_{21}} \tag{4.91}$$

In addition, the energy requirement to capture one kilogram of carbon dioxide is measured using this parameter

$$E_{CO_2-captured} = \frac{\dot{W}_{EAS}}{\dot{m}_{CO_2}} \tag{4.92}$$

Although this parameter captures the carbon capturing unit performance, it does not measure the performance of the solar collectors and carbon capturing unit combined performance. For this reason, two similar parameters that include this solar part of the integrated system are defined here.

$$R_{en,CO_2-captured} = \frac{\dot{Q}_{solar}(1 - \varepsilon)}{\dot{m}_{CO_2}} \tag{4.93}$$

$$R_{ex,CO_2-captured} = \frac{\dot{Q}_{solar}\left(1 - \frac{T_o}{T_{solar}}\right)(1 - \varepsilon)}{\dot{m}_{CO_2}} \tag{4.94}$$

Table 4.9: Mass and energy balance equations.

Component	Mass Balance	Energy Balance
Pump 1	$\dot{m}_6 = \dot{m}_7$	$\dot{m}_6\, h_6 + \dot{W}_{Pump1} = \dot{m}_7\, h_7$
Concentrated solar collectors	$\dot{m}_1 = \dot{m}_2$	$\dot{m}_1\, h_1 + \dot{Q}_{solar} = \dot{m}_2\, h_2$
Pump 2	$\dot{m}_9 = \dot{m}_{10}$	$\dot{m}_9\, h_9 + \dot{W}_{Pump2} = \dot{m}_{10}\, h_{10}$
Heat exchanger 2 (HX2)	$\dot{m}_3 = \dot{m}_8$, $\dot{m}_{10} = \dot{m}_{11}$	$\dot{m}_3\, h_3 + \dot{m}_{10}\, h_{10} = \dot{m}_8\, h_8 + \dot{m}_{11}\, h_{11}$
Turbine (T1)	$\dot{m}_4 = \dot{m}_5$	$\dot{m}_4\, h_4 = \dot{m}_5\, h_5 + \dot{W}_{T1}$
Heat Exchanger 1 (HX1)	$\dot{m}_5 = \dot{m}_6$	$\dot{m}_5\, h_5 = \dot{m}_6\, h_6 + \dot{Q}_{HX1}$
Electrochemical ammonia synthesizer (EAS)	$\dot{m}_{12} + \dot{m}_{39} = \dot{m}_{14} + \dot{m}_{15}$	$\dot{m}_{12}\, h_{12} + \dot{m}_{39}\, h_{39} + \dot{W}_{EAS} = \dot{m}_{14}\, h_{14} + \dot{m}_{15}\, h_{15} + \dot{Q}_{EAS,loss}$
Mixer	$\dot{m}_{15} + \dot{m}_{16} = \dot{m}_{17}$	$\dot{m}_{15}\, h_{15} + \dot{m}_{16}\, h_{16} = \dot{m}_{17}\, h_{17}$
Ammonium bicarbonate (AB) reactor	$\dot{m}_{17} + \dot{m}_{28} = \dot{m}_{18} + \dot{m}_{40}$	$\dot{m}_{17}\, h_{17} + \dot{m}_{28}\, h_{28} = \dot{m}_{18}\, h_{18} + \dot{m}_{40}\, h_{40} + \dot{Q}_{AB,loss}$
Condenser	$\dot{m}_{27} = \dot{m}_{28} + \dot{m}_{41}$	$\dot{m}_{27}\, h_{27} = \dot{m}_{28}\, h_{28} + \dot{m}_{41}\, h_{41} + \dot{Q}_{cond}$
Cryogenic air separation unit (ASU)	$\dot{m}_{19} = \dot{m}_{13} + \dot{m}_{20}$	$\dot{m}_{19}\, h_{19} + \dot{W}_{ASU} = \dot{m}_{13}\, h_{13} + \dot{m}_{20}\, h_{20} + \dot{Q}_{ASU}$
Compressor 1	$\dot{m}_{22} = \dot{m}_{23}$	$\dot{m}_{22}\, h_{22} + \dot{W}_{C1} = \dot{m}_{23}\, h_{23}$
Combustor	$\dot{m}_{20} + \dot{m}_{21} = \dot{m}_{27}$, $\dot{m}_{23} = \dot{m}_{24}$	$\dot{m}_{20}\, h_{20} + \dot{m}_{21}\, h_{21} + \dot{m}_{23}\, h_{23} = \dot{m}_{24}\, h_{24} + \dot{m}_{27}\, h_{27}$
Turbine 2 (T2)	$\dot{m}_{24} = \dot{m}_{25}$	$\dot{m}_{24}\, h_{24} = \dot{m}_{25}\, h_{25} + \dot{W}_{T2}$
Heat exchanger 3 (HX3)	$\dot{m}_{25} = \dot{m}_{26}$, $\dot{m}_{29} = \dot{m}_{30}$	$\dot{m}_{25}\, h_{25} + \dot{m}_{29}\, h_{29} = \dot{m}_{26}\, h_{26} + \dot{m}_{30}\, h_{30}$
Turbine 3 (T3)	$\dot{m}_{30} = \dot{m}_{31}$	$\dot{m}_{30}\, h_{30} = \dot{m}_{31}\, h_{31} + \dot{W}_{T3}$
Heat exchanger 4 (HX4)	$\dot{m}_{31} = \dot{m}_{32}$, $\dot{m}_{33} = \dot{m}_{34}$	$\dot{m}_{31}\, h_{31} + \dot{m}_{33}\, h_{33} = \dot{m}_{32}\, h_{32} + \dot{m}_{34}\, h_{34}$
Compressor 2	$\dot{m}_{32} = \dot{m}_{29}$	$\dot{m}_{32}\, h_{32} + \dot{W}_{C2} = \dot{m}_{29}\, h_{29}$
Multi-effect desalination (MED)	$\dot{m}_{34} = \dot{m}_{33}$, $\dot{m}_{35} = \dot{m}_{36} + \dot{m}_{37} + \dot{m}_{38}$	$\dot{m}_{34}\, h_{34} + \dot{m}_{35}\, h_{35} = \dot{m}_{33}\, h_{33} + \dot{m}_{36}\, h_{36} + \dot{m}_{37}\, h_{37} + \dot{m}_{38}\, h_{38}$

Table 4.10: Entropy and exergy balance equations.

Component	Entropy Balance	Exergy Balance
Pump 1	$\dot{m}_6\, s_6 + \dot{S}_{gen,Pump1} = \dot{m}_7\, s_7$	$\dot{m}_6\, ex_6 + \dot{W}_{Pump1} = \dot{m}_7\, ex_7 + \dot{E}x_{dest,Pump1}$
Concentrated solar collectors	$\dot{m}_1\, s_1 + \frac{\dot{Q}_{solar}}{T_{solar}} + \dot{S}_{gen,solar} = \dot{m}_2\, s_2$	$\dot{m}_1\, ex_1 + \dot{Q}_{solar}\left(1 - \frac{T_o}{T_{solar}}\right) = \dot{m}_2\, ex_2 + \dot{E}x_{dest,solar}$

Pump 2	$\dot{m}_9\, s_9 + \dot{S}_{gen,Pump2} = \dot{m}_{10}\, s_{10}$	$\dot{m}_9\, ex_9 + \dot{W}_{Pump2} = \dot{m}_{10}\, ex_{10} + \dot{E}x_{dest,Pump2}$
Heat exchanger 2 (HX2)	$\dot{m}_3\, s_3 + \dot{m}_{10}\, s_{10} + \dot{S}_{gen,HX2} = \dot{m}_8\, s_8 + \dot{m}_{11}\, s_{11}$	$\dot{m}_3\, ex_3 + \dot{m}_{10}\, ex_{10} = \dot{m}_8\, ex_8 + \dot{m}_{11}\, ex_{11} + \dot{E}x_{dest,HX2}$
Turbine 1 (T1)	$\dot{m}_4\, s_4 + \dot{S}_{gen,T1} = \dot{m}_5\, s_5$	$\dot{m}_4\, ex_4 = \dot{m}_5\, ex_5 + \dot{W}_{T1} + \dot{E}x_{dest,T1}$
Heat Exchanger 1 (HX1)	$\dot{m}_5\, s_5 + \dot{S}_{gen,HX1} = \dot{m}_6\, s_6 + \frac{\dot{Q}_{HX1}}{T_o}$	$\dot{m}_5\, ex_5 = \dot{m}_6\, ex_6 + \dot{E}x_{dest,HX1}$
Electrochemical ammonia synthesizer (EAS)	$\dot{m}_{12}\, s_{12} + \dot{m}_{39}\, s_{39} + \dot{S}_{gen,EAS} = \dot{m}_{14}\, s_{14} + \dot{m}_{15}\, s_{15} + \frac{\dot{Q}_{EAS,loss}}{T_o}$	$\dot{m}_{12}\, ex_{12} + \dot{m}_{39}\, ex_{39} + \dot{W}_{EAS} = \dot{m}_{14}\, ex_{14} + \dot{m}_{15}\, ex_{15} + \dot{E}x_{dest,EAS}$
Mixer	$\dot{m}_{15}\, s_{15} + \dot{m}_{16}\, s_{16} + \dot{S}_{gen,mixer} = \dot{m}_{17}\, s_{17}$	$\dot{m}_{15}\, ex_{15} + \dot{m}_{16}\, ex_{16} = \dot{m}_{17}\, ex_{17} + \dot{E}x_{dest,mixer}$
Ammonium bicarbonate (AB) reactor	$\dot{m}_{17}\, s_{17} + \dot{m}_{28}\, s_{28} + \dot{S}_{gen,AB} = \dot{m}_{18}\, s_{18} + \dot{m}_{40}\, s_{40} + \frac{\dot{Q}_{AB,loss}}{T_o}$	$\dot{m}_{17}\, ex_{17} + \dot{m}_{28}\, ex_{28} = \dot{m}_{18}\, ex_{18} + \dot{m}_{40}\, ex_{40} + \dot{E}x_{dest,AB}$
Condenser	$\dot{m}_{37}\, s_{37} + \dot{S}_{gen,cond} = \dot{m}_{28}\, s_{28} + \dot{m}_{41}\, s_{41} + \frac{\dot{Q}_{cond}}{T_o}$	$\dot{m}_{27}\, ex_{27} = \dot{m}_{28}\, ex_{28} + \dot{m}_{41}\, ex_{41} + \dot{E}x_{dest,cond}$
Cryogenic air separation unit (ASU)	$\dot{m}_{19}\, s_{19} + \dot{S}_{gen,ASU} = \dot{m}_{13}\, s_{13} + \dot{m}_{20}\, s_{20} + \frac{\dot{Q}_{ASU}}{T_o}$	$\dot{m}_{19}\, ex_{19} + \dot{W}_{ASU} = \dot{m}_{13}\, ex_{13} + \dot{m}_{20}\, ex_{20} + \dot{E}x_{dest,ASU}$
Compressor 1	$\dot{m}_{22}\, s_{22} + \dot{S}_{gen,C1} = \dot{m}_{23}\, s_{23}$	$\dot{m}_{22}\, ex_{22} + \dot{W}_{C1} = \dot{m}_{23}\, ex_{23} + \dot{E}x_{dest,C1}$
Combustor	$\dot{m}_{20}\, s_{20} + \dot{m}_{21}\, s_{21} + \dot{m}_{23}\, s_{23} + \dot{S}_{gen,combustor} = \dot{m}_{24}\, h_{24} + \dot{m}_{27}\, s_{27}$	$\dot{m}_{20}\, ex_{20} + \dot{m}_{21}\, ex_{21} + \dot{m}_{23}\, ex_{23} = \dot{m}_{24}\, ex_{24} + \dot{m}_{27}\, ex_{27} + \dot{E}x_{dest,combustor}$
Turbine 2 (T2)	$\dot{m}_{24}\, s_{24} + \dot{S}_{gen,T2} = \dot{m}_{25}\, s_{25}$	$\dot{m}_{24}\, ex_{24} = \dot{m}_{25}\, ex_{25} + \dot{W}_{T2} + \dot{E}x_{dest,T2}$
Heat Exchanger 3 (HX3)	$\dot{m}_{25}\, s_{25} + \dot{m}_{29}\, s_{29} + \dot{S}_{gen,HX3} = \dot{m}_{26}\, s_{26} + \dot{m}_{30}\, s_{30}$	$\dot{m}_{25}\, ex_{25} + \dot{m}_{29}\, ex_{29} = \dot{m}_{26}\, ex_{26} + \dot{m}_{30}\, ex_{30} + \dot{E}x_{dest,HX3}$
Turbine 3 (T3)	$\dot{m}_{30}\, s_{30} + \dot{S}_{gen,T3} = \dot{m}_{31}\, s_{31}$	$\dot{m}_{30}\, ex_{30} = \dot{m}_{31}\, ex_{31} + \dot{W}_{T3} + \dot{E}x_{dest,T3}$

Heat Exchanger 4 (HX4)	$\dot{m}_{31}\, s_{31} + \dot{m}_{33}\, s_{33} + \dot{S}_{gen,HX4} = \dot{m}_{32}\, s_{32} + \dot{m}_{34}\, s_{34}$	$\dot{m}_{31}\, ex_{31} + \dot{m}_{33}\, ex_{33} = \dot{m}_{32}\, ex_{32} + \dot{m}_{34}\, ex_{34} + \dot{E}x_{dest,HX4}$
Compressor 2	$\dot{m}_{32}\, s_{32} + \dot{S}_{gen,C2} = \dot{m}_{29}\, s_{29}$	$\dot{m}_{32}\, ex_{32} + \dot{W}_{C2} = \dot{m}_{29}\, ex_{29} + \dot{E}x_{dest,C2}$
Multi-effect desalination (MED)	$\dot{m}_{34}\, s_{34} + \dot{m}_{35}\, s_{35} + \dot{S}_{gen,MED} = \dot{m}_{33}\, s_{33} + \dot{m}_{36}\, s_{36} + \dot{m}_{37}\, s_{37} + \dot{m}_{38}\, s_{38}$	$\dot{m}_{34}\, ex_{34} + \dot{m}_{35}\, ex_{35} = \dot{m}_{33}\, ex_{33} + \dot{m}_{36}\, ex_{36} + \dot{m}_{37}\, ex_{37} + \dot{m}_{38}\, ex_{38} + \dot{E}x_{dest,MED}$

Next, the exergoeconomic analysis which combines the concepts of exergy analysis and basics of economics to evaluate integrated systems is described. This analysis starts with the cost balance equation which is written in the rate form as

$$\sum_{in} \dot{C}_{in,k} + \dot{C}_{q,k} + \dot{Z}_k = \sum_{out} \dot{C}_{out,k} + \dot{C}_{w,k} \tag{4.95}$$

In this balance equation, the total investment cost rate is calculated using the following expression

$$\dot{Z}_k = \frac{Z_k \times CRF \times \varphi}{N \times 3600} \tag{4.96}$$

Here, φ is the maintenance factor and it is taken to be 1.06 and N is the number of operating hours of the system in a year (7446 h) [114]. *CRF* is the Capital Recovery Factor, and it is expressed as

$$CRF = \frac{i_n(1\ +\ i_n)^n}{(1\ +\ i_n)^n\ -\ 1} \tag{4.97}$$

where i_n is the interest rate, and n is the system life, which are taken to be 10% and 20 years, respectively [114]. The explicit cost balance equations for each component of this integrated are presented in Table 4.11 along with their auxiliary equations and assumptions. The auxiliary equations are established using the Fuel-Principle (F-Principle) and Product-Principle (P-Principle) which were developed by Lazzaretto and Tsatsaronis [36], and by Shokati et al. [114]. The F-Principle can briefly be explained by saying the unit cost of fuel entering and exiting a component stays the same, while the P-Principle can briefly be explained by saying that products of a component share the same average unit cost. Also, the capital investment cost functions for every component in this system are listed in Table

4.12. In addition, the exergoeconomic analysis uses some performance parameters to evaluate the system. These are the cost per unit exergy of fuel and product, the exergy destruction cost rate, and the exergoeconomic factor, and these are defined respectively as [143]:

$$c_{F,k} = \frac{\dot{C}_{F,k}}{\dot{E}x_{F,k}} \tag{4.98}$$

$$c_{P,k} = \frac{\dot{C}_{P,k}}{\dot{E}x_{P,k}} \tag{4.99}$$

$$\dot{C}_{D,k} = c_{F,k}\dot{E}x_{dest,k} \tag{4.100}$$

$$f_k = \frac{\dot{Z}_k}{\dot{Z}_k + \dot{C}_{D,k}} \tag{4.101}$$

In addition, there are overall performance parameters that are required to be defined to evaluate the entire integrated system. The overall total investment cost rate is

$$\dot{Z}_{overall} = \sum_k \dot{Z}_k \tag{4.102}$$

The overall exergy destruction rate is

$$\dot{E}x_{dest,overall} = \sum_k \dot{E}x_{dest,k} \tag{4.103}$$

The overall cost per unit exergy of fuel and product are defined respectively as

$$c_{F,overall} = c_9 + c_{12} + c_{16} + c_{21} \tag{4.104}$$

$$c_{P,overall} = c_{w,T2} + c_{w,T3} + c_{18} + c_{38} + c_{q,ECD,heating} \tag{4.105}$$

The overall exergy destruction cost rate is

$$\dot{C}_{D,overall} = c_{F,overall}\dot{E}x_{dest,overall} \tag{4.106}$$

The overall exergoeconomic factor is

$$f_{overall} = \frac{\dot{Z}_{overall}}{\dot{Z}_{overall} + \dot{C}_{D,overall}} \tag{4.107}$$

Table 4.11: Cost balance equations.

Components	Cost Balance Equations	Auxiliary Equations & Assumptions
Pump 1	$\dot{C}_6 + \dot{C}_{w,pump1} + \dot{Z}_{pump1} = \dot{C}_7$	$c_{w,pump1} = c_{w,T1}$
Parabolic solar collectors	$\dot{C}_1 + \dot{C}_{q,solar} + \dot{Z}_{solar} = \dot{C}_2$	Assumption: $c_{q,solar} = 0$ [154]
Pump 2	$\dot{C}_9 + \dot{C}_{w,pump2} + \dot{Z}_{pump2} = \dot{C}_{10}$	$c_{w,pump2} = c_{w,T1}$, assumption: $c_9 = 2.404\ \$\ GJ^{-1}$ [155]
Heat exchanger 2 (HX2)	$\dot{C}_3 + \dot{C}_{10} + \dot{Z}_{HX2} = \dot{C}_8 + \dot{C}_{11}$	$c_3 = c_8$, F-Principle
Turbine 1 (T1)	$\dot{C}_4 + \dot{Z}_{T1} = \dot{C}_5 + \dot{C}_{w,T1}$	$c_4 = c_5$, F-Principle
Heat Exchanger 1 (HX1)	$\dot{C}_5 + \dot{Z}_{HX1} = \dot{C}_6 + \dot{C}_{q,HX1}$	$c_5 = c_6$, F-Principle
Elastocaloric cooling device (ECD)	$\dot{C}_{q,ECD,cooling} + \dot{C}_{w,ECD} + \dot{Z}_{ECD} = \dot{C}_{q,ECD,heating}$	Assumptions: $c_{w,ECD} = c_{w,T1}$, $c_{q,ECD,cooling} = 0$
Electrochemical ammonia synthesizer (EAS)	$\dot{C}_{12} + \dot{C}_{39} + \dot{C}_{w,EAS} + \dot{Z}_{EAS} = \dot{C}_{14} + \dot{C}_{15} + \dot{C}_{q,EAS}$	$c_{14} = c_{15} = c_{q,EAS}$, P-Principle Assumptions: $\dot{C}_{w,T1} = \dot{C}_{w,EAS}$, $c_{12} = 0$, $c_{39} = c_{13}$
Mixer	$\dot{C}_{15} + \dot{C}_{16} + \dot{Z}_{Mixer} = \dot{C}_{17}$	Assumptions: $\dot{Z}_{Mixer} = 0$, $c_{16} = c_{34}$
Ammonium bicarbonate (AB) reactor	$\dot{C}_{17} + \dot{C}_{28} + \dot{Z}_{AB} = \dot{C}_{18} + \dot{C}_{40} + \dot{C}_{q,AB}$	$c_{16} = c_{40} = c_{q,AB}$, P-Principle
Condenser	$\dot{C}_{27} + \dot{Z}_{Cond} = \dot{C}_{28} + \dot{C}_{41} + \dot{C}_{q,Cond}$	$c_{28} = c_{41} = c_{q,Cond}$, P-Principle
Cryogenic air separation unit (ASU)	$\dot{C}_{19} + \dot{C}_{w,ASU} + \dot{Z}_{ASU} = \dot{C}_{13} + \dot{C}_{20} + \dot{C}_{q,ASU}$	$c_{13} = c_{20} = c_{q,ASU}$, P-Principle Assumptions: $c_{w,ASU} = c_{w,T2}$, $c_{19} = 0$
Compressor 1	$\dot{C}_{22} + \dot{C}_{w,c1} + \dot{Z}_{c1} = \dot{C}_{23}$	Assumptions: $c_{w,c1} = c_{w,T2}$ because mechanical power for the compressor is drawn from turbine 2. Another assumption is air is free: $\dot{C}_{22} = 0$
Combustor	$\dot{C}_{20} + \dot{C}_{21} + \dot{C}_{23} + \dot{Z}_{combustor} = \dot{C}_{24} + \dot{C}_{27}$	$c_{24} = c_{27}$, P-Principle Assumptions: $c_{21} = 0.004\ \$\ MJ^{-1}$, $\dot{C}_{21} = c_{21}\dot{m}_{21}LHV_{CH4}$ [145] where LHV_{CH4} is the lower heating value of methane and it is taken as 50000 kJ kg^{-1} [133].
Turbine 2 (T2)	$\dot{C}_{24} + \dot{Z}_{T2} = \dot{C}_{25} + \dot{C}_{w,T2}$	$c_{24} = c_{25}$, F-Principle

Heat Exchanger 3 (HX3)	$\dot{C}_{25} + \dot{C}_{29} + \dot{Z}_{HX3} = \dot{C}_{26} + \dot{C}_{30}$	$c_{25} = c_{26}$, F-Principle
Turbine 3 (T3)	$\dot{C}_{30} + \dot{Z}_{T3} = \dot{C}_{31} + \dot{C}_{w,T3}$	$c_{30} = c_{31}$, F-Principle
Heat Exchanger 4 (HX4)	$\dot{C}_{31} + \dot{C}_{33} + \dot{Z}_{HX4} = \dot{C}_{32} + \dot{C}_{34}$	$c_{31} = c_{32}$, F-Principle
Compressor 2	$\dot{C}_{32} + \dot{C}_{w,c2} + \dot{Z}_{c2} = \dot{C}_{29}$	Assumption: $c_{w,c2} = c_{w,T3}$ because mechanical power for the compressor is drawn from turbine 3.
Multi-effect desalination (MED)	$\dot{C}_{34} + \dot{C}_{35} + \dot{Z}_{MED} = \dot{C}_{33} + \dot{C}_{36} + \dot{C}_{37} + \dot{C}_{38}$	$c_{36} = c_{37} = c_{38}$, P-Principle Assumption: $c_{35} = 0$, assuming seawater is free.

Table 4.12: Captial investment cost functions.

Components	Capital Investment Cost Functions	Additional Relations	Ref.
Pump 1	$Z_{pump1} = 3540\left(\dot{W}_{pump1}\right)^{0.71}$	None	[114]
Parabolic solar collectors	$Z_{solar} = 355 \times A_{solar}$	None	[156]
Pump 2	$Z_{pump2} = 3540\left(\dot{W}_{pump2}\right)^{0.71}$	None	[114]
Heat exchanger 2 (HX2)	$Z_{HX2} = 2681(A_{HX2})^{0.59}$	The heat exchanger area is $A_{HX2} = \frac{\dot{m}_3(h_3 - h_8)}{U_{HX2} LMTD_{HX2}}$, where $U_{HX2} = 3.0$ kW m^{-2} K^{-1}, and $LMTD_{HX2} = \frac{(T_3 - T_{11}) - (T_8 - T_{10})}{\ln\left(\frac{(T_3 - T_{11})}{(T_8 - T_{10})}\right)}$	[122]
Thermal energy storage unit (TES)	$Z_{TES} = \frac{22}{3600}\dot{m}_{11}(h_{11} - h_{10})$	None	[157]
Turbine 1 (T1)	$Z_{T1} = 6000\left(\dot{W}_{T1}\right)^{0.7}$	None	[126]
Heat Exchanger 1 (HX1)	$Z_{HX1} = 1773\dot{m}_5$	None	[114]
Elastocaloric cooling device (ECD)	$Z_{ECD} = 1000\dot{W}_{ECD}$	None	[121]
Electrochemical ammonia synthesizer (EAS)	$Z_{EAS} = \frac{2.6 \times 10^6}{150 \times 10^3}\dot{W}_{EAS}$	Economic data is taken from references [121,147].	[121,147]
Mixer	$Z_{Mixer} = 0$	None	-
Ammonium bicarbonate (AB) reactor	$\dot{Z}_{AB} = \frac{0.56}{580}\dot{m}_{28}$ (\$ s^{-1})	None	[125]
Condenser	$Z_{Cond} = 1773\dot{m}_{27}$	None	[114]
Cryogenic air separation unit (ASU)	$Z_{ASU} = 537.7 \times \dot{W}_{ASU}$	None	[152]
Compressor 1	$Z_{c1} = 71.1\left(\frac{\dot{m}_{22}}{0.92 - \eta_{c1}}\right)(r_{c1})\, ln(r_{c1})$	Pressure ratio is $r_{c1} = \frac{P_{23}}{P_{22}}$ Isentropic efficiency for compressor 1 is $\eta_{c1} = \frac{h_{23,s} - h_{22}}{h_{23} - h_{22}}$	[122,123]

Combustor	$Z_{combustor} = \frac{25.6 \times \dot{m}_{20} \times (1 + e^{(0.018 \times T_{24} - 26.4)})}{(0.995 - r_{combustor})}$	$r_{combustor} = \frac{P_{27}}{P_{21}} = 0.951$, [153]	[158]
Turbine 2 (T2)	$Z_{T2} = \dot{W}_{T2}(1318.5 - 98.328 \times ln\,(\dot{W}_{T2}))$	None	[148]
Heat Exchanger 3 (HX3)	$Z_{HX3} = 2681(A_{HX3})^{0.59}$	The heat exchanger area is $A_{HX3} = \frac{\dot{m}_{25}(h_{25} - h_{26})}{U_{HX3} LMTD_{HX3}}$, where $U_{HX3} = 3.0$ kW m^{-2} K^{-1}, and $LMTD_{HX3} = \frac{(T_{25} - T_{30}) - (T_{26} - T_{29})}{\ln\left(\frac{(T_{25} - T_{30})}{(T_{26} - T_{29})}\right)}$	[122]
Turbine 3 (T3)	$Z_{T3} = \dot{W}_{T3}(1318.5 - 98.328 \times ln\,(\dot{W}_{T3}))$	None	[148]
Heat Exchanger 4 (HX4)	$Z_{HX4} = 2681(A_{HX4})^{0.59}$	The heat exchanger area is $A_{HX4} = \frac{\dot{m}_{31}(h_{31} - h_{32})}{U_{HX4} LMTD_{HX4}}$, where $U_{HX4} = 3.0$ kW m^{-2} K^{-1}, and $LMTD_{HX4} = \frac{(T_{31} - T_{34}) - (T_{32} - T_{33})}{\ln\left(\frac{(T_{31} - T_{34})}{(T_{32} - T_{33})}\right)}$	[122]
Compressor 2	$Z_{c2} = 71.1\left(\frac{\dot{m}_{32}}{0.92 - \eta_{c2}}\right)(r_{c2})\,ln(r_{c2})$	Pressure ratio is $r_{c2} = \frac{P_{29}}{P_{32}}$ Isentropic efficiency for compressor 2 is $\eta_{c2} = \frac{h_{29,s} - h_{32}}{h_{29} - h_{32}}$	[122,123]
Multi-effect desalination (MED)	$Z_{MED} = 0.5(800 \times 3.6 \times 24 \times \dot{m}_{38})$	None	[142]

4.4 Multi-objective optimization procedure

The procedure starts by identifying the two objective functions that are desired to be minimized and have a trade-off relationship. These two objective functions are the overall unit cost of products and the overall exergy destruction rate for the entire integrated system. Minimizing the first objective functions means reducing the costs of producing the useful outputs of the integrated system while minimizing the second objective function indicates increasing the exergetic performance of the integrated system. The optimization procedure is taken from an earlier study by Al-Hamed and Dincer [159] and it is described here. The second step in this procedure is producing data points using EES which is the software used to analyze the system thermodynamically and exergoeconomically. The third step is inputting these data points to another piece of software named Eureqa to generate two explicit mathematical expressions for the chosen objective functions in this optimization study. The Eureqa software keeps running to find these expressions until the stopping

criterion which is 5 minutes of search time is reached and this is sufficient to produce expressions with a high correlation coefficient of 0.99 or higher. Next, a MATLAB code is written to implement the multi-objective genetic algorithm developed by Deb et al. [160]. This algorithm helps to find the Pareto front which consists of the set of optimum solutions and their corresponding operating conditions, where the two objective functions are optimized as best as possible. The cross-over is "intermediate" with a ratio of 1. The mutation operator is adaptive meaning it changes throughout the search. The search of this algorithm stops when either of the two conditions is reached. The first stopping condition is the average spread change in the Pareto front becomes less than 1×10^{-6}. The second stopping condition is reaching a generation number that is equivalent to 100 times the number of decision variables chosen in the optimization procedure. System 2 decision varibales and their corresponding constrainst are chosen according to the results of the parametric studies conducted on this system and these are listed in Table 4.13. Similarly, system 3 decision variables and their corresponding constraints for the optimization are outlined in Table 4.14.

Table 4.13: Decision variables and constraints for system 2.

Decision variable	**Constraints**
Geothermal fluid temperature (T_1)	428 – 593 K
Air compressor isentropic efficiency (η_c)	0.7 – 0.9
Turbine 3 isentropic efficiency (η_{T3})	0.65 – 0.76
Boiler pressure (P_{34})	1200 – 2200 kPa

Table 4.14: Decision variables and constraints for system 3.

Decision variable	**Constraints**
Solar irradiance ($\dot{S}_{solar}$)	0.45 – 0.9 kW m^{-2}
C1 compression ratio (r_{c1})	4 – 12
C1 and C2 isentropic efficiency (η_{c1})	0.7 – 0.9
T2 inlet temperature (T_{24})	1170 – 1870 K

4.5 Scale-up analysis

The experimental setup discussed previously can be scaled up to a full-scale plant using a few scaling factors for the batch reactor. To begin with, a general scaling factor can be defined as follows:

$$Y_X = \frac{X_{FS}}{X_{LS}} \tag{4.108}$$

where X_{FS} is the under consideration variable at full-scale and X_{LS} is the variable under consideration at the lab-scale. The first scaling factor needed for a batch reactor is the volumetric scaling factor and this is expressed as

$$Y_V = \frac{V_{FS}}{V_{LS}} = \left(\frac{D_{FS}}{D_{LS}}\right)^3 \tag{4.109}$$

where D_{FS} is the diamater of the full-scale reactor, and D_{LS} is the diamater of the lab-scale reactor. The second factor is the heat transfer area scaling factor which is defined as

$$Y_A = \frac{A_{FS}}{A_{LS}} = \left(\frac{D_{FS}}{D_{LS}}\right)^2 \tag{4.110}$$

After that, the captial cost scaling ratio to estimate the full-scale reactor is

$$\frac{CC_{FS}}{CC_{LS}} = \left(\frac{\dot{m}_{AB,FS}}{\dot{m}_{AB,LS}}\right)^{N_C} \tag{4.111}$$

where CC stands for the capital cost for both the lab-scale and full-scale reactors, $\dot{m}_{AB,FS}$ is the full-scale reactor ammonium bicarbonate production capacity, $\dot{m}_{AB,LS}$ is the lab-scale reactor ammonium bicarbonate production capacity, and N_C is the cost exponent for the batch reactor. The values of this exponent where chosen to have a range between 0.5 and 0.7 depending on the scaling factor to apporperiately represent the costs of scaling up the batch reactor. Next, the heat transfer and temperature aspects of the scaling up the batch reactor are investigated. This is done using the material and heat transfer differential equations described below. The material differential equation is expressed as

$$\frac{dN_{CO_2}}{dt} = r_{CO_2} V \tag{4.112}$$

and the heat transfer differential equation is

$$N_{CO_2} C_p \frac{dT}{dt} = \Delta H_{AB} r_{CO_2} V + UA(T_c - T) \tag{4.113}$$

where N_{CO_2} is the mole of carbon dioxide in the batch reactor (mole), $r_{CO_2}$is the rate of reaction (mol s^{-1} m^{-3}), V is the volume of the batch reactor (m^3), C_p is the heat capacity of the ammonia solution (J mol^{-1} K^{-1}), ΔH_{AB} is the heat of the reaction for producing

ammonium bicabronate (J mol^{-1}), U is the heat transfer coefficeint (J K^{-1} s^{-1} m^{-2}), A is the surface area of the batch reactor (m^2), and T_c is the cooling temperature (K). Some auxiliry equations to support this analysis are shown below. The surface area of the batch reactor is

$$A = \pi D^2 \tag{4.114}$$

and the volume is

$$V = \frac{\pi}{6} D^3 \tag{4.115}$$

the rate of reaction is evaluated using this expression:

$$r_{CO_2} = -k_0 e^{-\frac{k_1}{RT}} C_{CO_2} \tag{4.116}$$

where k_0 and k_1 are reaction constants experimentally evaluated as 0.0996 m s^{-1}, and 1.05 kJ mol^{-1}, respectively. R is the universal constant of ideal gases (J mol^{-1} K^{-1}). C_{CO_2} is the carbon dioxide concentration in the batch reactor (mol m^{-3}) and it is computed using this

$$C_{CO_2} = \frac{N_{CO_2}}{V} \tag{4.117}$$

Chapter 5: Results and Discussion

In this chapter, the results of the modeling of the three carbon capturing systems are presented and discussed. They each start with a base case to see the modeling results at a single operation point. Next, parametric studies are conducted on each system to evaluate their thermodynamic and exergoeconomic performances over ranges of operating conditions. Optimization studies are given to show the possible optimal operating conditions considering the overall exergy destruction rates and overall unit cost of products. The results of the experimental investigation mentioned earlier are provided and discussed later in this chapter.

5.1 Modeling results of system 1

This section discusses the results of the modeling of the first carbon capturing system described earlier. The first thing to discuss is the input of the parameters of the model used. These parameters are listed in Table 5.1. After inputting these values into the model of the system, the output parameters resulting from the model are presented in Table 5.2. There are some points to be outlined from the results shown in this table. Firstly, the hydrogen production rate of the PEM electrolyzer is 0.08663 kg h^{-1}, which is reasonable considering the power input to the electrolyzer. What is more, the heat losses of the electrolyzer are 1.594 kW, which is almost one-third of the power input to the electrolyzer.

Table 5.1: Input parameter values used for system 1 model.

Input parameter	**Value**
Air density	1.23 kg m^{-3}
Upstream wind stream	15 m s^{-1}
Swept area	6.88 m^2
PEM electrolyzer power input	5 kW
PEM electrolyzer operating temperature	313 K
Effective area of the cell	160 cm^2
Number of cells	12
PEM electrolyzer operating pressure	1000 kPa
Inlet water molar flow rate	0.1 kmol h^{-1}
ASR operating pressure	1000 kPa
ASR operating temperature	523 K
CO2CAPT operating pressure	101 kPa
CO2CAPT operating temperature	373 K
Separator efficiency	99%

As a result of these heat losses, the PEM electrolyzer energy and exergy efficiencies are reported to be 57.80%, and 48.50%, respectively. The nitrogen compressor requires 0.0377 kW which is computed from the simulation. This is small compared to what is supplied to the PEM electrolyzer because the mass flow rate of nitrogen is smaller compared to the water input and this compressor does not involve a chemical reaction, unlike other components in the system. Moving further down the system, the heat losses associated with the ammonia synthesis reactor and the CO_2 capture reactor are 0.3379 kW, and 1.022 kW, respectively. These are because the chemical reactions taking place are exothermic and the chemical products have lower heating values than the reactants. This system has very good CO_2 capture efficiency that is comparable to the traditional ammonia-based carbon capture systems proposed in the literature. One more point to be made from the results of this table is the energy requirement for capturing 1 kg of CO_2 is higher than the chilled ammonia process. This system requires almost 4.5 times more energy than the chilled ammonia process, but the present carbon capture system produces a valuable chemical commodity of ammonium bicarbonate at a rate of 2.2643 kg h^{-1}, which is orders of magnitude higher than the hydrogen produced by the PEM electrolyzer. Finally, the net investment cost of this carbon capturing system is reported from the exergoeconomic analysis is 0.122 \$ h^{-1}, and more interestingly is the cost of producing ammonium bicarbonate is very low, at 0.0185 \$ kg^{-1}, when compared to the market price which is \$0.25 per one kilogram of ammonium bicarbonate.

Table 5.2: Output parameter values resulted from system 1 model.

Output parameter	**Value**
Cell voltage	2.171 V
Current density	1.2 A cm^{-2}
Hydrogen production rate	0.08663 kg h^{-1}
PEM electrolyzer heat losses	1.594 kW
PEM electrolyzer energy efficiency	57.80%
PEM electrolyzer exergy efficiency	48.50%
$\dot{Q}_{ASR}$	0.3379 kW
$\dot{Q}_{CO2CAPT}$	1.022 kW
CO_2 capture efficiency	95.50%
Energy requirement for CO_2 capture	14.3 MJ kg^{-1} of CO_2 captured
Net investment cost rate	\$0.122 h^{-1}
Cost of producing ammonium bicarbonate using this system	\$0.0185 kg^{-1}

In addition, the thermodynamic state points of the carbon capture system are given in Table 5.3. Observing the mass flow rates of the different streams, it is noticed that the majority of the mass flow rate of the ammonium bicarbonate comes from the flue gases which contain CO_2 and the water input to the carbon capture reactor. Only 21.5% of the mass flow rate of the ammonium bicarbonate comes from the produced ammonia. This means that significant amounts of ammonium bicarbonate are produced, and CO_2 is captured using smaller amounts of ammonia and this directly reduces the energy requirements to produce hydrogen. The ratio of ammonium bicarbonate produced over hydrogen produced based on a mass basis is found to be 26.1. This is a huge ratio, and this means that 26 kg of ammonium bicarbonate can be produced using only 1 kg of hydrogen and the remaining mass comes from cheap and readily available chemical resources such as water, nitrogen, and CO_2 which is meant to be captured. Another point to be observed from this table is that the carbon capture reactor and the separator operate under moderate temperature and pressure levels which increases the feasibility and safety of this part of the system.

Table 5.3: Thermodynamic state points of system 1.

State #	Substance	Temperature (K)	Pressure (kPa)	Specific enthalpy (kJ kg^{-1})	Specific entropy (kJ kg^{-1} K^{-1})	Specific exergy (kJ kg^{-1})	Mass flow rate (kg h^{-1})
1	Nitrogen	298	100	0	0.00391	0	0.401
2	Nitrogen	619	1000	339	0.0892	313	0.401
3	Hydrogen	313	1000	215	-8.74	2840	0.0866
4	Ammonia	523	1000	-2180	-5.64	470	0.488
5	Ammonia	523	100	-2180	-4.52	135	0.488
6	Water	323	100	-15800	-8.72	4.67	1.80
7	Carbon dioxide	423	100	-8830	0.385	18.8	1.32
8	Ammonium bicarbonate+excess gases	373	100	-12400	-8.15	172	3.61
9	Excess gases	373	100	-13100	-1.90	460	1.35
10	Ammonium bicarbonate	373	100	-10700	-7.40	13.9	2.26

One part of the exergy analysis of this carbon capture system is calculating and comparing the exergy destruction rates of each component of the system. Table 5.4 shows the exergy destruction rate of each component, and it can be noticed that the highest destruction rate is found at the PEM electrolyzer with a value of 1.99 kW. This is an order of magnitude than all the other components of the system. This shows the need to improve the efficiency of the PEM electrolyzer to reduce the energy requirements to capture CO_2 more efficiently

in terms of exergy utilization. Looking at the carbon capture exergy destruction rate, it is only a small fraction of the heat losses reported earlier. This means that the heat losses at this reactor have very low energy quality and are not worth reducing or recovering.

Table 5.4: Exergy destruction rates of the components of system 1.

Component	**Exergy destruction rate (kW)**
PEM electrolyzer	1.99
Nitrogen Compressor	0.00283
Ammonia synthesis reactor	0.0243
Valve	0.0453
Carbon capture reactor	0.0264
Separator	0.164

5.1.1 Parametric studies of system 1

Moreover, some parameters of the system model are varied to see how the system behaves under these changing conditions. To begin with, Figure 5.1 presents the polarization curve of the PEM electrolyzer and it shows the initial nonlinear increase in the cell voltage as the current density increases. This entire curve agrees very well with the experimental modeling results of PEM electrolyzers [110,111,113]. Next, the power density of the electrolyzer versus the current density is shown in Figure 5.2. The relation is clearly linear throughout the range of current density from 0 to a little over 1.4 A cm^{-2}. This power density is for a single cell in the PEM electrolyzer, and the values range from 0 to 3.12 W cm^{-2}. This is expected because as more power is supplied to the electrolyzer, a higher current is going through the cells, while the cell voltage remains almost constant and does not change as rapidly as the power input. One real application for this plot is guiding the PEM electrolyzer designers on how choosing the effective area of the cells and their numbers could affect the power density inside the cells. A direct result of this increase in current density is the increase in hydrogen production rate as evident in Figure 5.3. The figure shows that as the power input increases from 0 to 6 kW, the hydrogen production rate increases almost linearly from 0 to 50 moles per hour. A real application for this plot is controlling the hydrogen production rate to reach desired levels by controlling the power input when operating this electrolyzer. Even though it seems reasonable for the hydrogen production rate to increase linearly, it is not sufficient to keep the PEM electrolyzer energy and exergy efficiencies steady.

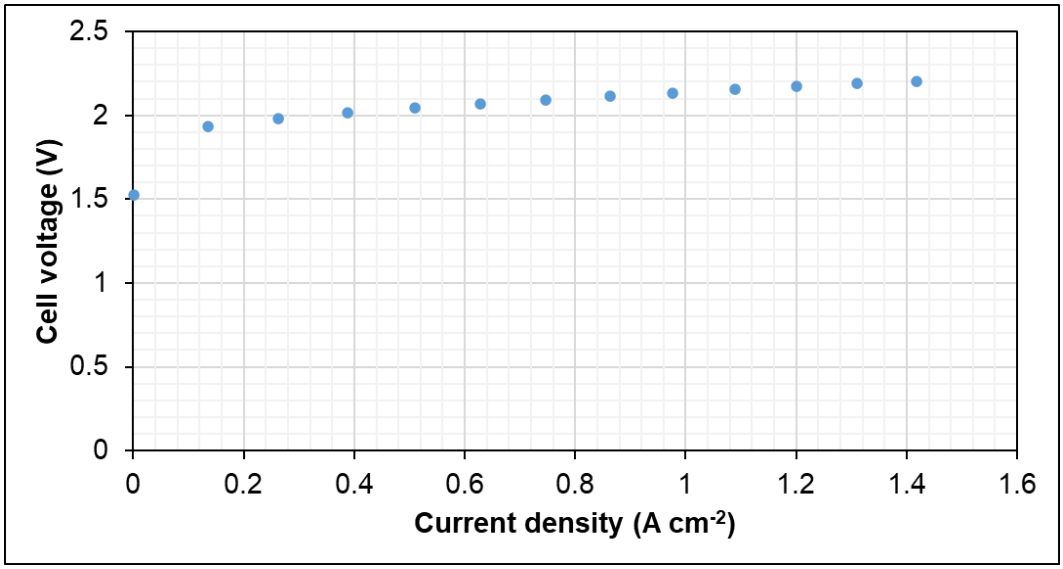

Figure 5.1: Polarization curve for the PEM electrolyzer.

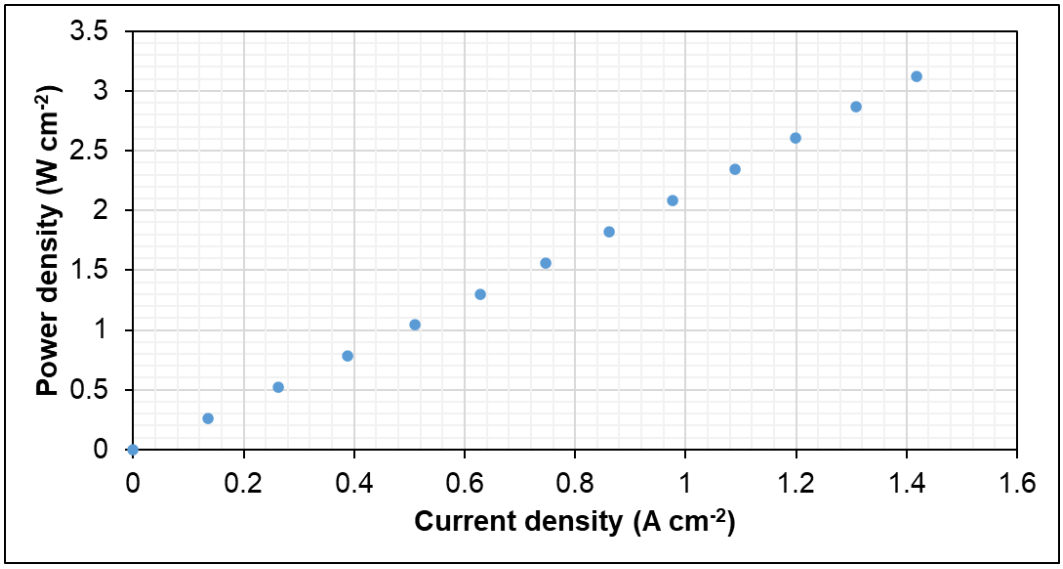

Figure 5.2: Power density curve against current density for the PEM electrolyzer.

Looking at Figure 5.4, the PEM electrolyzer energy efficiency drops nonlinearly but slow from a value of 0.644 at a current density of 0.135 A cm^{-2}, down to a value of 0.564 at a current density of 1.42 A cm^{-2}. Similarly, in Figure 5.5, the PEM electrolyzer exergy efficiency drops nonlinearly but slow from a value of 0.540 at a current density of 0.135 A cm^{-2}, down to a value of 0.473 at a current density of 1.42 A cm^{-2}. These results show that it is possible to achieve higher thermodynamic efficiencies by simply increasing the area of the cells used in the PEM electrolyzer to reduce the current density which in turn will increase the performance of the electrolyzer. The last two mentioned graphs have a real

engineering application. These can be used when designing the effective area of the PEM electrolyzer in order to reduce the energetic and exergetic losses at the component, not only for this system but for understanding the general behavior when producing hydrogen using a renewable energy source. All of the above parametric studies show the validation of the PEM electrolyzer model programmed using ASPEN Custom Modeler and offer some insights into the operation of this exergy destructive thermal component.

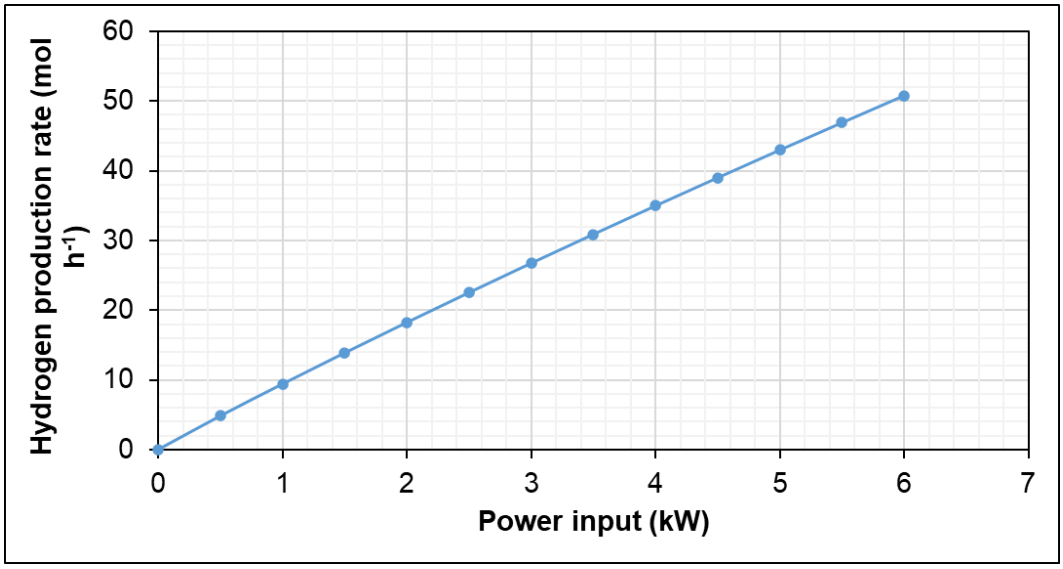

Figure 5.3: Hydrogen production rate curve against power input for the PEM electrolyzer.

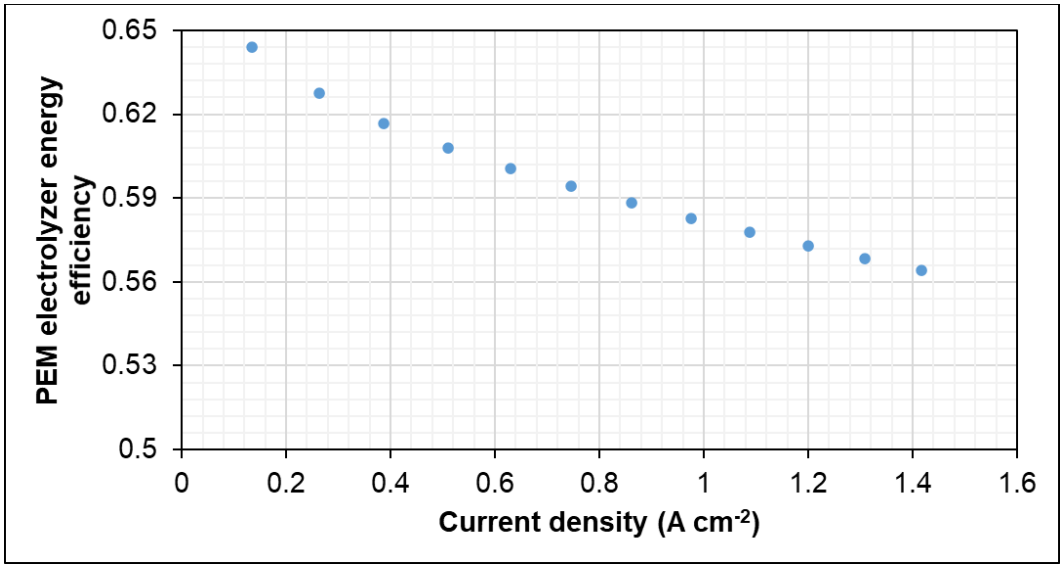

Figure 5.4: PEM electrolyzer energy efficiency against current density.

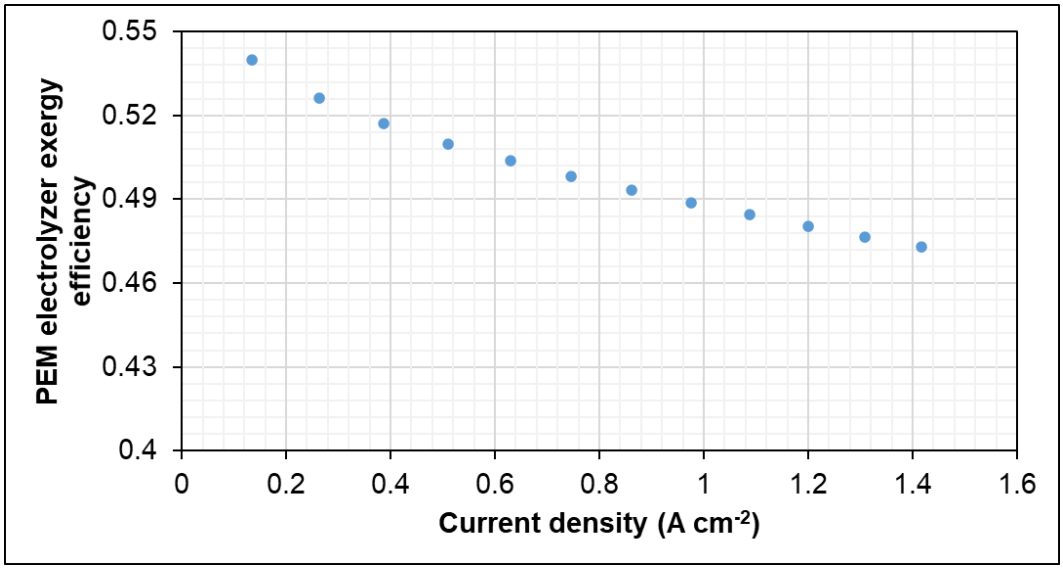

Figure 5.5: PEM electrolyzer exergy efficiency against current density.

In addition, Figure 5.6 presents the effects of wind turbine power input on the production of ammonium bicarbonate production rate in this system. As the power input goes from 0.5 to 6 kW, the ammonium bicarbonate production rate goes up linearly from 3.22 to 33.85 mol h^{-1} for the case of 100% conversion ratio of ammonia in the carbon capture reactor. This linear relation shows that the more power is supplied to the system, the more hydrogen is produced as it has been seen before, the more ammonium bicarbonate is produced linearly. As expected, the lower the conversion ratio, the lower production of ammonium bicarbonate and it seems that the drop is nonlinear. Another important factor to study is the CO_2 capture rate against varying wind turbine power input and this is shown in Figure 5.7. The CO_2 capture rate increases linearly as the power input increases from 0.5 to 6 kW for all the cases. The slopes of the CO_2 capture rate and the ammonium bicarbonate production rate are very similar due to the fact that the molar ratio in the chemical reaction in the carbon capture reactor is unity. Note that the mass flow rates of the water and carbon dioxide entering this reactor have been increased slightly over the values in the reference case to maximize the use of hydrogen. The previous two plots are used in the real application of understanding how variations in the supplied wind turbine power due to weather conditions could affect the rates of carbon dioxide capture and ammonium bicarbonate production. This data could help engineers design an electric storage system to make sure this carbon capturing system meets the minimum requirements for these two rates, namely carbon capturing, and ammonium bicarbonate production.

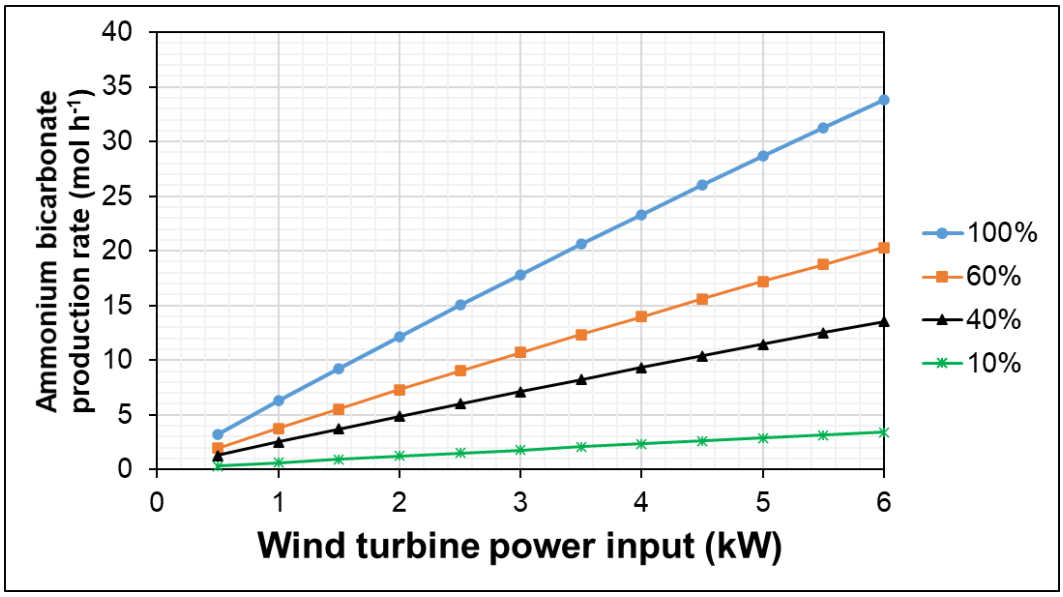

Figure 5.6: Ammonium bicarbonate production rate against wind turbine power input. The percentages represent the ammonia conversion ratio in the carbon capture reactor.

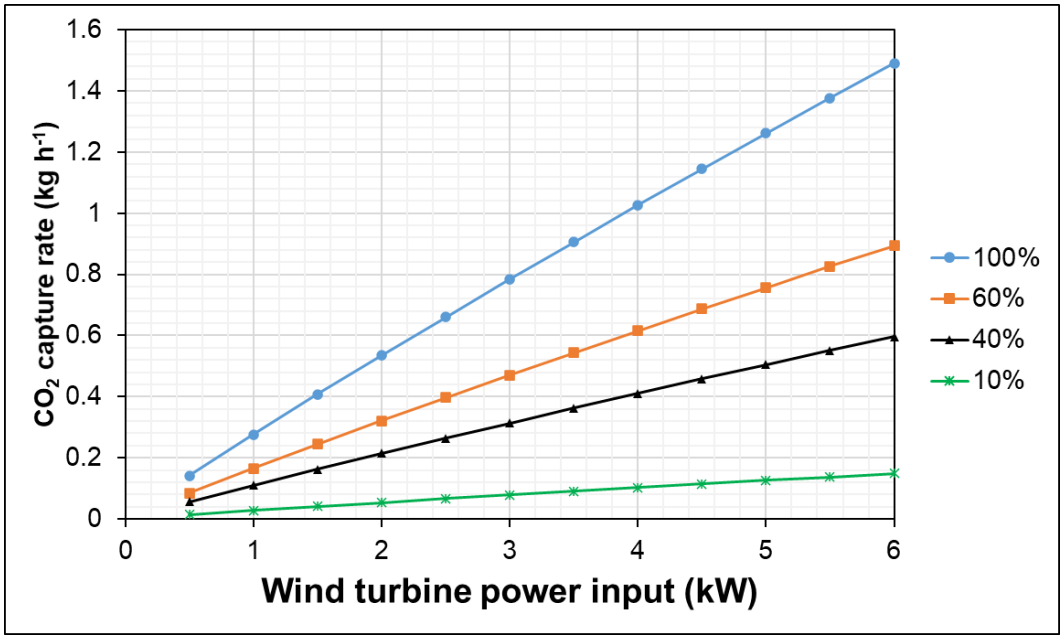

Figure 5.7: CO_2 capture rate against wind turbine power input. The percentages represent the ammonia conversion ratio in the carbon capture reactor.

Figure 5.8 shows how increasing the wind turbine power input affects the energy requirements for CO_2 capture in this present system. Since the carbon capture increases linearly with power input as shown earlier, the energy requirement has a nonlinear relation where the energy requirements increase from 12.7 to 14.5 MJ kg^{-1} of CO_2 captured as the power input of the wind turbine goes from 0.5 to 6 kW for the 100% case. It seems from the figure that the relation is mostly nonlinear from the range of 0.5 to 3 kW, beyond this

point the relationship between the energy requirement and the power input is mostly linear. Another interesting point to make is that, for the 10% case, the energy requirements increased dramatically compared to all the other cases to reach very undesirable values of around 140 MJ kg^{-1} of CO_2 captured. This is mainly because there is an inverse relationship between the energy requirements and the rate of CO_2 capturing as indicated in equation (8). This relation shows that there could be accelerated increases in energy requirements when the rate of CO_2 is very low. The real application of this plot can be how the conversion ratio at the carbon capturing reactor can significantly the design and rating of this system. It shows the importance of increasing the conversion ratio through the use of catalysts and increasing the residence time at this batch reactor to reduce the energy requirements of the carbon capturing process. Designers can be guided by such a plot to be motivated to increase the conversion ratio to at least a percentage of 40% to avoid extremely high energy requirements as shown in the figure.

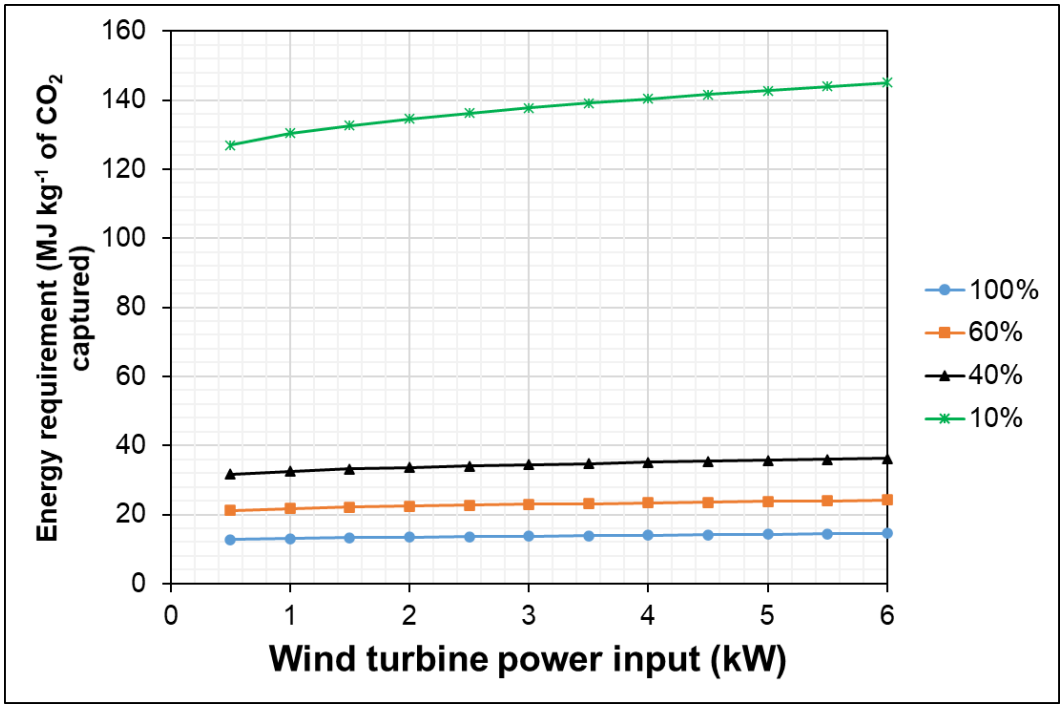

Figure 5.8: Energy requirement for CO_2 capture against wind turbine power input. The percentages represent the ammonia conversion ratio in the carbon capture reactor.

5.2 Modeling results of system 2

This section will present and discuss the results of the simulation work on the second carbon capturing integrated system. The first part presents a base case of operating this

integrated system and shows its results at this specific operating point. Next, parametric studies are conducted on the integrated system to observe its behavior under various operating conditions.

Before going to the results of the base case, Table 5.5 outlines the input quantities of the model used for this thermodynamic study on the present integrated system. After inserting these values into the thermodynamic model described earlier, some main output values are produced and listed in Table 5.6. Some interesting findings have resulted. To start with, a geothermal fluid mass flow rate of 49.6 kg s^{-1} is required to capture carbon dioxide and convert it to ammonium bicarbonate. The carbon dioxide produced by the SOFC subsystem is 0.353 kg s^{-1} and the ammonia production rate is 0.137 kg s^{-1}. This ammonia production rate consumes 4,390 kW of renewable electric power produced by the double-flash geothermal power plant. The estimated energy requirement for CO_2 capture is found to be 12.4 MJ kg^{-1} of CO_2 which is lower than the reported value from the first carbon capturing system where a value of 14.3 MJ kg^{-1} of CO_2 is reported, and it used a carbon capturing unit that involves the use of a proton-exchange membrane electrolyzer and a Haber-Bosch ammonia synthesis reactor. This sequence of processes for ammonia production to perform carbon capturing seems to require more energy to operate compared to the present carbon capturing unit in this work. However, a good rate of ammonium bicarbonate production is made from this process which is at a value of 0.634 kg s^{-1}. This could be sold to compensate for the operating costs of running this renewable-based carbon capturing unit.

Regarding the SOFC subsystem, a large amount of thermal energy exists in the integrated system at the SOFC with a rate of 4,130 kW as heat losses. This shows that increasing the SOFC energy efficiency is paramount to improving the electric power of the integrated system. The electric power output of the SOFC is 2,010 kW. Using waste heat management cycles, like the gas turbine and the SRC, the net electric power output of the SOFC subsystem increases to 2,270 kW, which is an increase of almost 13%. This multigeneration system produces space heating and freshwater at a rate of 87.2 kW, and 0.419 kg s^{-1}, respectively. The energy and exergy efficiencies of the SOFC subsystem are 44.5%, and 50.5%, respectively. These agree very well with previous results from by

Ghorbani et al. [39] where their energy and exergy efficiencies are reported to be 49.42% and 46.83%, respectively, for their developed SOFC system.

Table 5.7 lists the thermodynamic state points resulted from the model of the integrated system. This table contains some useful information about the integrated system. For instance, the geothermal fluid drawn from the geothermal reservoir has a high amount of thermal energy represented as enthalpy with a value of 1,037 kJ kg^{-1}. It is also noticed that flash chamber 1 and separator 1 produce a relatively good amount of steam from the geothermal fluid which is 9.33 kg s^{-1}, which represents 18.8% of the total geothermal fluid drawn from the ground. For flash chamber 2 and separator 2, these devices produce a much smaller percentage of steam compared to the first set at a percentage of 1.66%. This is a natural behavior of typical double-flash geothermal power plants, but an optimization study of these ratios to increase power production and efficiency of this plant is required. Next, looking at the ammonium bicarbonate reactor and its production of the useful chemical, it is seen that 0.6341 kg s^{-1} is produced of ammonium bicarbonate and this production consumes 0.1365 kg s^{-1} of ammonia produced by the electrochemical ammonia synthesizer. This means that most of the mass of the ammonium bicarbonate is composed of the added water at the mixer and the carbon dioxide stream at state 28. On a mass basis, carbon dioxide is captured almost 2.6 times more than the amount of ammonia produced needed to capture the carbon dioxide. From a materials consumption perspective, this is efficient. The geothermal fluid going to the ammonium bicarbonate reactor contains very small amounts of carbon dioxide in it in the range of 3000 - 4000 ppm. This means that this fluid contributes almost 0.000267 kg s^{-1} which is very small compared to the amount of ammonium bicarbonate produced by the SOFC-based multigeneration subsystem. The main reason behind this is that this geothermal power plant is utilizes reinjection which significantly reduces CO_2 emissions to nearly zero. Table 5.8 shows the molar basis composition of some of the exhaust gases that leave the SOFC and the WGSMR-afterburner components. Firstly, stream 22 has a high percentage of water and this is expected as steam is added at the anode side of the SOFC. Methane has electrochemically reacted to some carbon dioxide, but not completely due to the fact that there are some percentages of hydrogen (15%) and carbon monoxide (4%) as shown in the table. These two constituents will react in the WGSMR to produce hydrogen and then permeate it to the

other side to react with the remaining oxygen. Secondly, oxygen on the cathode side of the SOFC reduced significantly from 21% down to 7.54% in terms of molar percentages because lots of it got permeated to the anode side to electrochemically react with methane.

Table 5.5: Input values used for system 2 model.

Input quantity	**Value**
Temperature of geothermal reservoir	513 K
Faradaic efficiency (*FE*) of EAS	40%
Constant overpotential of EAS (*V*)	0.8 V
Operating temperature of EAS	293 K
Operating pressure of EAS	101 kPa
Excess air factor (λ)	1.1
Air compressor compression ratio (r_p)	8
SOFC energy efficiency	46.8%
Space desired temperature	296 K
Ambient temperature	293 K
Ambient pressure	101 kPa

Table 5.6: Output values produced from system 2 model.

Output quantity	**Value**
Mass flow rate of geothermal fluid	49.6 kg s^{-1}
Electric power output of T1	4,110 kW
Electric power output of T2	278 kW
Electricity supplied to EAS ($\dot{W}_{EAS}$)	4,390 kW
Ammonia production rate	0.137 kg s^{-1}
Carbon dioxide mass flow rate	0.353 kg s^{-1}
Ammonium bicarbonate production rate	0.634 kg s^{-1}
Energy requirement for CO_2 capture	12.4 MJ kg^{-1} of CO_2
Geothermal energy for CO_2 capture	58.7 MJ kg^{-1} of CO_2
Geothermal exergy for CO_2 capture	29.3 MJ kg^{-1} of CO_2
Electric power output of SOFC	2,010 kW
Heat losses by the SOFC	4,130 kW
Electric power output of T3	772 kW
Electric power output of T4	44.1 kW
Net electric power produced by SOFC subsystem	2,270 kW
Space heating supplied	87.2 kW
Freshwater production rate	0.419 kg s^{-1}
Energy efficiency of SOFC subsystem	44.5%
Exergy efficiency of SOFC subsystem	50.5%

One of the aims of performing an exergy analysis on this integrated system is to find the locations of the highest exergy destruction rates in order to identify where improvements in this integrated system can be made. Looking at Figure 5.9, it is seen that the highest exergy destruction rate occurs at T1 with a value of 5,370 kW, and it is followed by the SOFC with a value of 4,970 kW. The main reason for the high value of exergy destruction

rate of T1 is not the isentropic efficiency but the high mass flow rate going through this component compared to the SOFC as evident in Table 5.7.

Table 5.7: Thermodynamic state points of system 2.

State #	Material	Temperature (K)	Pressure (kPa)	Specific enthalpy (kJ kg^{-1})	Specific entropy (kJ kg^{-1} K^{-1})	Specific exergy (kJ kg^{-1})	Mass flow rate (kg s^{-1})
1	Water	513	3,338	1,037	2.7	248	49.55
2	Water	425	500	1,037	2.794	220.7	49.55
3	Water	425	500	2,748	6.821	751.5	9.325
4	Water	319	10	2,307	7.281	175.5	9.325
5	Water	425	500	640.1	1.86	97.62	40.23
6	Water	416.8	400	640.1	1.861	97.3	40.23
7	Water	416.8	400	2,738	6.896	719.5	0.6681
8	Water	319	10	2,323	7.33	176.8	0.6681
9	Water	416.8	400	604.7	1.776	86.79	39.56
10	Water	319	10	618.6	1.987	38.93	49.55
11	Water	293.2	101	-13,431	10.44	0	0.2167
12	Nitrogen	293.2	101	-5.188	6.819	0	0.1124
13	Oxygen	293.2	101	-4.566	6.393	0	0.1927
14	Ammonia	293.2	101	-2,708	11.28	22,506	0.1365
15	Aqueous ammonia	393.3	101	-8,020	11.45	28.48	0.281
16	Ammonium bicarbonate	373	101	-10,663	11.95	13.9	0.6341
17	Natural gas	293.2	808	-4,661	10.5	52,296	0.086
18	Natural gas	1295	808	-788.2	15.67	2,672	0.086
19	Air	293.2	101	293.6	5.68	0	1.623
20	Air	630.1	808	639.1	5.864	291.4	1.623
21	Air	990.1	808	1,035	6.36	542.1	1.623
22	Exhaust gases	1,130	808	-9,561	10.72	1,104	0.8041
23	Exhaust gases	1,110	808	889.8	7.608	653	1.099
24	CO_2+water	1,238	808	-9,841	9.583	1,116	0.7939
25	Exhaust gases	1,824	808	994.2	8.596	1,446	1.109
26	Exhaust gases	1,305	101	298.2	8.786	694.7	1.109
27	Water	373	101	-13,281	10.9	17.37	0.4407
28	CO_2	373	101	-8,875	5.052	8.22	0.3532
29	Exhaust gases	1,070	101	-2.096	8.533	468.7	1.109
30	Exhaust gases	585.1	101	-581.8	7.815	99.46	1.109
31	Exhaust gases	368.2	101	-823.2	7.3	9.003	1.109
32	Exhaust gases	296.1	101	-901.8	7.063	0.01801	1.109
33	Water	363.2	1,500	378.2	1.192	31.68	0.1
34	Water	580.9	1,500	3,055	6.95	1,021	0.1
35	Water	363.1	70	2,614	7.355	461.1	0.1
36	Water	363.1	70	376.8	1.192	30.2	0.1
37	Water	345.8	35	304.3	0.9877	17.65	0.09618
38	Water	345.8	35	2,631	7.715	372	0.09618
39	Sea water	303	100	98.71	0.344	0.14	4.615
40	Brine	329.2	100	214.4	0.7015	6.2	0.8671
41	Cooling water	312.4	100	156	0.532	1.3	3.326
42	Freshwater	329.2	100	235.2	0.783	6.432	0.4198
43	Steam	1,295	808	-11,270	12.57	1,537	0.1935
44	Water	500	101	-13,038	11.46	96.27	0.1445
45	Water+CO_2	319	10	618.6	1.987	38.93	0.496

Table 5.8: Molar basis composition of the exhaust gases of system 2.

Exhaust gases stream #	O_2	N_2	H_2O	H_2	CO	CO_2
22	0	0	65%	15%	4%	16%
23	7.54%	92.5%	0	0	0	0
24	0	0	75.3%	0	0	24.7%
25	2.12%	10.1%	87.8%	0	0	0

The SOFC has a high rate of exergy destruction that can be improved by operating this device at lower temperatures [161]. Other components with high exergy destruction rates are the ammonium bicarbonate reactor (2,130 kW), electrochemical ammonia synthesizer (1,770 kW), and Flash chamber 1 (1,356 kW). Flash chamber 1 has a high rate of exergy destruction compared to flash chamber 2 is due to the pressure drops in these devices and the amount of steam generated in both of them. A lot more steam is generated in flash chamber 1 and this causes the high exergy destruction rate. This ratio of steam generation which was discussed earlier reduces the exergy destruction rate in turbine 2 at a value of 363 kW in a similar manner as flash chamber 2. Another interesting component that has a high exergy destruction rate is condenser 1. This component ejects water and heat to purify the carbon dioxide for carbon capture. This device can be improved exergetically by utilizing the water and the heat lost for some useful purposes. The exergy destruction rate can be reduced from its current value of 875 kW down to a much lower value. Such improvements in the integrated system can enhance the overall energy efficiency and utilization of the energy and materials that flow through it.

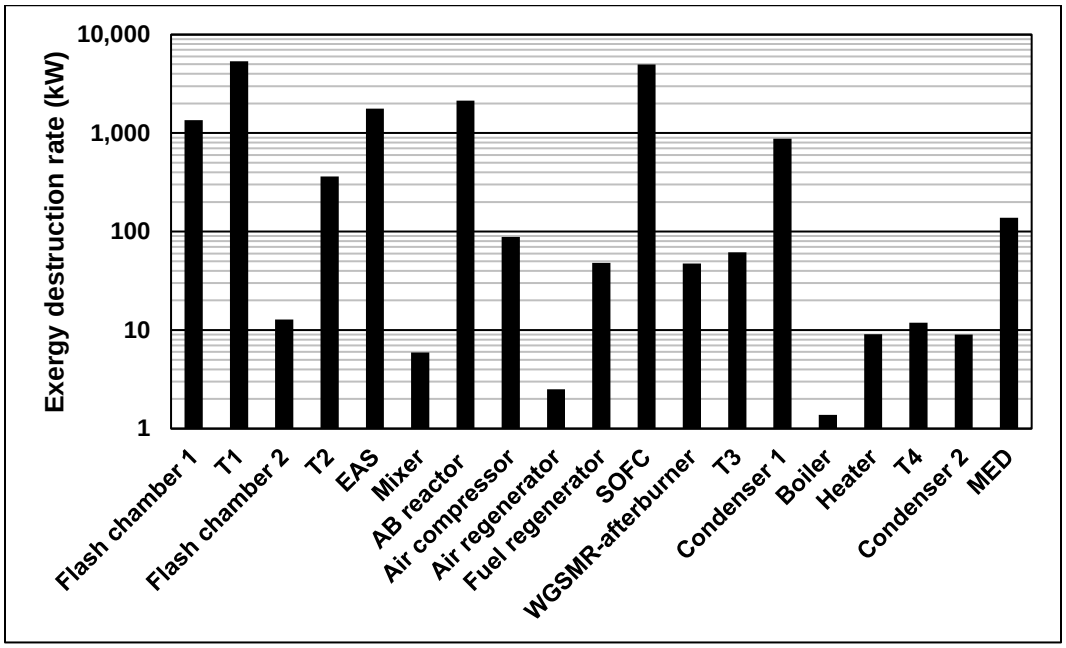

Figure 5.9: A logarithmic plot of the exergy destruction rate of the thermal components in system 2. A logarithmic scale is used for clarity to show the smaller values better.

The results of the exergoeconomic analysis at this base case are shown in the tables below. Table 5.9 lists the exergy rate, unit cost and cost rates of all the material streams in the

integrated system. A few state points are worth noting here. State point 3, steam entering turbine 1, has a cost rate of 1.02E-02 $ s^{-1}, while state point 7, steam entering turbine 2, has a cost rate of 7.05E-04 $ s^{-1}. Even though, these two state points have similar unit costs, they vary in their cost rate due to their exergy rates that are indicative of their potential to produce useful work. Turbine 1 does produce more power than turbine 2 which can justify the increased cost rate in state point 3. Another point state that needs to be discussed is 14 which is the ammonia stream produced by the electrochemical ammonia synthesizer. The cost rate of this stream is 1.96E-02 $ s^{-1}. This is higher than the geothermal fluid cost rate by 22.5%. State point 16 is the stream of ammonium bicarbonate and it has a 2.02E-02 $ s^{-1}, and this higher than ammonia by only 3.06%. However, the difference between the unit costs of state points 1 and 16 is more than 3 orders of magnitude. More importantly, the cost of production of ammonium bicarbonate is 0.0319 $ kg^{-1}, while the market price for food grade ammonium bicarbonate ranges between 0.2 and 0.25 $ kg^{-1} [162]. This means that the cost of producing ammonium bicarbonate is 12.7% of the market price of this chemical commodity. This indicates that this integrated system is economically feasible to produce monetary value when the carbon dioxide is captured and converted to ammonium bicarbonate.

Table 5.10 shows the exergy rates, unit costs, and cost rates associated with heat transfer and work streams in every component of the integrated system. The first point to make from these results is that the unit cost of work produced by turbine 1 (4.21E-06 $ kJ^{-1}) is less than the unit cost of work produced by turbine 2 (7.07E-06 $ kJ^{-1}). The other power producing components have similar unit costs for their respective work streams. For the SOFC, the unit cost is 4.17E-06 $ kJ^{-1}. For turbine 3, it is 5.92E-06 $ kJ^{-1}. For turbine 4, it is 1.30E-05 $ kJ^{-1}. The highest unit cost of work is the one in turbine 4 and this is because it cost much more to produce electric power from waste heat than to use fuel combustion directly. Condenser 1 has a heat transfer cost rate of 1.95E-02 $ s^{-1} which is high, and this means that this heat transfer should be utilized as a useful output for some application, if possible, to compensate for the high value of this cost rate. One parameter that is computed from this analysis is the overall exergy destruction rate of the integrated system and it is calculated to be 1.73E+03 kW.

Table 5.9: Exergy rate, unit cost, and cost rates of all the state points in system 2.

State No.	Exergy rate (kW)	Unit cost ($ kJ^{-1})	Cost rate ($ s^{-1})
1	1.23E+04	1.30E-06	1.60E-02
2	1.09E+04	1.46E-06	1.60E-02
3	7.01E+03	1.46E-06	1.02E-02
4	1.64E+03	1.46E-06	2.39E-03
5	3.93E+03	1.46E-06	5.74E-03
6	3.91E+03	1.47E-06	5.74E-03
7	4.81E+02	1.47E-06	7.05E-04
8	1.18E+02	1.47E-06	1.73E-04
9	3.43E+03	1.47E-06	5.03E-03
10	1.93E+03	3.94E-06	7.60E-03
11	0.00E+00	0.00E+00	0.00E+00
12	0.00E+00	3.41E-05	0.00E+00
13	0.00E+00	6.37E-06	0.00E+00
14	3.07E+03	6.37E-06	1.96E-02
15	8.00E+00	2.45E-03	1.96E-02
16	8.82E+00	2.29E-03	2.02E-02
17	4.30E+03	4.00E-06	1.72E-02
18	2.26E+02	7.89E-05	1.79E-02
19	0.00E+00	0.00E+00	0.00E+00
20	4.73E+02	7.11E-06	3.36E-03
21	8.84E+02	5.06E-06	4.48E-03
22	8.88E+02	2.29E-05	2.03E-02
23	7.18E+02	5.27E-06	3.78E-03
24	8.86E+02	2.30E-05	2.03E-02
25	1.60E+03	2.63E-06	4.21E-03
26	7.71E+02	2.63E-06	2.02E-03
27	7.66E+00	7.76E-05	5.94E-04
28	2.90E+00	7.76E-05	2.25E-04
29	5.23E+02	2.63E-06	1.37E-03
30	1.10E+02	2.63E-06	2.88E-04
31	9.98E+00	2.63E-06	2.62E-05
32	2.00E-02	2.63E-06	5.24E-08
33	3.17E+00	4.97E-06	1.58E-05
34	1.01E+02	3.18E-06	3.22E-04
35	4.59E+01	3.18E-06	1.46E-04
36	3.02E+00	3.18E-06	9.59E-06
37	0.00E+00	0.00E+00	0.00E+00
38	3.56E+01	3.85E-06	1.37E-04
39	0.00E+00	0.00E+00	0.00E+00
40	5.35E+00	1.24E-05	6.61E-05
41	4.30E+00	1.24E-05	5.31E-05
42	2.69E+00	1.24E-05	3.32E-05
43	2.94E+02	3.18E-06	9.33E-04
44	1.39E+01	3.18E-06	4.42E-05

Table 5.10: Exergy rate, unit cost, and cost rates of all heat transfer and work streams in system 2, and exergy destruction rates of all components. NA for not applicable.

Components	**Heat transfer exergy stream (kW)**	**Work exergy stream (kW)**	**Unit cost of heat transfer exergy ($ kJ^{-1})**	**Unit cost of work exergy ($ kJ^{-1})**	**Heat transfer cost rate ($ s^{-1})**	**Work cost rate ($ s^{-1})**	**Exergy destruction rate (kW)**
Flash chamber 1	NA	NA	NA	NA	NA	NA	1.36E+03
Separator 1	NA	NA	NA	NA	NA	NA	1.00E-04
Turbine 1 (T1)	NA	4.11E+03	NA	4.21E-06	NA	1.73E-02	5.37E+03
Flash chamber 2	NA	NA	NA	NA	NA	NA	1.28E+01
Separator 2	NA	NA	NA	NA	NA	NA	1.00E-04
Turbine 2 (T2)	NA	2.78E+02	NA	7.07E-06	NA	1.96E-03	3.63E+02
Electrochemical ammonia synthesizer (EAS)	6.28E+00	4.39E+03	6.37E-06	4.39E-06	4.00E-05	1.93E-02	1.77E+03
Mixer	NA	NA	NA	NA	NA	NA	5.91E+00
Ammonium bicarbonate (AB) reactor	0.00E+00	NA	2.29E-03	NA	0.00E+00	NA	2.13E+03
Air compressor	NA	5.61E+02	NA	5.92E-06	NA	3.32E-03	8.79E+01
Air regenerator	NA	NA	NA	NA	NA	NA	2.50E+00
Fuel regenerator	NA	NA	NA	NA	NA	NA	4.80E+01
Solid-Oxide Fuel Cell (SOFC)	0.00E+00	2.01E+03	4.17E-06	4.17E-06	0.00E+00	8.40E-03	4.97E+03
WGSMR-afterburner	NA	NA	NA	NA	NA	NA	4.74E+01
Turbine 3 (T3)	NA	7.72E+02	NA	5.92E-06	NA	4.57E-03	6.18E+01
Condenser 1	2.52E+02	NA	7.76E-05	NA	1.95E-02	NA	8.75E+02
Boiler	NA	NA	NA	NA	NA	NA	1.38E+00
Heater	8.83E-01	NA	5.39E-05	NA	4.76E-05	NA	9.08E+00
Turbine 4 (T4)	NA	4.37E+01	NA	1.30E-05	NA	5.68E-04	1.19E+01
Condenser 2	NA	NA	NA	NA	NA	NA	9.01E+00
Pump	NA	1.48E-01	NA	1.30E-05	NA	1.93E-06	1.00E-04
Multi-Effect Desalination (MED)	NA	NA	NA	NA	NA	NA	1.38E+02

Table 5.11 presents the total investment cost rate and the performance parameters for the exergoeconomic analysis of each component in the integrated system. To begin with, the components with the highest total investment cost rates, in order, are turbine 1 (9.44E-03 $ s^{-1}), SOFC (9.24E-03 $ s^{-1}), turbine 3 (2.38E-03 $ s^{-1}), and turbine 2 (1.43E-03 $ s^{-1}).

The total investment cost rate of the integrated system is 2.42E-02 \$ s^{-1}. Next, considering the exergy destruction cost rates of the components in this integrated system, the highest value is found to be in the SOFC which is 3.92E-01 \$ s^{-1}. Even though SOFC does not have the highest exergy destruction rate of all the components, it has the highest cost rate associated with exergy destruction and this is due to the unit cost of fuel for SOFC. Interestingly, the second highest exergy destruction cost rate is identified to be in condenser 1 at a value of 2.01E-02 \$ s^{-1}. This is further evidence that utilizing the heat and water rejected by this component is necessary to improve the exergetic performance of the integrated system. Lastly, looking at the exergoeconomic factors calculated here, the overall exergoeconomic factor for the entire system is 2.97%. Also, turbine 1 and turbine 2 have exergoeconomic factors of 54.60% and 72.91%, respectively. SOFC has it at a percentage of 2.30%, which indicates that lowering the exergy destruction cost rate is needed to improve the performance of the component in terms of exergoeconomics.

5.2.1 Parametric studies of system 2

Three parametric studies are considered in this subsection, namely geothermal fluid temperature, faradaic efficiency, and natural gas mass flow rate, to see how the integrated system and the carbon capturing unit behave under various operating conditions. To begin with, Figure 5.10 presents the effects of the geothermal fluid temperature on the geothermal energy for CO_2 capture. As the temperature of the fluid goes up from 428 to 593 K, the geothermal energy absorbed from the reservoir drops asymptotically from 535 to 29.9 MJ. This means that choosing a geothermal reservoir with a higher temperature is critical to the performance of the carbon capturing unit. To further confirm this point, it is seen from the figure that the geothermal exergy, required to capture one kilogram of CO_2, drops significantly from 121 down to 26.9 MJ. Also, the geothermal fluid mass flow rate drawn from the reservoir drops nonlinearly from a value of 458 to 25.0 kg s^{-1}. This dramatic drop in the mass flow rate can reduce the piping sizes, as well as the sizes of turbines and other components for the double-flash geothermal power plant. This is later is used to provide electricity to the EAS for ammonia production and carbon capture. The geothermal reservoir temperature becomes a less important factor in determining the energy required for carbon capturing as the temperature becomes higher than 480 K. This is because the

carbon capturing unit does not change much of its performance over the range between 480 K and 600 K. This wide range of temperature level of the geothermal reservoir gives this integrated system the advantage of being flexible, regarding the installation location of the double-flash geothermal power plant.

Table 5.11: Total investment cost rates and exergoeconomic performance parameters for each component in system 2 and the overall system.

Components	**Total investment cost rate ($ s^{-1})**	**Unit cost of fuel ($ kJ^{-1})**	**Unit cost of product ($ kJ^{-1})**	**Exergy destruction cost rate ($ s^{-1})**	**Exergoeconomic factor**
Flash chamber 1	0.00E+00	1.30E-06	1.46E-06	1.76E-03	0.00%
Separator 1	3.65E-10	1.46E-06	1.46E-06	5.06E-15	100.00%
Turbine 1 (T1)	9.44E-03	1.46E-06	4.21E-06	7.85E-03	54.60%
Flash chamber 2	0.00E+00	1.46E-06	1.47E-06	1.87E-05	0.00%
Separator 2	3.41E-10	1.47E-06	1.47E-06	0.00E+00	100.00%
Turbine 2 (T2)	1.43E-03	1.47E-06	7.07E-06	5.32E-04	72.91%
Electrochemical ammonia synthesizer (EAS)	3.53E-04	4.39E-06	6.37E-06	7.77E-03	4.35%
Mixer	0.00E+00	9.55E-06	2.45E-03	5.64E-05	0.00%
Ammonium bicarbonate (AB) reactor	3.41E-04	2.53E-03	2.29E-03	5.38E+00	0.01%
Air compressor	4.05E-05	5.92E-06	7.11E-06	5.21E-04	7.22%
Air regenerator	2.73E-05	2.63E-06	5.06E-06	6.02E-06	81.92%
Fuel regenerator	8.54E-06	2.63E-06	7.89E-05	1.27E-04	6.32%
Solid-Oxide Fuel Cell (SOFC)	9.24E-03	7.89E-05	4.17E-06	3.92E-01	2.30%
WGSMR-afterburner	4.30E-04	2.29E-05	2.63E-06	1.09E-03	28.38%
Turbine 3 (T3)	2.38E-03	2.63E-06	5.92E-06	1.62E-04	93.63%
Condenser 1	6.54E-06	2.30E-05	7.76E-05	2.01E-02	0.03%
Boiler	4.48E-05	2.63E-06	3.18E-06	3.61E-06	92.55%
Heater	2.14E-05	2.63E-06	5.39E-05	2.38E-05	47.34%
Turbine 4 (T4)	3.92E-04	3.18E-06	1.30E-05	3.74E-05	91.30%
Condenser 2	8.24E-07	3.18E-06	3.85E-06	2.85E-05	2.81%
Pump	4.24E-06	1.30E-05	4.97E-06	4.84E-10	99.99%
Multi-Effect Desalination (MED)	1.54E-05	3.85E-06	1.24E-05	5.30E-04	2.82%
Integrated system	2.42E-02	4.58E-05	2.38E-03	7.90E-01	2.97%

Figure 5.11 displays how the power outputs of the turbines in the geothermal power plant are changing with increasing the geothermal fluid temperature. As the temperature

increases from 428 to 593 K, the power output of turbine 1 increases asymptotically from 1,250 to 4,280 kW. In contrast, the power output of turbine 2 decreases in the opposite direction of turbine 1 from a value of 3,140 kW at a temperature of 428 K, down to 105 kW at a temperature of 593 K. This is evidence that using a double flash feature in a geothermal power plant becomes less necessary as the geothermal fluid temperature increases. So, increasing the geothermal fluid temperature by choosing a proper geothermal reservoir can reduce the capital and operation costs of this integrated system. This is because it is possible to simplify the power plant from double flash down to a single flash geothermal power plant. Looking deeper at the double-flash geothermal power plant, it is noticed that the geothermal reservoir temperature affects the ratio of power generation of turbine 1 and turbine 2 in the power plant. This ratio needs to be optimized by reducing costs and increasing total power generation to be supplied to the carbon capturing unit using two factors, namely the geothermal reservoir temperature (choosing a proper location), and through controlling the pressure drops across the two flash chambers. From the figure, most of the power generation supplied to the EAS is provided by turbine 1 when the geothermal reservoir temperature is higher than 570 K. This indicates that adjusting the pressure drops across flash chamber 1 needs to be optimized better, so that turbine 2 can produce more power.

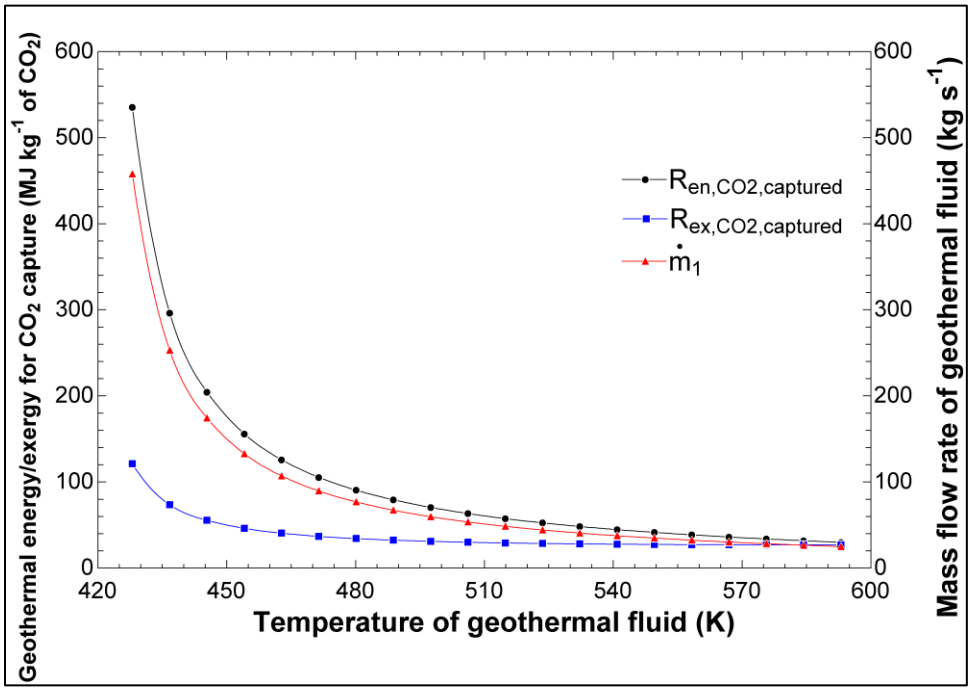

Figure 5.10: A plot of the geothermal energy/exergy for CO_2 capture and the geothermal fluid mass flow rate versus geothermal fluid temperature.

Figure 5.12 shows how the geothermal fluid temperature affects the exergy destruction rates of the turbines and flash chambers in the double-flash geothermal power plant. There is a strong correlation between the exergy destruction rate of turbine 1 and its electric power output. The exergy destruction rate of turbine 1 increases asymptotically from 1,630 kW at a geothermal fluid temperature of 428 K to as high as 5,590 kW when the temperature of the fluid is 593 K. However, the exergy destruction rate of turbine 2 has an inverse relation with the geothermal fluid temperature. In addition, looking at the exergy destruction rate of flash chamber 1, it increases linearly from 28.8 to 2,520 kW as the fluid temperature increases in the mentioned range. The slope of this increase is huge. On the other hand, the exergy destruction rate of flash chamber 2 is insignificant compared to turbines 1,2, and flash chamber 1 as seen in the figure. Looking deeper at this exergy analysis of the two turbines and flash chambers, it is noticed that flash chamber 1 exergy destruction rate increases as the temperature of the geothermal fluid increase in a linear manner, and this indicates that operating this component at higher temperature becomes a lot less efficient exergetically. One way to limit this linear increase in exergy destruction rate of flash chamber 1 is to control the pressure drop across this component. This will produce more steam while the temperature remains relatively high. This control method can reduce the total exergy destruction rates of all the four components in the geothermal power plant, namely turbine 1, turbine 2, flash chamber 1, flash chamber 2. Reducing the total exergy destruction rates directly means increasing the exergy efficiency of the entire integrated system.

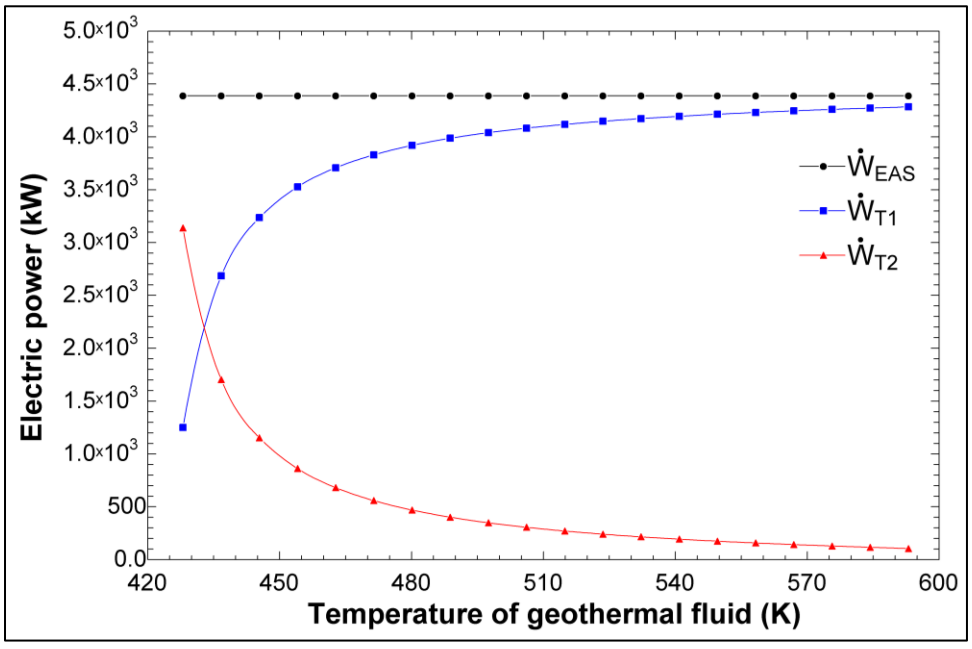

Figure 5.11: A plot of electric power values for turbines 1,2, and EAS versus geothermal fluid temperature.

Figure 5.13 shows a second parameter that is being changed to see how the system behaves. This parameter is the faradaic efficiency of the EAS. As the faradaic efficiency is increased from 14% to 60%, these values have been reached experimentally in [136,163,164], the geothermal energy and exergy required for capturing one kilogram of CO_2 reduce nonlinearly from 168, and 83.8 down to 39.1, and 19.6 MJ, respectively. Furthermore, the geothermal fluid mass flow rate, needed to supply electric power to the EAS, reduces similarly from a value of 142 kg s^{-1}, at a faradaic efficiency of 14%, to a value of 33.0 kg s^{-1}, at a faradaic efficiency of 60%. This shows that the EAS faradaic efficiency has significant effects on the design and performance of the carbon capturing unit as well as the double-flash geothermal power plant. When looking deeper at how the faradaic efficiency of EAS affects the geothermal energy and exergy requirements of carbon capturing, it is seen from the figure that increasing the faradaic efficiency of the device beyond the point of 40% does not reduce the energy and exergy requirements for carbon capturing by a huge difference. There is a good reason for limiting increasing this faradaic efficiency because increasing it to 60% without getting any energy and exergy reduction benefits will make operating this integrated system unnecessarily expensive. This is because increasing the faradaic efficiency directly increases the capital and operating costs of EAS.

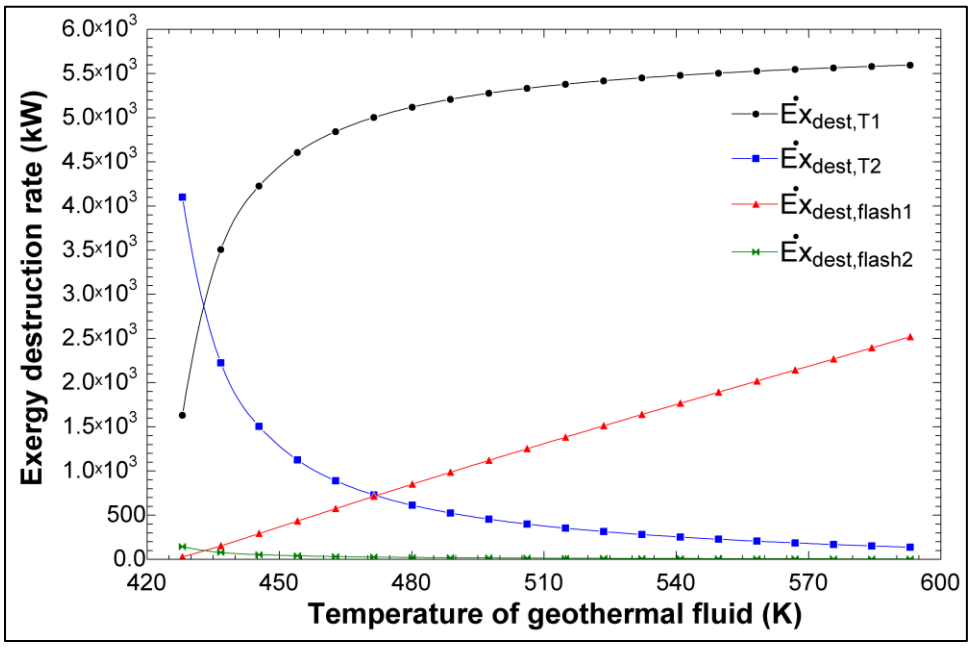

Figure 5.12: A plot of exergy destruction rates for turbines 1,2, and flash chambers 1,2 versus geothermal fluid temperature.

Figure 5.14 presents the main reason behind the nonlinear behaviors in the previous figure. As the faradaic efficiency of EAS increases, the power demands by the EAS to produce the same rate of ammonia for carbon capturing are reduced nonlinearly from 12,500 to 2,930 kW. Similarly, the exergy destruction rate reduces with increasing faradaic efficiency from a value of 9,920 to 309 kW. Also, it is observed that the gap between the power demand by the EAS and the exergy destruction rate of EAS becomes wider as the faradaic efficiency increases.

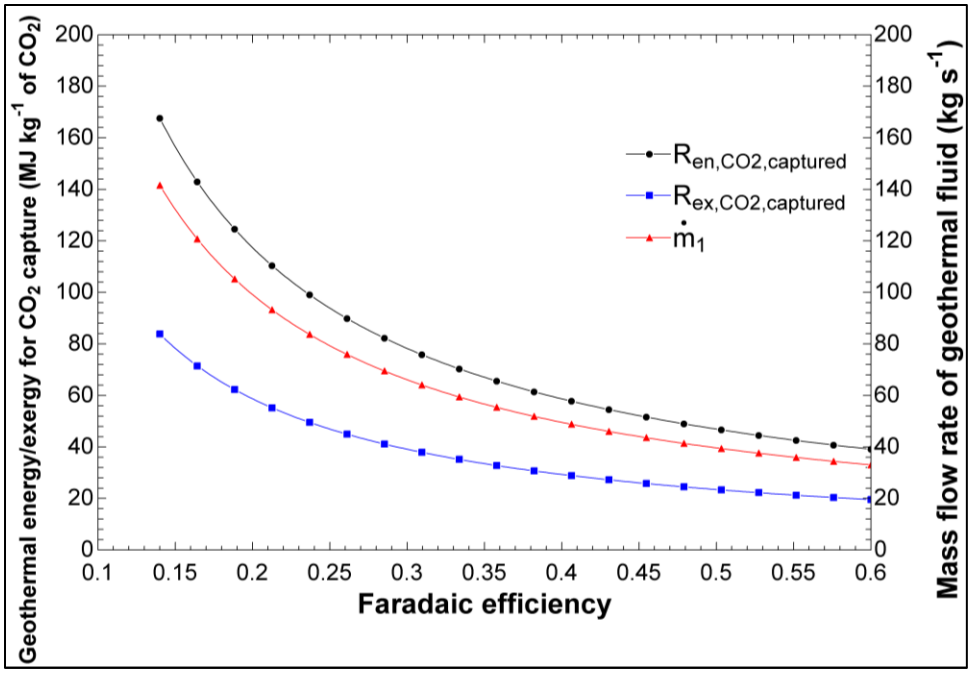

Figure 5.13: A plot of the geothermal energy/exergy for CO_2 capture and geothermal fluid mass flow rate versus faradaic efficiency.

In Figure 5.15, the energy requirement for CO_2 capture decreases significantly as the faradaic efficiency increases from a value of 35.5 MJ kg^{-1} of CO_2 when the faradaic efficiency is 14%, down to 8.28 MJ kg^{-1} of CO_2 when the faradaic efficiency is 60%. It seems that even when the faradaic efficiency is quite high, the energy requirements for CO_2 capture are more than double higher than a typical chilled ammonia process, however, this present carbon capturing unit is not only for carbon capturing but also produces a useful chemical commodity, that is ammonium bicarbonate. It is interesting to investigate the economics of comparing these two methods of carbon capturing in future work. Giving these two figures a deeper look, increasing the faradaic efficiency of EAS reduces the power consumption of this ammonia-producing device, which means it will cost less to

operate this integrated system. This is because the size of the geothermal power plant can be reduced, and the capital costs of this power plant are also reduced. However, the capital and operating costs of EAS will increase to maintain high faradaic efficiency. This trade-off between reducing the costs of the geothermal power plant and increasing the costs of EAS needs to be studied further to optimize the performance and costs of this integrated system. Other factors to be considered are the carbon capturing tax savings and ammonium bicarbonate product value which can make it more favorable to increase the faradaic efficiency of EAS. One way to reduce the costs is to receive electric power from the grid during off-peak hours to reduce the power production of the geothermal power plant which means reducing capital and operating costs.

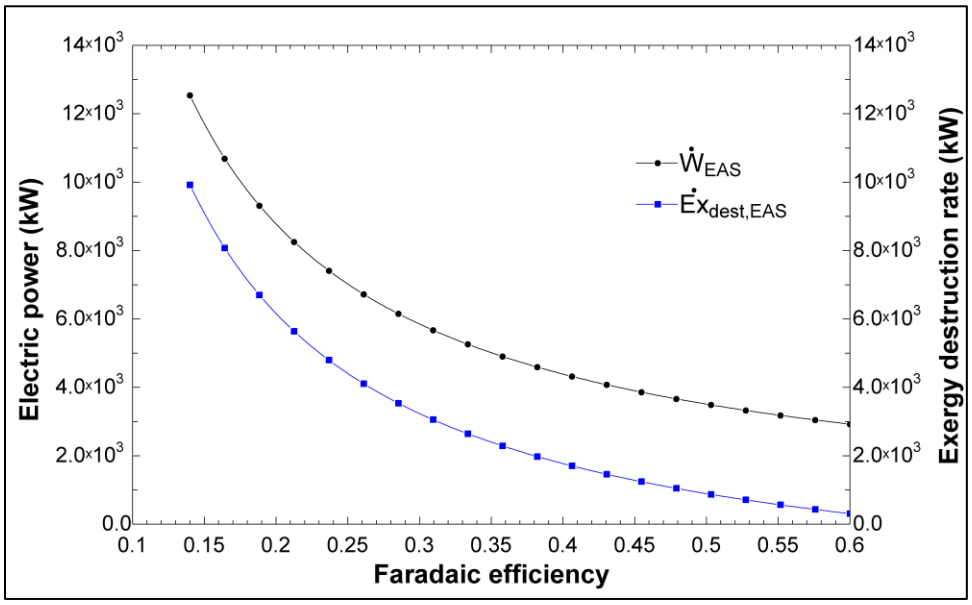

Figure 5.14: A plot of electric power values and exergy destruction rate for electrochemical ammonia synthesizer versus faradaic efficiency.

In Figure 5.16, the mass flow rate of the fuel injected into the SOFC subsystem is increased to observe its effects on the ammonia and ammonium bicarbonate production rates. It seems from the figure that both the ammonia and ammonium bicarbonate production rates are increased linearly, and the slopes of these two trends are similar. The ammonium bicarbonate production rate has a steeper slope than the ammonia production rate. As the mass flow rate of natural gas increases from 0.04 to 0.4 kg s^{-1}, the ammonium bicarbonate production rate increases from 0.295 to 2.95 kg s^{-1}. Similarly, the ammonia production rate increases at a rate from 0.0635 to 0.635 kg s^{-1} over the same range of natural gas mass flow

rate. In Figure 5.17, two other parameters are observed to change as the mass flow rate of natural gas input increases, which are the energy and exergy efficiencies of the SOFC subsystem. Both of these efficiencies increase asymptotically. The energy and exergy efficiencies increase from 0.442 and 0.504 to 0.462 and 0.512, respectively, as the mass flow rate of natural gas increase from 0.04 to 0.4 kg s^{-1}.

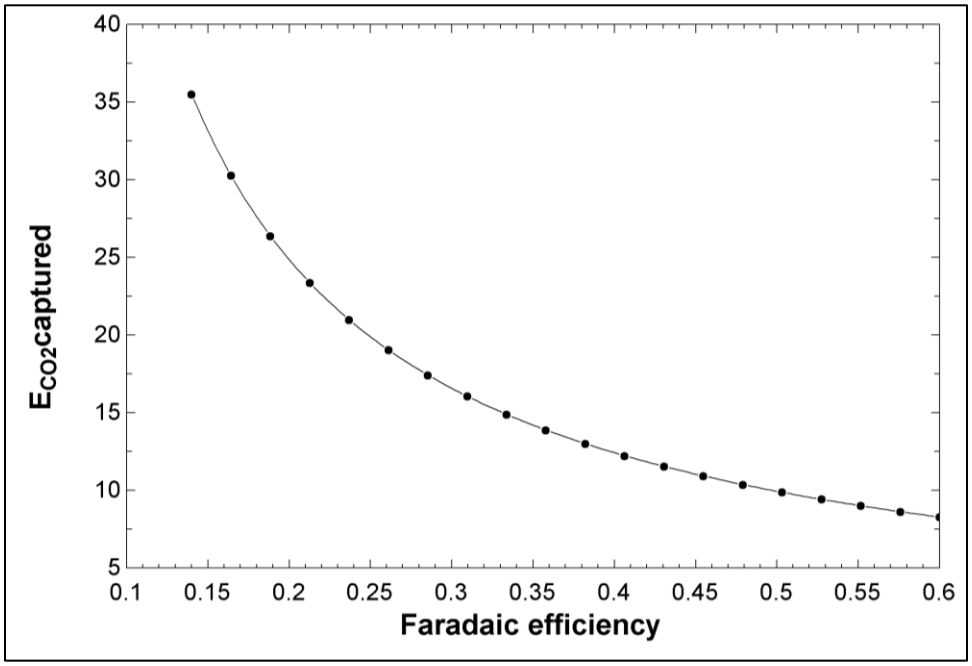

Figure 5.15: A plot of energy requirement for CO_2 capture versus faradaic efficiency.

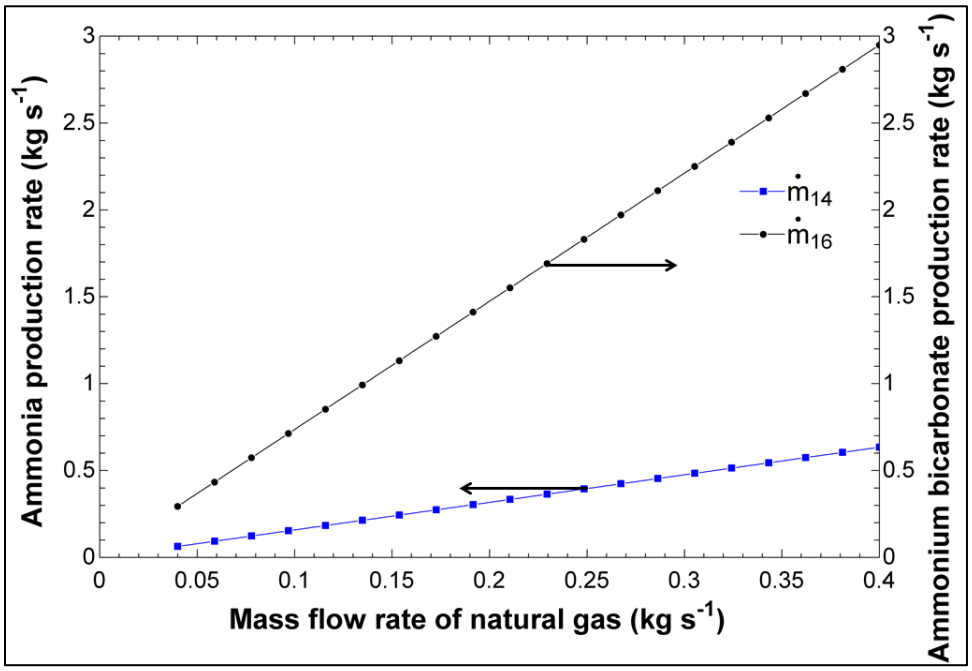

Figure 5.16: A plot of ammonia and ammonium bicarbonate production rates versus mass flow rate of natural gas.

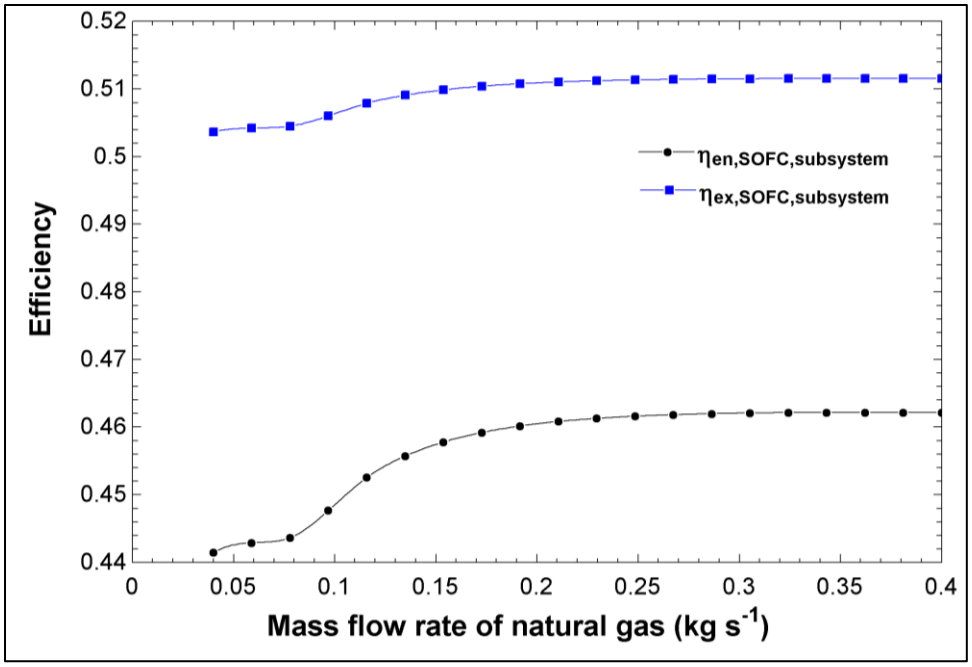

Figure 5.17: A plot of SOFC subsystem energy and exergy efficiencies versus mass flow rate of natural gas.

Now, discussions regarding the parametric studies conducted on the present integrated system are mentioned. The exergoeconomic performance parameters for the overall integrated system and some major components are analyzed here as some operating conditions are changed parametrically. In Figure 5.18, the effects of changing the geothermal fluid temperature on the overall exergy destruction rate and the total investment cost rates are observed. As the temperature of the geothermal fluid supplied to the double-flash geothermal power plant increases from 428 to 593 K, the overall exergy destruction rate goes up linearly from a value of 16075 kW to 18427 kW. Increasing the geothermal fluid temperature reduces the total investment cost rate of turbine 2 at a faster rate than how it increases the cost rate of turbine 1, and this is the reason for the overall decrease in the overall investment cost rate of the integrated system. This means that as the geothermal fluid temperature increases, it is more economical to use a single-flash geothermal power plant to supply electricity to the carbon capturing unit.

Figure 5.19 shows the effects of the geothermal fluid temperature on the unit costs of product for the overall system, for turbine 1, and turbine 2. Some interesting behaviors are shown for these unit costs. To start with, the overall unit cost of product has a parabolic curve opened upward. It reaches a minimum at a temperature of 480 K with a value of 2.364×10^{-3} \$ kJ^{-1}. As the temperature increases beyond 480 K, the overall unit cost of

products increases nonlinearly to reach a value of 2.466×10^{-3} \$ kJ^{-1}. Since the overall exergy destruction rate and the overall unit cost of product both increase beyond the temperature level of 480 K, it seems that it is not desirable to operate this double-flash geothermal power plant at a higher temperature for both performance and economic reasons.

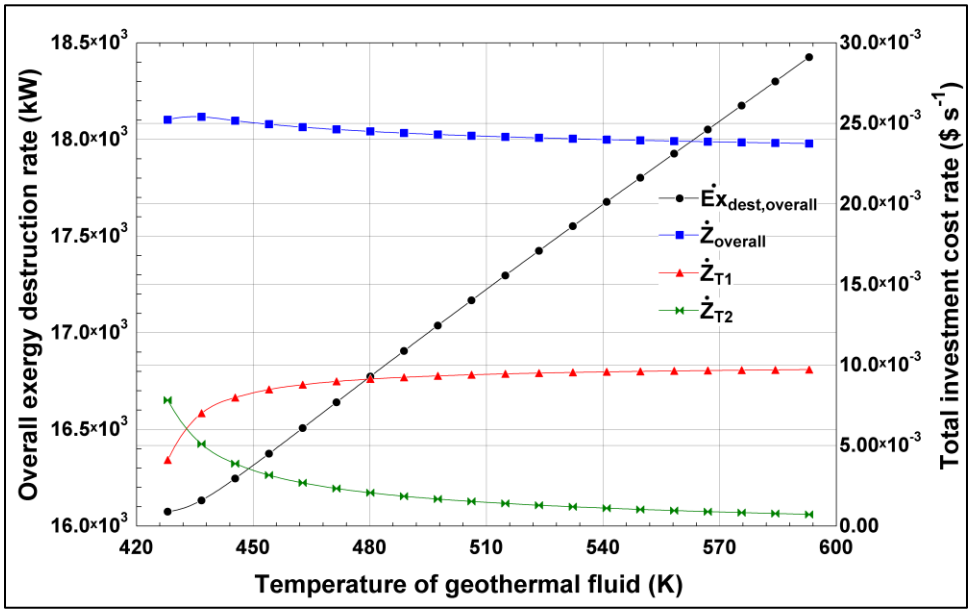

Figure 5.18: Effects of geothermal fluid temperature on the overall exergy destruction rate and the total investment cost rates of the integrated system, turbine 1, and turbine 2.

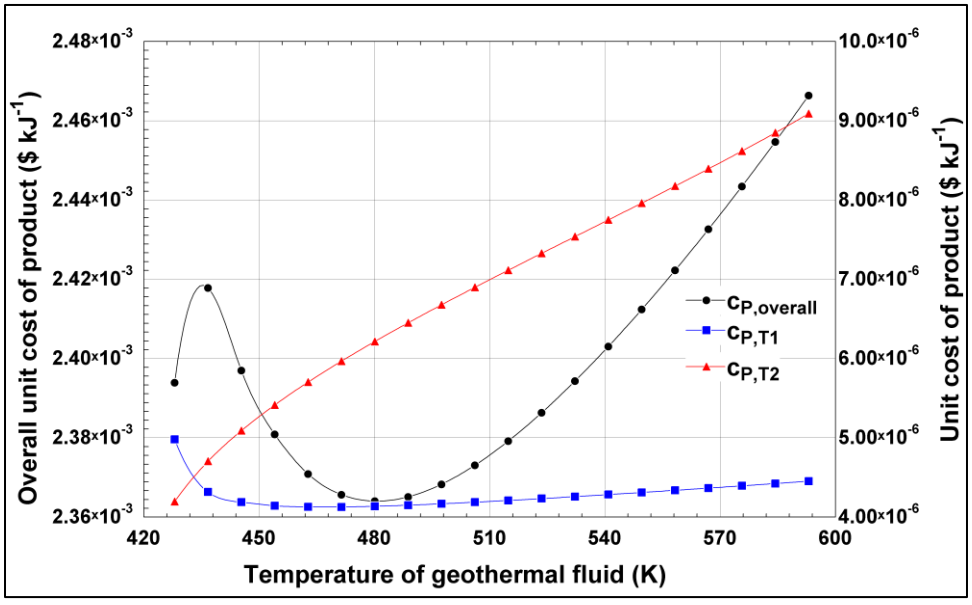

Figure 5.19: Effects of geothermal fluid temperature on the unit cost of products of the integrated system, turbine 1, and turbine 2.

Figure 5.20 investigates the effects of the geothermal fluid temperature on the overall exergy destruction rate cost rate and the exergy destruction cost rates of turbines 1 and 2. The overall exergy destruction cost rate rises with rising temperature from a value of 0.7355 \$ s^{-1} to 0.8431 \$ s^{-1} as the temperature goes from 428 to 593 K. This is because, as shown in previously, the overall exergy destruction rate increases significantly with rising temperature of the geothermal fluid. Another interesting trend shown in this figure is the sharp drop in the exergy destruction cost rate of turbine 2. At 428 K, its value is 5.352×10^{-3} \$ s^{-1}, and it gets reduced, when the temperature is 593 K, to a value of 0.230×10^{-3} \$ s^{-1}. This is drop of more than 23 times the original value.

Figure 5.21 displays the effects of this geothermal fluid temperature on the overall exergoeconomic factor, as well as the exergoeconomic factors of turbine 1 and turbine 2. Opposite behaviors of the exergoeconomic factors of these two turbines are present in this plot. As the temperature level rises, the exergoeconomic factor of turbine 1 reduces almost linearly, while the exergoeconomic factor of turbine 2 rises nonlinearly at the beginning, then linearly. These two trends are mainly caused by the changes in the investment cost rates and the exergy destruction cost rates of these two turbines. Looking at the overall exergoeconomic factor of the integrated system, it drops from a value of 3.32% down to 2.74% as the geothermal fluid temperature increases from 428 to 593 K.

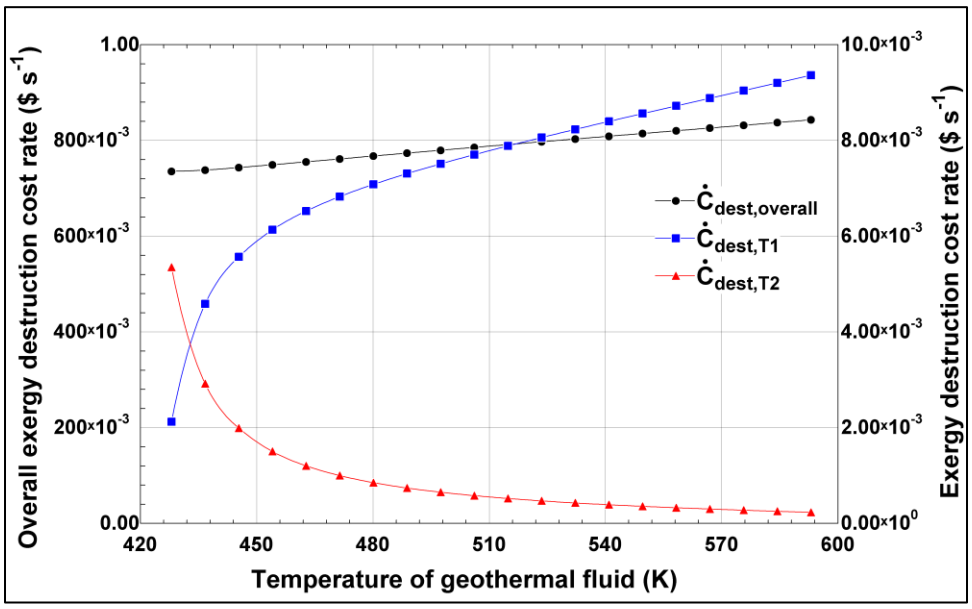

Figure 5.20: Effects of geothermal fluid temperature on the exergy destruction cost rates of the integrated system, turbine 1, and turbine 2.

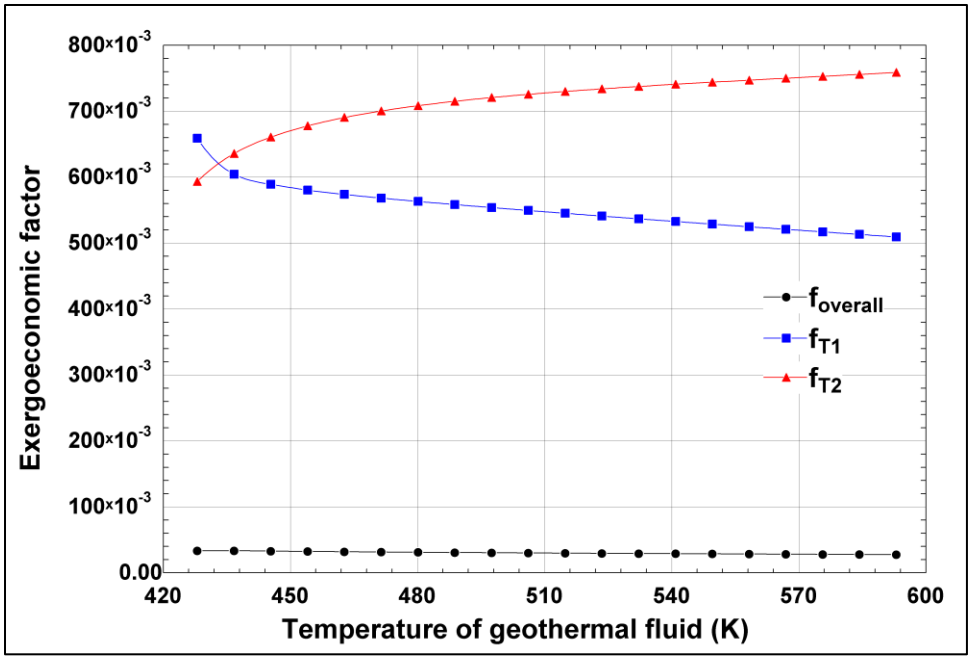

Figure 5.21: Effects of geothermal fluid temperature on exergoeconomic factors of the integrated system, turbine 1, and turbine 2.

Figure 5.22 shows a different parameter that is changed to observe the exergoeconomic behavior of this integrated system, which is the faradaic efficiency at the electrochemical ammonia synthesizer. As the faradaic efficiency of the EAS increases 14% to 60%, the overall exergy destruction rate decreases dramatically and nonlinearly from a high value of 38.61×10^{3} kW to a value of 13.44×10^{3} kW. This is obvious and expected since the higher the efficiency of the EAS, the lower the exergy destruction rate that would be in this component which is one of the most energy consuming components in the integrated system. Next, the overall investment cost rate of the integrated system also follows a similar trend of the exergy destruction rate. The cost rate decreases significantly, and this is due to three components, namely EAS, turbine 1, and turbine 2. These are strongly related because the electric power supplied by these two turbines is consumed by the EAS. The less power the EAS requires, the less power is generated by the turbines, which means lower total investment costs.

Figure 5.23 presents how the faradaic efficiency affects the unit cost of product of the overall integrated system, and the ammonium bicarbonate reactor, and the EAS. The overall unit cost of product drops by a large amount as the faradaic efficiency increases. The drop is from 5.50×10^{-3} \$ kJ^{-1} to as low as 1.75×10^{-3} \$ kJ^{-1}. This is a reduction of almost

4.5 times. This shows the importance of this component on not only the exergetic performance of the integrated system, but the costs of the integrated system, too. Both the ammonia and the ammonium bicarbonate unit costs of product reduce in a similar trend as that of the overall unit cost of product, which means that these two chemical commodities are the main drivers for the overall unit cost of products reductions.

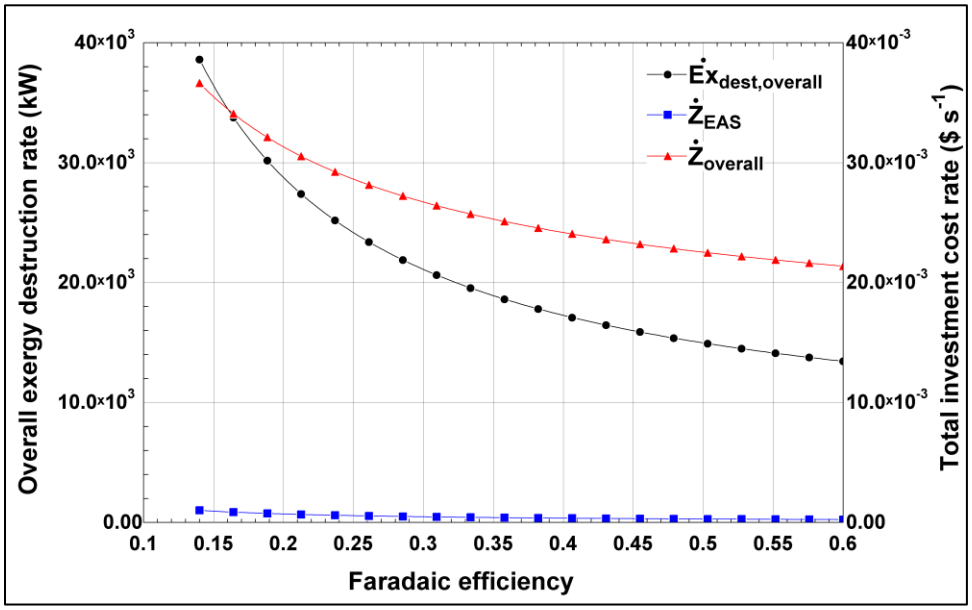

Figure 5.22: Effects of faradaic efficiency on the overall exergy destruction rate and the total investment cost rates of the integrated system, and EAS.

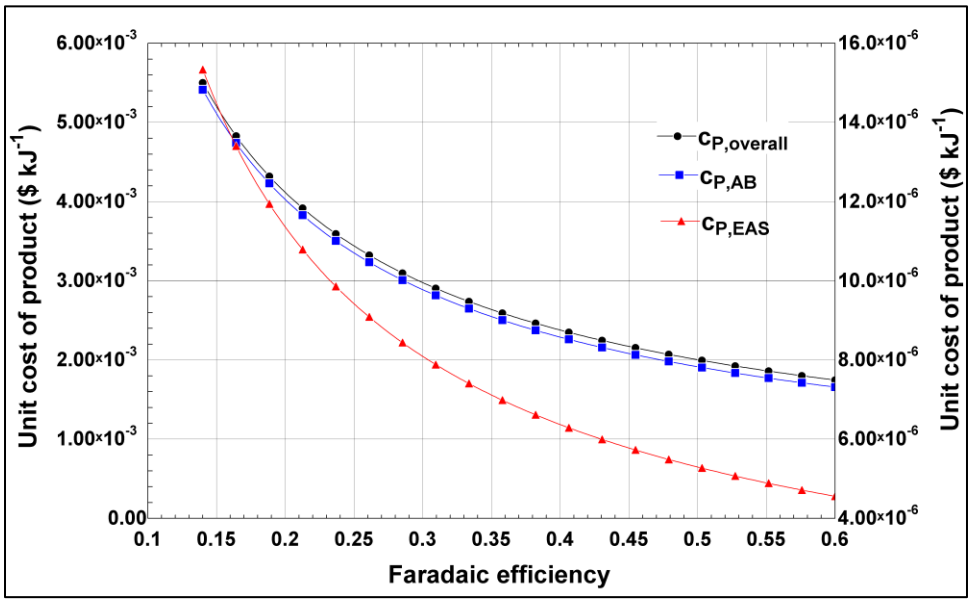

Figure 5.23: Effects of faradaic efficiency on the unit cost of products of the integrated system, and EAS.

Figure 5.24 is a plot of the effects of the faradaic efficiency on the cost rates associated with the exergy destruction rates of the overall integrated system and the EAS component. Both of these cost rates deceases in nonlinear manner and dramatically from 1.766 and 0.0369 \$ s^{-1} down to 0.615 and 0.00145 \$ s^{-1}, respectively, as the faradaic efficiency increase from 14% to 60%. It is clear from the values that the drop in the exergy destruction cost rate of EAS is much more tremendous than the overall integrated system. One reason for this is the fact that the EAS is only a part of the integrated system and other components do not have the same amount of drop in their exergy destruction cost rates as that of EAS.

Figure 5.25 confirms this last point of how the dramatic changes in the EAS only affects the overall system at a lower rate, although the effects of EAS are present and clear. This figure shows the exergoeconomic factors of the overall integrated system and EAS versus the faradaic efficiency. There is an exponential increase in the exergoeconomic factor of EAS as the faradaic efficiency rises. Its magnitude is enhanced from 2.67% up to 14.0%. However, the overall exergoeconomic factor is not affected exponentially, rather linearly and it goes from a value of 2.03% to 3.36%. This difference between the responses to the changes in faradaic efficiency are expected since not all the components in the integrated system respond equally to the EAS and the rise of the overall exergoeconomic factor is slowed by the unaffected components, such as SOFC, and turbine 3.

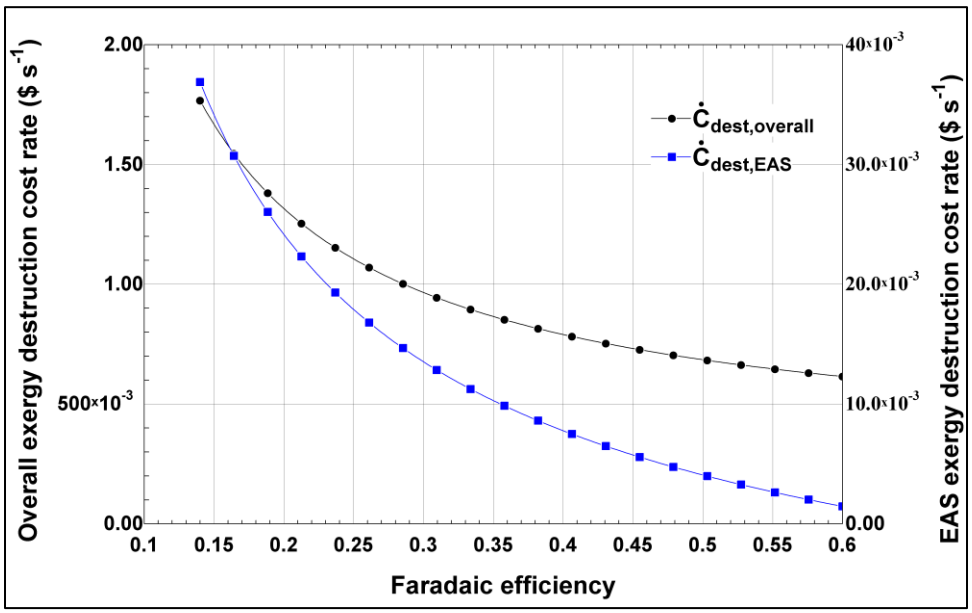

Figure 5.24: Effects of faradaic efficiency on the exergy destruction cost rates of the integrated system, and EAS.

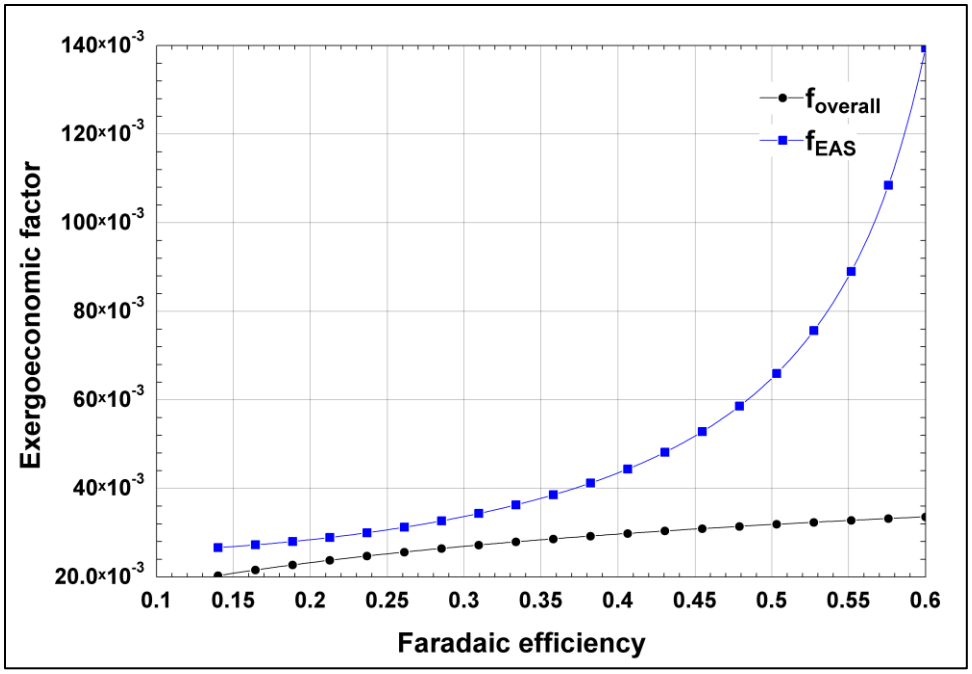

Figure 5.25: Effects of faradaic efficiency on exergoeconomic factors of the integrated system, and EAS.

Figure 5.26 presents the third parameter that is changed to observe the behavior of this integrated system in terms of exergoeconomic performance parameters and this parameter is the air compressor pressure ratio. The effects of changing the air compressor pressure ratio are observed on the overall exergy destruction rate of the integrated system. As the pressure ratio increases from 5.8 to 8, the overall exergy destruction rate rises slightly by a magnitude of only 34 kW, which is insignificant compared to the total value of 17236 kW. It is worth to note that this rise is linear in shape. A similar small rise is found in the total investment cost rate of the overall integrated system as shown in the figure. This cost rate increases by a small margin only and it is safe to say that it stays constant over the range of air compressor pressure ratios. The same can be said about the total investment cost rates of the air compressor and turbine 3. Turbine 3 is mentioned here since this is where the exhaust gases are expanded after they go through several other components, such as the SOFC, and the WGSMR.

Figure 5.27 shows the how the air compressor pressure ratio affects the unit costs of product for the integrated system and turbine 3. These two values undesirably rise linearly but at different rate. The overall system unit cost of product rises from a value of 2.36×10^{-3} \$ kJ^{-1} to 2.39×10^{-3} \$ kJ^{-1}. In contrast, the unit cost of product for turbine 3, which is simply the

unit cost of the electric power generated by the turbine, rises more noticeably from a value of 4.96×10^{-6} \$ kJ^{-1} to a value of 5.92×10^{-6} \$ kJ^{-1}. This is almost a 20% increase in unit cost of electric power generated by turbine 3. Therefore, it is essential to keep the air compressor pressure ratio at a manageable level to produce more power and to lower the costs of this component.

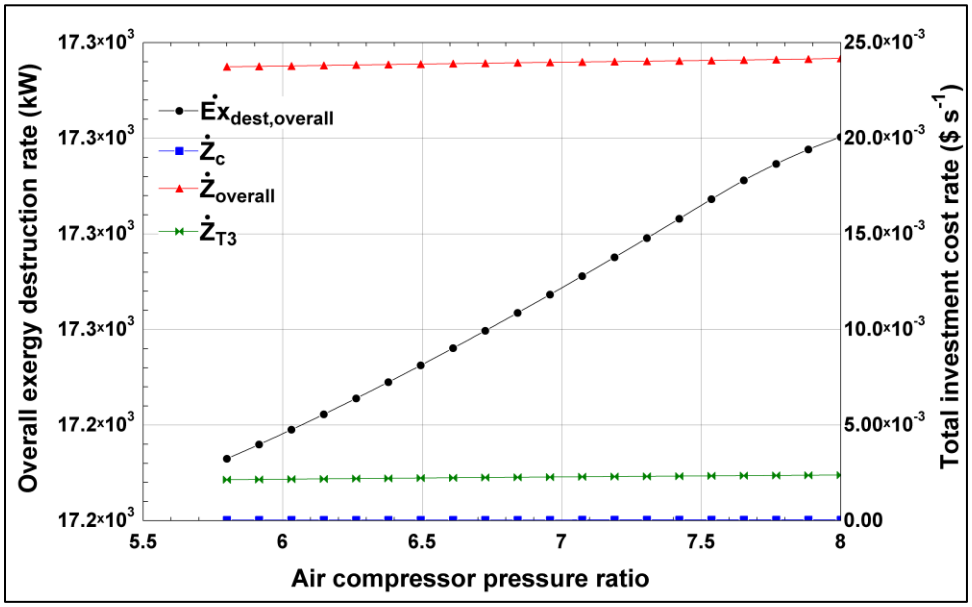

Figure 5.26: Effects of air compressor pressure ratio on the overall exergy destruction rate and the total investment cost rates of the integrated system, air compressor, and turbine 3.

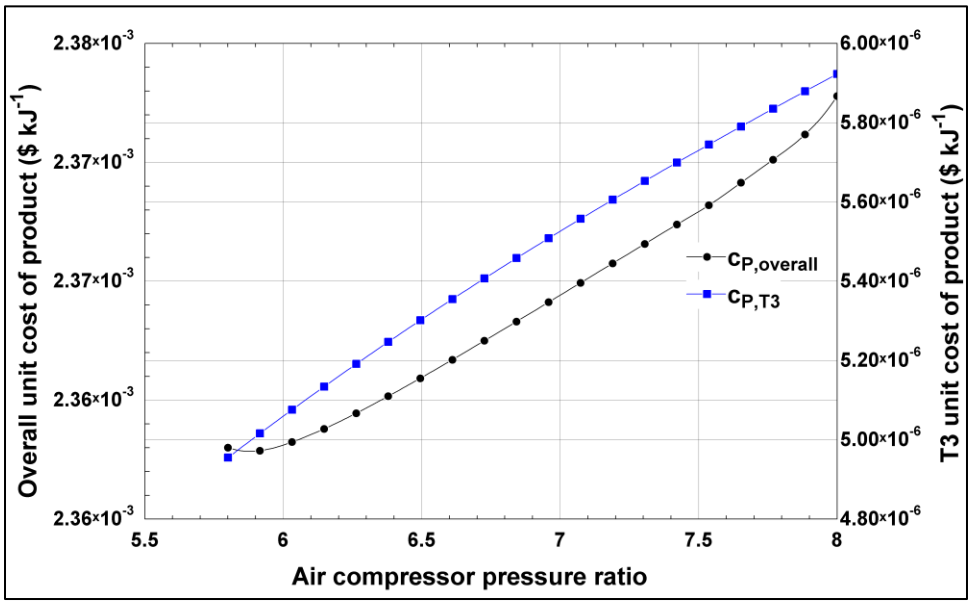

Figure 5.27: Effects of air compressor pressure ratio on the unit cost of products of the integrated system, air compressor, and turbine 3.

Figure 5.28 shows the effects of the air compressor pressure ratio on the exergy destruction rates of the overall integrated system, air compressor, and turbine 3. Both the air compressor and turbine 3 have linear trends over the range of pressure ratios and they increase since the exergy destruction rates of these components increase with rising pressure ratios. This is also how the power consumption for the air compressor and power production for turbine 3 change. On the other hand, there is a more complicated curve shown by the overall exergy destruction cost rate. There exists a minimum for the overall exergy destruction cost rate of 0.756 \$ s^{-1} when the air compressor pressure ratio is 6.03. After this point, the cost rate increases nonlinearly to reach a value of 0.790 \$ s^{-1} when the pressure ratio is 8.

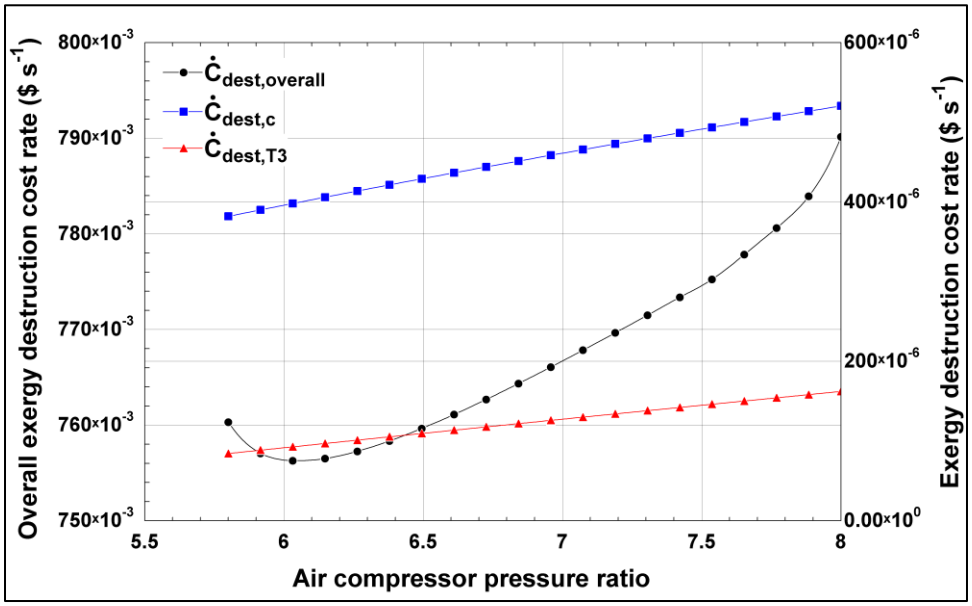

Figure 5.28: Effects of air compressor pressure ratio on the exergy destruction cost rates of the integrated system, air compressor, and turbine 3.

Figure 5.29 displays the behaviors of the exergoeconomic factors of the overall integrated system, the air compressor, and turbine 3. The exergoeconomic factor of the air compressor and turbine 3 almost do not change as the pressure ratio increases, but they have opposite trends. The exergoeconomic factor for the air compressor rises slightly from 6.11% to 7.22%, while the exergoeconomic factor for turbine 3 drops marginally from 96.2% to 93.6 %. Looking at the overall exergoeconomic factor, it is obvious that it has a parabolic curve opened downward. It has a maximum value of 3.05% when the pressure ratio of the air compressor reaches 6.15. This is very close to the point where the overall exergy

destruction cost rate is minimum from the previous figure. As the pressure ratio increases past this point, the overall exergoeconomic factor drops rapidly to reach a low value of 2.97%.

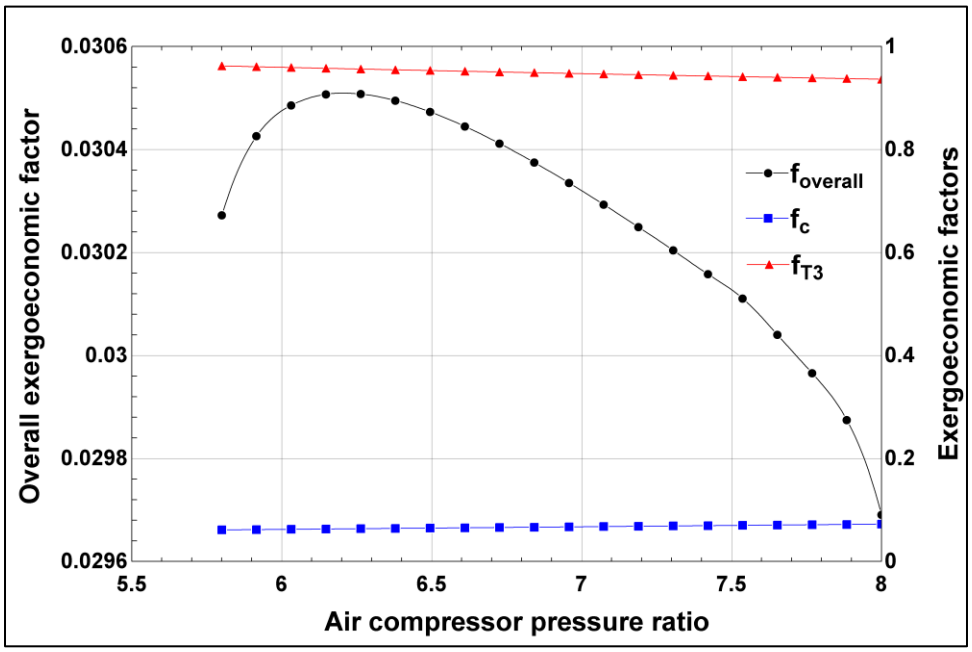

Figure 5.29: Effects of air compressor pressure ratio on exergoeconomic factors of the integrated system, air compressor, and turbine 3.

Figure 5.30 exhibits the effects of the air compressor isentropic efficiency on the overall exergy destruction rate and the total investment cost rates of the integrated system, and the air compressor. The first thing to notice is the declining overall exergy destruction rate of the integrated system and this decline is linear from a value of 17.3×10^3 kW, when the isentropic efficiency of the air compressor is 0.7, to 17.1×10^3 kW, when the air compressor isentropic efficiency is 0.9. Even though the decline is small compared to the overall value of the exergy destruction rate, it is noticeable when looking at the significant figures. Another thing to see from the figure is the change in the overall total investment cost rate which only occurs when the air compressor isentropic efficiency is higher than 0.85. This is mainly a reflection of the increase in the total investment cost rate increase in the same range of isentropic efficiency.

Figure 5.31 shows the effects of changing the air compressor isentropic efficiency on the overall unit cost of product and the air compressor unit cost of product, which is the compressed air leaving the compressor. Both unit costs of product behave almost exactly

the same and they have parabolic curves opened upward with minimum values at an air compressor isentropic efficiency of 0.847. The minimum value of the overall unit cost of product is 2.37×10^{-3} \$ kJ^{-1}, and the minimum value of the air compressor unit cost of product is 6.09×10^{-6} \$ kJ^{-1}. When the isentropic efficiency is higher than 0.85, the overall unit cost of product increase sharply. Since the overall exergy destruction rate decrease in this range, an optimization study is needed to find optimum solutions for the tradeoff between decreasing exergy inefficiencies and increasing unit costs of products.

Figure 5.32 presents how the air compressor isentropic efficiency affects the overall exergy destruction cost rate and the air compressor exergy destruction cost rate. The air compressor exergy destruction cost rate decreases almost linearly with increasing isentropic efficiency of the component as expected. The decrease goes from 0.521×10^{-3} \$ s^{-1} to 0.148×10^{-3} \$ s^{-1}, as the isentropic efficiency rises from 0.7 to 0.9. Next, the overall exergy destruction cost rate has a parabolic curve and not linear that matches the air compressor cost rate. This parabolic curve opens upward and reaches a minimum value of 0.757 \$ s^{-1}, when the air compressor isentropic efficiency is 0.847. This is the same point where a minimum in the overall unit cost of product is achieved.

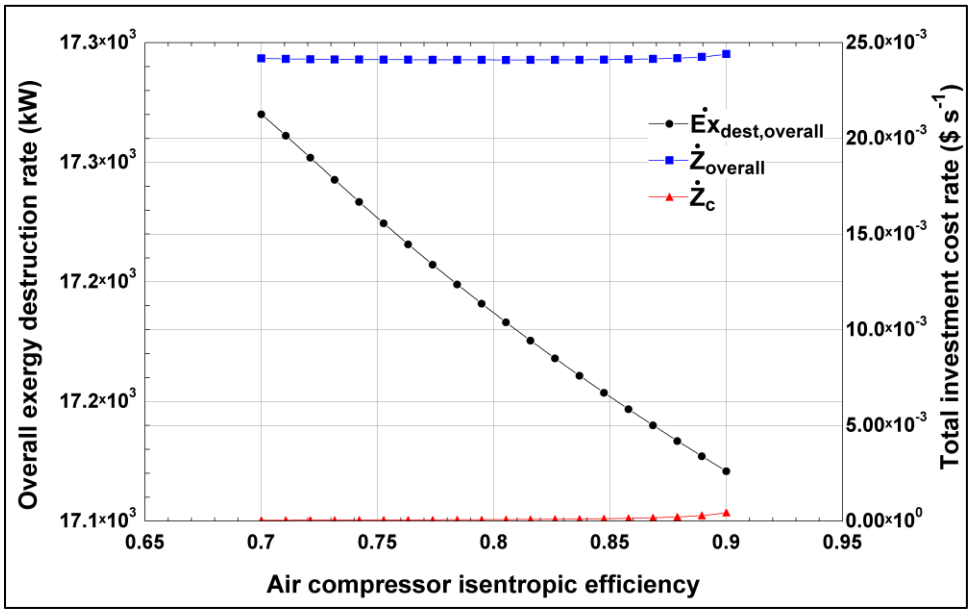

Figure 5.30: Effects of air compressor isentropic efficiency on the overall exergy destruction rate and the total investment cost rates of the integrated system, and air compressor.

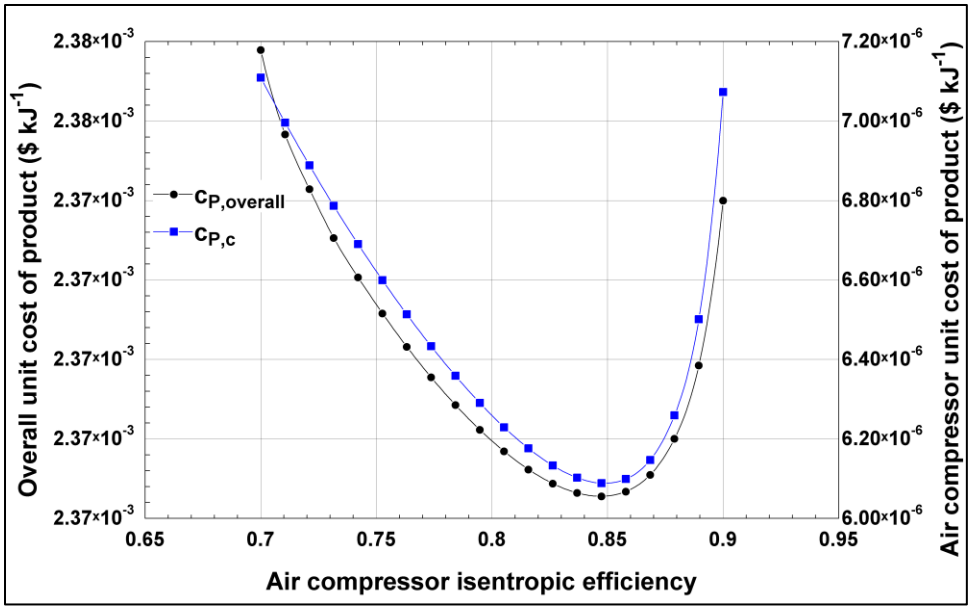

Figure 5.31: Effects of air compressor isentropic efficiency on the unit cost of products of the integrated system, and air compressor.

Figure 5.33 shows in what way the air compressor isentropic efficiency affects the overall exergoeconomic factor and the air compressor exergoeconomic factor. Starting with the overall exergoeconomic factor, it has a parabolic shape opened downward which means it has a maximum value of 3.09% when the air compressor isentropic efficiency is 0.858. This exergoeconomic factor increases in a nonlinear manner from the range of 0.7 to 0.858, then it drops slightly, and this is a result of the increase in the overall exergy destruction cost rate mentioned earlier. Moreover, the exergoeconomic factor of the air compressor increase in an exponential manner as the isentropic efficiency increases. This exergoeconomic factor increase from a value of 7.22% to a significantly high value of 75.1%. In general, it seems that the effects of the single air compressor do not necessarily mirror that of the overall integrated system beyond the point of 0.840. The two behaviors start to deviate significantly and other components in the integrated system begin to affect the overall exergoeconomic performance of the system in different ways.

Figure 5.34 shows another parameter considered in this work which is the isentropic efficiency of turbine 3. This turbine receives exhaust gases from the WGSMR after all the fuels have been completely burned. There are three things that are specifically observed in this figure which are the overall exergy destruction rate, and the total investment cost rates for the overall integrated system and turbine 3. To begin with, the overall exergy

destruction rate expectedly drops in magnitude linearly from 17.4×10^{3} kW, when the isentropic efficiency of turbine 3 is 0.65, to 17.3×10^{3} kW, when the air compressor isentropic efficiency is 0.76. This drop is due to the reduction in exergetic deficiencies that occur in turbine 3 which produces a significant amount of electric power in the integrated system. For the overall and turbine 3 total investment cost rates, they do not change significantly, and they can be said that they remain constant over the range of turbine 3 isentropic efficiency at values of 24.01×10^{-3} \$ s^{-1}, and 2.25×10^{-3} \$ s^{-1}, respectively.

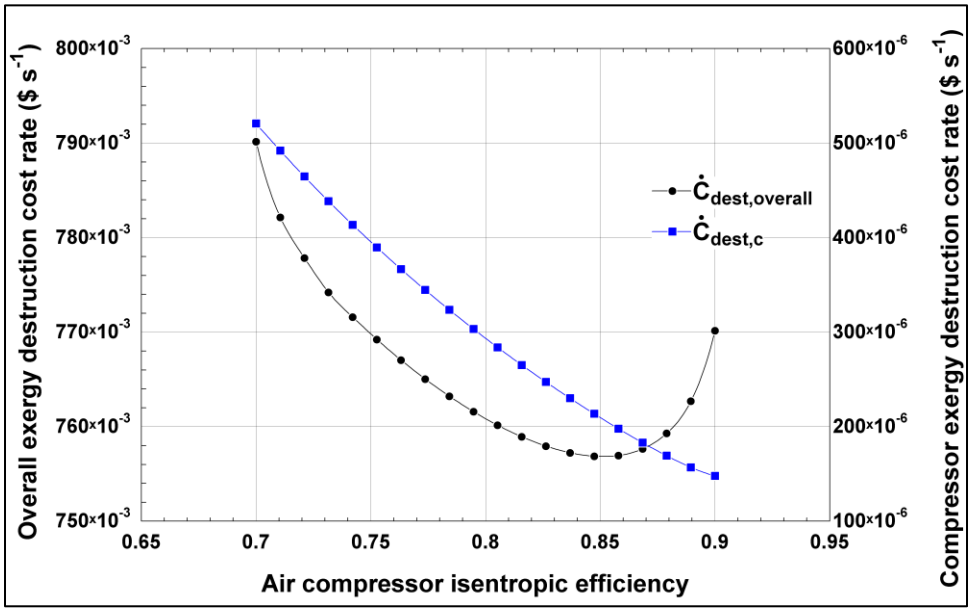

Figure 5.32: Effects of air compressor isentropic efficiency on the exergy destruction cost rates of the integrated system, and air compressor.

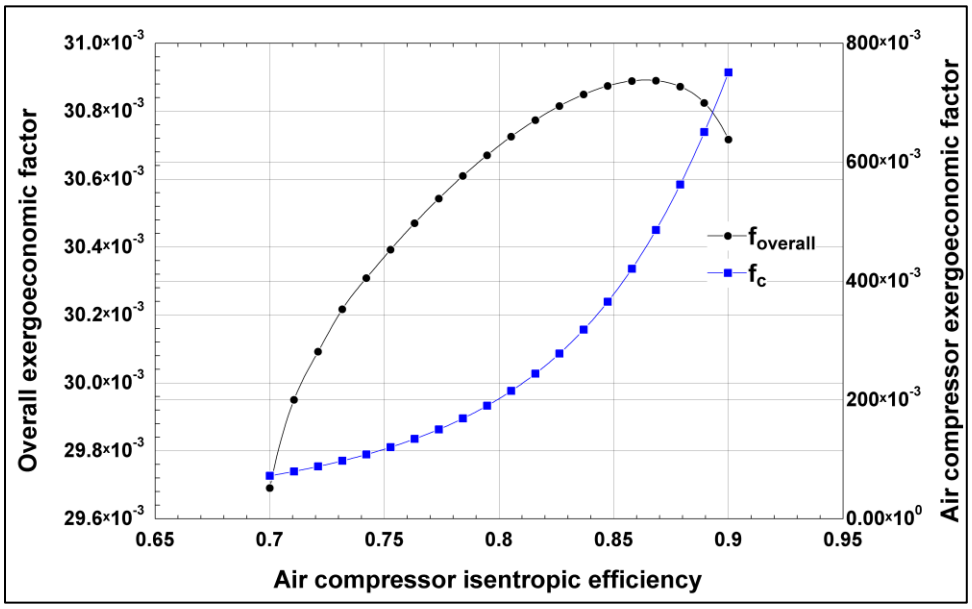

Figure 5.33: Effects of air compressor isentropic efficiency on exergoeconomic factors of the integrated system, and air compressor.

Figure 5.35 presents the outcomes of varying turbine 3 isentropic efficiency on the overall unit cost of product and the unit cost of product for turbine 3, which is the unit cost of the electric power generated by this turbine. Starting with the unit cost of product for turbine 3, the unit cost decreases nonlinearly as the isentropic efficiency of the turbine increases, and this is anticipated because the unit cost for producing electricity from this component becomes cheaper as the more electric power is generated instead of wasting it to the exhaust gases leaving the turbine. In contrast, the overall unit cost of product increases linearly as the isentropic efficiency of turbine 3 increases from 0.65 to 0.743. After this point, the increase in the overall unit cost of product becomes exponential to reach a maximum value of 2.38×10^{-3} \$ kJ^{-1}, when turbine 3 isentropic efficiency is 0.76. Comparing this figure to the previous one, it is seen that there is a tradeoff between decreasing overall exergy destruction rate and increasing overall unit cost of product as the isentropic efficiency of turbine 3 increase. An optimization investigation with this parameter is needed to find optimum solutions where this tradeoff is balanced to get the lowest possible unit cost of product and lowest exergy destruction rate for the integrated system.

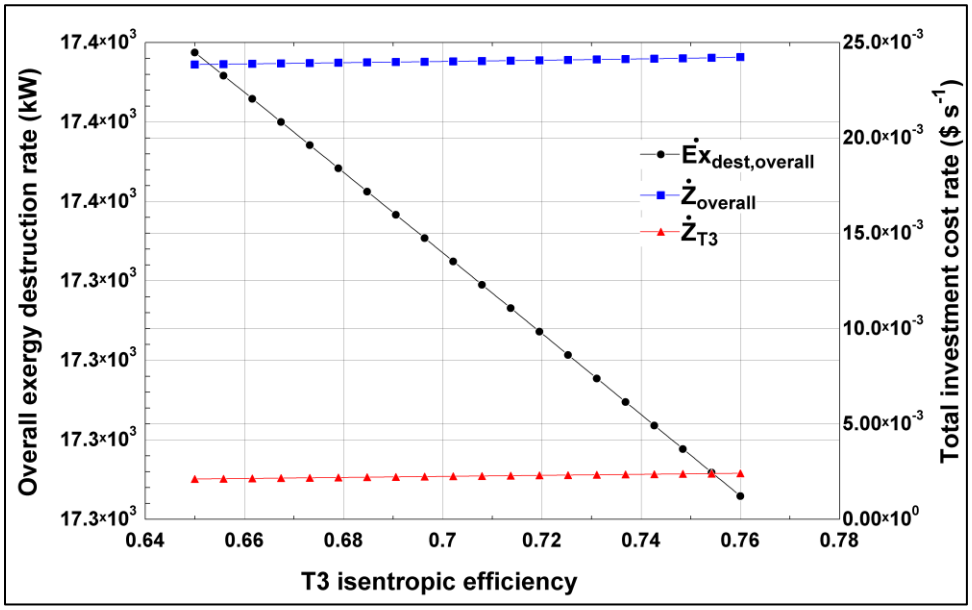

Figure 5.34: Effects of turbine 3 isentropic efficiency on the overall exergy destruction rate and the total investment cost rates of the integrated system, and turbine 3.

Figure 5.36 exhibits two other exergoeconomic performance parameters being affected by the changing isentropic efficiency of turbine 3. These two parameters are the overall exergy destruction cost rate and turbine 3 exergy destruction cost rate. Interestingly, these two

parameters have similar trends as their respective unit costs of product. Firstly, the overall exergy destruction cost rate increases linearly when the isentropic efficiency of turbine 3 increase from 0.65 to 0.743, and it does increase exponentially as the isentropic efficiency goes higher in value from 0.743 to 0.76. On the other hand, turbine 3 exergy destruction cost rate drop in value linearly as the isentropic efficiency of the turbine increase, and this agrees with the decrease in the exergy losses at this component when the isentropic efficiency is enhanced.

Figure 5.37 shows the last two exergoeconomic performance parameters being affected by the changing isentropic efficiency of turbine 3. These two parameters are the overall exergoeconomic factor and turbine 3 exergoeconomic factor. To begin with, the overall exergoeconomic factor has a parabolic behavior opened downward, which means that this factor reaches a maximum value of 2.97% when the isentropic efficiency of turbine 3 is 0.737. Past this point, the overall exergoeconomic factor drops to 2.94% which is only a slight drop. Secondly, the exergoeconomic factor of turbine 3 is enhanced linearly as the isentropic efficiency of this component is improved. The enhancement of the exergoeconomic factor is almost 3 percentage points as the isentropic efficiency goes from 0.65 to 0.76 for turbine 3, which is expected behavior because of the reduction in the exergy destruction cost rate seen earlier.

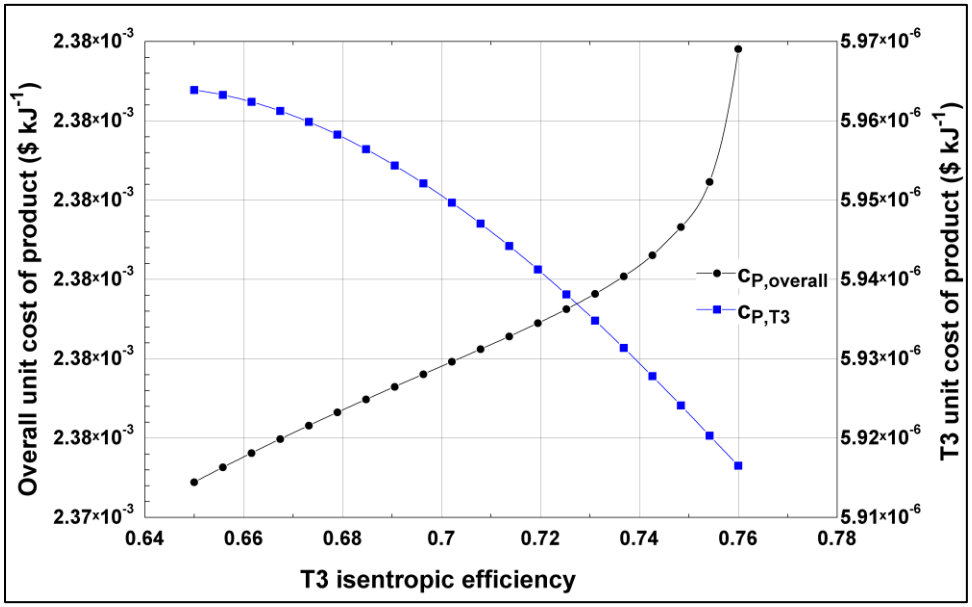

Figure 5.35: Effects of turbine 3 isentropic efficiency on the unit cost of products of the integrated system, and turbine 3.

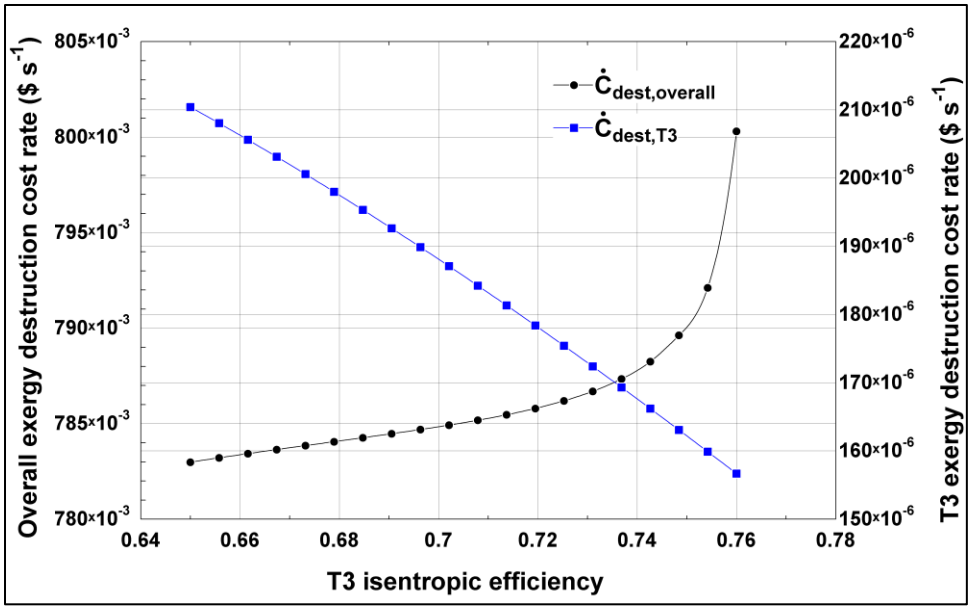

Figure 5.36: Effects of turbine 3 isentropic efficiency on the exergy destruction cost rates of the integrated system, and turbine 3.

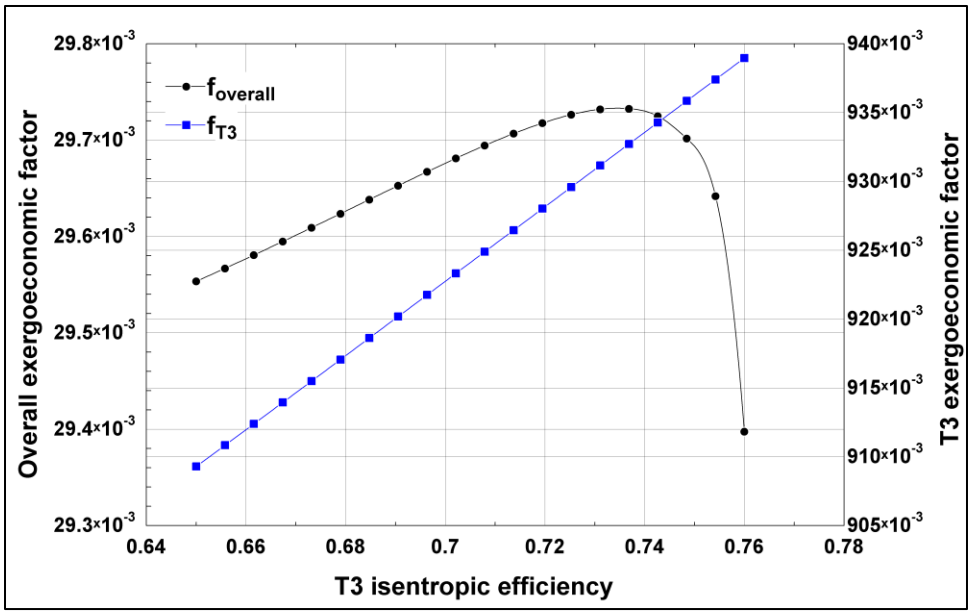

Figure 5.37: Effects of turbine 3 isentropic efficiency on exergoeconomic factors of the integrated system, and turbine 3.

Figure 5.38 considers the last parametric variable changed in this subsection to observe its effects on the exergoeconomic performance of the integrated system. This parametric variable is the boiler pressure which is changed from 1200 to 2200 kPa. This pressure represents the higher-pressure level in the steam Rankine cycle which absorbs waste heat from the exhaust gases leaving turbine 3. From this figure, the overall exergy destruction rate is first observed to decrease linearly but insignificantly as the boiler pressure increase

by almost the double. The decrease in the overall exergy destruction rate is only 11 kW and this represents 0.0637% of the total exergy destruction rate. Next, looking at the overall total investment cost rate and the total investment cost rate of turbine 4, they do not change over the span of the pressure range at the boiler.

Figure 5.39 shows how increasing the boiler pressure can affect the unit cost of product for the overall integrated system and the unit cost of product for turbine 4. Turbine 4 unit cost of product has a curve that represents a parabolic one with an opening being upward. This unit cost reaches a minimum value of 12.84×10^{-6} \$ kJ^{-1} at a boiler pressure level of 2042 kPa. This minimum value represents a drop of 2.95% from the highest unit cost of product of turbine 4 when the boiler pressure is 1200 kPa. In addition, the changes are not as significant for the overall unit cost of product. This is mainly because the steam Rankine cycle and the electric power production of turbine 4 are not major parts of the integrated system in terms of exergy streams flowing through them.

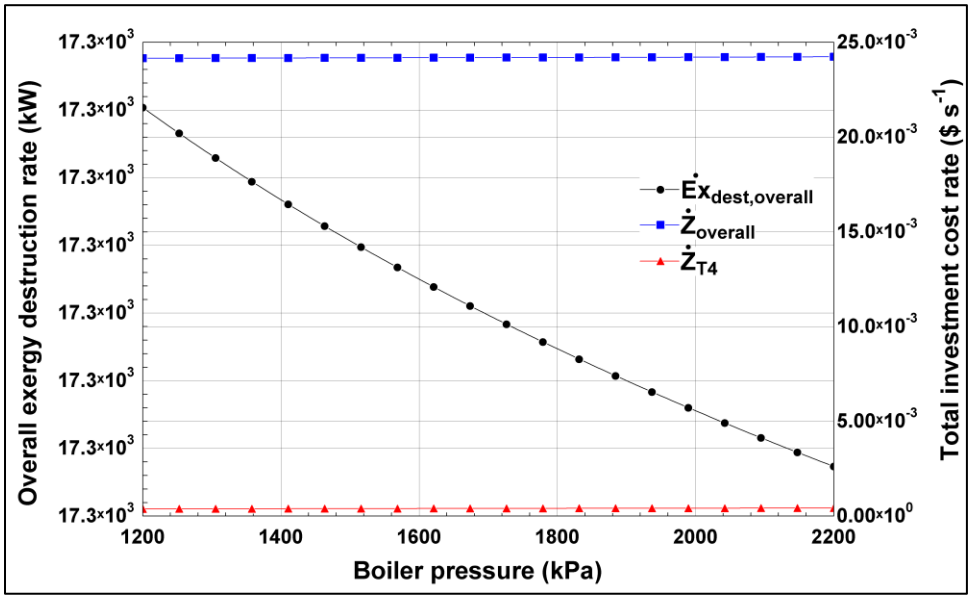

Figure 5.38: Effects of boiler pressure on the overall exergy destruction rate and the total investment cost rates of the integrated system, and turbine 4.

Figure 5.40 displays the effects of changing the boiler pressure on the overall exergy destruction cost rate and turbine 4 exergy destruction cost rate. Both of these cost rates have different behaviors. Firstly, the overall exergy destruction cost rate has an upward parabolic behavior, and its minimum value is reached when the boiler pressure is 1726 kPa and this value is 0.7898 \$ s^{-1}. As the pressure level increases beyond 1726 kPa, the overall

exergy destruction cost rate increases nonlinearly to reach a magnitude of 0.7946 \$ s^{-1}, when the boiler pressure is 2200 kPa. However, the exergy destruction cost rate of turbine 4 behaves in a linear manner. As the boiler pressure increases, the exergy destruction cost rate of turbine 4 increases from 35.5×10^{-6} to 43.1×10^{-6} \$ s^{-1}.

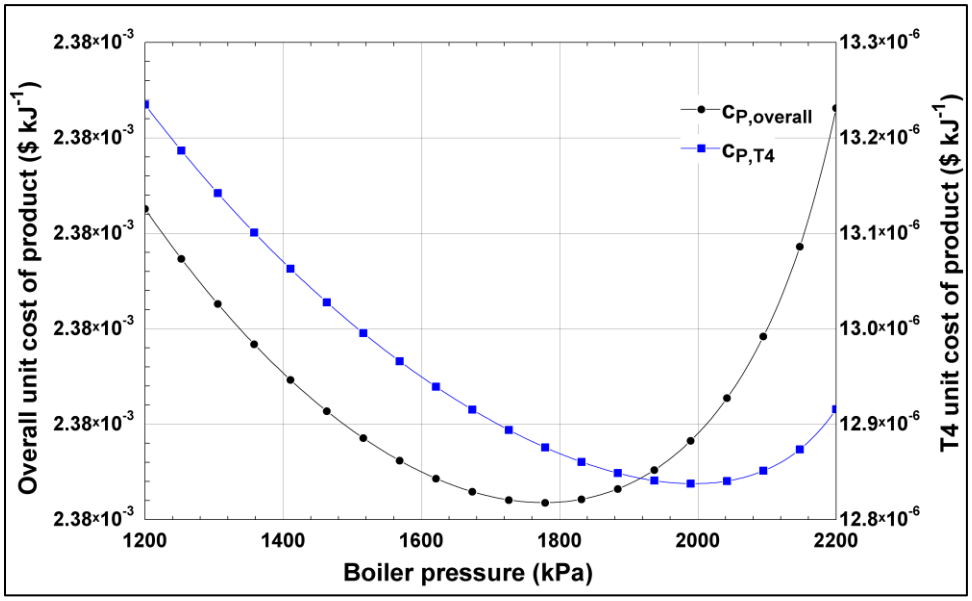

Figure 5.39: Effects of boiler pressure on the unit cost of products of the integrated system, and turbine 4.

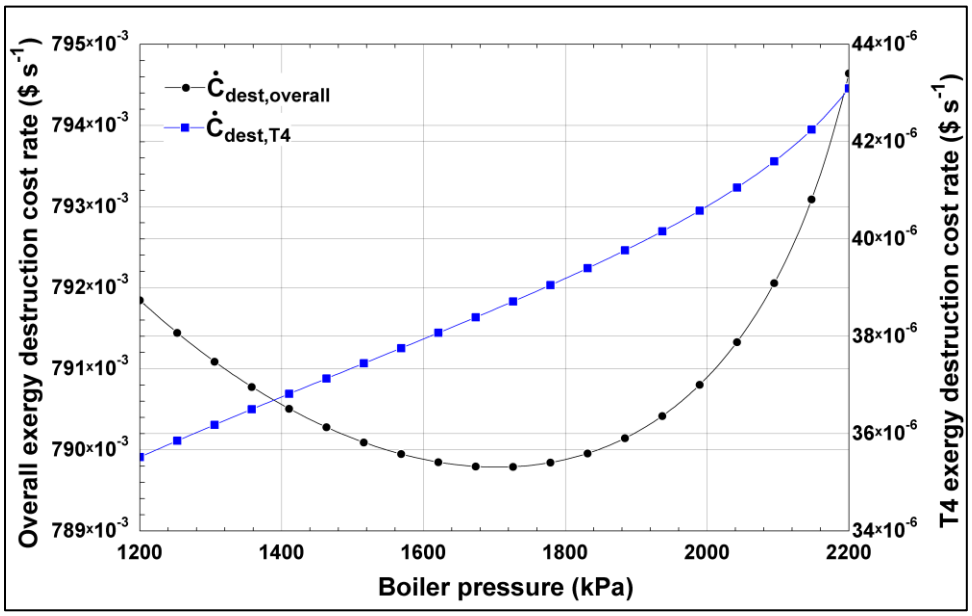

Figure 5.40: Effects of boiler pressure on the exergy destruction cost rates of the integrated system, and turbine 4.

Figure 5.41 shows the how the boiler pressure changes can affect the exergoeconomic factors of the overall integrated system and turbine 4. Starting with the overall

exergoeconomic factor, it has a parabolic behavior opened downward with a maximum magnitude of 2.97% at 1832 kPa. From 1200 kPa to this maximum, the increase in the overall exergoeconomic factor is slow but significant; however, from 1832 to 2200 kPa, there is a rapid drop in this factor, and it does reach a value of 2.96%. this drop is small since the boiler pressure is part of the steam Rankine cycle which is a minor part of the integrated system. Next is the exergoeconomic factor for turbine 4. This factor decreases in value in a nonlinear manner, and it goes from 91.4% down to 90.7% as the boiler pressure increases from 1200 to 2200 kPa.

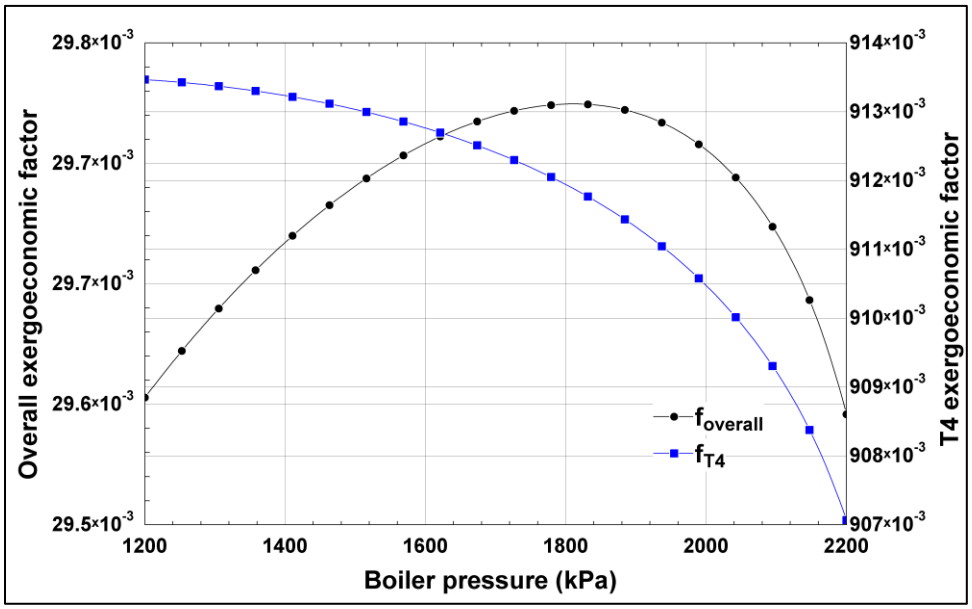

Figure 5.41: Effects of boiler pressure on exergoeconomic factors of the integrated system, and turbine 4.

5.2.2 Optimization study results of system 2

In this subsection, the results of the optimization study of this integrated system are considered. The decision variables in this optimization study are the geothermal fluid temperature, air compressor isentropic efficiency, turbine 3 isentropic efficiency, and boiler pressure. The two objective functions that need to be minimized are the overall exergy destruction rate and the overall unit cost of products. Minimizing the first objective results in increasing the overall exergetic performance of the integrated system and minimizing the second objective function means reducing the costs for producing the useful outputs of this integrated system, namely electric power, space heating, freshwater, and ammonium bicarbonate.

After producing thermodynamic and exergoeconomic data from EES software, these are inputted to the Eureqa software to produce explicit expressions for the objective functions. These expressions are presented in Table 5.12. A few things are worth noting regarding these expressions. Firstly, the geothermal fluid temperature seems to be the dominant decision variable in both expressions for the overall exergy destruction rate, as well as the overall unit cost of product. Secondly, none of the models of overall unit cost of products, the boiler pressure appears. There is no significant dependency of this objective function on boiler pressure.

Table 5.12: The selected objective functions models with their corresponding statistical indicators computed from Eureqa software after 5 minutes of search time.

Objective functions	**Genetic programming selected models**	**Correlation coefficient (R^2)**	**Mean absolute error**	**Mean squared error**
Overall exergy destruction rate	$\dot{Ex}_{dest,overall} = 9.38 \times 10^3 + 19.1 \times T_1 + 1.34 \times T_1 \times \eta_{T3} + 878 \times \eta_c^2 - 2.80 \times 10^3 \times \eta_c \times \eta_{T3} - 5.16 \times 10^{-3} \times T_1^2 - 1.97 \times 10^{-2} \times P_{34} \times \eta_c^2$	0.999	1.03	9.27
Overall unit cost of products	$c_{P,overall} = 9.52 \times 10^{-3} - \frac{5.51}{T_1} + \frac{1.17 \times 10^3}{T_1^2} + 9.94 \times 10^{-4} \times \eta_{T3} \times \eta_c^2 - 2.39 \times 10^{-6} \times T_1 \times \eta_c - 1.70 \times 10^{-9} \times \eta_{T3} \times T_1^2$	0.995	7.46×10^{-7}	3.89×10^{-12}

Figure 5.42 shows the pareto front of the multi-objective optimization algorithm implemented in this study. These results are tabulated in Table 5.13 where the objective functions values are presented, along with their corresponding decision variables values. There are four interesting points on these pareto front. The first point is point A which is where the overall exergy destruction rate is minimized as a single objective. At this point, the overall exergy destruction rate is 1.58×10^4 kW. The second point of interest is point B. This point represents where the overall unit cost of product is minimized, and it reaches a magnitude of 2.35×10^{-3} \$ kJ^{-1}. The third point is the ideal point which can be defined as the point where both objective functions are minimized without any dependency on each other. This point is impossible to reach, and it is only and ideal point of reference. The fourth point is point C which is the closest point to this ideal point on the pareto front. This

point has an overall exergy destruction rate of 1.62×10^{4} kW and an overall unit cost of product of 2.42×10^{-3} \$ kJ^{-1}.

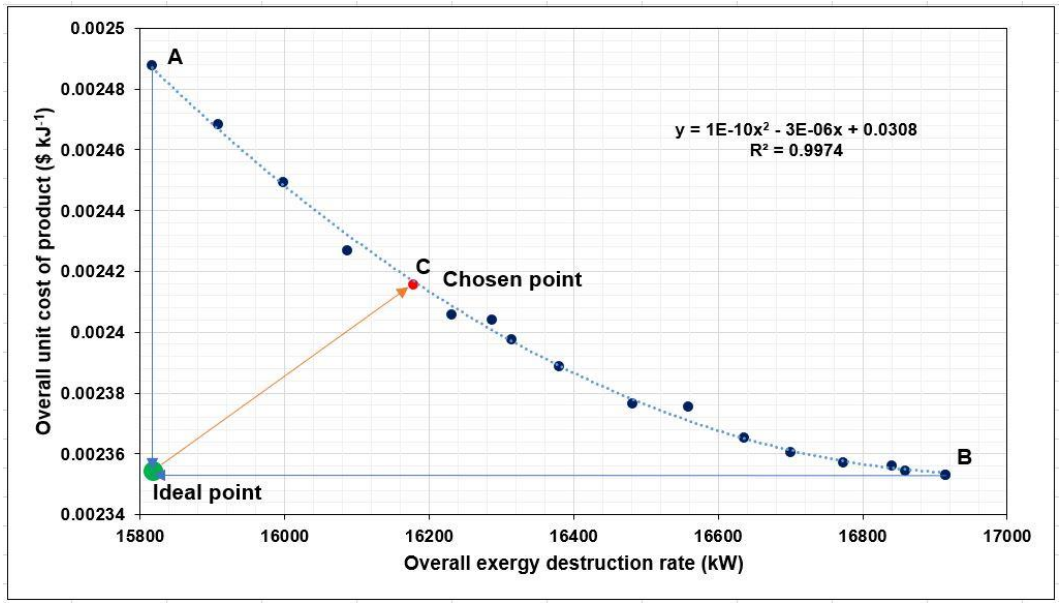

Figure 5.42: Pareto front of the optimization study between overall exergy destruction rate and overall unit cost of product.

Table 5.13: Decision variables values for the optimum operation points and their corresponding values of the two objective functions presented for system 2.

Geothermal fluid temperature (K)	**Air compressor isentropic efficiency**	**Turbine 3 isentropic efficiency**	**Boiler pressure (kPa)**	**Overall exergy destruction rate (kW)**	**Overall unit cost of products ($ kJ^{-1})**
4.28E+02	9.00E-01	7.60E-01	1.58E+03	1.58E+04	2.49E-03
4.86E+02	8.99E-01	6.50E-01	1.72E+03	1.69E+04	2.35E-03
4.68E+02	8.99E-01	6.56E-01	1.70E+03	1.66E+04	2.37E-03
4.44E+02	8.99E-01	6.71E-01	1.63E+03	1.62E+04	2.41E-03
4.86E+02	8.99E-01	6.50E-01	1.72E+03	1.69E+04	2.35E-03
4.35E+02	8.99E-01	6.73E-01	1.70E+03	1.61E+04	2.43E-03
4.58E+02	8.99E-01	6.58E-01	1.71E+03	1.65E+04	2.38E-03
4.82E+02	8.99E-01	6.51E-01	1.71E+03	1.69E+04	2.35E-03
4.72E+02	9.00E-01	6.52E-01	1.69E+03	1.67E+04	2.36E-03
4.77E+02	8.99E-01	6.51E-01	1.69E+03	1.68E+04	2.36E-03
4.32E+02	9.00E-01	7.45E-01	1.65E+03	1.59E+04	2.47E-03
4.53E+02	8.99E-01	6.70E-01	1.66E+03	1.64E+04	2.39E-03
4.50E+02	8.99E-01	6.91E-01	1.69E+03	1.63E+04	2.40E-03
4.50E+02	8.99E-01	6.77E-01	1.65E+03	1.63E+04	2.40E-03
4.42E+02	8.99E-01	6.84E-01	1.70E+03	1.62E+04	2.42E-03
4.35E+02	9.00E-01	7.19E-01	1.61E+03	1.60E+04	2.45E-03
4.82E+02	8.99E-01	6.54E-01	1.69E+03	1.68E+04	2.36E-03
4.65E+02	8.99E-01	6.73E-01	1.70E+03	1.66E+04	2.38E-03

5.3 Modeling results of system 3

Before going to the results of the base case, it is important to mention the chosen operating conditions for this base case of the integrated system. Table 5.14 outlines these operating conditions. For example, the solar irradiance for this base case is chosen to be 600 W m^{-2}, and the TES heat transfer fluid is Dowtherm A. For the elastocaloric cooling device, the hysteresis and entropy change of the phase transformation are 50 J kg^{-1}, and 20 J kg^{-1}, respectively [151]. These values are for the SMA called CuAlNi. Moving to the Brayton gas turbine cycle, the excess air factor is chosen to be 1.2, the compressor ratio of C1 is 8, and the inlet temperature of turbine 1 is set to be 1870 K. The mass flow rate of air changes so that this temperature is achieved at the inlet of the turbine.

Table 5.15 lists the outputs of the integrated system thermodynamic model. Firstly, the effective area of the solar collectors is estimated to be 0.140 km^2, and these receive 83,800 kW of solar heat transfer. Almost 40% of this thermal energy is stored in the TES, while the rest is used to produce enough electric power to support the electrochemical ammonia synthesizer and the elastocaloric cooling device. The energy and exergy COP of the ECD are 10.7 and 0.258, respectively. The EAS consumes 8,990 kW of electric power to produce ammonia at a mass rate of 0.280 kg s^{-1}. The carbon capturing unit at the end of its process makes ammonium bicarbonate at a value of 1.30 kg s^{-1}. Comparing the performance of carbon capturing of this integrated system that employs a solar energy source to a carbon capturing unit that uses geothermal energy discussed earlier, it is noticed that both systems share the same energy requirement for capturing 1 kilogram of carbon dioxide from the point of EAS to the ammonium bicarbonate reactor. This value is reported in the previous work and here to be 12.4 MJ kg^{-1} of CO_2. However, the energy and exergy requirements from the renewable energy source to the ammonium bicarbonate production are different. For the geothermal case, these were, respectively, reported to be 58.7 MJ kg^{-1} of CO_2, and 29.3 MJ kg^{-1} of CO_2. For the solar energy case, the present results show that these requirements, respectively, are 68.7 MJ kg^{-1} of CO_2, and 65.2 MJ kg^{-1} of CO_2. In both the energy and exergy measures, the geothermal-based carbon capturing system performs better than the present system. Still, setting up a solar energy-based system is more flexible than the geothermal one because engineers will be restricted to locations that have geothermal fluid reservoirs. The overall energy and exergy efficiencies of this integrated

system are 22.3%, and 11.9%, respectively. These values seem low but operating a typical Brayton cycle can have an energy efficiency of 33%. This value drops by almost 6% when air separation unit is utilized and 7% more if carbon capturing of natural gas is involved [30]. So, the expected energy efficiency is around 20%. This integrated system is performing almost 2 percentage points higher than this. This indicates that the results of the model developed for System 3 are validated as they compare well with the previously studied Brayton cycle with carbon capturing given in [30].

Table 5.14: Input values used for system 3 model.

Input quantity	**Value**
Solar irradiance	0.6 kW m^{-2}
Solar irradiance temperature	5770 K
Temperature of fluid leaving parabolic solar collectors	770 K
Operating pressure of parabolic solar collectors	3200 kPa
Temperature of hot storage tank	510 K
Heat transfer fluid for TES	Dowtherm A
SMA material	CuAlNi (Al 12 wt%, Cu 80 wt%)
Phase transformation entropy change (Δs)	20 J kg^{-1} K^{-1} ([151])
SMA hysteresis (compressive)	50 J kg^{-1} ([151])
ECD hot side temperature	306.3 K
ECD cold side temperature	285 K
Temperature span of ECD	21.3 K
Rate of phase transformations done by the SMA ($\dot{N}$)	7.08 Hz
Space cooling desired temperature	291 K
Cooling demands	400 kW
Excess air factor	1.2
ASU specific compressor work	829 kW kg^{-1} of O_2 ([152])
R_{ASU}	0.246 kg of O_2 kg^{-1} of air ([152])
Compressor ratio of C1	8
T2 inlet temperature	1870 K
Maximum pressure of the S-CO_2 cycle	25 MPa
Minimum pressure of the S-CO_2 cycle	8 MPa
Faradaic efficiency (*FE*) of EAS	40%
Constant overpotential of EAS (*V*)	0.8 V
Operating temperature of EAS	293 K
Operating pressure of EAS	101 kPa

Table 5.16 and Table 5.17 present the thermodynamic properties of the state points in the present integrated system. Multiple interesting things are noted from these tables. To begin with, the mass flow rate of Dowtherm A in the TES is calculated as 85.2 kg s^{-1}. Another point is the cryogenic air separation unit produces an oxygen-rich stream of 1.27 kg s^{-1} with a 95% molar-basis of oxygen. One more thing to note is the carbon dioxide-rich

exhaust gases at stream 28 contain 71.4% of CO_2 which high since the combustion is oxy-combustion type and the water was removed from the exhaust gases using the condenser. This makes it easier to make ammonium bicarbonate in the reactor in terms of requiring less energy.

Table 5.15: Output quantities resulting from system 3 model.

Output quantity	**Value**
Effective area of parabolic solar collectors	0.140 km^2
Solar heat transfer rate	83,800 kW
ε	0.407
Electric power output of T1	9,030 kW
Electric power supplied to ECD	37.2 kW
Energy COP of ECD	10.7
Exergy COP of ECD	0.258
Electric power supplied to EAS ($\dot{W}_{EAS}$)	8,990 kW
Heat losses by the EAS ($\dot{Q}_{EAS,loss}$)	3,790 kW
Ammonia production rate	0.280 kg s^{-1}
Carbon dioxide mass flow rate	0.724 kg s^{-1}
Ammonium bicarbonate production rate	1.30 kg s^{-1}
Energy requirement for CO_2 capture	12.4 MJ kg^{-1} of CO_2
Solar energy for CO_2 capture	68.7 MJ kg^{-1} of CO_2
Solar exergy for CO_2 capture	65.2 MJ kg^{-1} of CO_2
Electric power supplied to ASU	1,050 kW
Electric power output of T2	5,590 kW
Electric power output of T3	1,204 kW
Net electric power produced by integrated system	2,280 kW
Freshwater production rate	14.4 kg s^{-1}
Overall energy efficiency of integrated system	22.3%
Overall exergy efficiency of integrated system	11.9%

Figure 5.43 compares the exergy destruction rates of the components of the integrated system. It is seen that the highest exergy destruction rate is found at the parabolic solar collectors with a value of 46,500 kW. The second highest is HX1 with a value of 8,370 kW. One way to reduce the high exergy destruction rate at HX1 is to utilize the waste heat for further power generation using an organic Rankine cycle. Some of the fluids that can be utilized in such organic Rankine cycles may be R227ea, R236ea, R600 and ammonia. All of these fluids are able to receive low-temperature heat to produce electric power with a reasonable energy efficiency between 9% and 12.5% [165,166]. There are One noteworthy comparison is between EAS and AB reactor. The EAS has an exergy destruction rate of 3,630 kW, while the AB reactor has it at higher value of 4,390 kW. The

HX3 shows a low exergy destruction rate of 110 kW to show that the exergetic efficiency of this component when the waste heat recovered using the supercritical CO_2 cycle.

Table 5.16: Thermodynamic state points of system 3.

State #	Material	Temperature (K)	Pressure (kPa)	Specific enthalpy (kJ kg^{-1})	Specific entropy (kJ kg^{-1} K^{-1})	Specific exergy (kJ kg^{-1})	Mass flow rate (kg s^{-1})
1	Water	303.1	3200	128.3	0.4347	3.284	25.24
2	Water	770	3200	3448	7.195	1308	25.24
3	Water	770	3200	3448	7.195	1308	10.26
4	Water	770	3200	3448	7.195	1308	14.98
5	Water	458.3	120	2845	7.687	558.9	14.98
6	Water	303	120	125.2	0.4347	0.1925	14.98
7	Water	303.1	3200	128.3	0.4347	3.284	14.98
8	Water	303.1	3200	128.3	0.4347	3.284	10.26
9	Dowtherm A	298	101	16.15	0.0514	0	85.2
10	Dowtherm A	298	110	16.15	0.0514	0.008525	85.2
11	Dowtherm A	510	110	416	1.052	101.7	85.2
12	Water	298	101	-13422	10.48	0	0.444
13	Nitrogen	298	101	-0.1554	6.83	1.937	3.88
14	Oxygen	298	101	-0.1371	6.408	0	0.3946
15	Ammonia	298	101	-2698	11.32	22506	0.2795
16	Water	500	101	-13038	11.46	91.43	0.296
17	Aqueous ammonia	395.7	101	-8016	11.46	26.89	0.5755
18	Ammonium bicarbonate	373	101	-10663	11.95	13.9	1.299
19	Air	298	101	298.4	5.696	0	5.148
20	Oxygen-Nitrogen	298	101	-0.1379	6.427	3.97	1.268
21	Natural gas	298	101	-4650	11.61	51980	0.25
22	Air	298	101	298.4	5.696	0	8.632
23	Air	640.4	808	649.9	5.881	296.3	8.632
24	Air	1870	808	2090	7.119	1368	8.632
25	Air	1339	101	1443	7.309	663.7	8.632
26	Air	462.5	101	464.9	6.14	34.1	8.632
27	Exhaust gases	690.4	96.05	-8957	8.425	194.4	1.518
28	Exhaust gases	373	101	-6918	5.421	7.35	0.9261
29	Carbon dioxide	442.5	20000	46.86	-0.789	282.4	7.418
30	Carbon dioxide	1334	20000	1185	0.6207	1000	7.418
31	Carbon dioxide	1210	8000	1022	0.6716	822.7	7.418
32	Carbon dioxide	355.8	8000	-11.1	-0.8002	227.8	7.418
33	Water	345.8	35	304.3	0.9877	14.46	3.295
34	Water	345.8	35	2631	7.715	336.2	3.295
35	Sea water	303	100	98.71	0.344	0.14	158.1
36	Brine	329.2	100	214.4	0.7015	6.2	29.71
37	Cooling water	312.4	100	156	0.532	1.3	114
38	Freshwater	329.2	100	235.2	0.783	6.432	14.38
39	Nitrogen	298	101	-0.1557	6.836	0	0.2302
40	Exhaust gases	373	101	71.54	6.739	7.772	0.2026
41	Water	373	101	-13281	10.9	15.25	0.5919

Table 5.17: Molar basis composition of the exhaust gases in the integrated system.

Exhaust gases stream #	O_2	N_2	H_2O	CO_2
20	95%	5%	0	0
27	8.27%	3.53%	58.8%	29.4%
28	20.0%	8.57%	0	71.4%
40	70.0%	30.0%	0	0

The first set of results of this exergoeconomic analysis at this base case is presented in Table 5.18. The first thing to mention from these results is the cost rate of the fluid being stored in the thermal energy storage unit which is state 11 has a value of 9.41E-02 \$ s^{-1} which is a hundred times higher than the cost rate of the fluid going to the solar collectors. This indicates the high cost of producing steam using solar collectors due to the investment costs of this component. The cost rate difference between states 5 and 6 which are across HX1 is high and this indicates that the heat losses at this heat exchanger could be used for waste heat recovery to produce a more economically valuable product, like space heating or additional electric power using an organic Rankine cycle. The cost rate of ammonia at state 15 is 9.51E-02 \$ s^{-1}, while the cost rate of ammonium bicarbonate is lower at a value of 8.92E-02 \$ s^{-1}. The cost rate of the freshwater stream, state 38, is calculated at 7.97E-03 \$ s^{-1}. The financial production cost of ammonium bicarbonate per one kilogram in this integrated system is 0.0687 \$ kg^{-1}, and this is much lower than the market price for the food-grade ammonium bicarbonate which is valued between 0.20 and 0.25 \$ kg^{-1} according to values taken on October 28, 2021 [162].

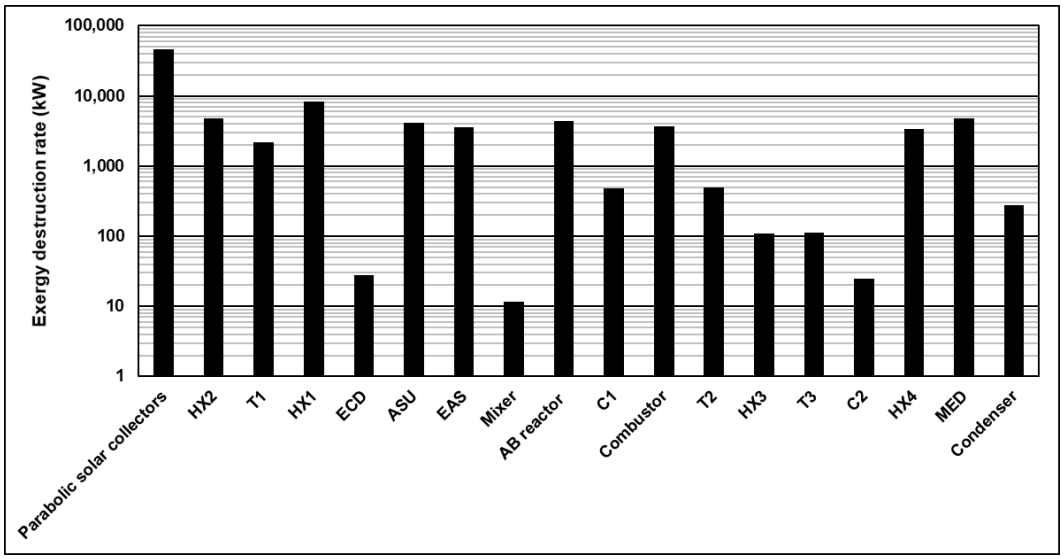

Figure 5.43: Exergy destruction rates of the components in the integrated system. A logarithmic scale is used for clarity.

This significant difference is the source of potential profits from using this carbon capturing unit. This way could attract the power industry to adopt such carbon capturing systems that produce valuable chemicals to reduce carbon dioxide emissions and make financial profits

at the same time. Since the rate of CO_2 captured here is found to be 0.661 kg s^{-1}, ammonium bicarbonate is considered to be a serious method of carbon capture.

Table 5.18: Exergy rate, unit cost, and cost rates of all state points.

State No.	Exergy rate (kW)	Unit cost ($ kJ^{-1})	Cost rate ($ s^{-1})
1	8.29E+01	1.20E-05	9.94E-04
2	3.30E+04	7.00E-06	2.31E-01
3	1.34E+04	7.00E-06	9.40E-02
4	1.96E+04	7.00E-06	1.37E-01
5	8.37E+03	7.00E-06	5.86E-02
6	2.88E+00	7.00E-06	2.02E-05
7	4.92E+01	1.54E-05	7.58E-04
8	3.37E+01	7.00E-06	2.36E-04
9	0.00E+00	2.40E-06	0.00E+00
10	7.27E-01	2.86E-05	2.08E-05
11	8.67E+03	1.09E-05	9.41E-02
12	0.00E+00	0.00E+00	0.00E+00
13	7.52E+00	6.42E-04	4.82E-03
14	1.75E-18	1.51E-05	2.65E-23
15	6.29E+03	1.51E-05	9.51E-02
16	2.71E+01	3.26E-05	8.81E-04
17	1.55E+01	6.20E-03	9.60E-02
18	1.81E+01	4.94E-03	8.92E-02
19	0.00E+00	0.00E+00	0.00E+00
20	5.03E+00	6.42E-04	3.23E-03
21	1.30E+04	4.00E-06	5.20E-02
22	0.00E+00	0.00E+00	0.00E+00
23	2.56E+03	1.25E-05	3.19E-02
24	1.18E+04	7.60E-06	8.98E-02
25	5.73E+03	7.60E-06	4.36E-02
26	2.94E+02	7.60E-06	2.24E-03
27	2.95E+02	7.60E-06	2.24E-03
28	6.81E+00	1.49E-05	1.02E-04
29	2.09E+03	9.02E-06	1.89E-02
30	7.42E+03	8.16E-06	6.05E-02
31	6.10E+03	8.16E-06	4.98E-02
32	1.69E+03	8.16E-06	1.38E-02
33	0.00E+00	0.00E+00	0.00E+00
34	1.11E+03	3.26E-05	3.61E-02
35	0.00E+00	0.00E+00	0.00E+00
36	1.84E+02	8.61E-05	1.59E-02
37	1.48E+02	8.61E-05	1.28E-02
38	9.25E+01	8.61E-05	7.97E-03
39	0.00E+00	6.42E-04	0.00E+00
40	1.57E+00	4.94E-03	7.78E-03
41	9.03E+00	1.49E-05	1.35E-04

In Table 5.19, the results of the cost rates and their corresponding unit costs for the heat transfer and work streams are listed. Several can be observed from these results. To begin with, the unit cost of work for turbine 1, turbine 2, and turbine 3 are 1.05E-05, 1.05E-05,

and 1.18E-05 \$ kJ^{-1}, respectively. The interesting observation is that the unit cost per exergy for turbine 1, which is produced using solar energy, and for turbine 2, which is produced using the oxy-combustion Brayton cycle, are almost the same. As expected, turbine 3-unit cost of work is higher than turbine 2 since it uses waste heat recovery and more components to produce this work. The unit cost of heat transfer exergy of HX1 and condenser are high at values of 8.74E-05 and 1.49E-05 \$ kJ^{-1}, respectively. These indicate that the heat losses in these heat exchangers have some economic potential to produce more valuable outputs. It would be interesting to see how these can be utilized in future studies.

Table 5.19: Exergy rate, unit cost, cost rates of all heat transfer and work streams, and exergy destruction rates for all components. NA for not applicable.

Components	**Heat transfer exergy stream (kW)**	**Work exergy stream (kW)**	**Unit cost of heat transfer exergy (\$ kJ^{-1})**	**Unit cost of work exergy (\$ kJ^{-1})**	**Heat transfer cost rate (\$ s^{-1})**	**Work cost rate (\$ s^{-1})**	**Exergy destruction rate (kW)**
Parabolic solar collectors	0.00E+00	NA	0.00E+00	NA	0.00E+00	NA	46515
HX2	NA	NA	NA	NA	NA	NA	4727
T1	NA	9.03E+03	NA	1.05E-05	NA	9.50E-02	2196
HX1	6.72E+02	NA	8.74E-05	NA	5.87E-02	NA	8368
ECD	1.18E+01	3.72E+01	4.77E-05	1.05E-05	5.65E-04	3.92E-04	27.6
ASU	8.66E+00	1.05E+03	6.42E-04	1.05E-05	5.56E-03	1.10E-02	4175
EAS	1.27E+01	8.99E+03	1.51E-05	1.05E-05	1.91E-04	9.46E-02	3627
Mixer	NA	NA	NA	NA	NA	NA	11.59
AB reactor	0.00E+00	NA	4.94E-03	NA	0.00E+00	NA	4388
C1	NA	3.03E+03	NA	1.05E-05	NA	3.17E-02	476.6
Combustor	NA	NA	NA	NA	NA	NA	3700
T2	NA	5.59E+03	NA	1.05E-05	NA	5.84E-02	489.6
HX3	NA	NA	NA	NA	NA	NA	110.4
T3	NA	1.20E+03	NA	1.18E-05	NA	1.42E-02	112.4
C2	NA	4.30E+02	NA	1.18E-05	NA	5.08E-03	24.84
HX4	NA	NA	NA	NA	NA	NA	3353
MED	NA	NA	NA	NA	NA	NA	4816
Condenser	1.35E+02	NA	1.49E-05	NA	2.02E-03	NA	279.2

Table 5.20 lists the total investment cost rates of every component in the integrated system as well as the exergoeconomic performance parameters. The exergoeconomic factors for HX1 and condenser are very low at values of 0.21% and 0.20%, respectively, and these low values confirm the need to investigate utilizing the heat losses from these components to enhance their exergoeconomic factors. The f factors of HX1 and Condenser depend on two parameters, the total investment costs and the exergy destruction cost rates as shown

in equation 11. The f factors of these two components are very low because the exergy destruction cost rates are much higher than their respective investment costs due to the heat losses that occur in them. Another point that can be drawn from this table is the exergoeconomic factors for all the three turbines are higher than 50% with turbine 1 being the lowest of them. This indicates that these turbines are producing power at reasonable cost rates and acceptable exergy losses. Looking at the integrated system, the overall total investment cost rate is 2.73E-01 \$ s^{-1}, the overall exergy destruction cost rate is found to be 3.40 \$ s^{-1}. These result in an exergoeconomic factor of 7.43% for the entire integrated system. There are multiple multigeneration integrated systems with solar energy that have low overall exergoeconomic factors that are similar to the one calculated in this study [167–169].

Table 5.20: Total investment cost rates and exergoeconomic performance parameters for all components and the integrated system.

Components	**Total investment cost rate (\$ s^{-1})**	**Unit cost of fuel (\$ kJ^{-1})**	**Unit cost of product (\$ kJ^{-1})**	**Exergy destruction cost rate (\$ s^{-1})**	**Exergoeconomic factor**
Parabolic solar collectors	2.30E-01	0.00E+00	7.00E-06	0.00E+00	100.00%
HX2	2.63E-04	7.00E-06	1.09E-05	3.31E-02	0.79%
T1	1.64E-02	7.00E-06	1.05E-05	1.54E-02	51.56%
HX1	1.23E-04	7.00E-06	8.74E-05	5.86E-02	0.21%
ECD	1.73E-04	1.05E-05	4.77E-05	2.91E-04	37.32%
ASU	2.63E-03	1.05E-05	6.42E-04	4.36E-02	5.68%
EAS	7.24E-04	1.05E-05	1.51E-05	3.82E-02	1.86%
Mixer	0.00E+00	4.77E-05	6.20E-03	5.52E-04	0.00%
AB reactor	8.94E-04	6.22E-03	4.94E-03	2.73E+01	0.003%
C1	2.16E-04	1.05E-05	1.25E-05	4.98E-03	4.15%
Combustor	4.88E-03	6.58E-04	7.60E-06	2.44E+00	0.20%
T2	1.22E-02	7.60E-06	1.05E-05	3.72E-03	76.63%
HX3	3.31E-04	7.60E-06	8.16E-06	8.39E-04	28.29%
T3	3.47E-03	8.16E-06	1.18E-05	9.18E-04	79.10%
C2	2.55E-05	1.18E-05	9.02E-06	2.93E-04	8.00%
HX4	5.74E-05	8.16E-06	3.26E-05	2.74E-02	0.21%
MED	5.29E-04	3.26E-05	8.61E-05	1.57E-01	0.34%
Condenser	1.25E-05	6.42E-04	1.49E-05	1.79E-01	0.01%
Integrated system	2.73E-01	3.90E-05	5.10E-03	3.40E+00	7.43%

Implementing such an integrated system that produces electricity for a community with net-zero emissions due to the carbon capturing system that is powered by solar collectors

has real-world possibilities to be implemented for some reasons. For example, the fossil fuel industry is keen on promoting carbon capturing to maintain its status in the economy without having to sacrifice its environmental goals [170]. Another reason for implementing such a system is that the produced ammonium bicarbonate could have positive financial outcomes for the company that adopts such a technology. The third reason is carbon capture and utilization systems that are both environmental and profitable are necessary to reach the 2050 Net-Zero emissions goals set by the Paris agreement since they can be implemented as a retrofitting unit to existing thermal power plants and gives us time to build the infrastructure for more sustainable solutions, such as wind turbines and photovoltaic solar cells.

5.3.1 Parametric studies of system 3

Now, the results of the performed parametric studies of this integrated system will be discussed in this subsection. Figure 5.44 shows how changing the first parameter, which is the solar irradiance, affects the overall energy and exergy efficiencies, and the TES ratio (ε). As the solar irradiance increases from 0.45 to 0.90 kW m^{-2}, the overall energy and exergy efficiencies increase along with it, but these increase at different rates. The overall energy efficiency rises faster than the exergy one and this is due to the high temperature of solar irradiance which is 5770 K. Also, the TES ratio increases rapidly with the increasing of solar irradiance, and this is due to the fact that less mass flow rate is needed to run turbine 1 so that it produces enough electric power for the EAS and ECD components.

Figure 5.45 presents the effects of varying the temperature of state 2 which is the temperature of the stream that leaves the parabolic solar collectors on the overall energy and exergy efficiencies and the TES ratio. Starting with the overall energy and exergy efficiencies, they increase with increasing state 2 temperature in nonlinear manners. The rates at which they increase are very similar. As the temperature increase from 620 to 1020 K, the overall energy and exergy efficiencies increase from 16.6%, and 10.4% to 29.8%, and 13.9%, respectively. Furthermore, the TES ratio is increased in a nonlinear manner from a value of 0.340 to a value of 0.493.

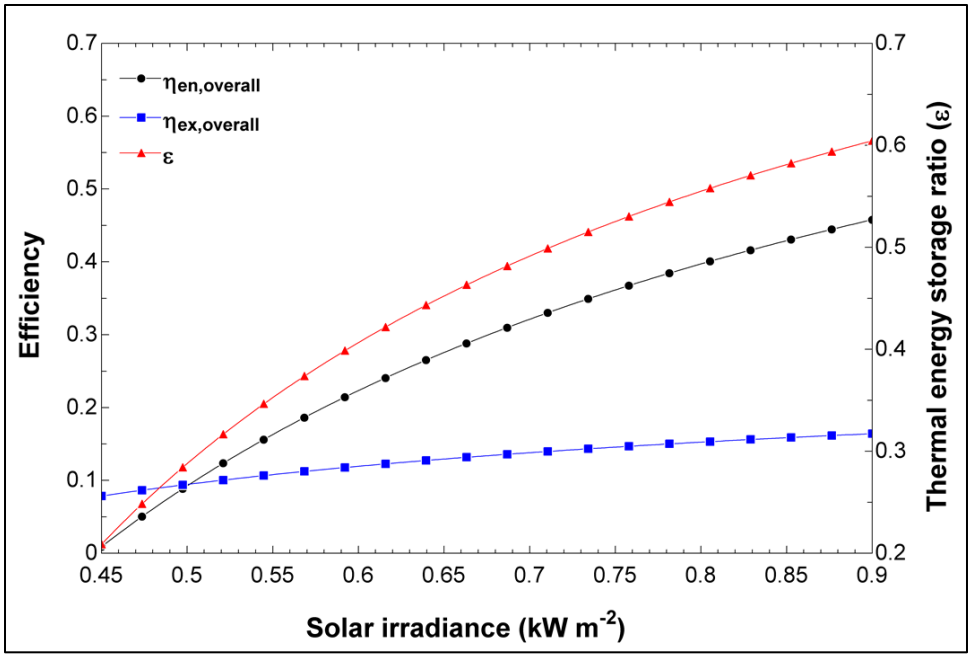

Figure 5.44: A plot of overall energy and exergy efficiencies and thermal energy storage ratio (ε) versus solar irradiance.

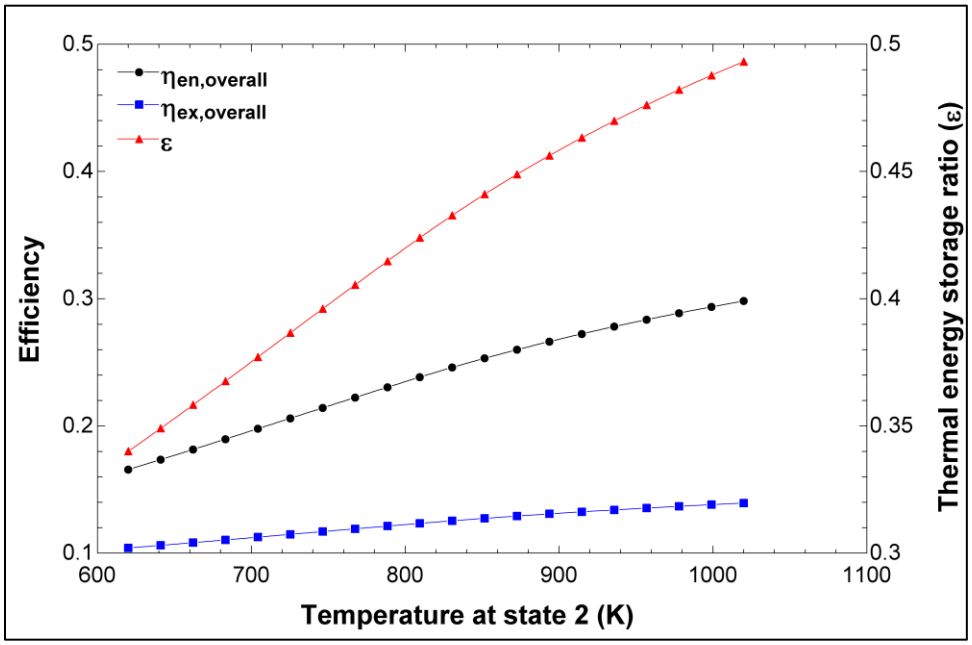

Figure 5.45: A plot of overall energy and exergy efficiencies and thermal energy storage ratio (ε) versus temperature of fluid leaving the parabolic solar collectors (state 2).

Figure 5.46 shows two other performance parameters that are affected by the state 2 temperature, which are the solar energy and exergy requirements for carbon capturing. The first thing to note is that the trends of these two performance parameters are dropping linearly with increasing magnitude of temperature 2. This means that less energy and

exergy from the solar subsystem is required to capture the same amount of CO_2 from the exhaust gases. The second thing to note is that the solar energy and exergy requirements for carbon capturing go from values of 76.4 and 72.5 MJ kg^{-1} of CO_2 down to 58.7 and 55.7 MJ kg^{-1} of CO_2, respectively, as the state 2 temperature increase from 620 to 1020 K.

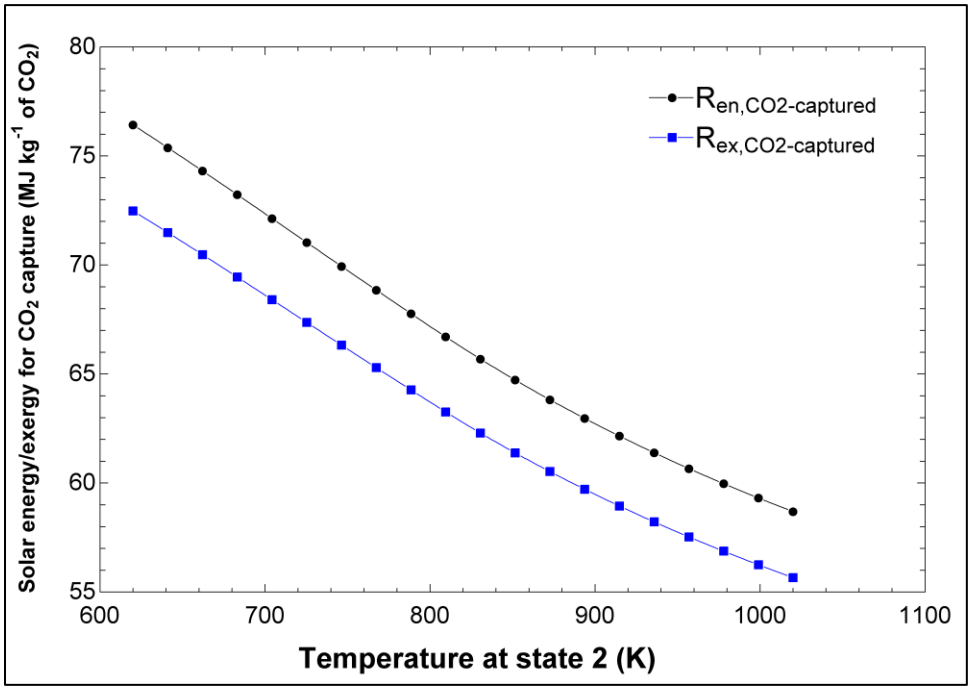

Figure 5.46: A plot of solar energy and exergy required for CO_2 capture versus temperature of fluid leaving the parabolic solar collectors (state 2).

Figure 5.47 is a plot of the trends of the TES ratio and the EAS power input as these are affected by the faradaic efficiency of the electrochemical ammonia synthesizer. The expected behavior of the EAS power input is clearly shown in the plot, as the efficiency of the device increases, less amount of electric power to produce the same mass rate of ammonia is needed. The interesting thing to note is that the trend of the EAS power input is decreasing nonlinearly from 12,400 kW down to 5,990 kW as the faradaic efficiency increases from 0.29 to 0.6. Regarding the TES ratio, the trend is opposite of the EAS power input. The ratio increases with increasing faradaic efficiency and this anticipated since less power output is needed from turbine 1.

Figure 5.48 shows how the single electrochemical component performance efficiency affects the overall energy and exergy efficiencies of the entire integrated system. First of all, the overall energy efficiency rises at a faster rate than the overall exergy efficiency over

this range of faradaic efficiency, that is 0.29 to 0.6. The overall energy efficiency goes from 2.95% to around 39.4%. Second of all, the overall exergy efficiency rises slow in a nonlinear manner from a value of 6.77% to a value of 16.5%. Thirdly, over the limited range between 0.29 and 0.31 of faradaic efficiency, the overall exergy efficiency is higher than the overall energy efficiency. Beyond this point, the overall energy efficiency becomes higher than the overall exergy efficiency. One reason for this behavior is that the TES ratio affects the overall energy efficiency than the overall exergy efficiency. This is observed when comparing the trends of TES ratio and overall energy efficiency.

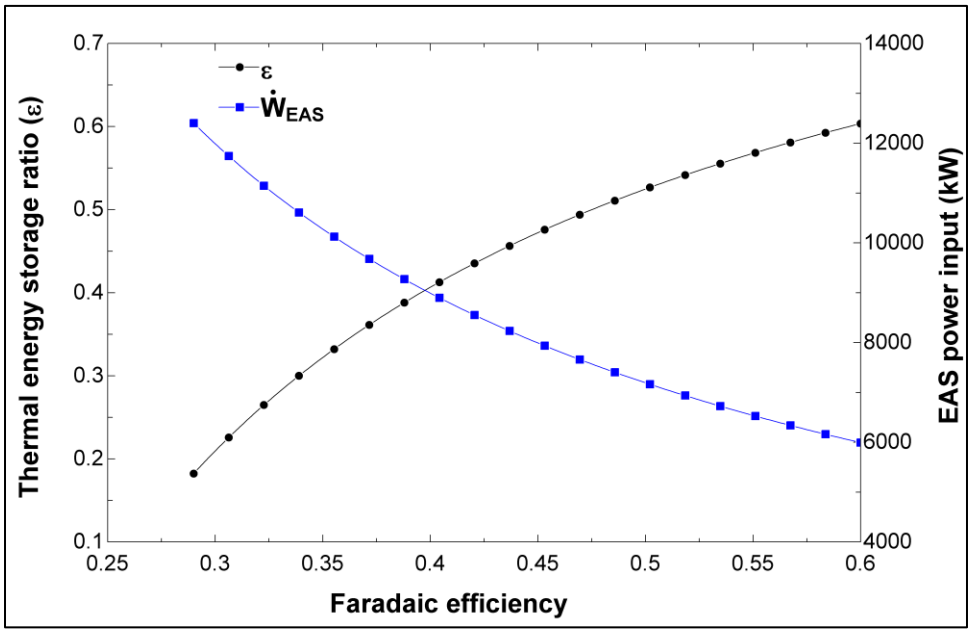

Figure 5.47: A plot of thermal energy storage ratio (ε) and EAS power input versus faradaic efficiency of EAS.

Figure 5.49 presents yet another parameter that is being changed to observe its effects on the integrated system. This parameter is the compression ratio of compressor 1 and it is changed from 4 to 12. In this range of compression ratio, the mass flow rate of air entering turbine 2 increases linearly from 8.05 kg s^{-1} to 9.11 kg s^{-1}. The reason behind this increase is to keep the inlet temperature of turbine 2 constant since increasing the compression ratio of C1 increases the temperature of air entering the combustor and this means more thermal energy will be involved in this component. If the mass flow rate was not increasing, then the added thermal energy from the compressor would result in increasing the temperature at state 24. Also, the net power production has an interesting parabolic behavior with a

maximum point at a compression ratio of 10.3 where the net power production reaches a value of 2,310 kW.

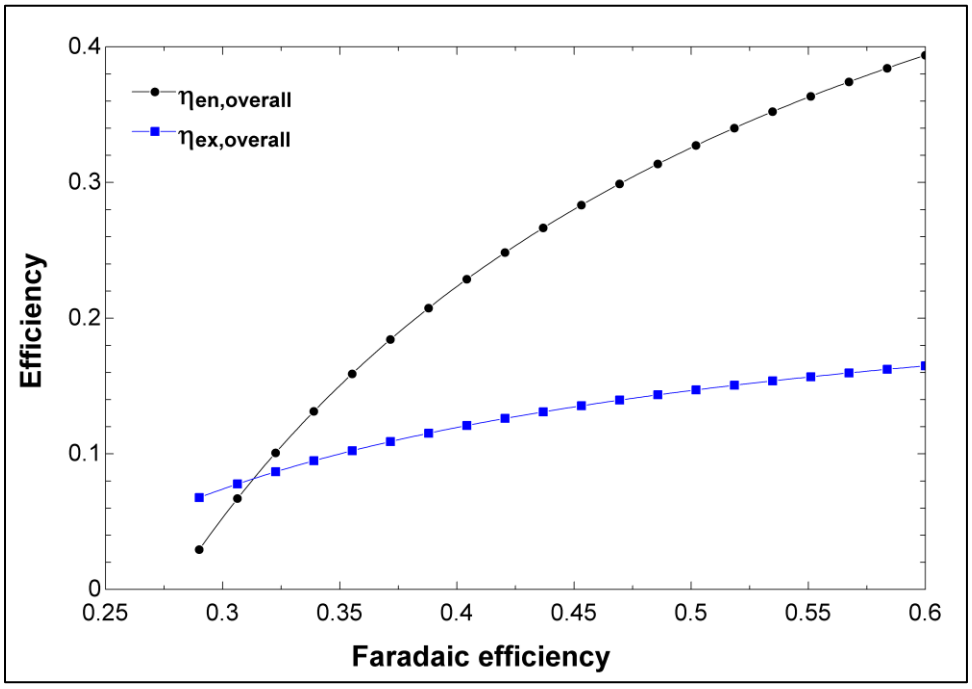

Figure 5.48: A plot of overall energy and exergy efficiencies versus faradaic efficiency of EAS.

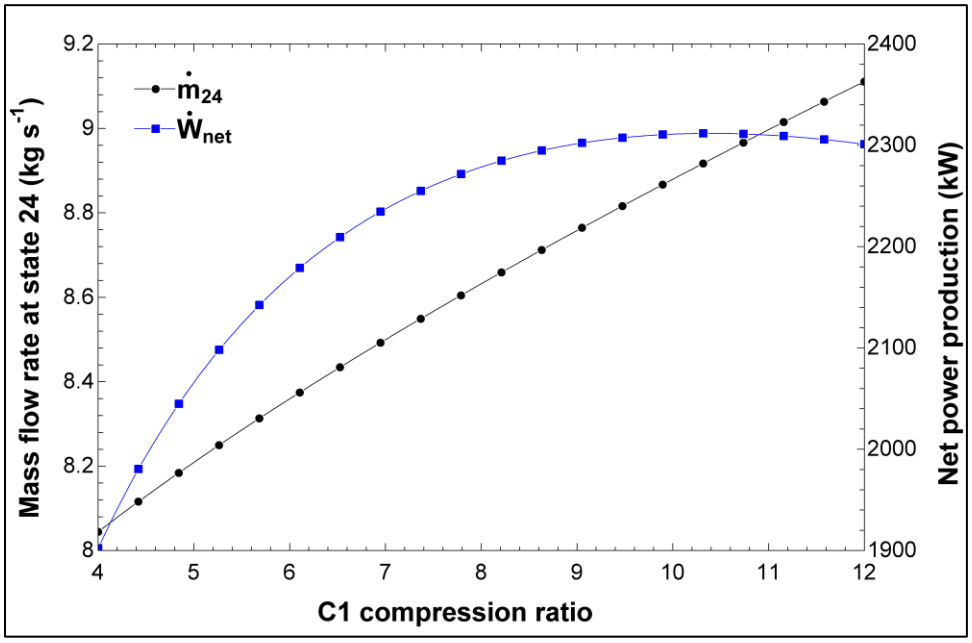

Figure 5.49: A plot of mass flow rate entering T2 (state 24) and net power production versus C1 compression ratio.

Figure 5.50 shows the behaviors of the overall energy and exergy efficiencies when the compression ratio of compressor 1 changes from 4 to 12. The overall energy efficiency is

improved in a nonlinear manner from 20.7% to 22.9% and there does not seem to be a maximum point that corresponds with the maximum point of net power production from the previous figure. The overall exergy efficiency also is enhanced from 11.5% to maximum points with a value of 12.0% over a range compression ratio between 9.47 and 11.6.

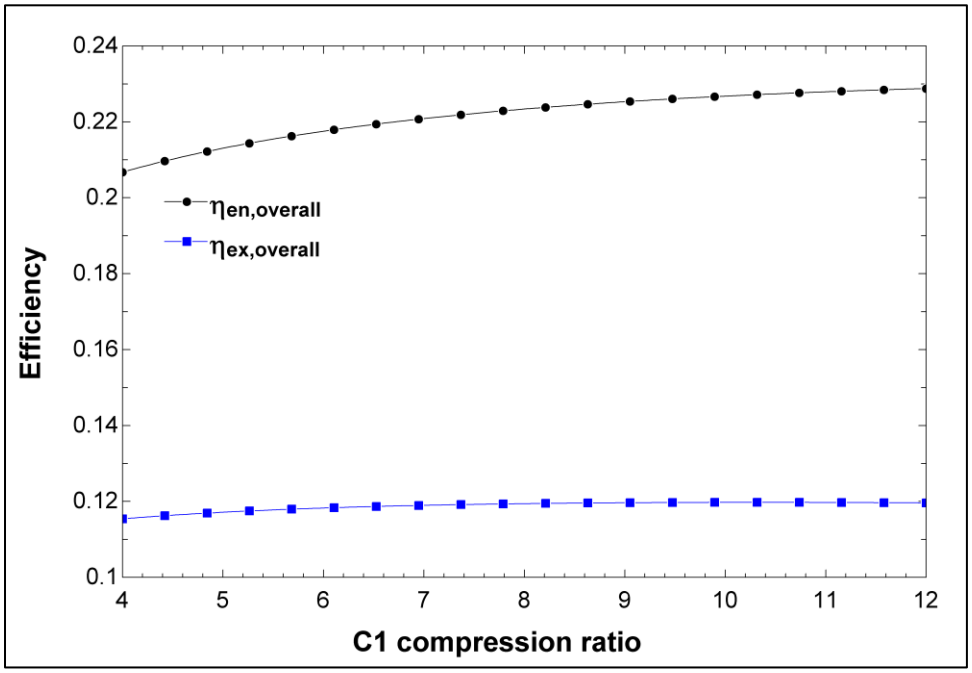

Figure 5.50: A plot of overall energy and exergy efficiencies versus C1 compression ratio.

Figure 5.51 displays how the mass flow rate at state 24 and the net power production are both affected by changing the isentropic efficiencies of C1 and C2. As the isentropic efficiencies increase go from 0.7 to 0.9, the mass flow rate of air entering turbine 2 decreases almost in a linear manner. This means less mass flow rate is needed to absorb the heat from the combustor since the stream leaving compressor 1 is at a lower temperature and this makes it easier to reach the set T2 inlet temperature. For the net power production, it obviously increases with the enhancement of the compressors isentropic efficiencies and this is because of power consumption of these two compressors is lowered with increasing isentropic efficiencies.

Figure 5.52 presents the effects of changing the isentropic efficiencies of compressor 1 and compressor 2 on the overall energy and exergy efficiencies. Generally, it seems that increasing the performance of both compressors does not have significant improvements

on the overall energy and exergy efficiencies. Even though the isentropic efficiencies increase by 20 percentage points, the overall energy efficiency is only improved by almost 1 percentage point, while the overall exergy efficiency is enhanced by less than 0.5%. There is some nonlinearity in both lines of the overall efficiencies, but this nonlinearity is insignificant. So, it is safe to say that these efficiencies have linear trends.

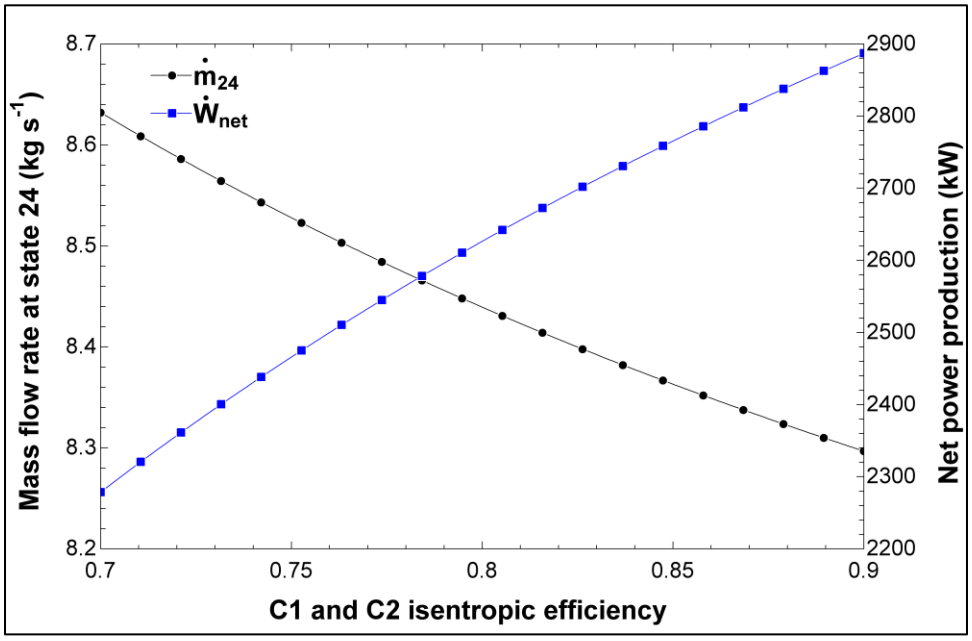

Figure 5.51: A plot of mass flow rate entering T2 (state 24) and net power production versus C1 and C2 isentropic efficiency.

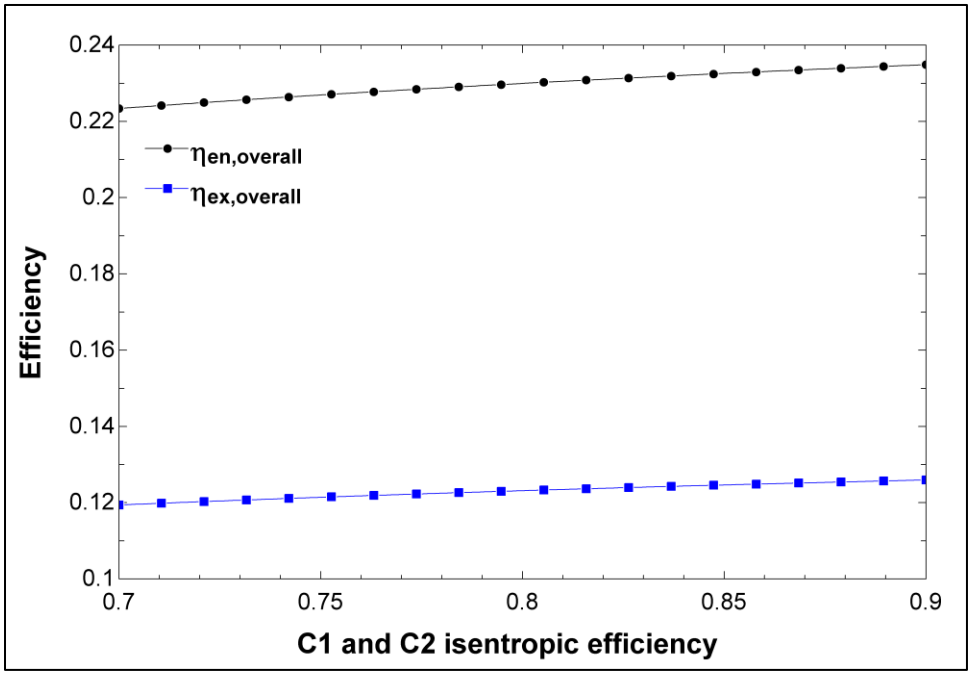

Figure 5.52: A plot of overall energy and exergy efficiencies versus C1 and C2 isentropic efficiency.

Figure 5.53 shows the results of improving the isentropic efficiencies of turbine 2 and turbine 3 on the mass flow rate at state 24 and the net power production. Interestingly, the mass flow rate entering turbine 2 stays constant over the range of isentropic efficiencies at value of 8.63 kg s^{-1}. This is because turbine 2 performance does not affect how much mass is needed to absorb the thermal energy from the combustor, only compressor performance affects this mass flow rate since it affects how much enthalpy enters the combustor. Looking at the net power production of the integrated system, there is an apparent increase, and it is significant in magnitude. As the isentropic efficiencies of T2 and T3 improve from 0.7 to 0.9, the net power production increase from 1860 kW to 3510 kW.

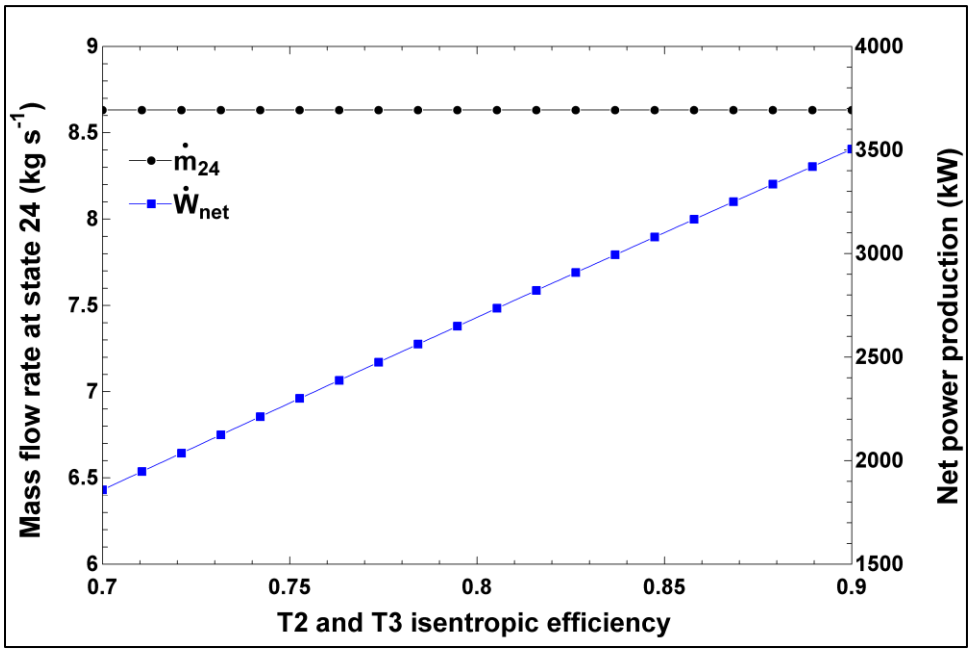

Figure 5.53: A plot of mass flow rate entering T2 (state 24) and net power production versus T2 and T3 isentropic efficiency.

Figure 5.54 contains the plots of the overall energy and exergy efficiencies and how these are affected by increasing the isentropic efficiencies of T2 and T3. Both energy and exergy efficiencies increase noticeably from values of 21.2% and 11.5% to 25.6% and 13.3%, respectively. These behaviors reflect the behavior of the net power production which increases with lowering the inefficiencies of turbine 2 and turbine 3. One thing to note about the behaviors of these efficiencies is that they are linear like the linear behavior of the net power production from the previous figure. However, the slopes of these

efficiencies are not the same, the overall energy efficiencies slope is higher than that of the overall exergy efficiency.

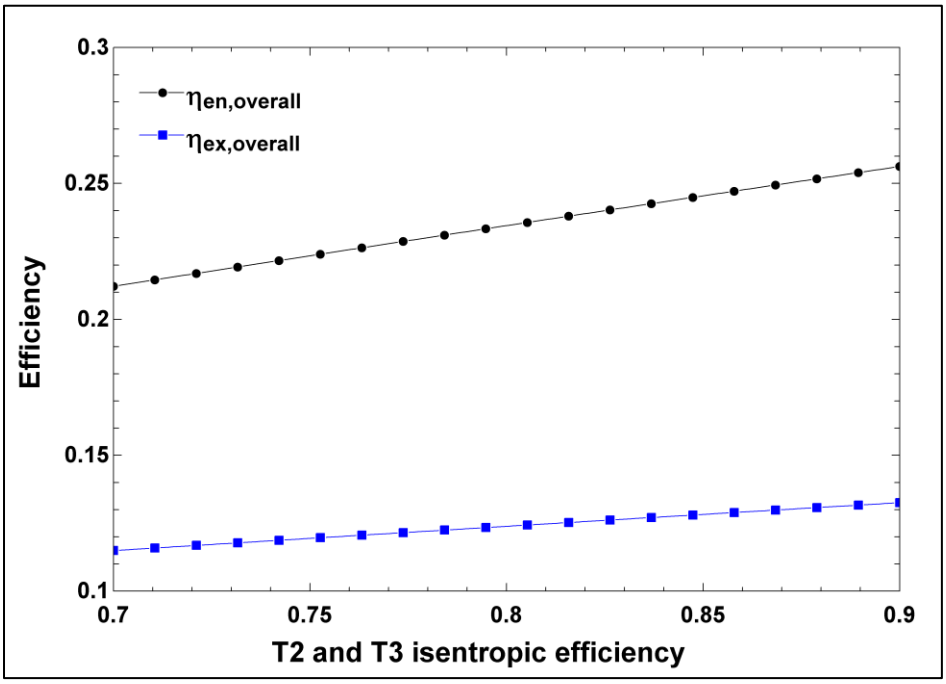

Figure 5.54: A plot of overall energy and exergy efficiencies versus T2 and T3 isentropic efficiency.

Figure 5.55 presents the last parameter being changed in this study which is the inlet temperature of turbine 2. The mass flow rate entering turbine 2 has a nonlinear decreasing trend from a value of 21.0 kg s^{-1} to a value of 8.63 kg s^{-1}. This is to allow the air to reach higher temperature levels when it goes through the combustor. For the net power production, the trend is as expected where it is improved with increasing the T2 inlet temperature from 1170 K to 1870 K. The trend of the net power production is nonlinear, and it increases from a low value of 444 kW to a much higher value of 2280 kW.

Figure 5.56 shows the effects of the inlet temperature to turbine 2 on the overall energy and exergy efficiencies of the integrated system. Both efficiencies increase in the same manner. The overall energy increase from a value of 20.8% to a value of 22.3%, and the overall exergy efficiency goes from 9.95% to a value of 11.9%. These increases occur as the T2 inlet temperature increase from 1170 K to 1870 K. Increasing this temperature has positive effects on the integrated system as shown because this increases the potential to produce more electric power using turbine 2. Also, this increases the temperature of the

waste heat that is supplied to the supercritical carbon dioxide cycle which is the bottoming cycle.

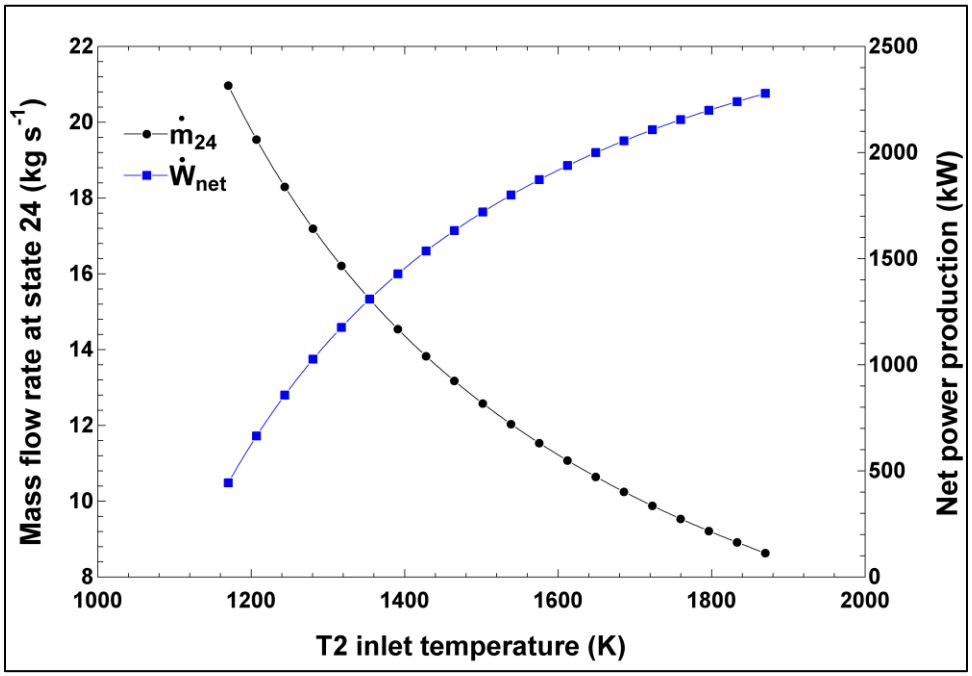

Figure 5.55: A plot of mass flow rate entering T2 (state 24) and net power production versus T2 inlet temperature (state 24).

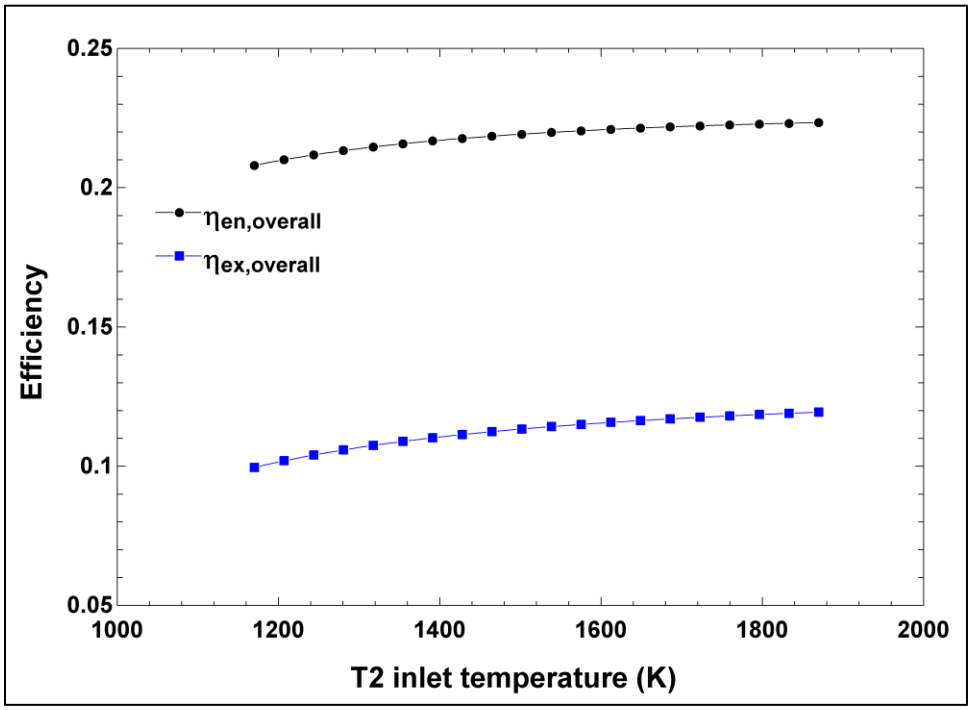

Figure 5.56: A plot of overall energy and exergy efficiencies versus T2 inlet temperature (state 24).

Figure 5.57 presents the carbon capture rate of this integrated system as it changes over a range of natural gas input to the system. There are two things to mention from this plot. Firstly, as the natural gas mass flow rate increases, the rate of carbon captured increases linearly. The increase of carbon capture rate goes from 0.289 to 1.16 kg s^{-1} as the natural gas input rate goes from 0.10 to 0.40 kg s^{-1}. Secondly, it is seen that the majority of the mass of the input natural gas becomes water that is rejected at the condenser rather than carbon dioxide mass flow rate since the slope of this linear trend is less than 0.5.

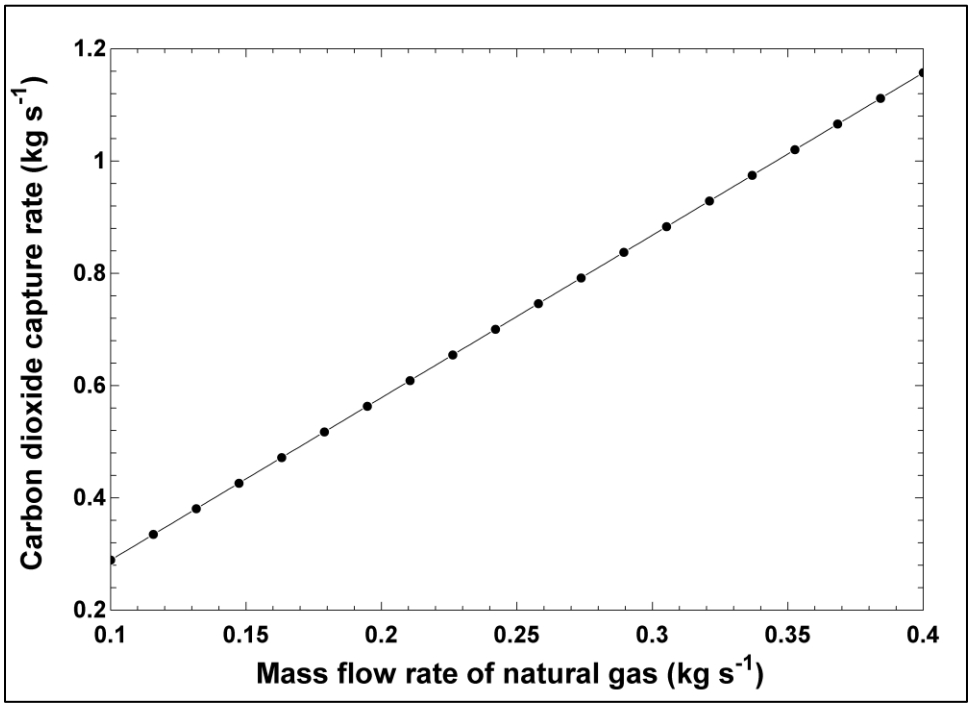

Figure 5.57: A plot of carbon dioxide capture rate versus mass flow rate of natural gas (state 21).

Figure 5.58 shows the change of ammonium bicarbonate production rate as the conversion rate of the chemical reaction at the ammonium bicarbonate reactor varies. The behavior of this production rate is linear, and it goes from 0.260 kg s^{-1} at a conversion rate of 0.20 to as high as 1.30 kg s^{-1}, when the conversion rate reaches unity. This plot shows that it is important to increase the conversion rate of this reactor to be able to produce more ammonium bicarbonate and increase the efficiency of the overall integrated system.

Figure 5.59 presents how the solar irradiance received by the solar collectors is affecting the overall exergy destruction rate, which is a measure of the exergetic performance of the entire integrated system, and the overall unit cost of products, which is a measure of the economic costs of producing all the useful outputs, namely electric power, space cooling,

freshwater, and ammonium bicarbonate. As the solar irradiance goes from 0.45 to 0.9 kW m^{-2}, the overall exergy destruction rate increases in a linear manner from around 72000 to as high as 116000 kW. In contrast, the overall unit cost of products drops as the solar irradiance increases. The value of the overall unit cost is from 0.0065 to 0.0038 \$ kJ^{-1}.

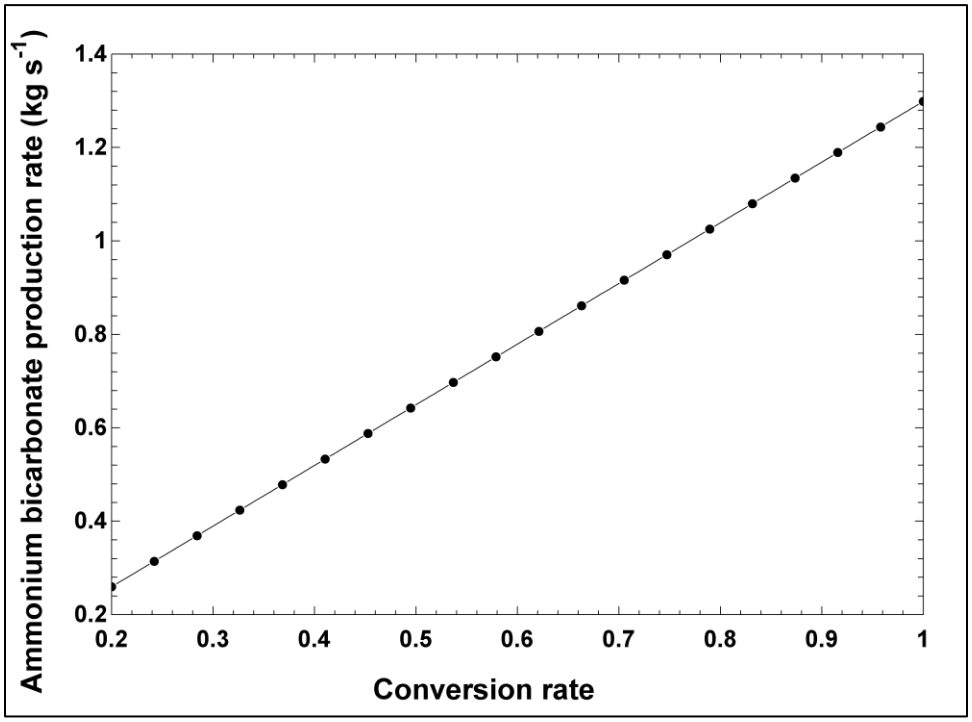

Figure 5.58: A plot of ammonium bicarbonate production rate (state 18) versus conversion rate.

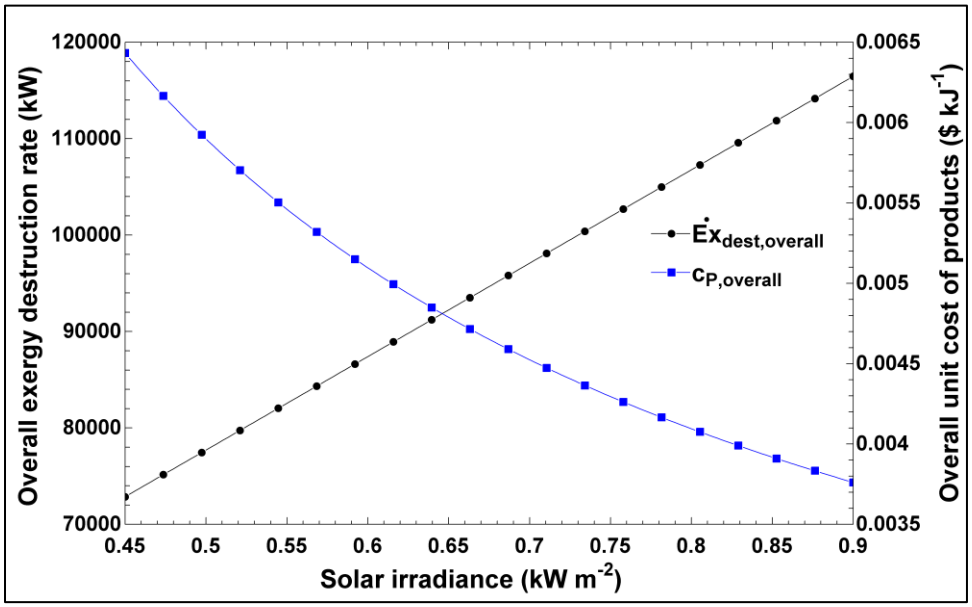

Figure 5.59: A plot of overall exergy destruction rate and overall unit cost of products versus solar irradiance.

Figure 5.60 shows the effects of solar irradiance on the overall total investment cost rate of the entire integrated system and the overall exergoeconomic factor. Two nonlinear trends appear from this plot. The first one is for the investment cost rate which increases as the solar irradiance rises. On the other hand, the overall exergoeconomic factor decreases from 0.088 to as low as 0.057. Decreasing the overall exergoeconomic factor means that the exergy destruction rate of the solar collectors due to increasing solar irradiance has measurable effects on the exergy destruction rate of the entire system. This means that better utilization of the thermal energy absorbed by the collectors could be suggested for further improvement of the integrated system.

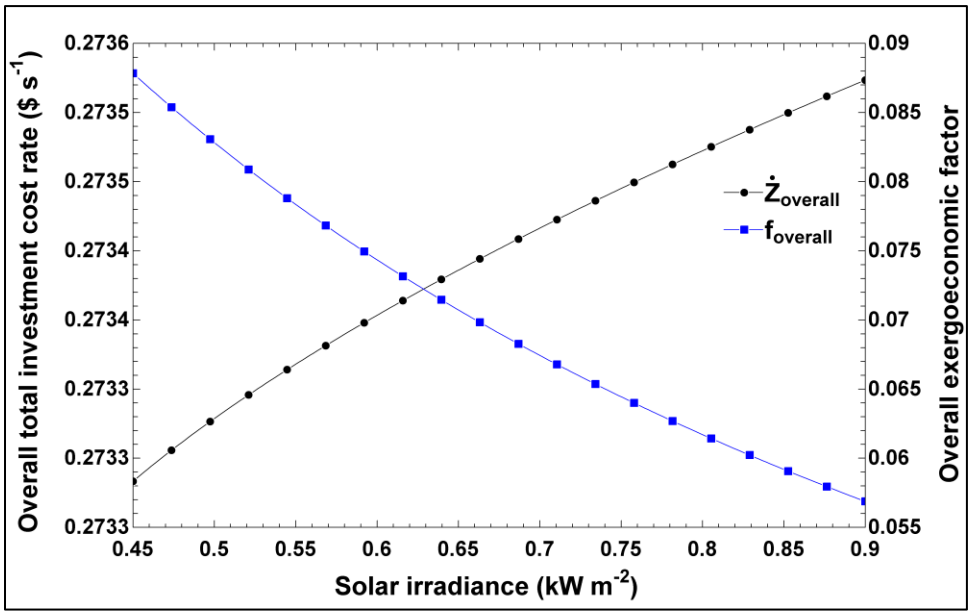

Figure 5.60: A plot of overall total investment cost rate and overall exergoeconomic factor versus solar irradiance.

Figure 5.61 displays the effects of varying the temperature of the fluid leaving the solar collectors on the overall exergy destruction rate and the overall unit cost of products of the integrated system. The good thing about increasing this temperature is that it reduces both the overall exergy destruction rate as well as the overall unit cost of products and these are desirable. The overall exergy destruction rate is reduced from around 88700 to 85500 kW in an almost linear trend, and the overall unit cost of products drops linearly from 0.0054 to 0.0045 \$ kJ^{-1}.

Figure 5.62 presents how this temperature affects the overall total investment cost rate and the overall exergoeconomic factor. Two opposite trends are noticed here. For the

investment cost rate, it decreases, and it goes from 0.274 to 0.2733 \$ s^{-1} in a nonlinear way as the temperature at state 2 increases from 620 to 1020 K. This is happening because increasing the temperature at state 2 means decreasing the mass flow rate going through the solar collectors. Lowering the mass flow going through the solar energy subsystem lowers the investment cost rates of each component in this subsystem. However, the exergoeconomic factor of the overall system rises in a somewhat linear manner from a value of 0.0732 to 0.0758 as the temperature at state 2 rises. This means that it is preferable to have the temperature at state 2 at higher values because this means that the overall exergy destruction cost rate of the integrated system is lowered, and better utilization of the solar energy is being done.

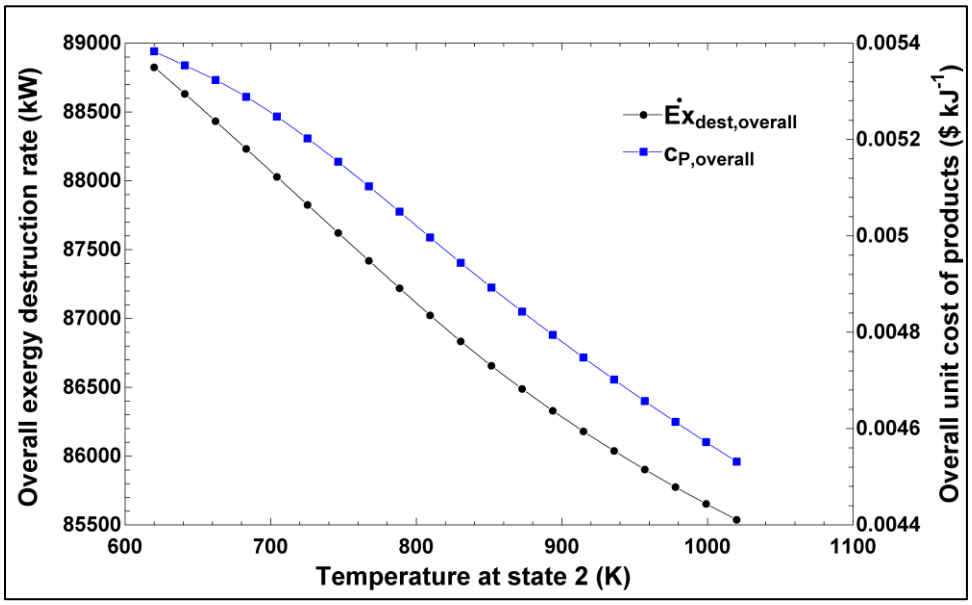

Figure 5.61: A plot of overall exergy destruction rate and overall unit cost of products versus temperature of fluid leaving the parabolic solar collectors (state 2).

Figure 5.63 shows how changing the compression ratio at compressor 1 for the oxy-combustion Brayton cycle influences the overall exergy destruction rate and the overall unit cost of products. As the compression ratio at C1 is increased from 4 to 12, the overall exergy destruction rate is reduced exponentially in a desirable way from a magnitude of 88200 to 87200 kW. On the contrary, the overall unit cost of products increases linearly from 0.005093 \$ kJ^{-1} when the compression ratio is 4 to 0.005101 \$ kJ^{-1} when the compression ratio is 12. Furthermore, Figure 5.64 presents the effects the compression ratio of compressor 1 has on the overall total investment cost rate and the overall

exergoeconomic factor. Some interesting patterns emerge from varying this parameter. First of all, the investment cost rate rises by a value of 0.006 \$ s^{-1} which is a 2.22% increase as the compression ratio goes from 4 to 12. The overall exergoeconomic factor has a parabolic pattern with a maximum value of 0.0743 when the C1 compression ratio is 7.2. This behavior of the exergoeconomic factor provides us with a range of optimum operations of the integrated system and this is why conducting such parametric studies is useful before going to the optimization study.

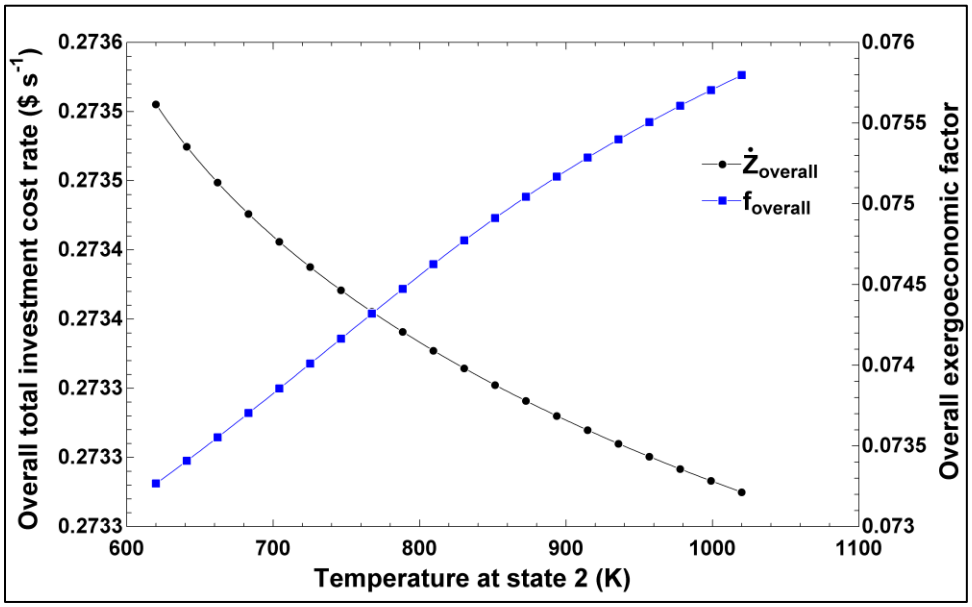

Figure 5.62: A plot of overall total investment cost rate and overall exergoeconomic factor versus temperature of fluid leaving the parabolic solar collectors (state 2).

Figure 5.65 is a plot of changing both the compressor 1 and compressor 2 isentropic efficiencies in the powering subsystem of the integrated system which includes the oxy-combustion Brayton cycle and the supercritical carbon dioxide cycle to see how these efficiencies affect the overall exergy destruction rate as well as the overall unit cost of products. As the isentropic efficiencies of both compressors increase from 0.7 to 0.9, the overall exergy destruction rate decreases linearly from 87400 to 86700 kW as expected because increasing the isentropic efficiency of these compressors directly means reducing the exergy losses at these two important components of the powering cycles. Also, the overall unit cost of products is minimized when the isentropic efficiency of these two compressors is set to be 0.87, but beyond this point, the overall unit cost is increased rapidly as shown in the figure.

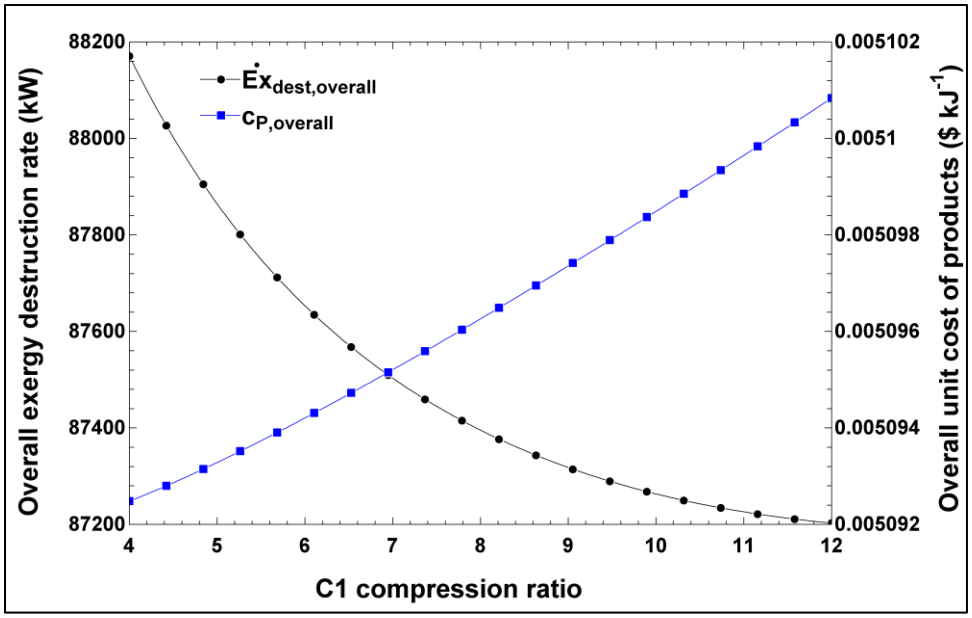

Figure 5.63: A plot of overall exergy destruction rate and overall unit cost of products versus C1 compression ratio.

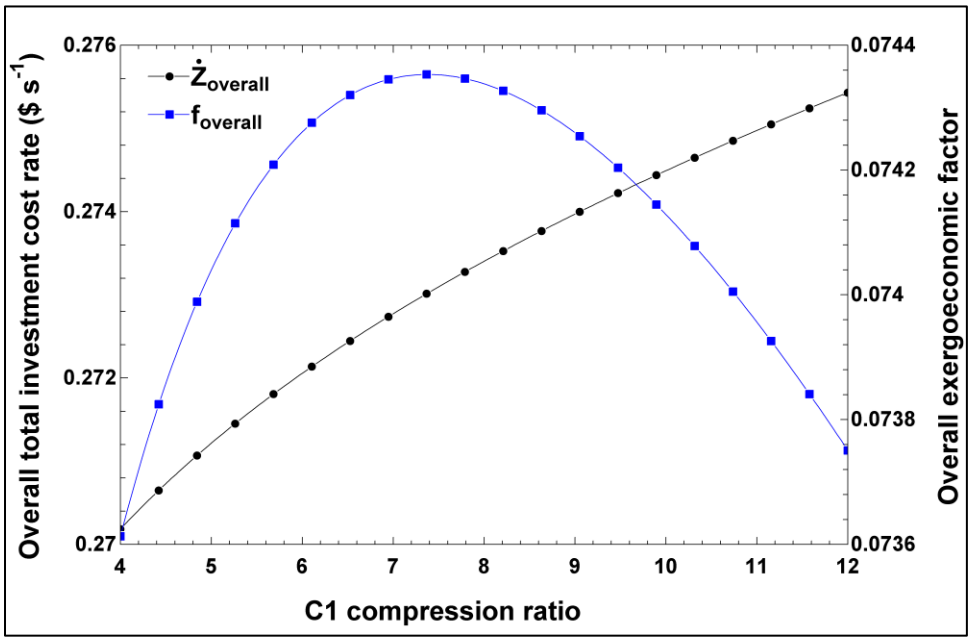

Figure 5.64: A plot of overall total investment cost rate and overall exergoeconomic factor versus C1 compression ratio.

Additionally, Figure 5.66 presents graphs of the overall total investment cost rate and the overall exergoeconomic factor as functions of the isentropic efficiency of compressors 1 and 2. The first thing to mention is the investment cost rate remains almost constant in the range between 0.7 and 0.85, but from 0.85 to 0.9, the investment cost rate rises very rapidly to a value of 0.2751 $ s^{-1}. The overall exergoeconomic factor has a parabolic behavior with

a maximum value of 0.078 at an isentropic efficiency of 0.88. This trend helps us in determining the range of isentropic efficiency so that this system is optimized regarding its exergoeconomic performance.

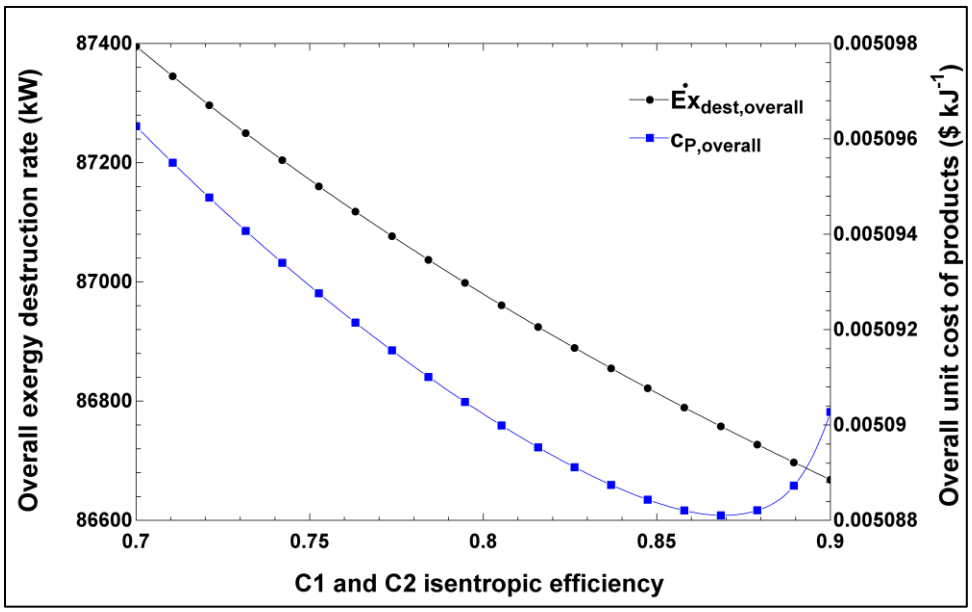

Figure 5.65: A plot of overall exergy destruction rate and overall unit cost of products versus C1 and C2 isentropic efficiency.

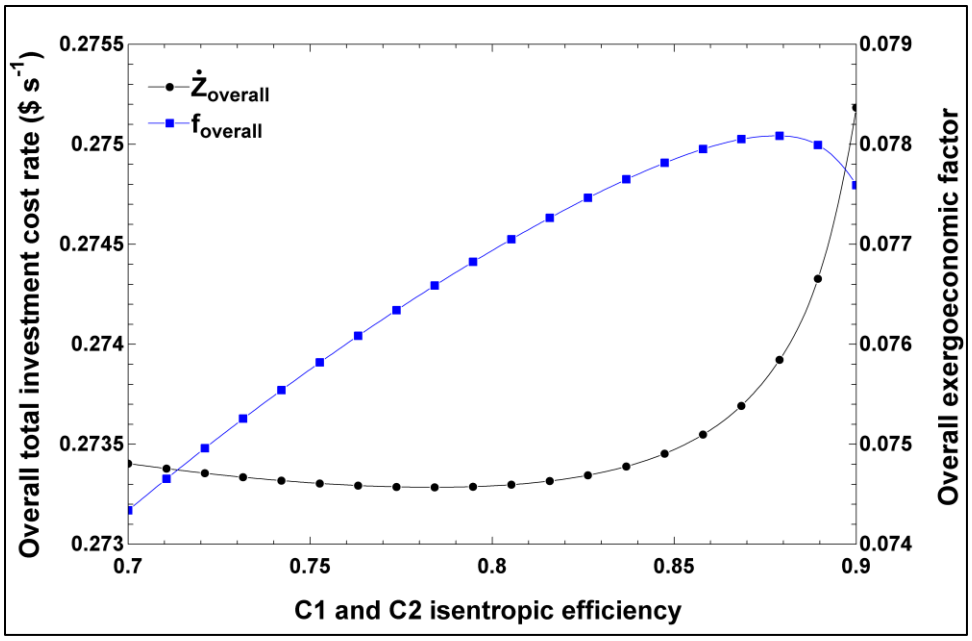

Figure 5.66: A plot of overall total investment cost rate and overall exergoeconomic factor versus C1 and C2 isentropic efficiency.

Figure 5.67 shows the overall exergy destruction rate and the overall unit cost of products behaviors as the isentropic efficiency of turbine 2 and turbine 3 are varied. As the isentropic

efficiencies of the two turbines increase in tandem from 0.7 to 0.9, a positive behavior of the overall exergy destruction rate is observed. This performance parameter of the integrated system is reduced from 88000 to 85500 kW. Similarly, the overall unit cost of products has a good trend of being reduced when the isentropic efficiency is enhanced. The unit cost goes from 0.0051 to 0.00508 \$ kJ^{-1}.

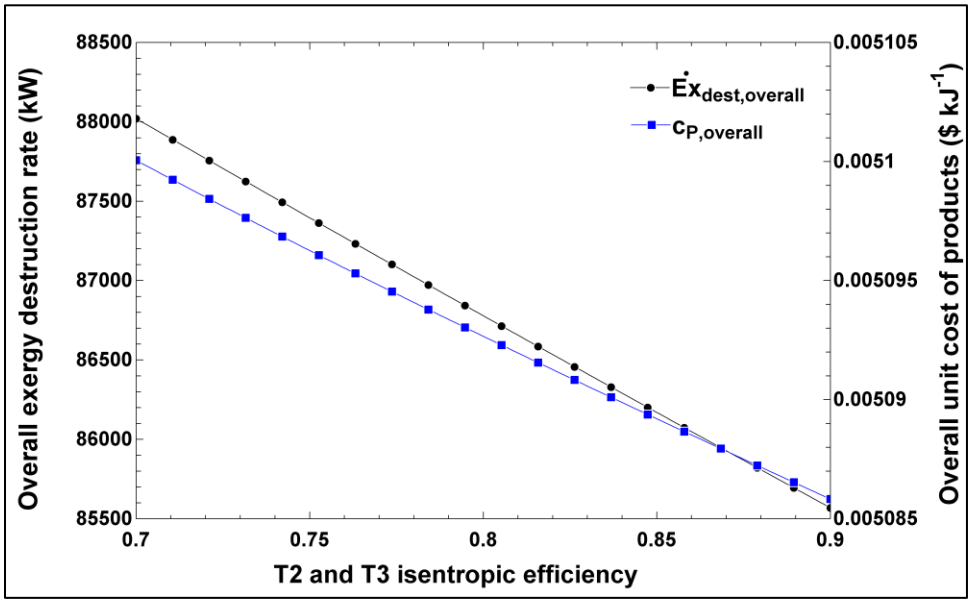

Figure 5.67: A plot of overall exergy destruction rate and overall unit cost of products versus T2 and T3 isentropic efficiency.

Figure 5.68 presents two other performance parameters of the integrated system, namely the overall total investment cost rate, and the overall exergoeconomic factor. When the isentropic efficiency of turbine 2 and turbine 3 go from 0.7 to 0.9, these two performance parameters rise in magnitude linearly. The investment cost rate rises by 1.1%, and the exergoeconomic factor improves by 12.5%.

Figure 5.69 illustrates the influences of altering the turbine 2 inlet temperature (state 24) on the overall exergy destruction rate and the overall unit cost of products. As the inlet temperature is increased from 1200 to 1870 K, the overall exergy destruction rate drops nonlinearly from 88700 to a little less than 87500 kW. Moreover, the unit cost of products has a parabolic curve with a minimum point of 0.00509 \$ kJ^{-1} when the inlet temperature is set at 1780 K. The highest value of this unit cost is reached when the inlet temperature is 1200 K. This means that this temperature should be in the vicinity of 1780 K to achieve a low overall unit cost of products for this integrated system.

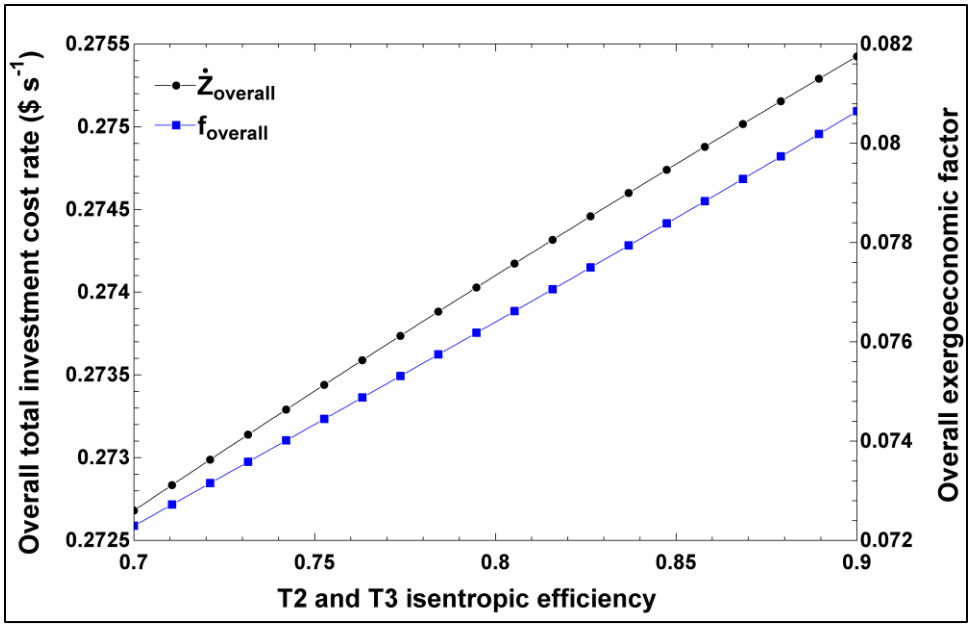

Figure 5.68: A plot of overall total investment cost rate and overall exergoeconomic factor versus T2 and T3 isentropic efficiency.

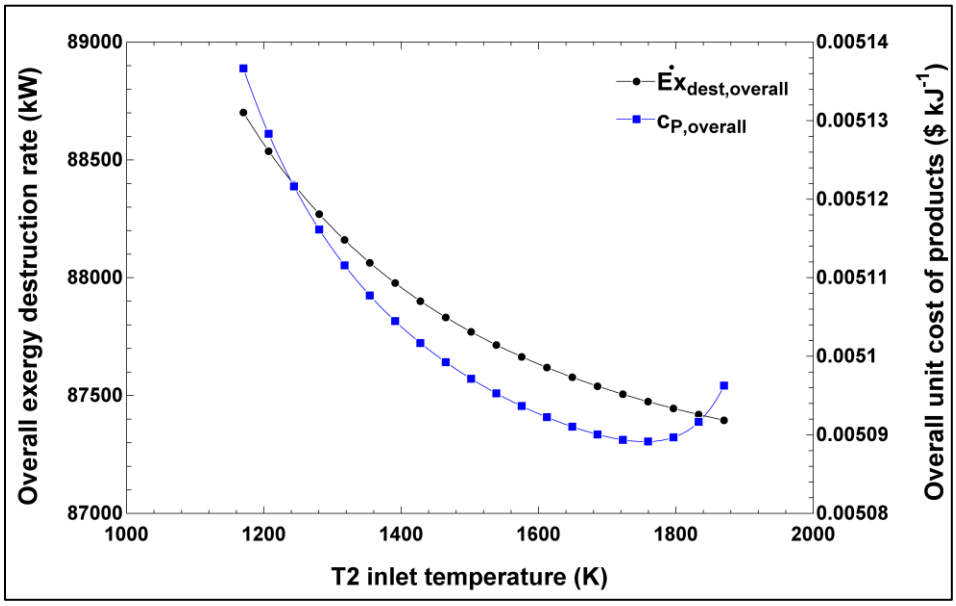

Figure 5.69: A plot of overall exergy destruction rate and overall unit cost of products versus T2 inlet temperature (state 24).

Figure 5.70 presents how turbine 2 inlet temperature changes the overall performance parameters of the integrated system which are the overall total investment cost rate and the overall exergoeconomic factor. When the inlet temperature is increased from 1200 to 1760 K, the overall total investment cost rate is reduced to a minimum value of 0.270 $ s^{-1}. When the inlet temperature is increased from 1760 to 1870 K, the cost rate rises dramatically. In

contrast, the overall exergoeconomic factor reaches a maximum of 0.0751 when the inlet temperature is 1760 K, then it drops significantly beyond this point.

A typical day in Jeddah, Saudi Arabia is taken as a case study to show the changes of solar irradiation in this location and how it affects the performance of the second integrated system. Figure 5.71 shows the variation of the overall energy and exergy efficiencies in the second integrated system over the time of day. When the time of day reaches the range where solar irradiance is high, the overall energy and exergy efficiencies are at their highest values during the entire day, while they reach lowest points when the sun is absent. Both of these efficiencies peak when the time of day is around 12 PM and the overall energy and exergy efficiencies have values of 35%, and 12% at this time. Figure 5.71 presents the changes of the power production of turbine 1 over a typical day. The power production curve peaks when the time is 12 PM and this coincides with the value of the highest energy and exergy efficiencies as discussed earlier. At this time, turbine 1 power production reaches a magnitude of 11,168 kW. When the sun is absent, the power production reaches low values, and the thermal energy storage unit must start to compensate for this lack of electric power.

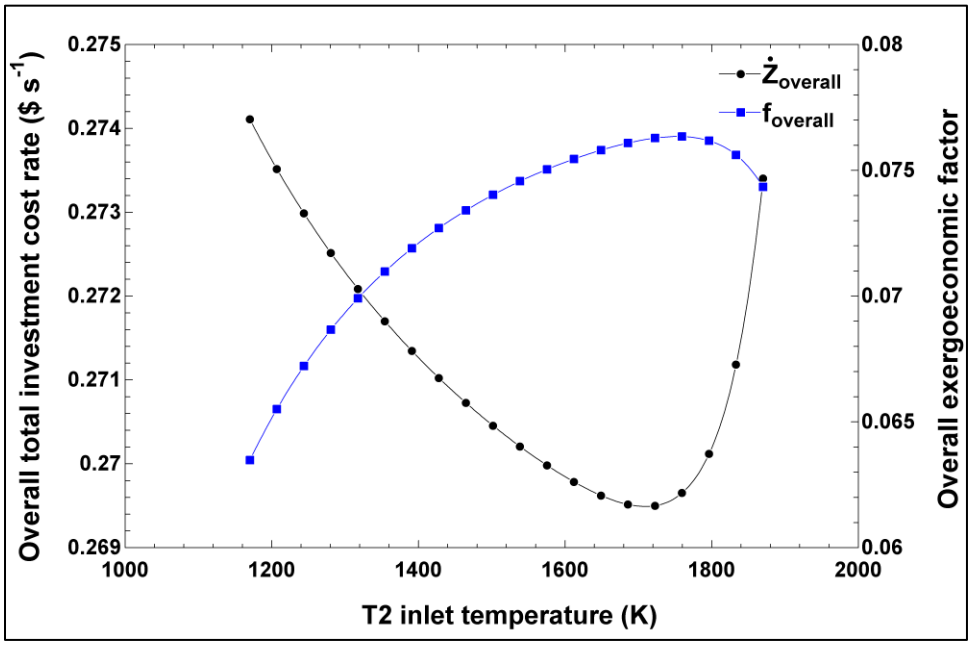

Figure 5.70: A plot of overall total investment cost rate and overall exergoeconomic factor versus T2 inlet temperature (state 24).

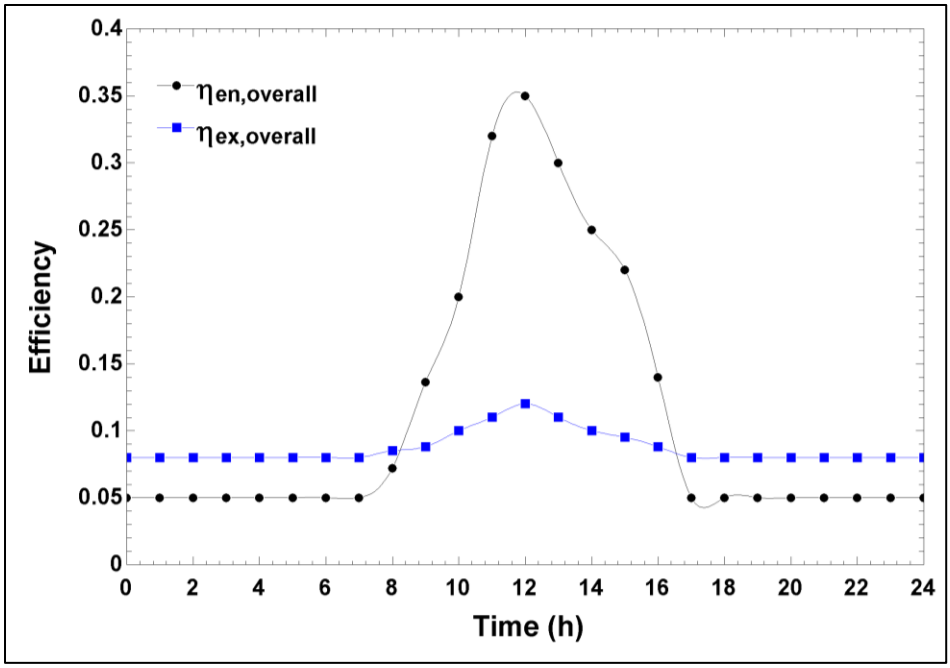

Figure 5.71: A plot of overall energy and exergy efficiencies versus time of day.

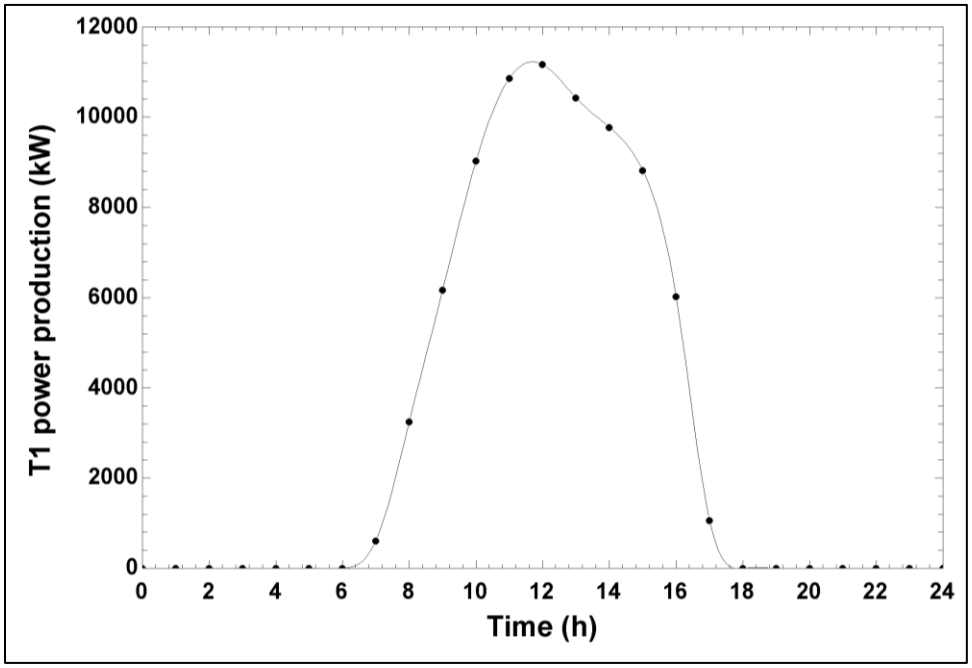

Figure 5.72: A plot of turbine 1 power production versus time of day.

5.3.2 Optimization study results of system 3

Now, the optimization findings of this present integrated system are discussed. Starting with Table 5.21, the objective functions and their selected models are presented. These were generated using the Eureqa software and it is noticed that these models have high

correlations with the trained data, higher than 0.999. This indicates that the accuracy of these models is reasonable and can be used to implement them in the multi-objective optimization method. One thing to notice in both models is that all four decision variables chosen for this optimization study are present in the objective function mathematical expressions generated using the genetic programming method.

Figure 5.73 shows the Pareto front produced after implementing the multi-objective optimization method using MATLAB. Three points are of interest to discuss here. The first point is Point A in the figure, and it represents where the overall exergy destruction rate is minimized, and the overall unit cost of products is relatively ignored. Point B is the opposite of this point, it indicates the point where the unit cost is minimized, and the overall exergy destruction rate is ignored. Thirdly, Point C is the chosen point because it is the closest point to the ideal point. This ideal point represents an imaginary point where both objective functions are minimized without a tradeoff. At the chosen point, the overall exergy destruction rate and the overall unit cost of products are 86000 kW and 5.19×10^{-3} \$ kJ^{-1}, respectively. A list of all the points on the Pareto front is given in Table 5.22.

Table 5.21: Objective functions models generated by Eureqa after five minutes of search time.

Objective functions	**Genetic programming selected models**	**Correlation coefficient (R^2)**	**Mean absolute error**	**Mean squared error**
Overall exergy destruction rate	$\dot{E}x_{dest,overall} = 17344 + 9.69\times10^{4}\times\dot{S}_{solar} + 25.74\times r_{c1} + 1.771\times T_{24} + \frac{7.839\times10^{6}}{T_{24}} + \frac{7200}{r_{c1}} + \frac{2309}{\eta_{c1}}$	0.999	5.09	61.2
Overall unit cost of products	$c_{P,overall} = 4.052\times10^{-4} + 1.026\times10^{-6}\times r_{c1} + 2.11\times10^{-7}\times T_{24} + \frac{0.5912}{T_{24}} + \frac{2.405\times10^{-3}}{\dot{S}_{solar}} - 5.14\times10^{-5}\times\eta_{c1}$	0.999	6.52×10^{-7}	1.09×10^{-12}

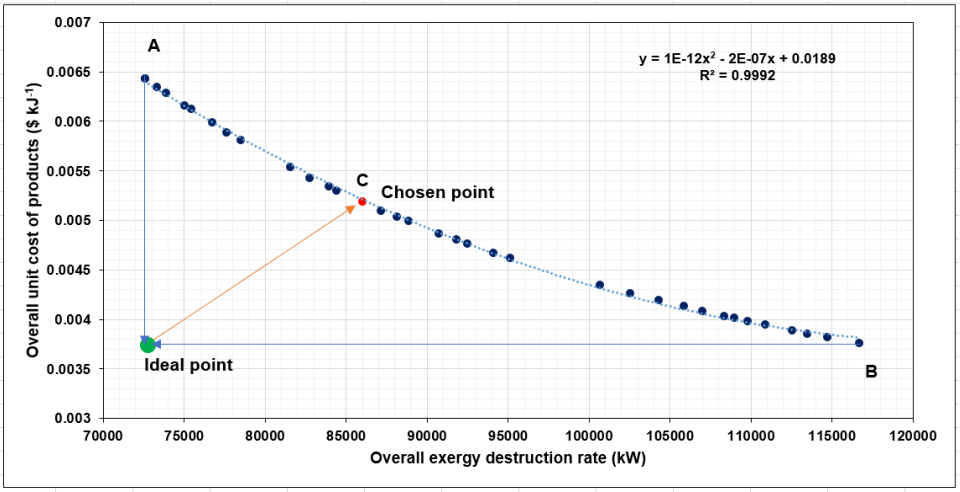

Figure 5.73: A plot of the Pareto front of the optimization study of the integrated system.

Table 5.22: Decision variables values for the optimum solutions and their corresponding objective functions values presented for system 3.

Solar irradiance (kW m^{-2})	**C1 compression ratio**	**C1 and C2 isentropic efficiency**	**T2 inlet temperature (K)**	**Overall exergy destruction rate (kW)**	**Overall unit cost of products ($ kJ^{-1})**
4.91E-01	8.22E+00	8.99E-01	1.37E+03	7.67E+04	5.99E-03
4.50E-01	1.19E+01	8.99E-01	1.38E+03	7.26E+04	6.43E-03
8.80E-01	5.99E+00	9.00E-01	1.37E+03	1.15E+05	3.82E-03
8.60E-01	7.53E+00	9.00E-01	1.36E+03	1.13E+05	3.89E-03
5.86E-01	7.80E+00	8.99E-01	1.37E+03	8.60E+04	5.19E-03
7.58E-01	9.43E+00	8.99E-01	1.37E+03	1.03E+05	4.26E-03
5.99E-01	9.51E+00	8.99E-01	1.37E+03	8.71E+04	5.10E-03
9.00E-01	5.81E+00	9.00E-01	1.36E+03	1.17E+05	3.76E-03
6.81E-01	9.17E+00	8.99E-01	1.37E+03	9.51E+04	4.62E-03
6.37E-01	1.06E+01	8.99E-01	1.37E+03	9.07E+04	4.87E-03
5.01E-01	9.58E+00	8.99E-01	1.36E+03	7.76E+04	5.89E-03
4.50E-01	1.19E+01	8.99E-01	1.38E+03	7.26E+04	6.43E-03
5.54E-01	9.75E+00	8.99E-01	1.37E+03	8.28E+04	5.43E-03
4.63E-01	9.48E+00	8.99E-01	1.37E+03	7.39E+04	6.29E-03
8.22E-01	6.73E+00	9.00E-01	1.36E+03	1.09E+05	4.01E-03
4.74E-01	8.71E+00	8.99E-01	1.37E+03	7.50E+04	6.16E-03
7.74E-01	7.12E+00	8.99E-01	1.36E+03	1.04E+05	4.19E-03
6.54E-01	9.62E+00	8.99E-01	1.37E+03	9.25E+04	4.76E-03
8.31E-01	7.12E+00	9.00E-01	1.37E+03	1.10E+05	3.98E-03
6.15E-01	7.63E+00	9.00E-01	1.37E+03	8.88E+04	5.00E-03
8.02E-01	7.15E+00	9.00E-01	1.36E+03	1.07E+05	4.09E-03
5.65E-01	7.52E+00	9.00E-01	1.37E+03	8.39E+04	5.35E-03
6.46E-01	7.87E+00	8.99E-01	1.37E+03	9.18E+04	4.81E-03
6.71E-01	8.75E+00	9.00E-01	1.37E+03	9.41E+04	4.67E-03
5.40E-01	7.36E+00	9.00E-01	1.37E+03	8.15E+04	5.54E-03
5.09E-01	8.46E+00	8.99E-01	1.37E+03	7.85E+04	5.81E-03
7.89E-01	6.23E+00	9.00E-01	1.37E+03	1.06E+05	4.13E-03
8.16E-01	7.16E+00	9.00E-01	1.36E+03	1.08E+05	4.03E-03
7.38E-01	8.59E+00	8.99E-01	1.37E+03	1.01E+05	4.35E-03
4.58E-01	1.12E+01	8.99E-01	1.38E+03	7.33E+04	6.35E-03
4.77E-01	7.25E+00	8.99E-01	1.37E+03	7.54E+04	6.13E-03
5.71E-01	9.37E+00	9.00E-01	1.36E+03	8.44E+04	5.30E-03
6.10E-01	9.35E+00	8.99E-01	1.37E+03	8.81E+04	5.04E-03
8.41E-01	6.61E+00	9.00E-01	1.36E+03	1.11E+05	3.95E-03
8.69E-01	6.91E+00	9.00E-01	1.36E+03	1.13E+05	3.86E-03

5.4 Experimental investigation results

In this section, the results of the experimental setup and procedure are presented and discussed. To begin with, Figure 5.74 shows a plot of temperature variation of the batch reactor for the different trials. Some things can be noticed from this figure. Firstly, the operating temperature for the baseline and catalyst cases are constant over the length of the trials and they are in the range of room temperature, which is between 23 and 24°C. One thing to observe is that the batch reactor temperature drops by almost 0.5°C from the start temperature to the end temperature. This is due to the fact that the ammonium bicarbonate reaction and the ammonia dissolution are endothermic reactions. Secondly, for the induction heating case, the operating temperature is higher than the other two cases by almost 12°C, but it starts at room temperature. The operating temperature of the induction heating case is between 35 and 40°C. Another observation is that it takes the induction heater less than 10 minutes to heat the batch reactor of 500 ml of mixture to the desired operating range.

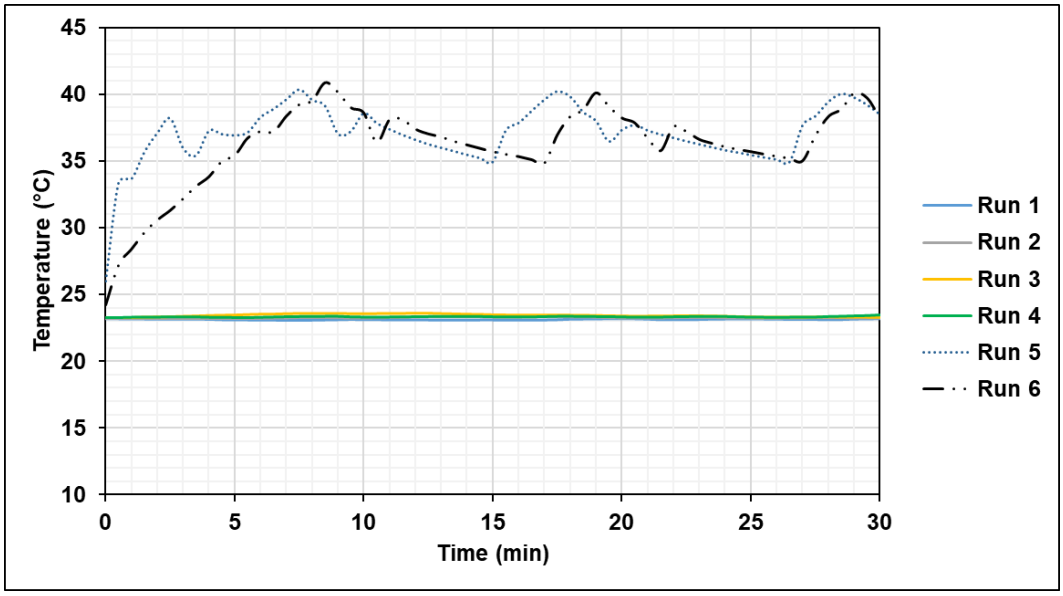

Figure 5.74: A plot of the batch reactor temperature over time for the different runs.

Figure 5.75 presents the mean temperature under which the batch reactor was operating for all the different experimental runs. It is noticed that the baseline and catalyst cases have similar temperatures with very minimal standard deviations, while the induction heating case are at a higher temperature level for the reactor which is in the desired range between 35 - 40.0°C. The standard deviations for the induction heating cases are larger due to the

wider range of operating temperature for these cases and for the fact that the induction heater was turned ON and OFF over the experimental time.

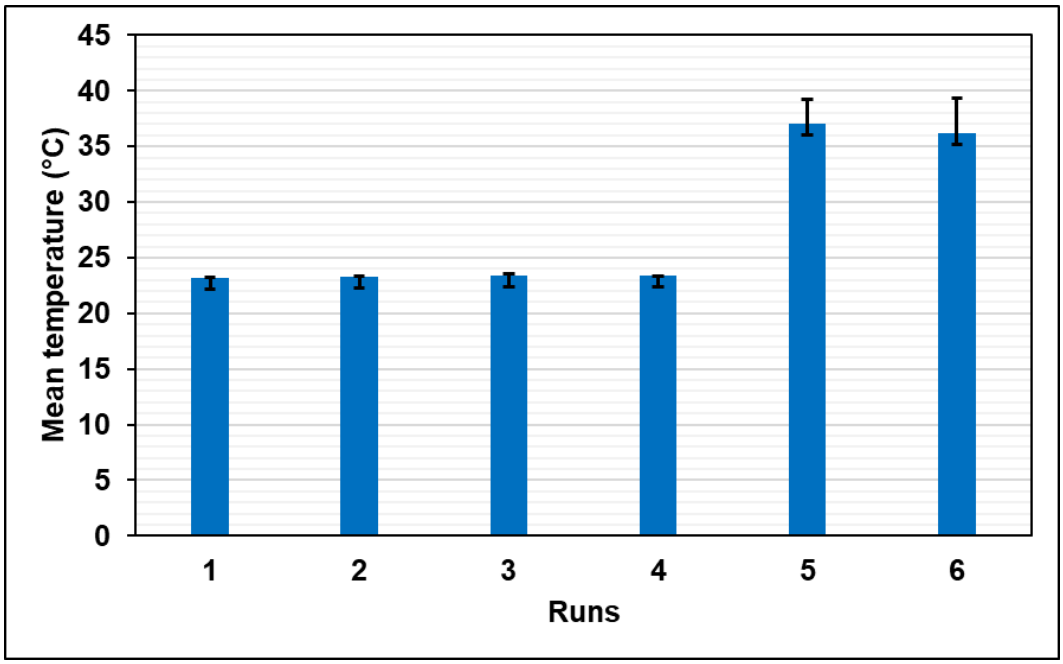

Figure 5.75: Mean operating temperature of the batch reactor for all the experimental runs.

Figure 5.76 displays a typical example of a pH level measurement after each trial in the experiment. This curve represents the pH level sensor converges to the true value of the solution after 50 seconds from the start of the measurement. When taking the final measurement of the pH level for each trial, only the last 50 seconds were taken into account and the reason behind this is this observed convergence of the sensor measurement. These pH level measurements were taken to ensure that the solution is at an acceptable range of pH for the formation of ammonium bicarbonate which is between 7 and 10.5.

Table 5.23 shows the complete pH level measurements for all the trials with their different compositions. It is noticed that the majority of the solutions fall in the range between 9 and 10.5 for the pH level and this is a good range for maintaining the formed ammonium bicarbonate according to studies and modeling done by Chen et al. [104]. This is to guarantee the purity of the formed ammonium bicarbonate. As the solution losses its ammonia content, this pH level reduces to 7 and the possibility of forming ammonium carbonate are reduced during the natural drying process. One thing to notice is that for the induction heating cases, the pH level is lower, and this could indicate more consumption

of ammonia in the solution to form ammonium bicarbonate compared to the other two cases.

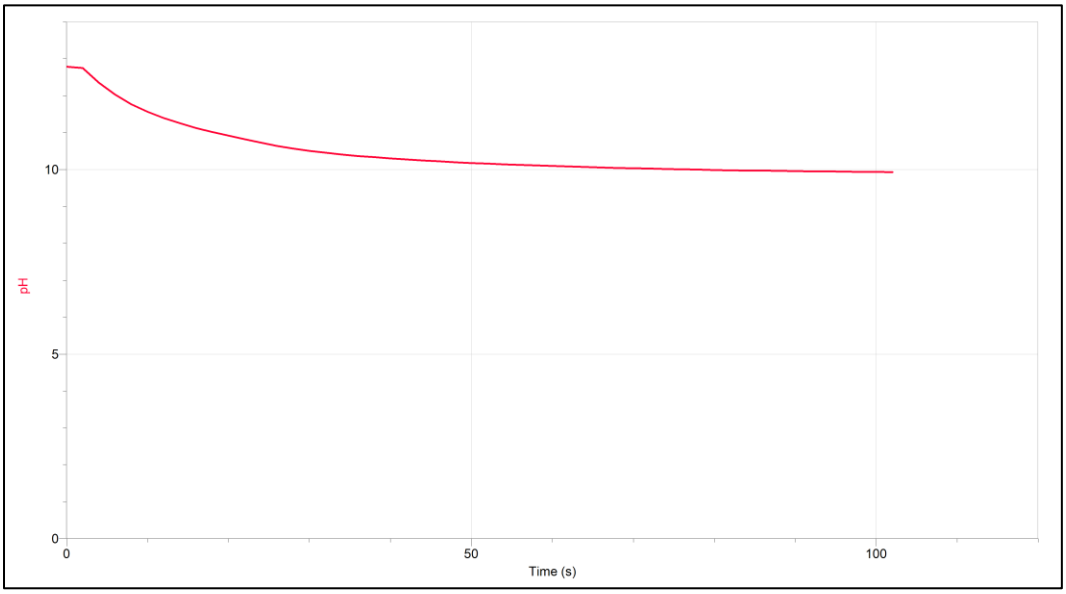

Figure 5.76: A plot of the solution pH level over time after the run is done for the Catalyst case with 80%mol of CO_2.

Table 5.23: pH level measurements of the end solutions of the different experimental runs.

Runs	**1**	**2**	**3**	**4**	**5**	**6**
pH level	10.3	9.8	10.8	10.9	10.4	9.1

Figure 5.77 presents the current measurements over the period of the trials for the induction heating cases. This current is the electric current supplied to the ZVS unit for the electromagnetic induction heater. It is noticed that the supply of electricity to the induction heater is mainly for the first 8 minutes of the experiment and after that, the current goes to zero because the temperature of the batch reactor remains within the desired range from time period between 8 and 16 minutes. After this point, the induction heater is switched on for a short time period (around 2 minutes) to reheat the batch reactor back to the desired operating temperature range. Then, this reheating lasts for another 8 minutes of the experiment. This indicates that there is no further need to supply heat to the reactor and this is another advantage of using this induction heater. It only needs to work at the beginning of the experiment, and it can be turned off quickly by cutting the current rather than a typical resistance heater that requires time to cool off and loss heat to the environment. Induction heaters only supply heat selectively to the metallic catalysts at desired times with short transients. All these features of the induction heater reduce the energy demand for this ammonium bicarbonate production process. Figure 5.78 shows the

energy consumption of the induction heater for the two runs of the induction heating case. The energy consumption for run 5, which is the experimental run with 30%mol CO_2 and a catalyst, is 22.1 kJ, while the energy consumption for run 6, which is the experimental run with 80%mol CO_2 and a catalyst, is 21.9 kJ. It does not seem that the CO_2 concentration has a significant effect on the amount of energy consumption by the induction heater.

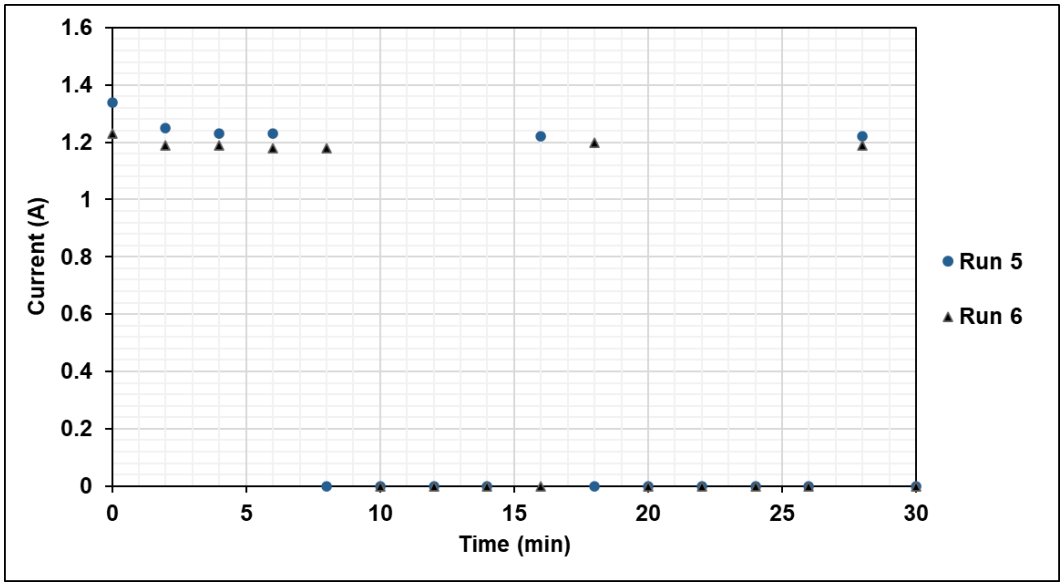

Figure 5.77: A plot of the supplied current to the induction heater over time for the Induction heating cases.

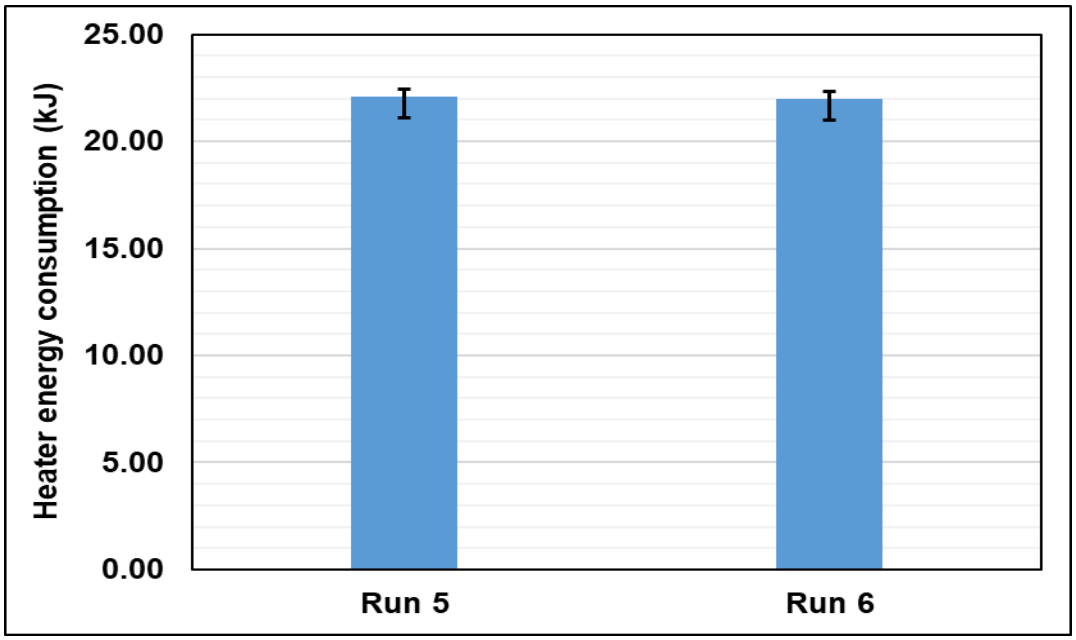

Figure 5.78: A plot of the energy consumption of the induction heater for the Induction heating cases.

Table 5.24 presents an initial screening of the significance of all the three factors and their four possible interactions up to the third order. First thing to notice is that the interactions

of BC and ABC have zero adjusted sum of squares and were not included in the results, and this means that these two interactions are purely insignificant and due to random error. Second thing to notice is that the two weakest sources of variance are C and AC according to their sum of squares, and these can be considered insignificant for this initial screening of variables. However, A, B, and AB sources of variance require further investigation, and this will be done in the second round of ANOVA treatment. It is interesting to find out that the use of an induction heater to increase the production of ammonium bicarbonate is statistically insignificant according to this analysis and the same goes for the interaction of the induction heater and the CO_2 concentration.

Table 5.25 lists the selected sources of variance and their ANOVA results. The most significant source of variance is B which is the addition of the steel catalyst which has a P-value of 0.2%. This indicates that there is a very low probability that the changes in the ammonium bicarbonate production were due to random errors. Another factor that is causing almost significant changes in the production of ammonium bicarbonate is the CO_2 concentration. Also, the interaction of these two factors seems to have a good chance of being significant enough to cause effects to the mass production from the batch reactor. Further investigation to this interaction is needed and it is suggested for future studies. Table 5.26 presents the regression equation that describes how the three sources of variance affects the mass produced by the batch reactor of ammonium bicarbonate.

Table 5.24: Comprehensive ANOVA results for all factors and their interactions.

Source of variance	**Degree of Freedom**	**Adjusted Sum of Squares**	**Adjusted Mean Square**	**F-Value**	**P-Value**
A	1	0.000083	0.000083	2.08	0.200
B	1	0.000422	0.000422	10.6	0.017
C	1	0.000002	0.000002	0.06	0.813
AB	1	0.000069	0.000069	1.74	0.236
AC	1	0.000005	0.000005	0.13	0.732
Error	6	0.000239	0.000040		
Total	11	0.00116			

Table 5.25: ANOVA results for the selected factors and interaction.

Source of variance	**Degree of Freedom**	**Adjusted Sum of Squares**	**Adjusted Mean Square**	**F-Value**	**P-Value**
A	1	0.000139	0.000139	4.53	0.066
B	1	0.000606	0.000606	19.7	0.002
AB	1	0.000069	0.000069	2.23	0.173

Error	8	0.000246	0.000031		
Total	11	0.00116			

Table 5.26: Regression equation for the selected factors and interaction.

Regression equation	Ammonium bicarbonate mass = 0.0228 + 0.00361×A + 0.00754×B + 0.00254×AB		
Term	Coefficient	SE Coefficient	P-value
Constant	0.02276	0.00170	0.000
A	0.00361	0.00170	0.066
B	0.00754	0.00170	0.002
AB	0.00254	0.00170	0.173

Figure 5.79 shows the main effects on the mass production of ammonium bicarbonate in the batch reactor and how it responds to the most significant sources of variance. B, which is the addition of the steel catalyst, has the highest positive effect on the production. AB, which is the interaction between the CO_2 concentration and the steel catalyst, also has a positive effect on the production of ammonium bicarbonate, but it is the lowest. In addition, it is noticed that increasing both the CO_2 concentration of flue gases and adding a steel catalyst seem to be statistically significant ways to improve the production of ammonium bicarbonate for carbon capturing and utilization.

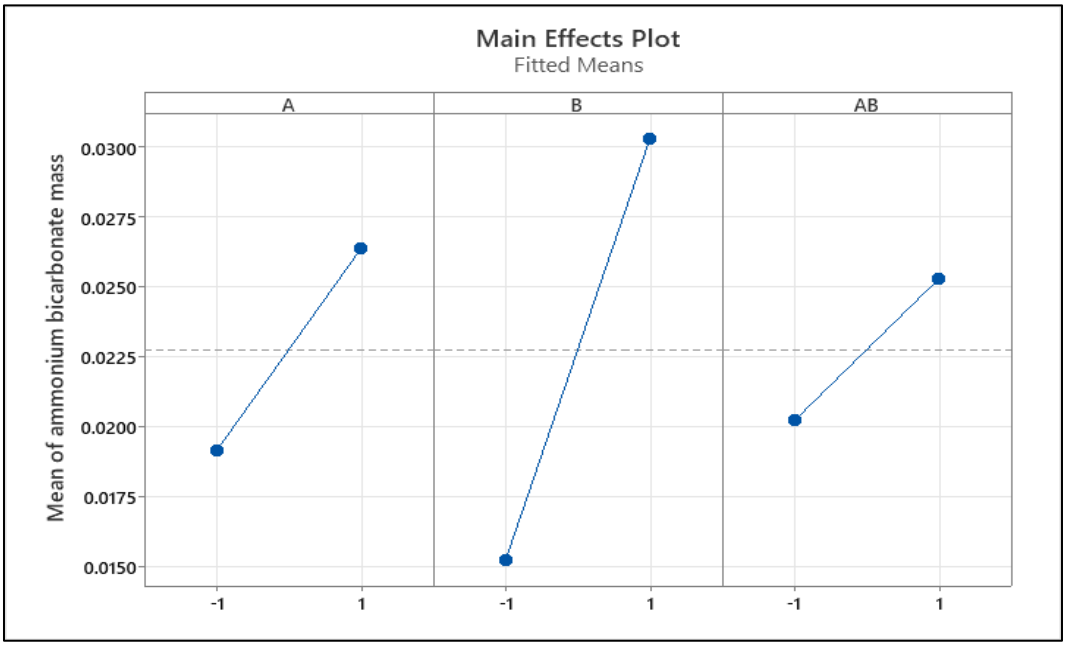

Figure 5.79: A plot of the main effects of the selected factors and interaction on the mass production of ammonium bicarbonate.

Figure 5.80 displays the 95% confidence interval for each run in the experiment according to Table 3.2 which shows the ammonium bicarbonate production mass. It clearly shows that when the induction heater is used, a larger interval is needed and this adds more evidence to the earlier results that showed using an induction heater is not a significant source of variance, unlike using a steel catalyst or changing the carbon dioxide concentration in the batch reactor. The shortest intervals exist when the induction heater is turned OFF and when a steel catalyst is used with low concentration of CO_2 is injected to the batch reactor.

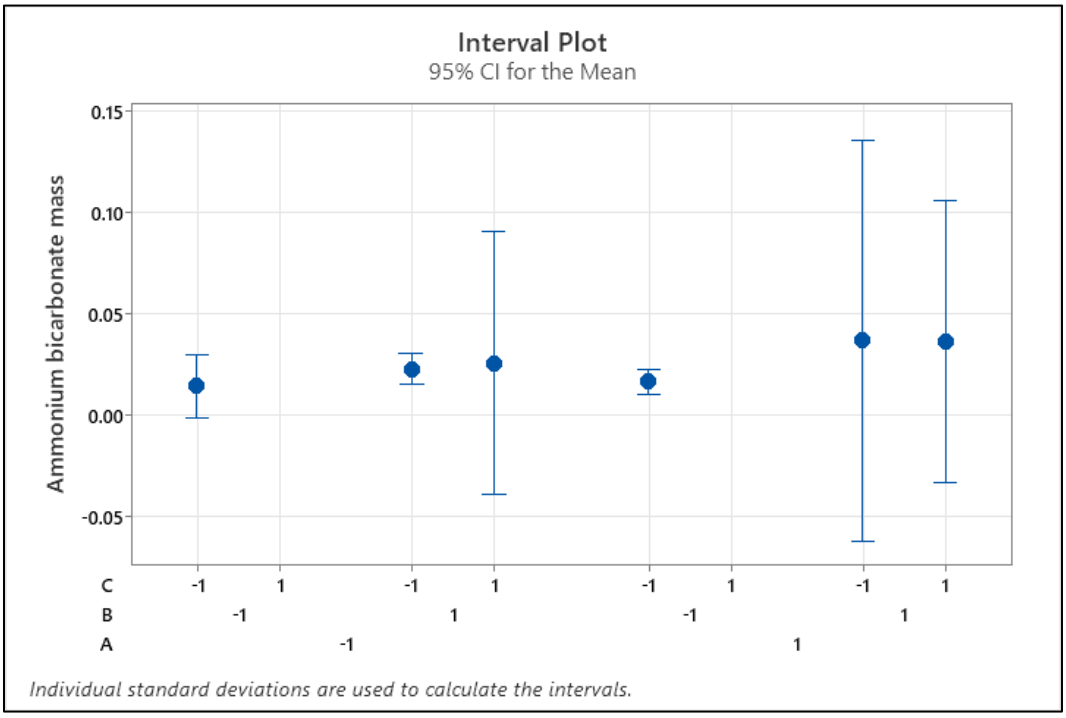

Figure 5.80: A plot of the mass production of ammonium bicarbonate over the different experimental runs.

5.5 Scale-up study results

The last part of the discussion here is the results of the scale-up analysis done to this batch reactor. Given that it this batch reactor would be placed in one of the multigeneration integrated systems with carbon capturing, the production capacities of system 2 are used here to estimate the size and capital cost of a full-scale batch reactor. The ratio of ammonium bicarbonate production rates between the lab-scale and the full-scale is found to be 27.8×10^{8}, when the induction heating case with 80%mol is taken. Taking this to be the same as the volume scaling factor, the diameter for the full-scale reactor is estimated

to be 29.8 m, knowing that the volume for the lab-scale reactor is 500 mL and its diameter is 0.0985 m, after using the spherical volume formula. From knowing this, we can find two more values. The heat transfer area scaling factor is calculated to be 91.5×10^{3}, while the capital cost for this full-scale reactor is estimated to be $\$7.94\times10^{8}$, when the cost for the lab-scale reactor is given to be \$194.7, which includes the capital costs of the reactor, catalysts, and the induction heater. The cost of the baseline reactor is \$132, while it is \$132.03 for the catalyst reactor when both are at lab-scale.

Figure 5.81 presents the capital costs of the full-scale reactor with induction heating at two different concentration levels of carbon dioxide. First thing to notice is that as the concentration of carbon dioxide increases, the capital costs of the full-scale reactor decrease significantly. This shows the importance of designing combustion methods that produce high concentration of carbon dioxide as part of the exhaust gases. One straightforward and easy way to increase the percentage of carbon dioxide in the exhaust gases is to use water condensers like what the proposed integrated systems in this work have suggested. The capital cost gaps between the three levels of concentration increase as the ammonium bicarbonate production rate increases. The largest gap exists between the 30mol% and the 80%mol which is $\$2.66\times10^{8}$, which is a tremendous amount of money to be invested. This amount of money could rather be directed to increase the CO_2 concentration in the exhaust gases by utilizing newer technologies in combustion, such as oxy-combustion, and solid-oxide fuel cells.

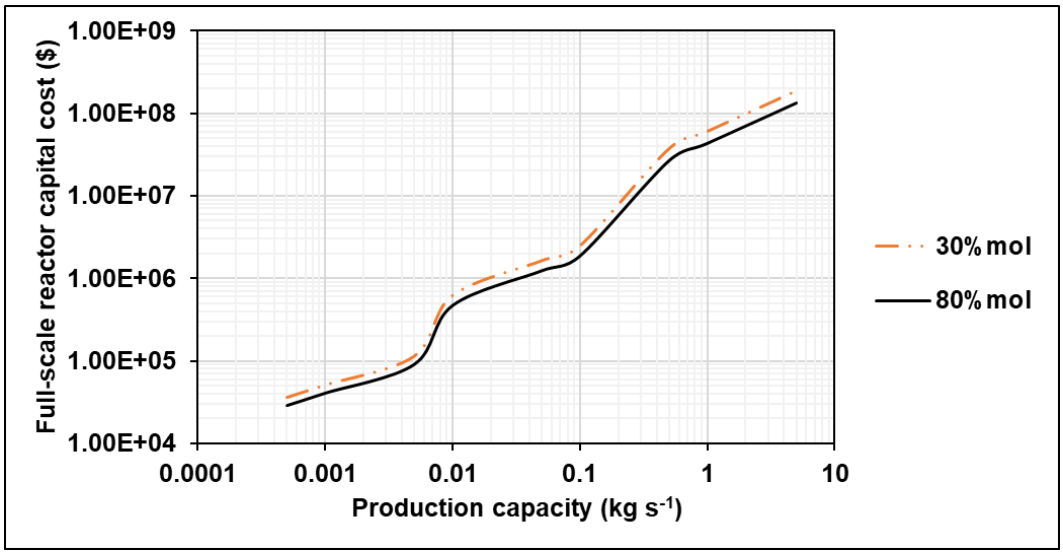

Figure 5.81: A plot of the full-scale reactor capital cost over a range of ammonium bicarbonate production rates. The percentages represent the initial concentration of CO_2 in the reactor for the induction heating case.

Figure 5.82 presents the capital costs comparison of the three cases of operation for the full-scale reactor. An interesting thing is noticed in this comparison which is that the lowest cost is identified with the catalyst case, and this is because of three reasons. Firstly, the catalyst case does not require an induction heater, and this lowers the capital cost of the reactor. The second reason is that it requires much smaller diameter to produce the same production rate of ammonium bicarbonate compared to the baseline. Thirdly, the catalyst used in this reaction is a cheap steel catalyst which does not affect the capital costs compared to the induction heater. At a production rate of 5 kg s^{-1}, the capital cost for the full-scale reactor operating under catalyst case conditions is $\$7.16\times10^{8}$, while they are $\$9.36\times10^{8}$, and $\$7.94\times10^{8}$, for the baseline case and the induction heating case, respectively.

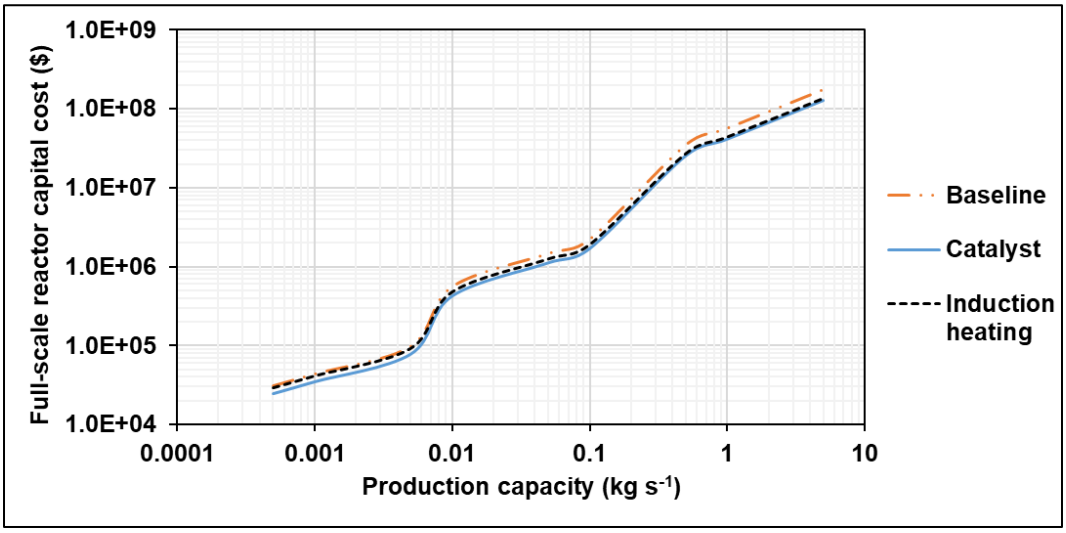

Figure 5.82: A plot of the full-scale reactor capital cost over a range of ammonium bicarbonate production rates for the three cases. The percentage chosen is 80%mol of CO_2.

Next, the effects of the geometric scaling up on the heat transfer and temperature aspects of the batch reactor are investigated. Table 5.27 presents the geometric changes of the volume and diameter as well as the surface area to volume ratio on the batch reactor as the scaling up factor increases. Figure 5.83 presents how the surface area over volume of the batch reactor reduces exponentially as the scaling factor increases due to the fact that the volume increases at a faster rate than the surface area. This poses some technical and heat transfer challenges when scaling up the batch reactor because the surface area is what helps in releasing excess thermal energy in the reactor to the surroundings. Since this surface area does not grow to keep up with the volume increase of the batch reactor during scaling

up, more thermal energy will be trapped in the reactor, and this will translate into higher operating temperature at some point of the reaction. This can be mitigated by two means, increasing the number of reactors working in parallel instead of having a single batch reactor to balance the surface area to volume ratio, and to reduce the temperature of the cooling fluid for this batch reactor to increase the heat transfer rate.

Table 5.27: Geometric parameters of the scaled-up batch reactor.

Scaling factor	**V (L)**	**V(m^3)**	**D (m)**	**A (m^2)**	**A/V (m^{-1})**
1	0.5	0.0005	0.0985	0.0305	60.9
10	5	0.005	0.212	0.141	28.3
100	50	0.05	0.457	0.656	13.1
1000	500	0.5	0.985	3.05	6.09
10000	5000	5	2.12	14.1	2.83
100000	50000	50	4.57	65.6	1.31

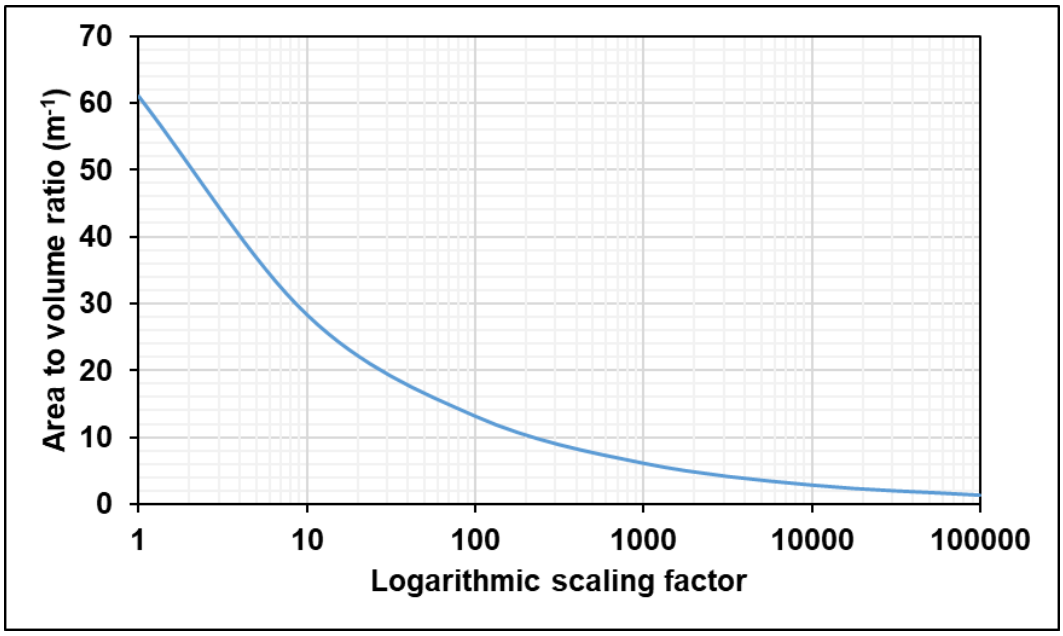

Figure 5.83: A plot of surface area over volume of the batch reactor over a range of scaling factor.

Figure 5.84 shows the effects of scaling factor on the peak temperature of the batch reactor to produce ammonium bicarbonate when the inlet gases contain 30%mol of CO_2. As the scaling factor increases by orders of magnitude, the peak temperature goes from a moderate level of 346 K, when the scaling factor is unity, to as high as 782 K, when the scaling factor is 1,000. The consequence of reaching this high temperature level is the disintegration of ammonium bicarbonate in the first 10 minutes of the reaction time in the batch reactor which does not help the production of ammonium bicarbonate and carbon capturing. For

this reason, it is suggested to elongate the reaction time to 40 minutes to compensate for the effects of reaching a peak temperature when scaling up the batch reactor.

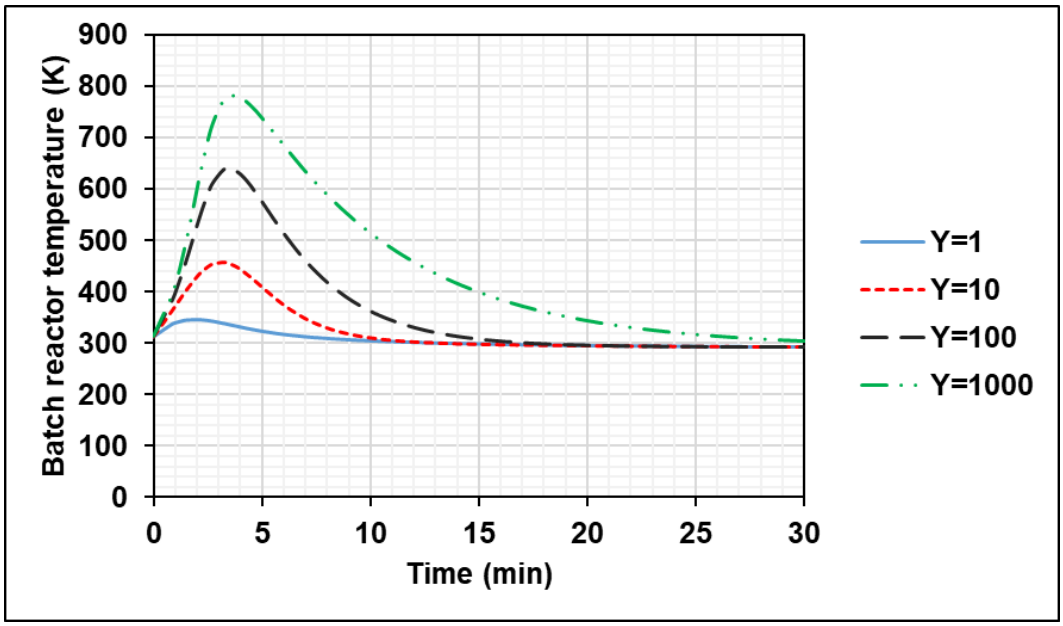

Figure 5.84: A plot of batch reactor temperature over time for different scaling factors for 30%mol of CO_2.

Figure 5.85 presents similar trends as the previous plot for 80%mol of CO_2 of inlet exhaust gases. However, the peak temperatures are significantly higher, and they range from 508 K to 888 K as the scaling factor grows from 1 to 1,000. This poses another limitation on the batch reactor that needs to be considered when scaling it up. Lowering the concentration of CO_2 reduces the peak temperature which reduces the rate of backward reaction for producing ammonium bicarbonate. A tradeoff between reducing costs and reducing peak temperatures for the scaling up of this batch reactor needs further investigation. Looking at the case where the scaling factor is 1,000 with 80%mol of CO_2, the operating temperature remains above the 60°C mark, which is the highest possible temperature for ammonium bicarbonate production, even after 30 minutes of operation. Possible solutions for this issue can be reducing the cooling temperature or separating the batch reactor into smaller parallel batch reactor working in synchronization for carbon capturing and ammonium bicarbonate production.

Figure 5.86 shows the effects of cooling fluid temperature on the behavior of batch reactor temperature over the operation time. A case of 80%mol is taken here because it is more severe than the 30%mol to show how increasing the cooling temperature can help the scaling up limitations. After looking at these results that are plotted here, it turns out that

decreasing the cooling temperature does affect the peak temperature marginally and it is not a possible way to reduce the effects of scaling up. Therefore, another approach must be considered here. Figure 5.87 displays the effects of changing the initial temperature of the batch reactor on the peak temperature of the same case mentioned above and similar conclusions can be drawn. Changing the initial temperature of the reactor reduces the peak temperature only by a small difference and it does not count as a viable approach to resolve the issue of increasing the peak temperature to such high levels.

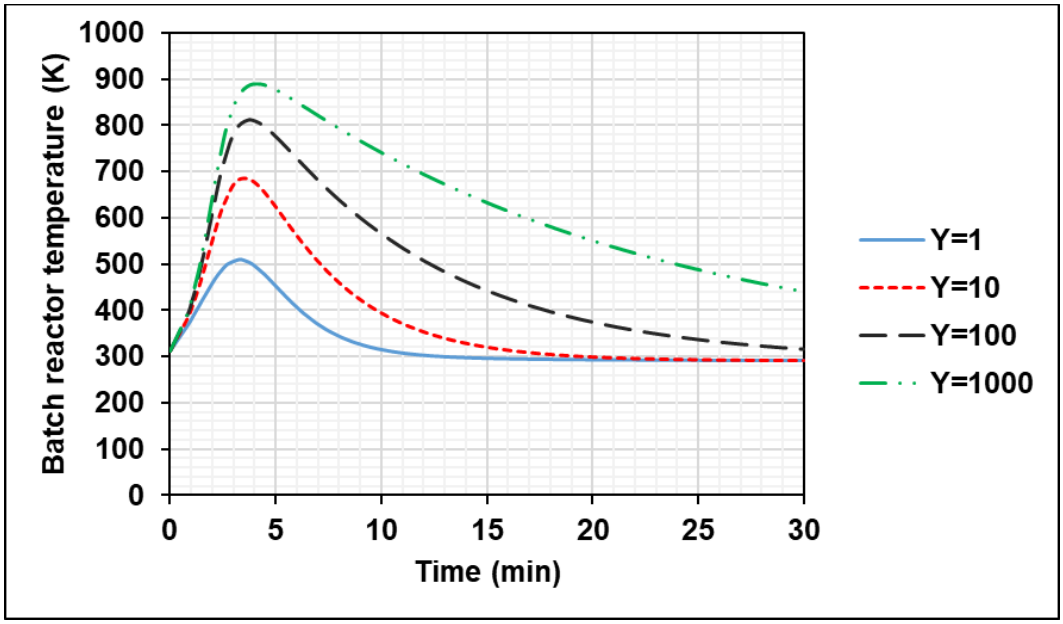

Figure 5.85: A plot of batch reactor temperature over time for different scaling factors for 80%mol of CO_2.

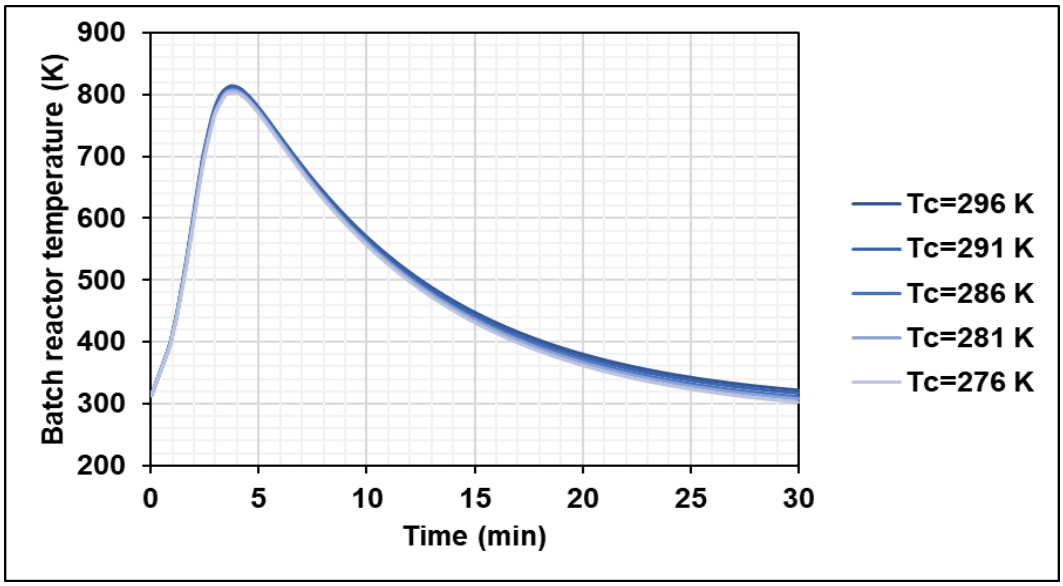

Figure 5.86: A plot of batch reactor temperature over time for different cooling fluid temperatures for 80%mol of CO_2.

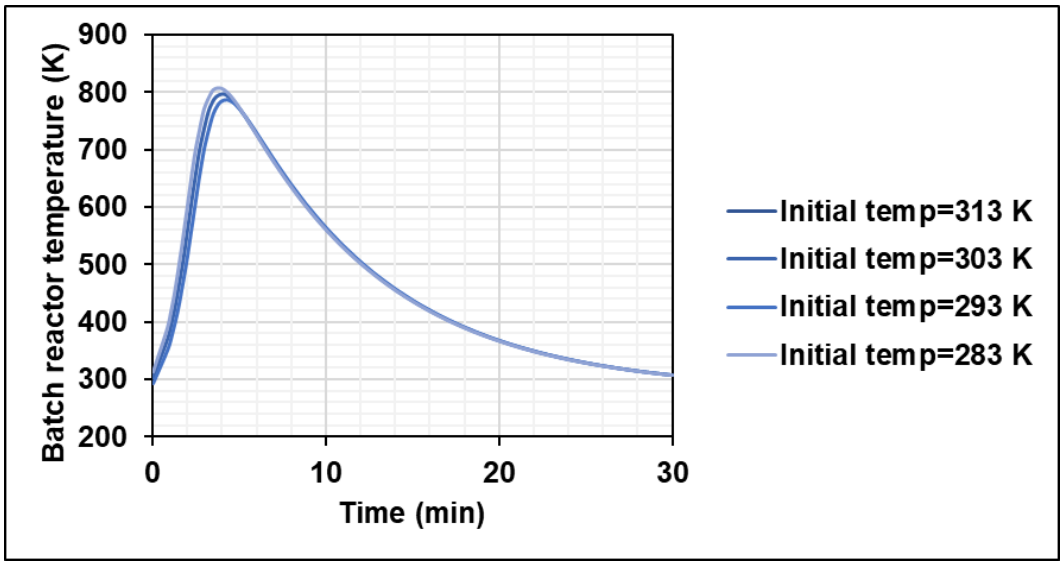

Figure 5.87: A plot of batch reactor temperature over time for different initial temperatures for 80%mol of CO_2.

Chapter 6: Conclusions and Recommendations

In this chapter, the main conclusions of this thesis work are drawn and mentioned. Next, recommendations of future research and ideas to extend this work are outlined which are based on the findings of this thesis.

6.1 Conclusions

This thesis has introduced and investigated several carbon capturing systems thermodynamically and economically using the exergy and exergoeconomic tools. Also, it has investigated a batch reactor for carbon capturing and production of ammonium bicarbonate. The main findings of this thesis are listed below:

- From the analysis of carbon capturing system 1, the PEM electrolyzer heat losses are the highest in the system and this results in high exergy destruction rate of this component, which consists of 88.3% of the total exergy destruction rate of the system.
- Also, there is a high amount of ammonium bicarbonate produced using very little hydrogen production rate. The ratio of these two chemicals in the system is 26. This useful chemical can be sold to offset the high energy requirements of the present carbon capture system.
- From the analysis of carbon capturing system 2, the use of an electrochemical ammonia synthesizer has lower energy requirements compared to the use of a PEM electrolyzer and the Haber-Bosch process for ammonia synthesis.
- This carbon capturing unit requires 13.3% less energy to capture the carbon than the carbon capturing scheme for system 1.
- Also, the temperature of the geothermal fluid and the faradaic efficiency of the electrochemical ammonia synthesizer have major effects on the performance of the double-flash geothermal power plant and the carbon capturing unit with ammonium bicarbonate production.
- In addition, for system 2, ammonia is produced with a cost rate of 1.96×10^{-2} \$ s^{-1}, and ammonium bicarbonate is produced with a cost rate of 2.02×10^{-2} \$ s^{-1}.

- From the analysis of carbon capturing system 3, the overall energy and exergy efficiencies of this integrated system are 22.3%, and 11.9%, respectively.
- Heat exchanger 1 of system 3 has a high exergy destruction rate of 8,370 kW. It is suggested to utilize the waste heat from this component for further power generation using an organic Rankine cycle.
- Comparing all the systems in terms of ammonium bicarbonate production cost, the lowest production cost of ammonium bicarbonate per one kilogram is by system 2 with a value of 0.0319 $ kg^{-1}, and this is 12.7% of the market price.
- The ammonium bicarbonate production improves by 1.98 when a steel catalyst and a high concentration of carbon dioxide are implemented compared to the baseline case of low carbon dioxide concentration.

6.2 Recommendations

Some future research ideas that are based on this work are suggested here:

- Prototypes of the conceptually proposed integrated systems should be built, tested, and optimized to validate the thermodynamic performance of these systems. Pilot-scale prototypes should be built, tested, and optimized for the batch reactor.
- Testing various catalysts in the carbon capturing reactor for producing ammonium bicarbonate should be considered for future work.
- Dynamic analyses have to be performed on the carbon capturing systems to gain more operational data and to further optimize their performance.
- It is important to study the proposed systems using exergoenvironmental analysis to assess their environmental impact.
- Life cycle costing assessments should be studied on the proposed carbon capturing systems to identify the costs of the stages of building and operation for these systems.
- Multi-objective optimization studies should be conducted which consider more objectives, such as environmental impacts, and dynamic operation of the carbon capturing systems.
- Developing new renewable energy-based carbon capturing systems using hydro power, and osmotic power is of interest for future research.

References

[1] B. Dutcher, M. Fan, and A. G. Russell, “Amine-based CO2 capture technology development from the beginning of 2013-A review,” *ACS Appl. Mater. Interfaces*, vol. 7, no. 4, pp. 2137–2148, 2015, doi: 10.1021/am507465f.

[2] “Carbon Emissions Linked To Global Warming In Simple Linear Relationship -- ScienceDaily.” https://www.sciencedaily.com/releases/2009/06/090610154453.htm (accessed Jan. 05, 2021).

[3] P. Freund, “Making deep reductions in CO_2 emissions from coal-fired power plant using capture and storage of CO_2,” *Proc. Inst. Mech. Eng. Part A J. Power Energy*, vol. 217, no. 1, pp. 1–7, Feb. 2003, doi: 10.1243/095765003321148628.

[4] IEA, “CCUS in Clean Energy Transitions,” 2020. [Online]. Available: https://www.iea.org/reports/ccus-in-clean-energy-transitions.

[5] Y. Yang *et al.*, “Gasification of refuse-derived fuel from municipal solid waste for energy production: a review,” *Environ. Chem. Lett.*, no. 0123456789, 2021, doi: 10.1007/s10311-020-01177-5.

[6] J. Davison, “Performance and costs of power plants with capture and storage of CO_2,” *Energy*, vol. 32, no. 7, pp. 1163–1176, 2007, doi: 10.1016/j.energy.2006.07.039.

[7] T. Lockwood, “A Compararitive Review of Next-generation Carbon Capture Technologies for Coal-fired Power Plant,” in *Energy Procedia*, Jul. 2017, vol. 114, pp. 2658–2670, doi: 10.1016/j.egypro.2017.03.1850.

[8] H. Balat and C. Öz, “Technical and economic aspects of carbon capture and storage - A review,” *Energy Exploration and Exploitation*, vol. 25, no. 5. pp. 357–392, 2007, doi: 10.1260/014459807783528883.

[9] T. Wilberforce, A. G. Olabi, E. T. Sayed, K. Elsaid, and M. A. Abdelkareem, “Progress in carbon capture technologies,” *Sci. Total Environ.*, p. 143203, Nov. 2020, doi: 10.1016/j.scitotenv.2020.143203.

[10] M. R. Hamilton, H. J. Herzog, and J. E. Parsons, “Cost and U.S. public policy for new coal power plants with carbon capture and sequestration,” in *Energy Procedia*, Feb. 2009, vol. 1, no. 1, pp. 4487–4494, doi: 10.1016/j.egypro.2009.02.266.

[11] Z. Liang *et al.*, “Recent progress and new developments in post-combustion carbon-capture technology with amine based solvents,” *Int. J. Greenh. Gas*

Control, vol. 40, pp. 26–54, 2015, doi: 10.1016/j.ijggc.2015.06.017.

[12] A. Mukherjee, J. A. Okolie, A. Abdelrasoul, C. Niu, and A. K. Dalai, "Review of post-combustion carbon dioxide capture technologies using activated carbon," *Journal of Environmental Sciences (China)*, vol. 83. Chinese Academy of Sciences, pp. 46–63, Sep. 01, 2019, doi: 10.1016/j.jes.2019.03.014.

[13] K. E. Zanganeh, A. Shafeen, and C. Salvador, "CO_2 Capture and Development of an Advanced Pilot-Scale Cryogenic Separation and Compression Unit," in *Energy Procedia*, Feb. 2009, vol. 1, no. 1, pp. 247–252, doi: 10.1016/j.egypro.2009.01.035.

[14] U. W. R. Siagian, A. Raksajati, N. F. Himma, K. Khoiruddin, and I. G. Wenten, "Membrane-based carbon capture technologies: Membrane gas separation vs. membrane contactor," *Journal of Natural Gas Science and Engineering*, vol. 67. Elsevier B.V., pp. 172–195, Jul. 01, 2019, doi: 10.1016/j.jngse.2019.04.008.

[15] T. C. Dos Santos and C. M. Ronconi, "Self-assembled 3D mesoporous graphene oxides (MEGOs) as adsorbents and recyclable solids for CO_2 and CH_4 capture," *J. CO_2 Util.*, vol. 20, pp. 292–300, Jul. 2017, doi: 10.1016/j.jcou.2017.05.018.

[16] C. Y. Chuah, W. Li, Y. Yang, and T.-H. Bae, "Evaluation of porous adsorbents for CO_2 capture under humid conditions: The importance of recyclability," *Chem. Eng. J. Adv.*, vol. 3, p. 100021, Nov. 2020, doi: 10.1016/j.ceja.2020.100021.

[17] A. D. Ebner *et al.*, "Suitability of a solid amine sorbent for CO_2 capture by pressure swing adsorption," *Ind. Eng. Chem. Res.*, vol. 50, no. 9, pp. 5634–5641, May 2011, doi: 10.1021/ie2000709.

[18] L. Lu, Z. Huang, G. H. Rau, and Z. J. Ren, "Microbial Electrolytic Carbon Capture for Carbon Negative and Energy Positive Wastewater Treatment," *Environ. Sci. Technol.*, vol. 49, no. 13, pp. 8193–8201, 2015, doi: 10.1021/acs.est.5b00875.

[19] I. Jayaweera *et al.*, "Results from Process Modeling of the Mixed-salt Technology for CO_2 Capture from Post-combustion-related Applications," in *Energy Procedia*, Jul. 2017, vol. 114, pp. 771–780, doi: 10.1016/j.egypro.2017.03.1220.

[20] D. P. Hanak, C. Biliyok, and V. Manovic, "Rate-based model development, validation and analysis of chilled ammonia process as an alternative CO_2 capture technology for coal-fired power plants," *Int. J. Greenh. Gas Control*, vol. 34, pp. 52–62, Mar. 2015, doi: 10.1016/j.ijggc.2014.12.013.

[21] J. Liu, "Investigation of Energy-Saving Designs for an Aqueous Ammonia-Based Carbon Capture Process," *Ind. Eng. Chem. Res.*, vol. 57, no. 45, pp. 15460–15472, 2018, doi: 10.1021/acs.iecr.8b03658.

[22] E. J. Novek, E. Shaulsky, Z. S. Fishman, L. D. Pfefferle, and M. Elimelech, “Low-Temperature Carbon Capture Using Aqueous Ammonia and Organic Solvents,” *Environ. Sci. Technol. Lett.*, vol. 3, no. 8, pp. 291–296, 2016, doi: 10.1021/acs.estlett.6b00253.

[23] J. Wang, L. Liu, X. Zeng, and K. Li, “Solar-Assisted CO_2 Capture with Amine And Ammonia-Based Chemical Absorption: A Comparative Study,” *Therm. Sci.*, p. 25, 2020, doi: https://doi.org/10.2298/tsci191222149w.

[24] L. Liu, J. Zhao, S. Deng, and Q. An, “A technical and economic study on solar-assisted ammonia-based post-combustion CO_2 capture of power plant,” *Appl. Therm. Eng.*, vol. 102, pp. 412–422, 2016, doi: 10.1016/j.applthermaleng.2016.03.154.

[25] H. Ishaq, O. Siddiqui, G. Chehade, and I. Dincer, “A solar and wind driven energy system for hydrogen and urea production with CO_2 capturing,” *Int. J. Hydrogen Energy*, pp. 1–12, 2020, doi: 10.1016/j.ijhydene.2020.01.208.

[26] A. Sánchez, L. M. Gil, and M. Martín, “Sustainable DMC production from CO_2 and renewable ammonia and methanol,” *J. CO_2 Util.*, vol. 33, no. August, pp. 521–531, 2019, doi: 10.1016/j.jcou.2019.08.010.

[27] H. Z. Tan *et al.*, “Review on the synthesis of dimethyl carbonate,” *Catal. Today*, vol. 316, pp. 2–12, Oct. 2018, doi: 10.1016/j.cattod.2018.02.021.

[28] O. Siddiqui, H. Ishaq, G. Chehade, and I. Dincer, “Performance investigation of a new renewable energy-based carbon dioxide capturing system with aqueous ammonia,” *Int. J. Energy Res.*, vol. 44, no. 3, pp. 2252–2263, Mar. 2020, doi: 10.1002/er.5087.

[29] G. Valenti, D. Bonalumi, and E. MacChi, “A parametric investigation of the Chilled Ammonia Process from energy and economic perspectives,” *Fuel*, vol. 101, pp. 74–83, Nov. 2012, doi: 10.1016/j.fuel.2011.06.035.

[30] C. Descamps, C. Bouallou, and M. Kanniche, “Efficiency of an Integrated Gasification Combined Cycle (IGCC) power plant including CO_2 removal,” *Energy*, vol. 33, no. 6, pp. 874–881, 2008, doi: 10.1016/j.energy.2007.07.013.

[31] E. M. A. Mokheimer, M. R. Shakeel, Y. S. Sanusi, and M. Mahmoud, “Thermo-economic comparative analysis of solar-assisted and carbon capture integrated conventional cogeneration plant of power and process steam,” *Int. J. Energy Res.*, vol. 44, no. 11, pp. 8455–8479, Sep. 2020, doi: 10.1002/er.5532.

[32] D. Ravikumar, G. Keoleian, and S. Miller, “The environmental opportunity cost of using renewable energy for carbon capture and utilization for methanol

production," *Appl. Energy*, vol. 279, p. 115770, Dec. 2020, doi: 10.1016/j.apenergy.2020.115770.

[33] K. H. M. Al-Hamed and I. Dincer, "A comparative review of potential ammonia-based carbon capture systems," *J. Environ. Manage.*, vol. 287, p. 112357, Jun. 2021, doi: 10.1016/j.jenvman.2021.112357.

[34] G. D. Surywanshi, B. Basant Kumar Pillai, V. S. Patnaikuni, R. Vooradi, and S. B. Anne, "Energy and exergy analyses of chemical looping combustion-based 660 MWe supercritical coal-fired power plant," *Int. J. Exergy*, vol. 31, no. 1, pp. 14–33, 2020, doi: 10.1504/ijex.2020.104723.

[35] A. A. O. Villa, J. C. C. Dutra, J. R. H. Guerrero, and C. A. C. Santos, "Techno-economic and Exergoeconomic Analysis of a micro cogeneration system for a residential use," *Eng. Mecânica*, 2015.

[36] A. Lazzaretto and G. Tsatsaronis, "SPECO: A systematic and general methodology for calculating efficiencies and costs in thermal systems," *Energy*, vol. 31, no. 8–9, pp. 1257–1289, 2006, doi: 10.1016/j.energy.2005.03.011.

[37] Y. Wang *et al.*, "Advanced exergy and exergoeconomic analysis of an integrated system combining CO_2 capture-storage and waste heat utilization processes," *Energy*, vol. 219, p. 119600, Mar. 2021, doi: 10.1016/j.energy.2020.119600.

[38] X. Zhang *et al.*, "Conventional and energy level based exergoeconomic analysis of biomass and natural gas fired polygeneration system integrated with ground source heat pump and PEM electrolyzer," *Energy Convers. Manag.*, vol. 195, pp. 313–327, Sep. 2019, doi: 10.1016/j.enconman.2019.05.017.

[39] S. Ghorbani, M. H. Khoshgoftar-Manesh, M. Nourpour, and A. M. Blanco-Marigorta, "Exergoeconomic and exergoenvironmental analyses of an integrated SOFC-GT-ORC hybrid system," *Energy*, vol. 206, p. 118151, Sep. 2020, doi: 10.1016/j.energy.2020.118151.

[40] S. M. Alirahmi, E. Assareh, N. N. Pourghassab, M. Delpisheh, L. Barelli, and A. Baldinelli, "Green hydrogen & electricity production via geothermal-driven multi-generation system: Thermodynamic modeling and optimization," *Fuel*, vol. 308, p. 122049, Jan. 2022, doi: 10.1016/j.fuel.2021.122049.

[41] M. Abdollahi Haghghi, S. Ghazanfari Holagh, A. Chitsaz, and K. Parham, "Thermodynamic assessment of a novel multi-generation solid oxide fuel cell-based system for production of electrical power, cooling, fresh water, and hydrogen," *Energy Convers. Manag.*, vol. 197, p. 111895, Oct. 2019, doi: 10.1016/j.enconman.2019.111895.

[42] Y. He, L. Zhu, J. Fan, and L. Li, “Comparative exergy and exergoeconomic analysis between liquid fuels production through chemical looping hydrogen generation and methane reforming with CO_2,” *Energy Convers. Manag.*, vol. 222, p. 113239, Oct. 2020, doi: 10.1016/j.enconman.2020.113239.

[43] A. R. Singh, B. A. Rohr, M. J. Statt, J. A. Schwalbe, M. Cargnello, and J. K. Nørskov, “Strategies toward Selective Electrochemical Ammonia Synthesis,” *ACS Catal.*, vol. 9, no. 9, pp. 8316–8324, Sep. 2019, doi: 10.1021/acscatal.9b02245.

[44] R. Zhao *et al.*, “Recent progress in the electrochemical ammonia synthesis under ambient conditions,” *EnergyChem*, vol. 1, no. 2, p. 100011, Sep. 2019, doi: 10.1016/j.enchem.2019.100011.

[45] X. Zhang, R. M. Kong, H. Du, L. Xia, and F. Qu, “Highly efficient electrochemical ammonia synthesis: Via nitrogen reduction reactions on a VN nanowire array under ambient conditions,” *Chem. Commun.*, vol. 54, no. 42, pp. 5323–5325, May 2018, doi: 10.1039/c8cc00459e.

[46] S. L’Orange Seigo, S. Dohle, and M. Siegrist, “Public perception of carbon capture and storage (CCS): A review,” *Renew. Sustain. Energy Rev.*, vol. 38, pp. 848–863, Oct. 2014, doi: 10.1016/j.rser.2014.07.017.

[47] W. L. Theo, J. S. Lim, H. Hashim, A. A. Mustaffa, and W. S. Ho, “Review of pre-combustion capture and ionic liquid in carbon capture and storage,” *Applied Energy*, vol. 183. Elsevier Ltd, pp. 1633–1663, Dec. 01, 2016, doi: 10.1016/j.apenergy.2016.09.103.

[48] S. Nandi *et al.*, “A single-ligand ultra-microporous MOF for precombustion CO_2 capture and hydrogen purification,” *Sci. Adv.*, vol. 1, no. 11, p. e1500421, Dec. 2015, doi: 10.1126/sciadv.1500421.

[49] J. Hua, M. Wu, and K. Kumar, “Numerical simulation of the combustion of hydrogen-air mixture in micro-scaled chambers Part II: CFD analysis for a micro-combustor,” *Chem. Eng. Sci.*, vol. 60, no. 13, pp. 3507–3515, Jul. 2005, doi: 10.1016/j.ces.2005.01.042.

[50] Z. Dai, L. Ansaloni, and L. Deng, “Recent advances in multi-layer composite polymeric membranes for CO_2 separation: A review,” *Green Energy and Environment*, vol. 1, no. 2. KeAi Publishing Communications Ltd., pp. 102–128, Jul. 01, 2016, doi: 10.1016/j.gee.2016.08.001.

[51] R. Stanger *et al.*, “Oxyfuel combustion for CO_2 capture in power plants,” *Int. J. Greenh. Gas Control*, vol. 40, pp. 55–125, Sep. 2015, doi: 10.1016/j.ijggc.2015.06.010.

[52] K. Goto, K. Yogo, and T. Higashii, “A review of efficiency penalty in a coal-fired power plant with post-combustion CO_2 capture,” *Applied Energy*, vol. 111. Elsevier Ltd, pp. 710–720, Nov. 01, 2013, doi: 10.1016/j.apenergy.2013.05.020.

[53] A. I. Escudero *et al.*, “Minimization of CO_2 capture energy penalty in second generation oxy-fuel power plants,” *Appl. Therm. Eng.*, vol. 103, pp. 274–281, Jun. 2016, doi: 10.1016/j.applthermaleng.2016.04.116.

[54] H. M. Kvamsdal, J. P. Jakobsen, and K. A. Hoff, “Dynamic modeling and simulation of a CO_2 absorber column for post-combustion CO_2 capture,” *Chem. Eng. Process. Process Intensif.*, vol. 48, no. 1, pp. 135–144, Jan. 2009, doi: 10.1016/j.cep.2008.03.002.

[55] U. Ali *et al.*, “Process simulation and thermodynamic analysis of a micro turbine with post-combustion CO_2 capture and exhaust gas recirculation,” in *Energy Procedia*, Jan. 2014, vol. 63, pp. 986–996, doi: 10.1016/j.egypro.2014.11.107.

[56] S. S. Warudkar, K. R. Cox, M. S. Wong, and G. J. Hirasaki, “Influence of stripper operating parameters on the performance of amine absorption systems for post-combustion carbon capture: Part I. High pressure strippers,” *Int. J. Greenh. Gas Control*, vol. 16, pp. 342–350, Aug. 2013, doi: 10.1016/j.ijggc.2013.01.050.

[57] D. Y. C. Leung, G. Caramanna, and M. M. Maroto-Valer, “An overview of current status of carbon dioxide capture and storage technologies,” *Renewable and Sustainable Energy Reviews*, vol. 39, pp. 426–443, Nov. 01, 2014, doi: 10.1016/j.rser.2014.07.093.

[58] A. B. Rao and E. S. Rubin, “A technical, economic, and environmental assessment of amine-based CO_2 capture technology for power plant greenhouse gas control,” *Environ. Sci. Technol.*, vol. 36, no. 20, pp. 4467–4475, Oct. 2002, doi: 10.1021/es0158861.

[59] M. Wang, A. Lawal, P. Stephenson, J. Sidders, and C. Ramshaw, “Post-combustion CO2 capture with chemical absorption: A state-of-the-art review,” *Chem. Eng. Res. Des.*, vol. 89, no. 9, pp. 1609–1624, Sep. 2011, doi: 10.1016/j.cherd.2010.11.005.

[60] A. Ali, K. Maqsood, A. Redza, K. Hii, A. B. M. Shariff, and S. Ganguly, “Performance enhancement using multiple cryogenic desublimation based pipeline network during dehydration and carbon capture from natural gas,” *Chem. Eng. Res. Des.*, vol. 109, pp. 519–531, May 2016, doi: 10.1016/j.cherd.2016.01.020.

[61] M. J. Jensen *et al.*, “Prediction and validation of external cooling loop cryogenic carbon capture (CCC-ECL) for full-scale coal-fired power plant retrofit,” *Int. J. Greenh. Gas Control*, vol. 42, pp. 200–212, Nov. 2015, doi:

10.1016/j.ijggc.2015.04.009.

[62] C. Song, Y. Kitamura, and S. Li, “Energy analysis of the cryogenic CO_2 capture process based on Stirling coolers,” *Energy*, vol. 65, pp. 580–589, Feb. 2014, doi: 10.1016/j.energy.2013.10.087.

[63] L. Baxter, A. Baxter, and S. Burt, “Cryogenic CO_2 capture as a cost-effective CO_2 capture process,” *26th Annu. Int. Pittsburgh Coal Conf. 2009, PCC 2009*, vol. 1, no. December, pp. 762–775, 2009.

[64] T. N.Borhani and M. Wang, “Role of solvents in CO_2 capture processes: The review of selection and design methods,” *Renewable and Sustainable Energy Reviews*, vol. 114. Elsevier Ltd, Oct. 01, 2019, doi: 10.1016/j.rser.2019.109299.

[65] F. O. Ochedi, J. Yu, H. Yu, Y. Liu, and A. Hussain, *Carbon dioxide capture using liquid absorption methods: a review*, no. 0123456789. Springer International Publishing, 2020.

[66] Y. Zhang, P. Yu, and Y. Luo, “Absorption of CO_2 by amino acid-functionalized and traditional dicationic ionic liquids: Properties, Henry’s law constants and mechanisms,” *Chem. Eng. J.*, vol. 214, pp. 355–363, Jan. 2013, doi: 10.1016/j.cej.2012.10.080.

[67] C. Cadena, J. L. Anthony, J. K. Shah, T. I. Morrow, J. F. Brennecke, and E. J. Maginn, “Why is CO_2 so Soluble in Imidazolium-Based Ionic Liquids?,” *J. Am. Chem. Soc.*, vol. 126, no. 16, pp. 5300–5308, Apr. 2004, doi: 10.1021/ja039615x.

[68] N. MacDowell *et al.*, “An overview of CO_2 capture technologies,” *Energy Environ. Sci.*, vol. 3, no. 11, pp. 1645–1669, 2010, doi: 10.1039/c004106h.

[69] M. A. Kassim and T. K. Meng, “Carbon dioxide (CO_2) biofixation by microalgae and its potential for biorefinery and biofuel production,” *Sci. Total Environ.*, vol. 584–585, pp. 1121–1129, Apr. 2017, doi: 10.1016/j.scitotenv.2017.01.172.

[70] W. Zhou *et al.*, “Bio-mitigation of carbon dioxide using microalgal systems: Advances and perspectives,” *Renewable and Sustainable Energy Reviews*, vol. 76. Elsevier Ltd, pp. 1163–1175, Sep. 01, 2017, doi: 10.1016/j.rser.2017.03.065.

[71] M. Zhou, H. He, T. Jin, and H. Wang, “Power generation enhancement in novel microbial carbon capture cells with immobilized Chlorella vulgaris,” *J. Power Sources*, vol. 214, pp. 216–219, Sep. 2012, doi: 10.1016/j.jpowsour.2012.04.043.

[72] X. Wang *et al.*, “Sequestration of CO_2 discharged from anode by algal cathode in microbial carbon capture cells (MCCs),” *Biosens. Bioelectron.*, vol. 25, no. 12, pp. 2639–2643, Aug. 2010, doi: 10.1016/j.bios.2010.04.036.

[73] B. Neethu, G. D. Bhowmick, and M. M. Ghangrekar, “Enhancement of bioelectricity generation and algal productivity in microbial carbon-capture cell using low cost coconut shell as membrane separator,” *Biochem. Eng. J.*, vol. 133, pp. 205–213, May 2018, doi: 10.1016/j.bej.2018.02.014.

[74] M. Rezakazemi, A. Ebadi Amooghin, M. M. Montazer-Rahmati, A. F. Ismail, and T. Matsuura, “State-of-the-art membrane based CO_2 separation using mixed matrix membranes (MMMs): An overview on current status and future directions,” *Progress in Polymer Science*, vol. 39, no. 5. Elsevier Ltd, pp. 817–861, May 01, 2014, doi: 10.1016/j.progpolymsci.2014.01.003.

[75] E. Favre, “Carbon dioxide recovery from post-combustion processes: Can gas permeation membranes compete with absorption?,” *J. Memb. Sci.*, vol. 294, no. 1–2, pp. 50–59, May 2007, doi: 10.1016/j.memsci.2007.02.007.

[76] C. Song *et al.*, “Reducing the energy consumption of membrane-cryogenic hybrid CO_2 capture by process optimization,” *Energy*, vol. 124, pp. 29–39, Apr. 2017, doi: 10.1016/j.energy.2017.02.054.

[77] A. Janusz-Cygan, J. Jaschik, A. Wojdyła, and M. Tańczyk, “The separative performance of modules with polymeric membranes for a hybrid adsorptive/membrane process of CO_2 capture from flue gas,” *Membranes (Basel).*, vol. 10, no. 11, pp. 1–18, Oct. 2020, doi: 10.3390/membranes10110309.

[78] C. Song *et al.*, “Alternative pathways for efficient CO_2 capture by hybrid processes—A review,” *Renewable and Sustainable Energy Reviews*, vol. 82. Elsevier Ltd, pp. 215–231, Feb. 01, 2018, doi: 10.1016/j.rser.2017.09.040.

[79] E. Koohestanian, J. Sadeghi, D. Mohebbi-Kalhori, F. Shahraki, and A. Samimi, “A novel process for CO_2 capture from the flue gases to produce urea and ammonia,” *Energy*, vol. 144, pp. 279–285, 2018, doi: 10.1016/j.energy.2017.12.034.

[80] F. F. T. De Groot *et al.*, “The industrial production of dimethyl carbonate from methanol and carbon dioxide,” *Chem. Eng. Trans.*, vol. 39, no. Special Issue, pp. 1561–1566, 2014, doi: 10.3303/CET1439261.

[81] O. Siddiqui, H. Ishaq, G. Chehade, and I. Dincer, “Performance investigation of a new renewable energy-based carbon dioxide capturing system with aqueous ammonia,” *Int. J. Energy Res.*, vol. 44, no. 3, pp. 2252–2263, 2020, doi: 10.1002/er.5087.

[82] G. Lombardo, R. Agarwal, and J. Askander, “Chilled ammonia process at technology center Mongstad-first results,” in *Energy Procedia*, Jan. 2014, vol. 51, pp. 31–39, doi: 10.1016/j.egypro.2014.07.004.

[83] C. u. Bak, M. Asif, and W. S. Kim, “Experimental study on CO_2 capture by chilled ammonia process,” *Chem. Eng. J.*, vol. 265, pp. 1–8, 2015, doi: 10.1016/j.cej.2014.11.145.

[84] D. Bonalumi, G. Valenti, S. Lillia, P. L. Fosbøl, and K. Thomsen, “A layout for the carbon capture with aqueous ammonia without salt precipitation,” *Energy Procedia*, vol. 86, pp. 134–143, 2016, doi: 10.1016/j.egypro.2016.01.014.

[85] D. Bonalumi, S. Lillia, and G. Valenti, “Rate-based simulation and techno-economic analysis of coal-fired power plants with aqueous ammonia carbon capture,” *Energy Convers. Manag.*, vol. 199, Nov. 2019, doi: 10.1016/j.enconman.2019.111966.

[86] J. Liu and D. Chen, “Process Design of Aqueous Ammonia-based Post-combustion CO_2 Capture,” in *6th International Symposium on Advanced Control of Industrial Processes (AdCONIP)*, 2017, pp. 1–6.

[87] K. Jiang, K. Li, H. Yu, and P. H. M. Feron, “Piperazine-promoted aqueous-ammonia-based CO_2 capture: Process optimisation and modification,” *Chem. Eng. J.*, vol. 347, no. February, pp. 334–342, 2018, doi: 10.1016/j.cej.2018.04.103.

[88] C. A. Obek, F. K. Ayittey, and A. Saptoro, “ Improved process modifications of aqueous ammonia-based CO_2 capture system ,” *MATEC Web Conf.*, vol. 268, p. 02004, 2019, doi: 10.1051/matecconf/201926802004.

[89] K. Jiang, K. Li, H. Yu, Z. Chen, L. Wardhaugh, and P. Feron, “Advancement of ammonia based post-combustion CO_2 capture using the advanced flash stripper process,” *Appl. Energy*, vol. 202, pp. 496–506, 2017, doi: 10.1016/j.apenergy.2017.05.143.

[90] J. Liu, D. S. H. Wong, and D. S. Chen, “Energy-saving performance of advanced stripper configurations for CO_2 capture by ammonia-based solvents,” *J. Taiwan Inst. Chem. Eng.*, vol. 113, pp. 273–284, 2020, doi: 10.1016/j.jtice.2020.08.024.

[91] F. Wang, S. Deng, J. Zhao, and J. Yan, “A novel ammonia-based CO_2 capture process hybrid ammonia absorption refrigeration,” *Energy Procedia*, vol. 142, pp. 3734–3740, 2017, doi: 10.1016/j.egypro.2017.12.269.

[92] A. Ullah, M. I. Soomro, and W. S. Kim, “Analysis of a rich vapor compression method for an ammonia-based CO_2 capture process and freshwater production using membrane distillation technology,” *Chem. Eng. Res. Des.*, vol. 147, pp. 244–258, 2019, doi: 10.1016/j.cherd.2019.05.005.

[93] C. Descamps, C. Bouallou, and M. Kanniche, “Efficiency of an Integrated Gasification Combined Cycle (IGCC) power plant including CO_2 removal,”

Energy, vol. 33, no. 6, pp. 874–881, 2008, doi: 10.1016/j.energy.2007.07.013.

[94] D. Bonalumi and A. Giuffrida, "Investigations of an air-blown integrated gasification combined cycle fired with high-sulphur coal with post-combustion carbon capture by aqueous ammonia," *Energy*, vol. 117, pp. 439–449, 2016, doi: 10.1016/j.energy.2016.04.025.

[95] L. Petrescu, D. Bonalumi, G. Valenti, A. M. Cormos, and C. C. Cormos, "Life Cycle Assessment for supercritical pulverized coal power plants with post-combustion carbon capture and storage," *J. Clean. Prod.*, vol. 157, pp. 10–21, 2017, doi: 10.1016/j.jclepro.2017.03.225.

[96] M. Asif, C. U. Bak, M. W. Saleem, and W. S. Kim, "Performance evaluation of integrated gasification combined cycle (IGCC) utilizing a blended solution of ammonia and 2-amino-2-methyl-1-propanol (AMP) for CO_2 capture," *Fuel*, vol. 160, pp. 513–524, Nov. 2015, doi: 10.1016/j.fuel.2015.08.008.

[97] P. Versteeg and E. S. Rubin, "A technical and economic assessment of ammonia-based post-combustion CO_2 capture at coal-fired power plants," *Int. J. Greenh. Gas Control*, vol. 5, no. 6, pp. 1596–1605, Nov. 2011, doi: 10.1016/j.ijggc.2011.09.006.

[98] L. E. Øi and S. H. P. Kvam, "Comparison of energy consumption for different CO_2 absorption configurations using different simulation tools," in *Energy Procedia*, 2014, vol. 63, pp. 1186–1195, doi: 10.1016/j.egypro.2014.11.128.

[99] "Ammonium bicarbonate | CH2O3.H3N - PubChem." https://pubchem.ncbi.nlm.nih.gov/compound/Ammonium-bicarbonate#section=Uses (accessed Oct. 15, 2021).

[100] "Ammonium Bicarbonate – Structure, Properties, Production and Uses." https://www.vedantu.com/chemistry/ammonium-bicarbonate (accessed Oct. 15, 2021).

[101] A. Vojvodic *et al.*, "Exploring the limits: A low-pressure, low-temperature Haber-Bosch process," *Chem. Phys. Lett.*, vol. 598, pp. 108–112, Apr. 2014, doi: 10.1016/j.cplett.2014.03.003.

[102] M. El Haj Assad, E. Bani-Hani, and M. Khalil, "Performance of geothermal power plants (single, dual, and binary) to compensate for LHC-CERN power consumption: comparative study," *Geotherm. Energy*, vol. 5, no. 1, 2017, doi: 10.1186/s40517-017-0074-z.

[103] "Geothermal Energy for Power Generation." https://geothermalcommunities.eu/assets/elearning/7.21.geothermalscan.pdf.

(accessed Aug. 05, 2021)

[104] P. C. Chen *et al.*, “Interpretation of gas-liquid reactive crystallization data using a size-independent agglomeration model,” *J. Cryst. Growth*, vol. 257, no. 3–4, pp. 333–343, Oct. 2003, doi: 10.1016/s0022-0248(03)01425-8.

[105] A. Chitsaz, M. A. Haghghi, and J. Hosseinpour, “Thermodynamic and exergoeconomic analyses of a proton exchange membrane fuel cell (PEMFC) system and the feasibility evaluation of integrating with a proton exchange membrane electrolyzer (PEME),” *Energy Convers. Manag.*, vol. 186, pp. 487–499, Apr. 2019, doi: 10.1016/j.enconman.2019.03.004.

[106] V. Darde, W. J. M. Van Well, E. H. Stenby, and K. Thomsen, “Modeling of carbon dioxide absorption by aqueous ammonia solutions using the extended UNIQUAC model,” *Ind. Eng. Chem. Res.*, vol. 49, no. 24, pp. 12663–12674, Dec. 2010, doi: 10.1021/ie1009519.

[107] F. Milella and M. Mazzotti, “Estimation of the Growth and the Dissolution Kinetics of Ammonium Bicarbonate in Aqueous Ammonia Solutions from Batch Crystallization Experiments,” *Cryst. Growth Des.*, vol. 19, no. 10, pp. 5907–5922, 2019, doi: 10.1021/acs.cgd.9b00941.

[108] L. Mihet-Popa and V. Groza, “Dynamic modeling, simulation and control strategies for 2 MW wind generating systems,” *Int. Rev. Model. Simulations*, vol. 3, no. 6, pp. 1410–1418, 2010.

[109] M. E. Lebbal and S. Lecœuche, “Identification and monitoring of a PEM electrolyser based on dynamical modelling,” *Int. J. Hydrogen Energy*, vol. 34, no. 14, pp. 5992–5999, Jul. 2009, doi: 10.1016/j.ijhydene.2009.02.003.

[110] M. Carmo, D. L. Fritz, J. Mergel, and D. Stolten, “A comprehensive review on PEM water electrolysis,” *International Journal of Hydrogen Energy*, vol. 38, no. 12. Pergamon, pp. 4901–4934, Apr. 22, 2013, doi: 10.1016/j.ijhydene.2013.01.151.

[111] F. Marangio, M. Santarelli, and M. Calì, “Theoretical model and experimental analysis of a high pressure PEM water electrolyser for hydrogen production,” *Int. J. Hydrogen Energy*, vol. 34, no. 3, pp. 1143–1158, Feb. 2009, doi: 10.1016/j.ijhydene.2008.11.083.

[112] R. W. Kopitzke, C. A. Linkous, H. R. Anderson, and G. L. Nelson, “Conductivity and Water Uptake of Aromatic-Based Proton Exchange Membrane Electrolytes,” *J. Electrochem. Soc.*, vol. 147, no. 5, p. 1677, May 2000, doi: 10.1149/1.1393417.

[113] P. Colbertaldo, S. L. Gómez Aláez, and S. Campanari, “Zero-dimensional dynamic

modeling of PEM electrolyzers," *Energy Procedia*, vol. 142, pp. 1468–1473, 2017, doi: 10.1016/j.egypro.2017.12.594.

[114] N. Shokati, F. Ranjbar, and M. Yari, "Comparative and parametric study of double flash and single flash/ORC combined cycles based on exergoeconomic criteria," *Appl. Therm. Eng.*, vol. 91, pp. 479–495, 2015, doi: 10.1016/j.applthermaleng.2015.08.031.

[115] "Historical electricity rates | Ontario Energy Board." https://www.oeb.ca/rates-and-your-bill/electricity-rates/historical-electricity-rates (accessed Apr. 05, 2021).

[116] H. Kianfard, S. Khalilarya, and S. Jafarmadar, "Exergy and exergoeconomic evaluation of hydrogen and distilled water production via combination of PEM electrolyzer, RO desalination unit and geothermal driven dual fluid ORC," *Energy Convers. Manag.*, vol. 177, no. October, pp. 339–349, 2018, doi: 10.1016/j.enconman.2018.09.057.

[117] S. Alharbi, M. L. Elsayed, and L. C. Chow, "Exergoeconomic analysis and optimization of an integrated system of supercritical CO_2 Brayton cycle and multi-effect desalination," *Energy*, vol. 197, p. 117225, 2020, doi: 10.1016/j.energy.2020.117225.

[118] S. K. Tyagi, G. M. Chen, Q. Wang, and S. C. Kaushik, "Thermodynamic analysis and parametric study of an irreversible regenerative-intercooled-reheat Brayton cycle," *Int. J. Therm. Sci.*, vol. 45, no. 8, pp. 829–840, Aug. 2006, doi: 10.1016/j.ijthermalsci.2005.10.011.

[119] C. Fúnez Guerra, L. Reyes-Bozo, E. Vyhmeister, M. Jaén Caparrós, J. L. Salazar, and C. Clemente-Jul, "Technical-economic analysis for a green ammonia production plant in Chile and its subsequent transport to Japan," *Renew. Energy*, vol. 157, pp. 404–414, Sep. 2020, doi: 10.1016/j.renene.2020.05.041.

[120] G. Ferrara, A. Lanzini, P. Leone, M. T. Ho, and D. E. Wiley, "Exergetic and exergoeconomic analysis of post-combustion CO_2 capture using MEA-solvent chemical absorption," *Energy*, vol. 130, pp. 113–128, 2017, doi: 10.1016/j.energy.2017.04.096.

[121] M. Abdolalipouradl, F. Mohammadkhani, and S. Khalilarya, "A comparative analysis of novel combined flash-binary cycles for Sabalan geothermal wells: Thermodynamic and exergoeconomic viewpoints," *Energy*, vol. 209, p. 118235, 2020, doi: 10.1016/j.energy.2020.118235.

[122] "EES: Engineering Equation Solver | F-Chart Software : Engineering Software," *F-Chart Software*, 2021. http://fchart.com/ees/ (accessed Jun. 17, 2021).

[123] F. E. Tolon, A. Karabuga, M. Tolon, and Z. Utlu, “Evaluation of Thermodynamic Analysis of Solar Energy Systems Integrated into Sustainable Buildings with Artificial Neural Network: A Case Study,” in *Procedia Computer Science*, Jan. 2019, vol. 158, pp. 91–98, doi: 10.1016/j.procs.2019.09.031.

[124] D. Wu *et al.*, “Thermodynamic performance analyses and collaborative optimization for a novel integrated energy system coupled with organic Rankine cycle,” *Energy Convers. Manag.*, vol. 225, p. 113484, Dec. 2020, doi: 10.1016/j.enconman.2020.113484.

[125] P. Ahmadi, I. Dincer, and M. A. Rosen, “Thermoeconomic multi-objective optimization of a novel biomass-based integrated energy system,” *Energy*, vol. 68, pp. 958–970, Apr. 2014, doi: 10.1016/j.energy.2014.01.085.

[126] P. Zhao, J. Wang, and Y. Dai, “Thermodynamic analysis of an integrated energy system based on compressed air energy storage (CAES) system and Kalina cycle,” *Energy Convers. Manag.*, vol. 98, pp. 161–172, Jul. 2015, doi: 10.1016/j.enconman.2015.03.094.

[127] K. H. M. Al-Hamed and I. Dincer, “A novel integrated solid-oxide fuel cell powering system for clean rail applications,” *Energy Convers. Manag.*, vol. 205, p. 112327, Feb. 2020, doi: 10.1016/j.enconman.2019.112327.

[128] S. Lee, C. Kim, S. Lee, S. Oh, J. Kim, and J. Lee, “Characteristics of non-methane hydrocarbons and methane emissions in exhaust gases under natural-gas/diesel dual-fuel combustion,” *Fuel*, vol. 290, p. 120009, Apr. 2021, doi: 10.1016/j.fuel.2020.120009.

[129] P. Aguiar, C. S. Adjiman, and N. P. Brandon, “Anode-supported intermediate temperature direct internal reforming solid oxide fuel cell. I: Model-based steady-state performance,” *J. Power Sources*, vol. 138, no. 1–2, pp. 120–136, 2004, doi: 10.1016/j.jpowsour.2004.06.040.

[130] Q. Meng, J. Han, L. Kong, H. Liu, T. Zhang, and Z. Yu, “Thermodynamic analysis of combined power generation system based on SOFC/GT and transcritical carbon dioxide cycle,” *Int. J. Hydrogen Energy*, vol. 42, no. 7, pp. 4673–4678, Feb. 2017, doi: 10.1016/j.ijhydene.2016.09.067.

[131] R. Toonssen, S. Sollai, P. V. Aravind, N. Woudstra, and A. H. M. Verkooijen, “Alternative system designs of biomass gasification SOFC/GT hybrid systems,” in *International Journal of Hydrogen Energy*, Aug. 2011, vol. 36, no. 16, pp. 10414–10425, doi: 10.1016/j.ijhydene.2010.06.069.

[132] A. V. Akkaya, B. Sahin, and H. H. Erdem, “Thermodynamic model for exergetic performance of a tubular SOFC module,” *Renew. Energy*, vol. 34, no. 7, pp. 1863–

1870, Jul. 2009, doi: 10.1016/j.renene.2008.11.017.

[133] B. Boundy, S. W. Diegel, L. Wright, and S. C. Davis. Biomass Energy Data Book. U.S. Department of Energy. 2011.

[134] S. Authayanun, P. Aunsup, Y. Patcharavorachot, and A. Arpornwichanop, "Theoretical analysis of a biogas-fed PEMFC system with different hydrogen purifications: Conventional and membrane-based water gas shift processes," *Energy Convers. Manag.*, vol. 86, pp. 60–69, Oct. 2014, doi: 10.1016/j.enconman.2014.04.093.

[135] H. T. El-Dessouky, H. M. Ettouney, and F. Mandani, "Performance of parallel feed multiple effect evaporation system for seawater desalination," *Appl. Therm. Eng.*, vol. 20, no. 17, pp. 1679–1706, 2000, doi: 10.1016/S1359-4311(99)00098-8.

[136] F. Zhou *et al.*, "Electro-synthesis of ammonia from nitrogen at ambient temperature and pressure in ionic liquids," *Energy Environ. Sci.*, vol. 10, no. 12, pp. 2516–2520, 2017, doi: 10.1039/c7ee02716h.

[137] R. Kumar, "A critical review on energy, exergy, exergoeconomic and economic (4-E) analysis of thermal power plants," *Eng. Sci. Technol. an Int. J.*, vol. 20, no. 1, pp. 283–292, Feb. 2017, doi: 10.1016/j.jestch.2016.08.018.

[138] A. Abusoglu and M. Kanoglu, "Exergoeconomic analysis and optimization of combined heat and power production: A review," *Renewable and Sustainable Energy Reviews*, vol. 13, no. 9. Pergamon, pp. 2295–2308, Dec. 01, 2009, doi: 10.1016/j.rser.2009.05.004.

[139] Y.-H. Kwon, H.-Y. Kwak, and S.-D. Oh, "Exergoeconomic analysis of gas turbine cogeneration systems," *Exergy, An Int. J.*, vol. 1, no. 1, pp. 31–40, 2001, doi: 10.1016/s1164-0235(01)00007-3.

[140] G. Singh, P. J. Singh, V. V. Tyagi, P. Barnwal, and A. K. Pandey, "Energy, exergy and exergoeconomic analysis of high temperature short time milk pasteurisation plant," *Int. J. Exergy*, vol. 30, no. 1, pp. 26–62, 2019, doi: 10.1504/ijex.2019.101626.

[141] P. Ahmadi, I. Dincer, and M. A. Rosen, "Exergy, exergoeconomic and environmental analyses and evolutionary algorithm based multi-objective optimization of combined cycle power plants," *Energy*, vol. 36, no. 10, pp. 5886–5898, Oct. 2011, doi: 10.1016/j.energy.2011.08.034.

[142] F. Calise, M. D. D'Accadia, A. Macaluso, A. Piacentino, and L. Vanoli, "Exergetic and exergoeconomic analysis of a novel hybrid solar–geothermal polygeneration system producing energy and water," *Energy Convers. Manag.*,

vol. 115, pp. 200–220, 2016, doi: 10.1016/j.enconman.2016.02.029.

[143] G. M. Fellah, F. A. Mgherbi, and S. M. Aboghres, “Exergoeconomic Analysis for Unit Gt14 of South Tripoli Gas Turbine Power Plant Turbine Power Plant,” *J. Mech. Ind. Eng.*, vol. 4, no. 4, pp. 507–516, 2010.

[144] M. J. Zonouz and M. Mehrpooya, “Parametric study of a hybrid one column air separation unit (ASU) and CO_2 power cycle based on advanced exergy cost analysis results,” *Energy*, vol. 140, pp. 261–275, 2017, doi: 10.1016/j.energy.2017.08.118.

[145] S. O. Oyedepo, R. O. Fagbenle, S. S. Adefila, and M. M. Alam, “Exergy costing analysis and performance evaluation of selected gas turbine power plants,” *Cogent Eng.*, vol. 2, no. 1, pp. 0–21, 2015, doi: 10.1080/23311916.2015.1101048.

[146] M. Abdolalipouradl, F. Mohammadkhani, S. Khalilarya, and M. Yari, “Thermodynamic and exergoeconomic analysis of two novel tri-generation cycles for power, hydrogen and freshwater production from geothermal energy,” *Energy Convers. Manag.*, vol. 226, no. September, p. 113544, 2020, doi: 10.1016/j.enconman.2020.113544.

[147] J. R. Gomez, J. Baca, and F. Garzon, “Techno-economic analysis and life cycle assessment for electrochemical ammonia production using proton conducting membrane,” *Int. J. Hydrogen Energy*, vol. 45, no. 1, pp. 721–737, 2020, doi: 10.1016/j.ijhydene.2019.10.174.

[148] M. Meratizaman, S. Monadizadeh, and M. Amidpour, “Introduction of an efficient small-scale freshwater-power generation cycle (SOFC-GT-MED), simulation, parametric study and economic assessment,” *Desalination*, vol. 351, pp. 43–58, 2014, doi: 10.1016/j.desal.2014.07.023.

[149] A. Abuadala and I. Dincer, “Exergoeconomic analysis of a hybrid system based on steam biomass gasification products for hydrogen production,” *Int. J. Hydrogen Energy*, vol. 36, no. 20, pp. 12780–12793, 2011, doi: 10.1016/j.ijhydene.2011.07.067.

[150] E. Zarza, M. E. Rojas, L. González, J. M. Caballero, and F. Rueda, “INDITEP: The first pre-commercial DSG solar power plant,” *Sol. Energy*, vol. 80, no. 10, pp. 1270–1276, Oct. 2006, doi: 10.1016/j.solener.2005.04.019.

[151] S. Qian, J. Ling, Y. Hwang, R. Radermacher, and I. Takeuchi, “Thermodynamics cycle analysis and numerical modeling of thermoelastic cooling systems,” *Int. J. Refrig.*, vol. 56, pp. 65–80, 2015, doi: 10.1016/j.ijrefrig.2015.04.001.

[152] A. Skorek-Osikowska, Ł. Bartela, and J. Kotowicz, “A comparative

thermodynamic, economic and risk analysis concerning implementation of oxy-combustion power plants integrated with cryogenic and hybrid air separation units," *Energy Convers. Manag.*, vol. 92, pp. 421–430, 2015, doi: 10.1016/j.enconman.2014.12.079.

[153] S. Wang, C. Liu, J. Li, Z. Sun, X. Chen, and X. Wang, "Exergoeconomic analysis of a novel trigeneration system containing supercritical CO_2 Brayton cycle, organic Rankine cycle and absorption refrigeration cycle for gas turbine waste heat recovery," *Energy Convers. Manag.*, vol. 221, no. June, p. 113064, 2020, doi: 10.1016/j.enconman.2020.113064.

[154] M. A. Haghghi, Z. Mohammadi, S. M. Pesteei, A. Chitsaz, and K. Parham, "Exergoeconomic evaluation of a system driven by parabolic trough solar collectors for combined cooling, heating, and power generation; a case study," *Energy*, vol. 192, p. 116594, 2020, doi: 10.1016/j.energy.2019.116594.

[155] Z. Xi, S. Eshaghi, and F. Sardari, "Energy, exergy, and exergoeconomic analysis of a polygeneration system driven by solar energy with a thermal energy storage tank for power, heating, and freshwater production," *J. Energy Storage*, vol. 36, no. September 2020, p. 102429, 2021, doi: 10.1016/j.est.2021.102429.

[156] S. Khanmohammadi, F. Musharavati, O. Kizilkan, and D. Duc Nguyen, "Proposal of a new parabolic solar collector assisted power-refrigeration system integrated with thermoelectric generator using 3E analyses: Energy, exergy, and exergo-economic," *Energy Convers. Manag.*, vol. 220, no. March, p. 113055, 2020, doi: 10.1016/j.enconman.2020.113055.

[157] R. S. El-Emam and I. Dincer, "Investigation and assessment of a novel solar-driven integrated energy system," *Energy Convers. Manag.*, vol. 158, no. June 2016, pp. 246–255, 2018, doi: 10.1016/j.enconman.2017.12.062.

[158] S. M. Seyyedi, H. Ajam, and S. Farahat, "A new approach for optimization of thermal power plant based on the exergoeconomic analysis and structural optimization method: Application to the CGAM problem," *Energy Convers. Manag.*, vol. 51, no. 11, pp. 2202–2211, 2010, doi: 10.1016/j.enconman.2010.03.014.

[159] K. H. M. Al-Hamed and I. Dincer, "Development and optimization of a novel solid oxide fuel cell-engine powering system for cleaner locomotives," *Appl. Therm. Eng.*, vol. 183, p. 116150, Jan. 2021, doi: 10.1016/j.applthermaleng.2020.116150.

[160] K. Deb, A. Pratap, S. Agarwal, and T. Meyarivan, "A fast and elitist multiobjective genetic algorithm: NSGA-II," *IEEE Trans. Evol. Comput.*, vol. 6, no. 2, pp. 182–197, Apr. 2002, doi: 10.1109/4235.996017.

[161] E. D. Wachsman and K. T. Lee, “Lowering the Temperature of Solid Oxide Fuel Cells,” *Science (80-.).*, vol. 334, no. 6058, pp. 935–939, 2011.

[162] “Ammonium Bicarbonate Food Grade For Baking Powder.” https://www.alibaba.com/product-detail/Ammonium-Bicarbonate-Food-Grade-For Baking_1600145986426.html?spm=a2700.7724857.normal_offer.d_title.2cdec97b G6vC2v (accessed Oct. 28, 2021).

[163] J. Nash, X. Yang, J. Anibal, J. Wang, Y. Yan, and B. Xu, “Electrochemical Nitrogen Reduction Reaction on Noble Metal Catalysts in Proton and Hydroxide Exchange Membrane Electrolyzers,” *J. Electrochem. Soc.*, vol. 164, no. 14, pp. F1712–F1716, 2017, doi: 10.1149/2.0071802jes.

[164] L. Qiao *et al.*, “Electrochemical ammonia synthesis catalyzed with a CoFe layered double hydroxide – A new initiative in clean fuel synthesis,” *J. Clean. Prod.*, vol. 250, p. 119525, 2020, doi: 10.1016/j.jclepro.2019.119525.

[165] B. Saleh, G. Koglbauer, M. Wendland, and J. Fischer, “Working fluids for low-temperature organic Rankine cycles,” *Energy*, vol. 32, no. 7, pp. 1210–1221, Jul. 2007, doi: 10.1016/j.energy.2006.07.001.

[166] H. Yu, X. Feng, and Y. Wang, “Working Fluid Selection for Organic Rankine Cycle (ORC) Considering the Characteristics of Waste Heat Sources,” *Ind. Eng. Chem. Res.*, vol. 55, no. 5, pp. 1309–1321, Feb. 2016, doi: 10.1021/acs.iecr.5b02277.

[167] A. Ahmadzadeh, M. R. Salimpour, and A. Sedaghat, “Thermal and exergoeconomic analysis of a novel solar driven combined power and ejector refrigeration (CPER) system,” *Int. J. Refrig.*, vol. 83, pp. 143–156, Nov. 2017, doi: 10.1016/j.ijrefrig.2017.07.015.

[168] A. Baghernejad and M. Yaghoubi, “Exergoeconomic analysis and optimization of an Integrated Solar Combined Cycle System (ISCCS) using genetic algorithm,” *Energy Convers. Manag.*, vol. 52, no. 5, pp. 2193–2203, May 2011, doi: 10.1016/j.enconman.2010.12.019.

[169] N. Sarabchi, S. M. S. Mahmoudi, M. Yari, and A. Farzi, “Exergoeconomic analysis and optimization of a novel hybrid cogeneration system: High-temperature proton exchange membrane fuel cell/Kalina cycle, driven by solar energy,” *Energy Convers. Manag.*, vol. 190, pp. 14–33, Jun. 2019, doi: 10.1016/j.enconman.2019.03.037.

[170] N. Kusnetz, “Fossil Fuel Companies Are Quietly Scoring Big Money for Their Preferred Climate Solution: Carbon Capture and Storage - Inside Climate News,” *Inside Climate News*, 2021.

Appendix

Copyright Permission

The high similarity of this thesis is mainly due to the published journal papers by the candidate. As a result, some critical information, equations and illustrations which cannot be revised without losing the fundamental essence of the work were maintained. For this reason, permissions were duly obtained from the publishers to include this information in the thesis.

The following is the obtained permission from the publisher Elsevier for the reuse of the published work based on this Ph.D. thesis.

Article: Submission declaration and verification in the Guide for authors:

"*Submission of an article implies that the work described has not been published previously (except in the form of an abstract, a published lecture or academic thesis, see 'Multiple, redundant or concurrent publication' for more information), that it is not under consideration for publication elsewhere, that its publication is approved by all authors and tacitly or explicitly by the responsible authorities where the work was carried out, and that, if accepted, it will not be published elsewhere in the same form, in English or in any other language, including electronically without the written consent of the copyright-holder. To verify originality, your article may be checked by the originality detection service Crossref Similarity Check.*"